THE DEVELOPMENT OF AN INJECTION SYSTEM FOR A COMPACT H^- CYCLOTRON, THE CONCOMITANT MEASUREMENT OF INJECTED BEAM PROPERTIES AND THE EXPERIMENTAL CHARACTERIZATION OF THE SPIRAL INFLECTOR

by

MORGAN PATRICK DEHNEL

B.A.Sc., The University of British Columbia, 1986
M.A.Sc., The University of British Columbia, 1987

A THESIS SUBMITTED IN PARTIAL FULFILLMENT OF

THE REQUIREMENTS FOR THE DEGREE OF

DOCTOR OF PHILOSOPHY

in

THE FACULTY OF GRADUATE STUDIES

(Department of Physics)

We accept this thesis as conforming
to the required standard

THE UNIVERSITY OF BRITISH COLUMBIA

February 1995

In presenting this thesis in partial fulfilment of the requirements for an advanced degree at the University of British Columbia, I agree that the Library shall make it freely available for reference and study. I further agree that permission for extensive copying of this thesis for scholarly purposes may be granted by the head of my department or by his or her representatives. It is understood that copying or publication of this thesis for financial gain shall not be allowed without my written permission.

Department of PHYSICS

The University of British Columbia
Vancouver, Canada

Date MARCH 3, 1995

DE-6 (2/88)

ABSTRACT

This thesis addresses two major problems. One is of interest to commercial cyclotron manufacturers and the other is of interest to the accelerator physics community.

The industrial problem was to produce a compact and modular ion source and injection system for the new TR13 H^- cyclotron, which is capable of transporting and injecting a high quality and well matched beam into the cyclotron.

The accelerator physics problem was to advance the science of inflector ion optical design, analysis and troubleshooting from the realm of pure simulation to the realm of measurement and experimentation.

The industrial problem was solved by designing candidate injection systems in parallel with the TR13 cyclotron design. These systems were fabricated and then experimentally optimized along with the ion source on a 1 MeV test cyclotron. This work resulted in a set of ion source and injection systems with well documented and understood properties. The recommended solution for the TR13 was a cost effective injection system composed of only two axially rotated quadrupole magnets.

The accelerator physics problem is the lack of measured cyclotron inflector optical data and beam related properties in the immediate vicinity of a cyclotron inflector. This required the development of an experimental technique to overcome the numerous technical difficulties associated with making measurements near a device as inaccessible as a cyclotron inflector. A diverse assembly of equipment and procedures was required: a well understood injection system, a pinhole collimator for producing beamlets for ray-tracing, a specially configured center region to expose the inflector to view, a system of scintillators in close proximity to the inflector for producing visible beamspots, a TV camera and frame grabber to record images and a set of image analysis and data processing procedures. The results obtained using this technique were: (a) measured constraints on the coefficients of an inflector's transport matrix, (b) measurement of the beam's centering, size, shape and orientation in phase space at the entrance and exit of an inflector, (c) measurements of beam displacement as a function of field and energy perturbations at an inflector exit and (d) comparison of an inflector simulation code's capabilities against detailed measured data. Such properties of a beam have not heretofore been determined experimentally.

TABLE OF CONTENTS

LIST OF TABLES

LIST OF FIGURES

LIST OF ACRONYMS AND ABBREVIATIONS

• Amps	Amperes
• a.u.	arbitrary units
• AWG	American wire gauge
• bmp	bitmap
• CASINO	CAlculation of Spiral Inflector Orbits: a computer program
• cc/min	cubic centimetres per minute
• CCW	Counter ClockWise
• coll	collimator
• CL	Centre Line
• cm	centimetre
• C.R.M.	Centre Region Model cyclotron
• CW	ClockWise
• c/w	complete with
• CYCLONE	a computer program for performing cyclotron ion-optical calculations
• DC	Direct Current
• ex	exit
• en	entrance
• GeV	Giga-electron Volt
• H^-	negative Hydrogen ion
• ha	half-turn
• IBS	Ion source BeamStop
• I.D.	Inner Diameter
• INF	INFlector
• I.S.	Injection System
• I.S.I.S.	Ion Source and Injection System
• keV	kilo-electron Volt
• kG	kiloGauss
• kV	kiloVolt
• kW	kiloWatt
• L###/PL##/EL##/NL or WL	This abbreviation corresponds to ion source configurations of Length L = ### millimetres, Plasma electrode bore PL = ## millimetres, Extraction eLectrode bore EL = ## millimetres, and an extraction electrode with No Lip (NL) or With Lip (WL). Refer to Figure 4.4.
• mA	milli-Ampere
• μA	micro-Ampere
• max	maximum
• MeV	Mega-electron Volt
• Mhz	MegaHertz
• mm	millimetre
• mrad	milliradian
• mTorr	milliTorr
• NE102	a plastic scintillator material
• P.E.T.	Positron Emission Tomography
• PLC	Programmable Logic Controller
• Q#	Quadrupole magnet number
• Q-based	Quadrupole magnet based
• 2Q	an injection line composed of two Quadrupole magnets
• 3Q	an injection line composed of three Quadrupole magnets
• 4Q	an injection line composed of four Quadrupole magnets
• R	Radius

• RELAX3D	a program for calculating electric fields via a relaxation technique
• RF	Radio-Frequency
• rms	root mean square
• SQQ	an injection line composed of a Solenoid magnet and two non-identical Quadrupole magnets
• tga	targa
• TR	designation given to cyclotrons manufactured by Ebco Technologies
• TR13	a 13 MeV cyclotron manufactured by Ebco Technologies
• TR30	a 30 MeV cyclotron manufactured by Ebco Technologies
• TRANSOPTR	a charged particle transport program
• TRANSPORT	a charged particle transport program
• TRIUMF	TRI–University Meson Facility
• TV	TeleVision
• ZGOUBI	a charged particle transport program

ACKNOWLEDGMENTS

I would like to express my gratitude to Dr. E. Auld and Dr. K Erdman for their supervision, guidance and mentorship as my academic and industrial supervisors, respectively. They both gave freely of their time and provided much useful intellectual, strategical and/or administrative support.

I would like to thank Ebco Technologies, TRIUMF and the B.C. Science Council for financially supporting this work.

Numerous scientific, engineering, technical and office staff members from both TRIUMF and Ebco Technologies offered helpful suggestions throughout the course of my thesis work. I thank all of these people for their time and effort.

Dr. T. Kuo provided me with an extensive education in how to perform a thorough "hands on" experiment. His patience and perseverance are greatly appreciated, and his contributions as a co-experimenter in the work of chapter 4 are gratefully acknowledged.

I would like to thank Dr. L. Root for the many many long discussions we had on the topic of accelerator physics, and the helpful suggestions he offered from time to time.

I would like to thank Dr. A. Altman, Dr. R. Baartman, Dr. B. Laxdal, Dr. K. Jayamanna, Dr. B. Milton, Dr. P. Schmor, Dr. G. Stinson and Dr. D. Yuan for the discussions we had from time to time on the topic of accelerator physics.

I would like to thank my wife, Trish, for her support of my work and her patience over the past four years. I would also like to thank the rest of my family for their support of all my endeavours, and, in particular, Kent for drawing many of the figures in this thesis.

1.0 INTRODUCTION

Over the last 20 years a rapid growth in the use of particle accelerators for the purpose of producing biomedical radioisotopes has occurred [1]. The accelerator of choice has generally been the cyclotron [1–8], and in recent years compact, low-maintenance, highly efficient, and, most importantly for the radioisotope producer, "user-friendly" commercial cyclotrons have become the norm [9–23].

The TR13 is a commercial cyclotron which has been specifically developed to produce radioisotopes in a hospital environment for Positron Emission Tomography (P.E.T.) [24–25]. The TR13 is a self-shielded H^- cyclotron capable of providing a total of 100 μA of dually extracted beam onto its production targets. This cyclotron has recently been built by Ebco Technologies through a technology transfer agreement with Canada's national meson research facility TRIUMF.

One of the key features of the TR13 cyclotron system is the external *ion source* and the axial *injection system* (I.S.I.S.) which prepares, transports and injects the beam into the cyclotron. The most critical I.S.I.S. component is the inflector. The inflector has the important task of transporting the axially injected beam through a curved trajectory so that upon leaving its exit the beam is in the acceleration plane of the cyclotron and properly centered for further acceleration. Besides altering the central trajectory of the beam, the inflector optically affects the beam in other ways. For example, the TR13's spiral inflector couples the axial and radial motions of the beam's ions. The inflector's importance is related to the major influence it has on the beam quality and transmission rate if its centering and other optical functions are not properly utilized.

This thesis describes the solution of two main problems. The first problem addressed in the thesis is the selection of a compact and modular I.S.I.S. for the TR13 cyclotron. The selected I.S.I.S. has good beam transport characteristics and is capable of injecting a high quality well matched beam into the cyclotron. The solution of this problem is of considerable interest to commercial cyclotron manufacturers.

Before introducing the second problem addressed in this thesis, a brief discussion of the state of the art with respect to inflector design, analysis and troubleshooting is necessary.

A number of analytically and numerically based software codes [26–33] have been developed for designing inflectors and studying their optical behaviour. These codes are certainly useful, but are limited

in the following ways. Analytical solutions to the inflector problem can only be achieved when special ideal electric and magnetic field configurations are used to describe the inflector. Codes which take this approach are not able to represent truly the actual behaviour of the inflector. The numerically based codes can integrate ion trajectories through full three-dimensional field maps. The accuracy of the numerical codes depends on any approximations inherent in the field maps, any approximations inherent in the codes, the integration technique used and the manner in which any available adjustable parameters have been set. These numerically based codes are only error checked against the special analytical cases. In fact, neither analytical nor numerical inflector simulation codes have ever been checked against detailed measured data.

Techniques for analyzing inflector performance and, in particular, techniques for troubleshooting actual beam quality or transmission problems are of considerable interest. As is clearly shown by the literature [26–46], the cyclotron community has always used the aforementioned simulation techniques to analyze the performance of a cyclotron inflector. Measured inflector transport characteristics and the beam's measured phase space distributions and centering in the vicinity of the inflector have never been available for assessing inflector performance. This is a very unsatisfactory situation because the number of parameters which can affect inflector performance is large and at present the only hard data used for analysis is the beam transmission rate or possibly the size and emittance of the beam after it has been accelerated through several turns in the cyclotron. This means that even if computer simulations are capable of representing reality well, there is insufficient information to establish exactly what is occurring.

The lack of detailed measured data pertaining to the optics of cyclotron inflectors is related to the inflector's inaccessibility and to many specific technical problems which must be overcome in the confined space surrounding the inflector.

The second problem addressed in this thesis is that there have been no techniques available for obtaining measured inflector transport characteristics and the beam's properties in the immediate vicinity of the inflector. As a consequence of this, scant measured data on actual inflector performance has been published, cyclotron inflector simulation codes have not been compared to such data, and the analysis of

inflector behaviour has not been studied with respect to such data. This thesis provides a solution to this by:

i) describing an experimental technique complete with a description of all necessary hardware, software, data handling procedures and analysis strategies which enables one to measure the inflector's optical characteristics and the beam's properties in the immediate vicinity of the inflector.

ii) documenting the first transport matrix representing a cyclotron inflector in its actual operating environment to be determined using coefficients constrained by measured data.

iii) documenting the first measurements of the injected beam's properties at the entrance and exit of a cyclotron inflector. The measured properties include: the centering, size, shape and orientation of the beam in four-dimensional phase space (x, dx/dz, y, dy/dz).

iv) documenting the first measurements of beam displacement at the exit of a cyclotron inflector as a function of changes in the inflector electrode potentials, the cyclotron magnetic field and the beam kinetic energy.

v) comparing simulations produced by an inflector optics code, CASINO [33], to measured data for the first time. The measured data from points ii, iii and iv are used for this comparison.

The chapters of this thesis are laid out in the order in which the work was completed. Chapter 2 describes the basics of single-particle and multi-particle (beam) transport as an introduction to the accelerator physics pertinent to this thesis. In addition, the basic sub-systems used in the I.S.I.S. are described.

In chapter 3 injection system design is done in parallel with the TR13 cyclotron design yielding primary and secondary injection system candidates [47]. The availability of the TR type center region model 1 MeV test cyclotron (C.R.M.) [48] for prototype I.S.I.S. testing impacts heavily on the design stage, as the number and variety of design studies can be reduced when prototype testing is feasible. Consequently, not one but three types of injection line are proposed for prototype testing, these being the 4Q, 3Q and 2Q (four, three and two quadrupole magnet) injection lines. The chapter closes with a listing of the engineering details needed for producing the prototype injection lines.

Chapter 4 discusses the prototype I.S.I.S. testing using the 1 MeV test cyclotron facility. The chapter begins by describing the re-commissioning of the test cyclotron with an existing I.S.I.S. normally used by the TR30 [49] cyclotron. The performance of this I.S.I.S. establishes a baseline to compare with the 4Q, 3Q and 2Q systems. Subsequent to the baseline tests, an investigation of the ion source, and, in particular, its lens configuration in the 0–7 ampere arc current range is undertaken. The study centers

around investigating and improving the ion source emittance and the total output current [50]. The beam transmission capabilities of the various prototype injection lines from the ion source to the inflector exit beamstop and to the 1.125 MeV beamstop are documented next. Of particular interest are measurements of beam transmission as a function of injection line axial orientation angle, which have been discussed theoretically in the literature [26, 27, 51–54], but have not been extensively studied experimentally. The chapter culminates with a detailed study of the radial and axial characteristics of the accelerated beam in the central region of the test cyclotron. Emittances are calculated based on diagnostic probe scans and a technique is described for establishing the accelerated RF phase band of the cyclotron. The sensitivity of beam current transmission rates to changes in the main magnetic field, the inflector electrode potentials, and the injection line quadrupole field settings are reported.

Work accomplished in Chapter 4 established a nominal ion source configuration, a 4Q injection line and a test cyclotron set-up whose operating parameters and beam transmission characteristics were well understood. This entire arrangement provided a useful "tool" for investigating the ion optical properties of the cyclotron's spiral inflector.

Chapter 5 begins by describing the specialized equipment required for the inflector experiments. In addition, modifications to the test cyclotron required to facilitate the inflector experiments are described. The first experimental results discussed are the full beam size, shape, orientation and centering at the inflector entrance and exit, and after one half-turn. Subsequent to this, beamlet ray tracing experiments are used to produce a set of measured constraints on the elements of the linear ion-optical transport matrices of the inflector. Inflector transport matrices from the software code CASINO are then compared to the measured constraints. The phase space distribution of the beam at the inflector exit is computed using a novel technique, and the emittance growth due to inflector cross-plane coupling [55] is computed. Lastly, beam displacements at the inflector exit as a function of the cyclotron magnetic field, the inflector electrode potentials and the beam's kinetic energy are reported and compared to simulations.

Chapter 6 summarizes the main results of the thesis, gives the recommended injection line for the TR13 cyclotron, and presents general conclusions concerning the results and techniques presented in this thesis. Lastly, suggestions for future work are given.

2.0 FUNDAMENTALS OF AXIAL INJECTION

This chapter covers the basic concepts needed to understand the goals of this thesis and the means by which these goals are achieved. The chapter is divided into two main sections. The first section gives an overview of charged particle optics and transport, and the second section discusses the main sub-systems required to axially inject an ion beam into a cyclotron.

2.1 CHARGED PARTICLE OPTICS AND TRANSPORT

A large number of charged particle beam transport systems have been built over the past fifty years, and, thus, it is not surprising that there are a number of good books and papers describing such systems [56–68]. Charged particle transport systems are typically designed to guide an input charged particle beam to the exit of the transport system with minimal particle loss and without a degradation in beam quality. In addition, specific optical properties may be forced upon the beam during transport to enhance the usefulness of the beam upon exiting the system. Beam transport as it pertains to this thesis involves both of these concepts. The injection system is intended to provide the transport of the ion source H^- beam to the central region of the cyclotron with a high transmission rate and minimal beam quality degradation. As well, the beam character is optically adjusted to be most appropriate for the acceleration of the beam within the cyclotron. The rest of this section is dedicated to illustrating these concepts and techniques in more detail.

2.1.1 PHASE SPACE

A good description of phase space is given by Banford [57]:

"Consider a particle moving in a three dimensional Cartesian coordinate system 0x, 0y, 0z. For present purposes a particle is completely specified if we know where it is and where it is going, that is to say we require to know the three coordinates x, y, z and the three momentum components p_x, p_y, p_z. All this information can be represented by the position of a point in a six-dimensional space with coordinates x, y, z, p_x, p_y, p_z. This six-dimensional space is known as phase space."

A representative H^- ion which has just been extracted from the ion source is located in phase space, and as it proceeds through the injection system it describes a curve in phase space. Similarly, each of the

beam's ions can be represented by a point in phase space, and beam transport can be considered to be the manipulation of the finite region occupied by these points in phase space.

Having introduced the concept of phase space, it is now prudent to introduce Liouville's theorem. The ramifications of this theorem affect nearly all aspects of charged particle transport. As presented in [57], the theorem states that:

"Under the action of forces which can be derived from a Hamiltonian, the motion of a group of particles is such that the local density of the representative points in the appropriate phase space remains everywhere constant."

The consequence of this theorem is that if satisfied, the hypervolume of the region occupied by the beam in phase space is conserved. The orientation and shape of the beam region may change throughout the transport process. However, if a particular phase space dimension of the beam shrinks, one or more of the other dimensions grows to maintain the hypervolume occupied by the beam. It is often the case that the hypervolume of the beam in a lower dimensional sub-space is also conserved during transport. This occurs when the motions of the particles in the sub-space are independent or uncoupled from their other phase space dimensions. In fact, a large number of transport systems are designed such that the (x, p_X), (y, p_Y) and (z, p_Z) sub-spaces act independently of each other.

Transport systems are usually designed to ensure that Liouville's theorem is applicable. A Hamiltonian can be written for any charged particle beam acted upon by forces arising from external macroscopic electric and/or magnetic fields. For such beams, the theorem applies. However, if particles are lost from the beam due to collimation, if interactions with targets occur, or if synchrotron radiation is emitted by the beam, the theorem does not apply [69]. Although a Hamiltonian in a higher dimensional space can be found, in principle, for electrostatic interactions between individual charged particles within the beam (space charge) [57], we limit ourselves to six dimensions. Within this six dimensional space, the beam does not adhere to Liouville's theorem for space charge interactions.

2.1.2 LINEAR CHARGED PARTICLE TRANSPORT

2.1.2.1 Coordinate System

A fixed (x, y, z) coordinate system is of limited utility for most transport systems. The mathematical expression for the trajectory of an individual particle becomes extremely complicated in all but the

simplest transport systems when a fixed coordinate system is used. The coordinate system which is best suited to describing charged particle trajectories is the curvilinear system illustrated in Figure 2.1. This is an orthogonal right-handed coordinate system which moves with an ideal mono-energetic charged particle along the central trajectory of the transport system. The unit vector **z** is the coordinate tangential to the central trajectory and in the direction of motion. The transverse coordinates **x** and **y** measure the displacement of a particle from the central trajectory. It is usual for **x** to be the coordinate in the lab horizontal plane and **y** to be the coordinate in the lab vertical plane.

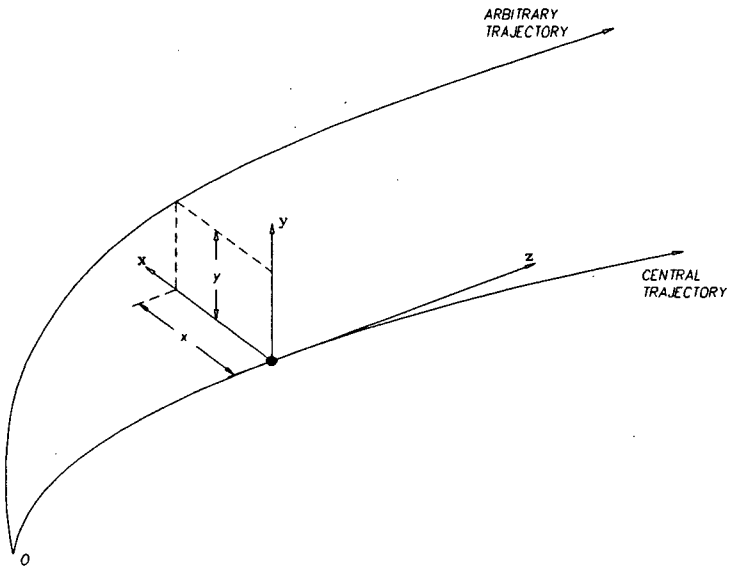

Figure 2.1: *The curvilinear coordinate system.*

The commonly used TRANSPORT [63] formalism for describing charged particle transport utilizes the curvilinear coordinate system described above. The full description of the six coordinates in TRANSPORT's version of phase space are as follows:

- **x** = the horizontal displacement of the arbitrary trajectory or ray with respect to the central trajectory.
- **x'** = the angle the arbitrary ray makes in the horizontal plane with respect to the central trajectory.
- **y** = the vertical displacement of the arbitrary ray with respect to the central trajectory.
- **y'** = the angle the arbitrary ray makes in the vertical plane with respect to the central trajectory.
- **l** = the path length difference between the arbitrary ray and the central trajectory.
- δ = the fractional momentum deviation of the ray from the central trajectory ($\Delta p/p_{Tot}$).

The momenta in Banford's description of phase space are not explicitly used here. However, they are included in the sense that the angular divergence of a particle relative to the beam axis (x' = dx/dz, and y' = dy/dz) is equal to the ratio of transverse and axial momenta.

The fractional momentum deviation in the beam output by the TR13 ion source is negligible (≈1/50,000), and the path length difference associated with arbitrary trajectories is of no consequence in this thesis. Thus, phase space from this point hence will be limited to the four dimensions (x, x', y, y'). As is shown in [55, 57], Liouville's theorem still applies in this lower dimensional phase space.

2.1.2.2 Linear Transport Matrices

Charged particle transport can be simplified to a process of matrix multiplication. The particle's coordinates are contained in a column vector $\mathbf{X}_1 = (x_1, x'_1, y_1, y'_1)$. The subscript 1 indicates that the transverse coordinates are with respect to the curvilinear coordinate system at some position 1 along the central trajectory within the transport system. Similarly, the particle's coordinates at some position 2 along the central trajectory are then $\mathbf{X}_2 = (x_2, x'_2, y_2, y'_2)$. The goal in charged particle transport is to be able to calculate a particle's coordinates at 2 knowing $\mathbf{X}_1$ and the linear transport matrix $\mathbf{R}_{12}$. The matrix $\mathbf{R}_{12}$ provides a very good approximation to the optical transformation that occurs between positions 1 and 2. The multiplication that is performed is as follows:

$$\mathbf{X}_2 = \mathbf{R}_{12} \cdot \mathbf{X}_1. \tag{2.1}$$

The standard linear transport matrices used in this thesis can all be derived using theory based on mirror symmetric magnetic systems. The derivation of these matrices starts, for a particle of mass m and charge q, with the Lorentz equation

$$\frac{d\mathbf{p}}{dt} = \frac{d(m\mathbf{v})}{dt} = q(\mathbf{v} \times \mathbf{B}), \tag{2.2}$$

where **p** is the momentum, **v** is the velocity, **B** is the magnetic flux density, and t is time.

By breaking this equation into its constituent (x, y, z) components, changing the variable of differentiation from time to distance along the trajectory, and performing some algebraic manipulation as done in [65, 69], one arrives at the following two equations

$$x'' = \frac{q}{p}\sqrt{1 + x'^2 + y'^2}[x'y'B_x - (1 + x'^2)B_y + y'B_z] \tag{2.3}$$

$$y'' = \frac{q}{p}\sqrt{1 + x'^2 + y'^2}[(1 + y'^2)B_x - x'y'B_y - x'B_z], \tag{2.4}$$

where primes (') indicate differentiation with respect to distance along the trajectory. As yet, no simplifying assumptions have been made. Therefore, equations 2.3 and 2.4 are valid to any order.

In solving equations 2.3 and 2.4 for the linear case, one makes the paraxial ray approximation which removes terms of order higher than x' and y'. To tailor the equations to describe transport through a particular device, one uses the appropriate magnetic field expansion for the device to substitute for the variables (B_x, B_y, B_z). The simplest example is the case of a field free region, which is known as a drift space in the jargon of charged particle optics. Equations 2.3 and 2.4 become

$$x'' = 0 \quad \text{and} \quad y'' = 0, \tag{2.5}$$

for a drift space.

Solving (2.5) for a drift of length L between positions 1 and 2 along the central trajectory results in the solution

$$x_2 = x_1 + Lx_1' \quad \text{and} \quad x_2' = x_1' \tag{2.6}$$
$$y_2 = y_1 + Ly_1' \quad \text{and} \quad y_2' = y_1', \tag{2.7}$$

which can be written as

$$\begin{pmatrix} x_2 \\ x_2' \\ y_2 \\ y_2' \end{pmatrix} = \begin{pmatrix} 1 & L & 0 & 0 \\ 0 & 1 & 0 & 0 \\ 0 & 0 & 1 & L \\ 0 & 0 & 0 & 1 \end{pmatrix} \cdot \begin{pmatrix} x_1 \\ x_1' \\ y_1 \\ y_1' \end{pmatrix}. \tag{2.8}$$

The linear transport matrix $\mathbf{R}_{12}$ for any magnetic optical element can be derived following this same procedure. An analogous procedure can, of course, be developed for electric field based optical elements. The standard optical elements used in the study undertaken for this thesis include: the drift space, the dipole magnet, the quadrupole magnet, the solenoid magnet and the coordinate rotation.

Linear transport matrices are also used to represent non-standard magnetic and/or electric field based optical elements. The injection system has three such non-standard optical elements. They are the axial bore of the cyclotron, the spiral inflector, and the central region of the cyclotron. The appropriate matrix for a non-standard element is produced by first integrating four linearly independent paraxial particle coordinate vectors from the input of the element (position 1) through to the output of the element (position 2) using an orbit tracking code such as CASINO or CYCLONE [70], and appropriate field maps.

The four input particle coordinate vectors (X^1_1, X^2_1, X^3_1, X^4_1) are assembled into the columns of a matrix as are the four output beam column vectors (X^1_2, X^2_2, X^3_2, X^4_2). One can then solve for the linear transport matrix representing the device by performing the following matrix operation

$$\left[X^1_2, X^2_2, X^3_2, X^4_2\right] \cdot \left[X^1_1, X^2_1, X^3_1, X^4_1\right]^{-1} = \mathbf{R}_{12}. \tag{2.9}$$

A linear transport system is usually composed of a number of optical elements. If the input coordinates of a charged particle are known, then the particle coordinates at the output of an N element system can be calculated as follows

$$\mathbf{X}_N = \mathbf{R}_{(N-1)N} \cdot \cdots \cdot \mathbf{R}_{12} \cdot \mathbf{X}_1. \tag{2.10}$$

Space charge forces can be included as an impulse (thin lens) after each application of an **R** matrix. The strength of each impulse is calculated with the linear space charge approximation [71], which is a function of the beam current and cross-section. In the code TRANSPORT the distance traveled between each impulse must be optimized for best results. In the code TRANSOPTR [72] linear space charge forces, and all other first order optical elements can be computed using an infinitesimal transport matrix formalism which elegantly incorporates the fact that **R** becomes a function of the beam size when space charge forces are included [73].

2.1.3 HIGHER ORDER CHARGED PARTICLE TRANSPORT

In single pass transport systems the effect of non-linearity's are often quite small. However, in accelerators and storage rings where particles may be transported through many tens of thousands of identical focusing elements, the compounding of even relatively small higher order effects can have a dramatic effect on beam size and stability.

If higher order terms from equations (2.3) and (2.4) are retained in the procedure of section 2.1.2.2., one can construct matrices which represent transport to a higher order. For example, to second order, as described by [65] and used in TRANSPORT and TRANSOPTR, one can compute the coordinates of an output beam vector (position 2) in terms of the original (position 1) using

$$\mathbf{X}(i)_2 = \mathbf{R}(i,j)_{12} \cdot \mathbf{X}(j)_1 + \mathbf{T}(i,j,k)_{12} \cdot \mathbf{X}(j)_1 \cdot \mathbf{X}(k)_1 \tag{2.11}$$

where **T** is the second order transport matrix. Most charged particle transport programs offer at least a second order option.

In recent years, the need for dealing with higher order charged particle optics for repetitive systems has lead to sophisticated differential algebraic techniques which provide maps from initial beam coordinates and system parameters to final beam coordinates. These maps can be created to arbitrary order and can describe standard optical elements, fringe fields and even radiation effects. These techniques are not necessary for the work in this thesis and have only been mentioned for completeness. The reader can refer to [74] and [75] for an introduction to these techniques.

As alluded to in section 2.1.2.2, another common technique for studying nonlinear effects is to determine a particle's trajectory by numerically solving the equation of motion for the particle as it passes through the appropriate electric and magnetic field maps. The accuracy of such techniques depends on the integration algorithm, the step size and any approximations that are inherent in the field maps. The codes CASINO, CYCLONE and ZGOUBI [76] are three such codes used in this thesis.

2.1.4 CHARGED PARTICLE BEAM TRANSPORT

Thus far single-particle transport has been discussed. It is, however, usually much more informative to consider the transport of a multi-particle beam. In particular, one is often interested in the transverse envelope of the beam as a function of position along the central ray. One way to simulate charged particle beam transport is to choose a number of representative particles within the region occupied by the beam in phase space, and to calculate the trajectories of each of these particles with the matrix formalism introduced previously. In this manner the size of the beam can be ascertained by considering the particles with the outermost transverse coordinates at various positions along the central trajectory. This method is particularly useful when particles removed from the beam by collimation are to be considered, since this can be easily done by comparing the collimator's (x, y) boundaries with the coordinates of the particles, and then removing those particles with excessive (x, y) coordinates from further transport computations.

Liouville's theorem permits a different approach to simulating charged particle beam optics. One can bound the beam with an appropriately sized and shaped surface in phase space, and then transport this surface using the fact that the hypervolume of this closed surface in phase space must remain constant.

The standard surface to use for this purpose is an ellipsoid. An ellipsoid is chosen for two main reasons. The first is that the transport of an ellipsoid is relatively easy to describe with the transport matrix approach, and the second is that, although actual beams can have almost any shape in phase space, the ellipsoidal shape corresponds well with measured beams, as is the case in this thesis.

The equation for an n dimensional ellipsoid defined by a positive definite symmetric matrix σ is given by [67]

$$\mathbf{X}^T\sigma^{-1}\mathbf{X} = 1. \tag{2.12}$$

The hypervolume enclosed by such an ellipsoid is

$$\mathbf{V} = \frac{\pi^{n/2}}{\Gamma(n/2+1)}\sqrt{\det(\sigma)}\,. \tag{2.13}$$

As already mentioned, the two and four dimensional sub-spaces of phase space are of interest in this thesis. The hypervolume of a four dimensional (4D) ellipsoid is $(\pi^2/2)\{\det(\sigma_{4D})\}^{1/2}$, and the area of a two dimensional (2D) ellipse is given by $\pi\{\det(\sigma_{2D})\}^{1/2}$.

Recall that $\mathbf{X}_i$ corresponds to a beam vector at position (i) along the central ray. The matrix σ_i corresponds to the beam ellipsoid at this position (i), and for the two dimensional case we have

$$\mathbf{X}_i = \begin{pmatrix} x(i) \\ x'(i) \end{pmatrix} \quad \text{and} \quad \sigma_i = \begin{pmatrix} \sigma_{11}(i) & \sigma_{12}(i) \\ \sigma_{21}(i) & \sigma_{22}(i) \end{pmatrix} \tag{2.14}$$

which yields

$$\mathbf{X}_i^T\sigma_i^{-1}\mathbf{X}_i = 1 \quad \text{or} \quad \sigma_{22}x^2(i) - 2\sigma_{21}x(i)x'(i) + \sigma_{11}x'^2(i) = \det(\sigma_i). \tag{2.15}$$

Note that $\sigma_{12}(i)$ is equal to $\sigma_{21}(i)$. Beam transport from position 1 to position 2 along the central ray is accomplished within the linear matrix formalism by performing the following matrix operation

$$\sigma_2 = \mathbf{R}_{12}\sigma_1\mathbf{R}_{12}^T. \tag{2.16}$$

For beam envelope computations in either 2 or 4 dimensional spaces one could invert the σ_i matrix at each position (i) and use the analytical formulation of the ellipsoid as indicated in (2.15). However, it can be shown that the square root of the diagonal components of σ_i are the projections of the extreme points of the ellipsoid on the coordinate axes. For example, $\{\sigma_{11}(i)\}^{1/2}$ is equal to $x_{max}(i)$, and $\{\sigma_{33}(i)\}^{1/2}$ is equal to $y_{max}(i)$. Thus, a plot of the x and y envelope of the beam as a function of positions (i) along the

central ray can easily be produced by using the matrix elements of σ_i at each position (i). As an example, Figure 2.2 illustrates a projection of the four dimensional beam ellipsoid onto the (x, x') plane.

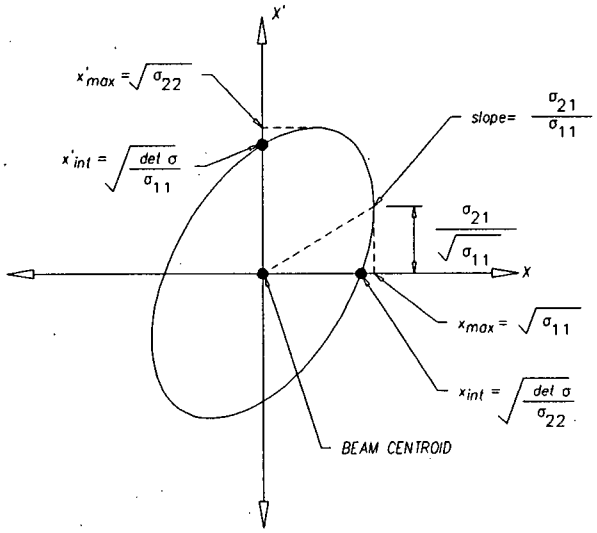

Figure 2.2: *A projection of the beam ellipsoid onto the (x, x') plane. Note the dependence of the (x, x') ellipse's size and orientation on the σ matrix elements.*

Recall that Liouville's theorem requires that the hypervolume of a beam ellipsoid at position 1 must equal that at position 2. This corresponds to requiring that

$$\det(\sigma_1) = \det(\sigma_2), \tag{2.17}$$

and this implies that

$$\det(\mathbf{R}_{12}) = 1. \tag{2.18}$$

That the determinant of the transport matrices is equal to one is just a manifestation of Liouville's theorem. This result is built into the **R** matrix as well as the higher order transport matrices as a result of their derivation from Hamiltonian based systems.

2.1.5 BEAM EMITTANCE

So far we have not addressed how best to specify the size of the ellipsoid representing the beam. The emittance is a term used to describe the size of the beam in either the (x, x') or (y, y') phase space. It is defined by the equation [55, 69]

$$\varepsilon = \sqrt{\det(\sigma)}, \tag{2.19}$$

where σ, when used to compute emittances, corresponds to the two dimensional sub-space associated with either (x, x') or (y, y'). The emittance of the beam is usually specified for the (x, x') and (y, y') phase space

projections with units of (mm·mrad). Using equation (2.13) it is apparent that the area of the beam in the (x, x') sub-space is equal to $\pi\varepsilon_{xx'}$, and in the (y, y') sub-space it is equal to $\pi\varepsilon_{yy'}$.

The emittance is a good measure of the size of the beam in the (x, x') and (y, y') phase spaces, as it is proportional to the area of the beam in these spaces. The emittance is often thought of as being related to the quality of the beam. A beam of small emittance corresponds to a high quality beam. This is so because the (x, y) projection of a small emittance beam is easier to maintain with small dimensions than a beam with a large emittance. This in turn means that a high quality beam usually loses fewer particles during transport than a low quality beam.

As indicated in [77], the emittance of a finite beam with a uniform charge distribution in phase space is well defined. However, as the charge density of most actual beams is rarely even close to being uniform, the emittance of an actual beam must then be related to the fraction of particles included within an idealized beam ellipse. A common way to compute the emittance of the idealized beam ellipse, in a manner which is a fair representation of the real physical beam it corresponds to, is to ensure that the idealized beam and the actual beam have the same integrated intensity and the same second moments [78]. The second moments of a beam in the (x, x') sub-space are

$$\overline{x^2}, \quad \overline{x'^2} \quad \text{and} \quad \overline{xx'} \tag{2.20}$$

and a representative calculation for the first term is as follows

$$\overline{x^2} = \frac{\iint x^2 \rho(x, x')dxdx'}{\iint \rho(x, x')dxdx'}, \tag{2.21}$$

where ρ is the current density. If one computes these quantities for a real beam, and represents this real beam using the idealized ellipse of uniform charge density defined by the 4rms emittance [78]

$$\varepsilon_{4rms\ xx'} = 4\left[\overline{x^2 x'^2} - (\overline{xx'})^2\right]^{1/2}, \tag{2.23}$$

then both beams will have the same integrated intensity and the same second moments. Note that ε_{4rms}, as calculated in (2.23), is accurate regardless of the real beam phase space orientation at the time of

measurement. The 4rms emittance is particularly pertinent to this thesis, as it was the emittance measured by the beam diagnostic equipment used during the experiments described in chapter 4.

Many real beams are quite closely approximated with a gaussian distribution. In the case of a real beam having a gaussian distribution, ε_{4rms} defines an idealized ellipse whose boundary contains 86% of the real beam.

An important point to note concerning emittances is that they vary as a function of the total momentum (p_{Tot}) of the beam. That this is so can be illustrated by noting that in two dimensions

$$\varepsilon_{xx'} = x_{max} \cdot x'_{int}, \tag{2.24}$$

for the x_{max} and x'_{int} defined in Figure 2.2, and since $x'_{int} = p_{x\,int}/p_{Tot}$, it is apparent that the emittance of this beam will decrease as p_{Tot} increases. So, if beams of different total momentum are being compared, as is done at different points during acceleration, one normally uses the normalized emittance of the beam. The normalized emittance of the beam is calculated with the formula

$$\varepsilon_{nxx'} = \varepsilon_{xx'}\beta\gamma = x_{max} \cdot \frac{p_{x\,int}}{mc}, \tag{2.25}$$

where m is the mass of the particle, c is the speed of light and β and γ are the usual relativistic parameters. The normalized emittance describes the beam size with respect to transverse momentum and transverse dimensions regardless of the total momentum.

2.1.6 EMITTANCE GROWTH

Recall that a beam with a small emittance is considered to be a high quality beam. This is because a beam with a small emittance is usually easier to transport than a beam with a large emittance. Therefore, it is important that every effort is made to create and maintain a beam of small emittance. Unfortunately, there are a number of ways in which the emittance can grow.

In linear transport systems with midplane symmetry, the (x, x') and (y, y') sub-spaces are uncoupled, and the emittances corresponding to these sub-spaces remain constant. A linear transport system in which cross-plane coupling exists maintains a constant beam volume in the full four dimensional phase space, however, the projection of the beam phase space ellipsoid onto the (x, x') and (y, y') sub-spaces results in

two dimensional ellipses with equal to, or larger emittances than the projected (x, x') and (y, y') beam ellipses at the beginning of the system [55].

Non-linear beam transport systems which satisfy Liouville's theorem can introduce an effective emittance growth, although the actual volume of the beam in phase space remains constant. This sort of emittance growth is illustrated for a two dimensional sub-space in Figure 2.3. As can be seen, the ellipse which effectively represents the beam, as far as the transport system is concerned, occupies a larger portion of the two dimensional sub-space than the region actually occupied by the beam particles.

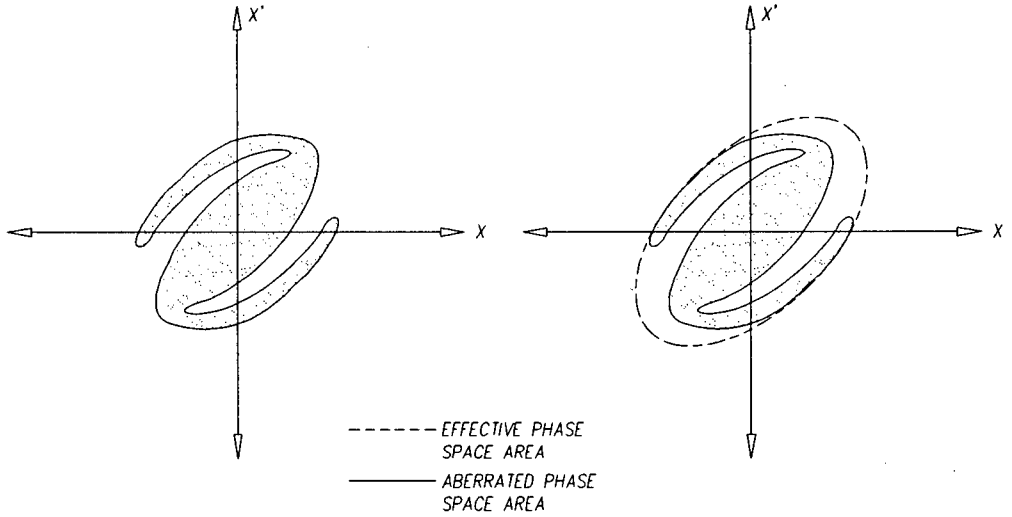

Figure 2.3: *The effective emittance region of an aberrated beam in phase space.*

When a beam is injected into an accelerator or a storage ring there are (x, x') and (y, y') machine ellipses of particular orientations and aspect ratios to which these machines force the beam ellipses to conform to. If the injected beam ellipses do not have the required (x, x') and (y, y') shapes and orientations at injection, then new beam ellipses similar to the machine ellipses become filled (refer to Figure 2.4), or effectively filled, if the beam ellipses simply rotate within the machine ellipses. If new ellipses are filled or effectively filled, emittance growth will have occurred. The process of manipulating the characteristics of a beam so that the beam ellipses are already similar to the machine ellipses at the injection point is called beam matching.

As an example of emittance growth due to mismatched beam and machine ellipses, consider the trajectories of charged particles traveling within a dipole magnetic field. To first order these particles have

sinusoidal trajectories. A few sample trajectories are shown in Figure 2.5, and the elliptical curves that these particles describe in phase space are shown in Figure 2.6.

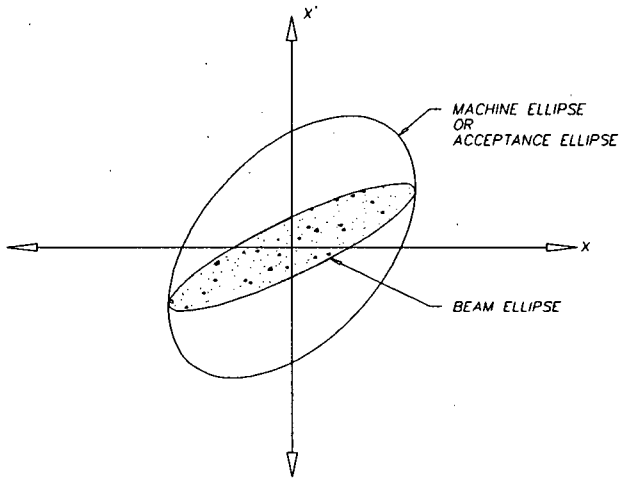

Figure 2.4: *An arbitrary machine ellipse bounding the input beam ellipse. The machine ellipse becomes filled or effectively filled yielding a new beam ellipse which has experienced emittance growth.*

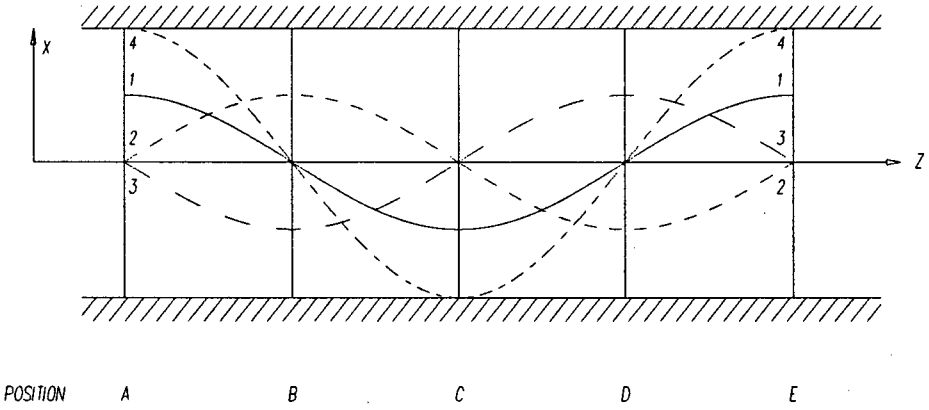

Figure 2.5: *Single-particle trajectories within a dipole magnetic field.*

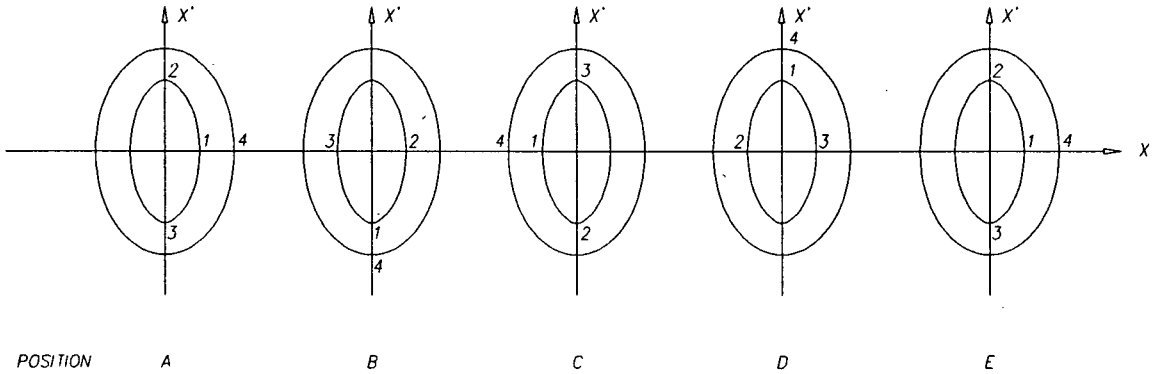

Figure 2.6: *Elliptical phase space curves described by single particle trajectories within a dipole magnetic field.*

It is apparent that the machine ellipse for a dipole magnet is an upright ellipse. It is also apparent that if a multi-particle beam of charged particles is circulating within a dipole magnetic field and if the beam particles are in phase with each other, then the beam ellipse associated with the particles will circulate as a distinct entity within a new effective beam ellipse which is similar to the dipole machine ellipse. Figure 2.7 illustrates this phenomenon.

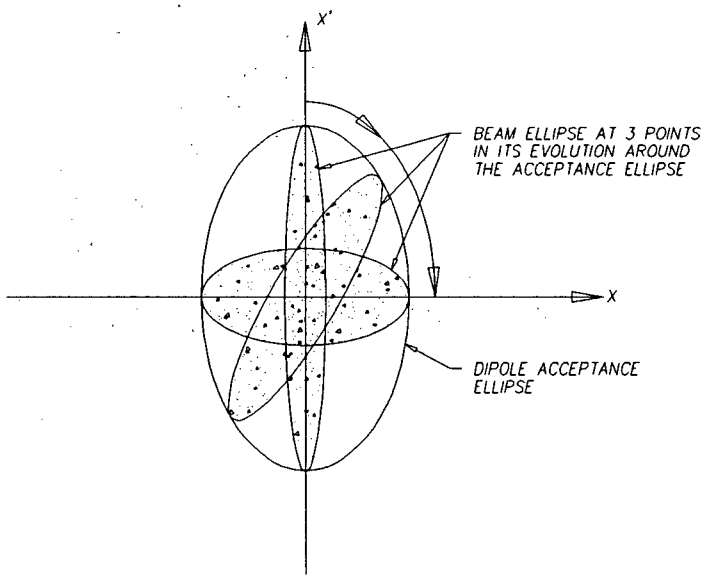

Figure 2.7: *A mismatched injected beam results in a new effective beam ellipse that is similar to the upright dipole machine ellipse.*

In the case of multi-turn extraction in a cyclotron, several circulating beam ellipses, each at a different phase, are extracted at once. When this occurs the effective beam ellipse is actually filled with particles, and the emittance growth is particularly obvious. As described in [26], the phases become mixed and the matched ellipse becomes filled.

In section 2.1.1, it was pointed out that Liouville's theorem does not apply for space charge forces, interactions with targets, or, in the case of a H^- cyclotron, interactions with extraction foils. Consequently, emittance growth is associated with these phenomena. These phenomena are not factors in this thesis, however.

2.1.7 ACCEPTANCE

At the point where the central trajectory of a charged particle beam crosses the entrance of a device in a transport system, one can define an acceptance region in four dimensional phase space. This region

corresponds to the coordinates of all particles which, if injected at the entrance of the device, would be transmitted. It is apparent that if the four dimensional hyper-volume of the beam is larger than the acceptance of a device, particles will be lost. In this case the region of phase space occupied by the beam will shrink. Typically this is not an acceptable way to create a beam with a small emittance. It is also common to define two dimensional acceptances in the (x, x') and (y, y') phase spaces with units compatible with the beam emittances.

If devices with narrow apertures in (x, y) space are present in the transport system, and if the beam emittance is relatively large, the focusing elements of the system can often be used to cause the beam ellipse to be oriented so that most of the emittance is distributed along the x' and y' axes at the location of each device with a narrow aperture. Consequently, the projection of the beam in (x, y) space will be small enough to allow a high rate of transmission through each narrow device. Tailoring the beam in this manner is one of the main goals of beam transport.

2.2 AXIAL INJECTION SUB-SYSTEMS

The following sub-sections describe the cyclotron sub-systems which are relevant to this thesis.

2.2.1 ION SOURCE

The design criteria for the overall TR13 cyclotron system largely governs the choice of ion source. The TR13 cyclotron is to be used in a confined environment where reliable, reproducible and low maintenance operation is essential. As well, an intense high-quality H^- beam is required in order to produce the necessary 100 μA of extracted protons without unwanted beam-spill [24–25]. The volume H^- ion source with multi-cusp plasma confinement is a well known choice for satisfying these particular requirements [79–81], and, thus, it is the choice of ion source for the TR13 cyclotron. The main drawback for the volume production type source is that it is less efficient in terms of power consumption than a surface conversion type source [80], however, it is a more reliable source with a brighter beam [82].

2.2.1.1 Plasma Formation

The ion source maintains a confined plasma from which H^- ions are preferentially extracted. A plasma is considered to be a collection of gaseous ions, electrons and neutrals which are charge quasi-

neutral. In the case of the TR13 ion source, the plasma confinement region is located in the ion source chamber. This chamber is supplied with a flow of H_2 gas, so the plasma is largely made up of various species of hydrogen ions and neutrals as well as electrons. The plasma is initially formed by first filling the ion source chamber, refer to Figure 2.8, with H_2 and then heating the source filament with a large circulating (approx. 200 ampere) current to cause thermionic emission of electrons which ionize the H_2 gas. An equilibrium is soon reached where a central, electrically screened and quasi-neutral environment is surrounded by a space charge dominated plasma sheath [83].

2.2.1.2 H^- Creation and Plasma Confinement

The reaction which provides the best yield of H^- in the plasma environment is a two step process [84]

$$e + H_2(v=0) \rightarrow H_2(v>0) + e \tag{2.26}$$

$$e + H_2(v>0) \rightarrow H_2^-(v>0) \rightarrow H^- + H, \tag{2.27}$$

where v refers to the vibrational quantum number.

The yield of vibrationally, and possibly rotationally [85], excited H_2 molecules in reaction (2.26) is peaked for fairly "hot" (40 eV) electrons, whereas the yield of H^- in (2.27) is maximized with relatively "cold" electrons (1 eV) [84].

As a consequence, the ion source plasma is divided into two distinct regions by a magnetic filter (BL = 0.2 kG·cm [82]) as indicated in Figure 2.9. This filter is sufficiently strong to keep energetic electrons out of the "cold" electron region, but it is not strong enough to keep the excited ions produced in the "hot" electron region out as required by (2.27) for H^- formation. A "cold" electron population is maintained by secondary emission of electrons from the plasma electrode. A bias voltage is applied to the plasma electrode to enhance surface bombardment by positive ions or electrons, depending on the sign of the bias voltage, and this results in an increased production of secondary electrons.

The bulk of the plasma encourages the existence of energetic ions and electrons as dictated by (2.26). The efficiency of generating such energetic plasma constituents is greatly enhanced by magnetic cusp confinement as illustrated in Figure 2.10. The cusp field is such that the center of the source is devoid of magnetic field lines. As a charged particle proceeds radially outwards from the plasma, it typically

encounters field lines which are perpendicular to its motion which cause the charged particle to circle back to the center portion of the plasma. Thus, energetic electrons and ions are re-cycled. This reduces the need for these plasma constituents to be generated from a "cold" state. Cusp confinement can also be described in terms of the outward kinetic pressure of the plasma being balanced by an inward magnetic pressure. Thus, any charged particle which attempts to leave the plasma with a trajectory normal to the plasma boundary is pushed back in by the increased magnetic pressure it experiences. The magnetic pressure increases in the direction normal to the plasma boundary because the density of magnetic flux lines increases in this direction.

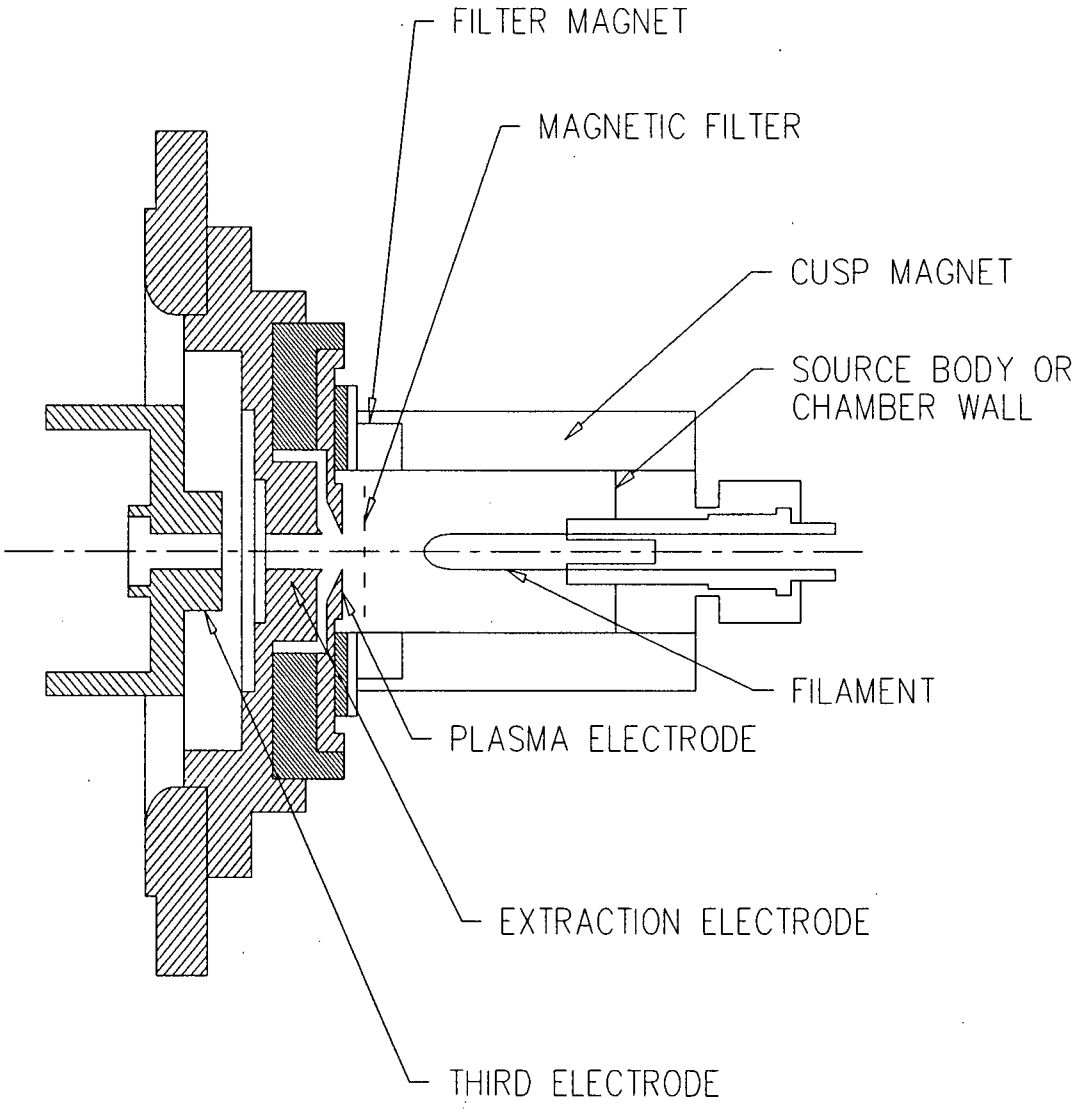

Figure 2.8: *A schematic illustration of the TR13 type ion source.*

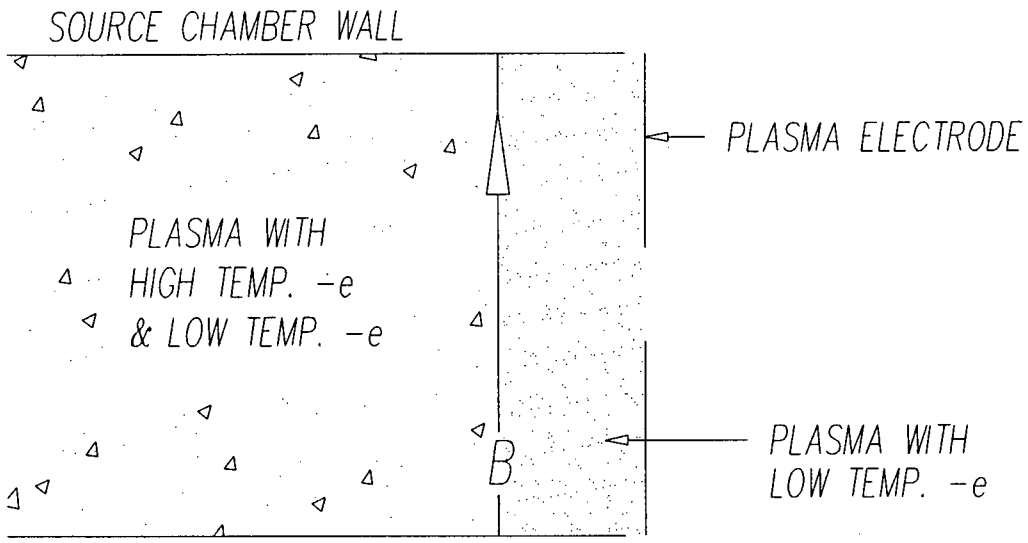

Figure 2.9: *The "hot" and "cold" electron regions of the ion source plasma.*

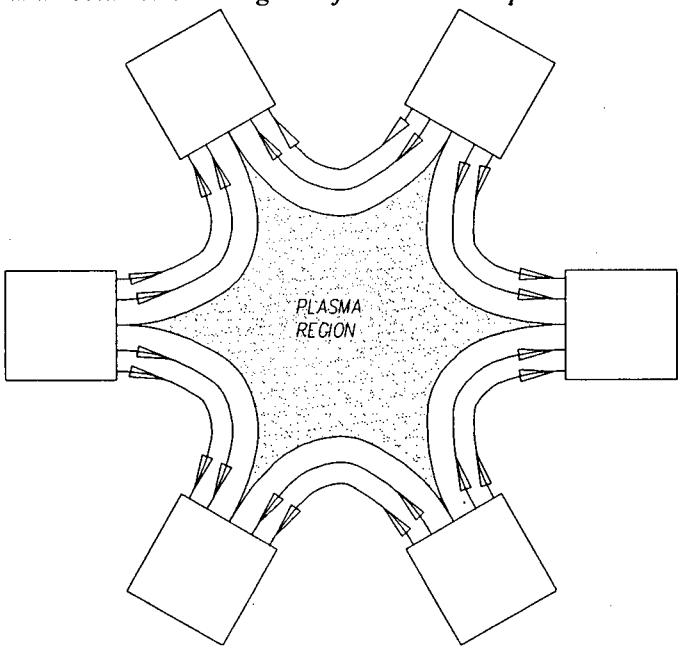

Figure 2.10: *An illustration of cusp magnetic field plasma confinement in an ion source.*

2.2.1.3 Extraction and Acceleration

A plasma shields itself from an applied electric field by a space charge dominated region which, for the bulk of the plasma, is called the plasma sheath. However, in the extraction region, the 2 to 3 kilovolt potential on the extraction electrode enlarges the size of the space charge dominated region. The plasma boundary layer is perturbed into a meniscus as shown in Figure 2.11. H^- ions that exit the plasma due to

their kinetic energy, and which do so in the meniscus region, are focused according to the meniscus curvature and are accelerated by the axial electric fields associated with the extraction electrode voltage. The extracted H^- beam is accelerated by the extraction electrode and then by the 3rd electrode, which brings the beam kinetic energy to 25 keV. These electrodes can be configured to be either focusing or defocusing.

The extraction and acceleration process is nearly axially symmetric. Perturbations to axial symmetry arise due to the removal of extracted electrons by a magnetic filter as shown in Figure 2.11, or due to slight manufacturing imperfections. This filter is sufficiently strong to remove the electrons but does not significantly affect the beam [82].

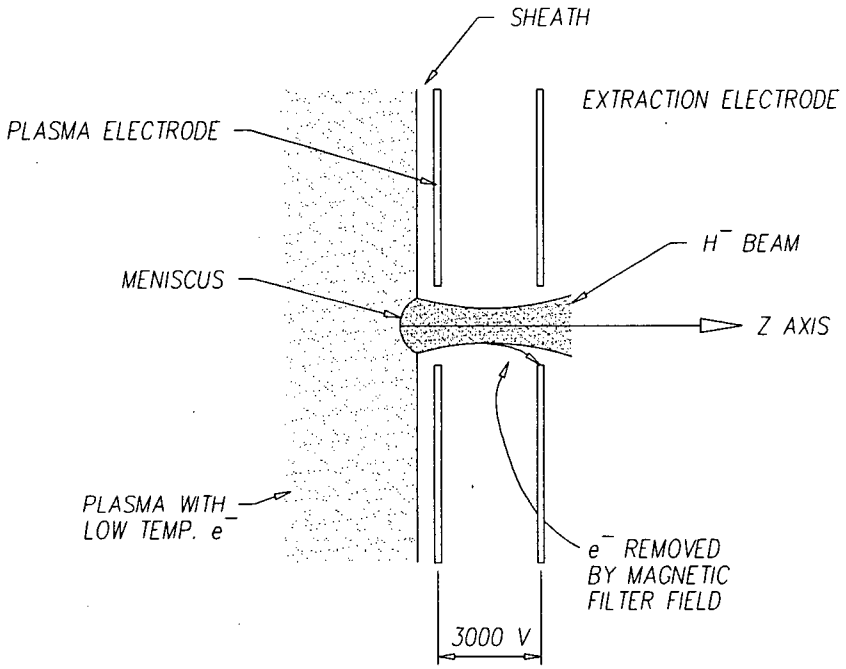

Figure 2.11: *The plasma meniscus and the electron filter in the extraction region.*

2.2.1.4 Ion Source Parameters

In order to maximize beam current on target with as little beam spill as possible throughout the TR13 cyclotron system, the initial beam current, beam emittance and the initial phase space shape associated with the beam emittance must be optimized. In a simplified sense, the beam current magnitude can be most readily increased by increasing the arc current or the diameter of the plasma, extraction and 3rd electrode apertures. In the case of the TR13, the maximum arc current has been limited to 7 amperes.

Thus, the electrode aperture diameters must be carefully adjusted to obtain sufficient current levels without overly decreasing the beam quality. An overly wide aperture diameter will often result in a flattening of the base of the meniscus which will result in an undesirable phase space projection with a large effective area as shown in Figure 2.12.

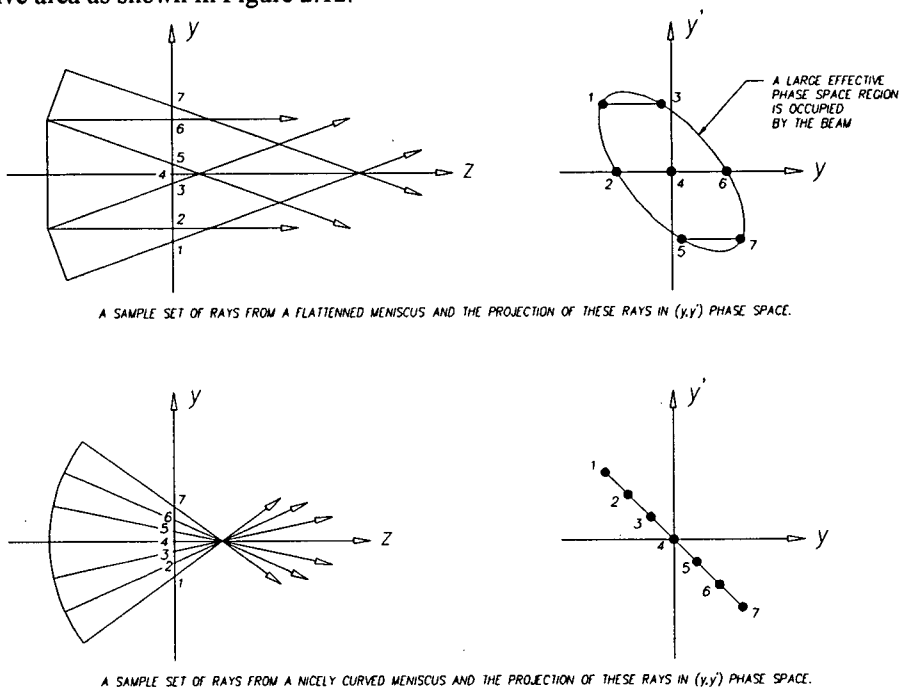

Figure 2.12: *A comparison of the phase space region occupied by a beam emanating from a nicely curved plasma meniscus to one from a flattened plasma meniscus.*

The ion source parameters which affect the matching of the source beam to the rest of the cyclotron are simply listed below without a detailed analysis. Note that the ion source is not a device which produces a beam of static characteristics to be subsequently massaged by the injection line. It is a device which can be used to optimize beam characteristics in order to produce the best optical results in concert with the whole cyclotron system. This is a point which is sometimes forgotten in the design and development of cyclotron systems.

VARIABLE TR13 ION SOURCE PARAMETERS

- Arc current
- Filament current
- Plasma electrode voltage
- Bias voltage
- Extraction electrode lip shape
- Filament and/or arc current direction
- Arc voltage
- Hydrogen flow rate
- Extraction electrode voltage
- Electrode aperture diameters
- Filament length
- Source volume

2.2.2 INJECTION LINE TRANSPORT COMPONENTS

In section 2.1.2.2 a summary of how to derive linear transport matrices is given. In this section the transport matrices for the standard optical components relevant to this thesis are revealed and a brief description of each component is given. More detailed information on these devices can be obtained from [57, 61, 65–69, 83].

2.2.2.1 Dipole Magnet

The primary use of a dipole or bending magnet is to cause a charged particle beam to be transported along a curved trajectory. There are many reasons why such a feature is desirous. Four common reasons for using a dipole magnet are to enable the transport system to avoid physical obstacles, to maintain particles on a circular or racetrack orbit, to permit momentum selection and to select different beamlines for transport. Dipole magnets can have first order focusing effects and higher order effects, as well. Dipole magnets are somewhat restrictive in their focusing capabilities because the magnitude of the magnetic field is usually fixed for achieving a particular bending requirement, and therefore the focusing effects can not be easily adjusted.

The field of a dipole magnet is as illustrated in Figure 2.13 (a). Note that the typical dipole field bows outward as shown, and that for the purposes of bending calculations an effective length is established over which the peak pole tip field effectively acts. This is best described by the following integral

$$\int \mathrm{B}\,\mathrm{dl} = \mathrm{B}_0 \mathrm{L}, \tag{2.28}$$

where B is the magnitude of the magnetic field that the central ray experiences along its trajectory, dl is the differential path length, B_0 is the peak pole tip magnetic field and L is the effective length of the magnet. The field B_0 needed for a particular beam steering requirement can be calculated by using

$$\mathrm{B}_0\rho(\mathrm{kG}\cdot\mathrm{m}) = 33.356\mathrm{p}(\mathrm{GeV}/\mathrm{c}), \tag{2.29}$$

and $\rho \approx L/\theta$. Note that ρ is the radius of curvature of the charged particle in the dipole field, p is the momentum, and θ is the azimuthal angle traversed by the particle's trajectory in the dipole field (refer to Figure 2.13 (b)). The momentum of the charged particle is calculated with the following formula

$$p = T\sqrt{1+2\frac{M}{T}}. \tag{2.30}$$

The units of p are in (GeV/c), if the rest mass M and the kinetic energy T of the particle are both given in (GeV).

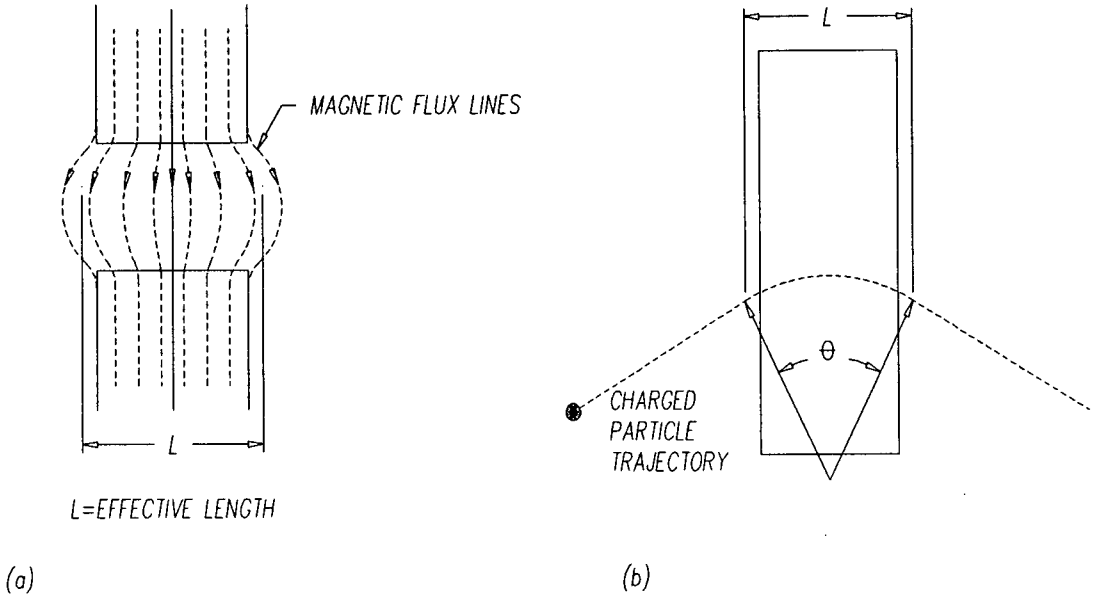

Figure 2.13: (a) *Side view of a dipole magnet* (b) *Plan view of a dipole magnet.*

The first order focusing effects of a dipole magnet can be described in terms of the field index which is defined as the negative of the fractional change in field associated with a fractional change in radius [56], and is given by

$$n = -\frac{dB/B}{d\rho/\rho}. \tag{2.31}$$

This quantity is used to describe the magnetic field at a given radius within the dipole magnet. The focusing induced beam oscillations related to the field index are known as betatron oscillations. Vertical or axial oscillations are described in terms of the axial tune ν_y which is the number of axial oscillations per revolution of the central ray around the dipole ($\theta = 2\pi$). The axial tune is calculated using

$$\nu_y = \sqrt{n}. \tag{2.32}$$

Similarly, the radial tune ν_x describes the number of radial oscillations per revolution around the dipole, and is given by

$$\nu_x = \sqrt{1-n}. \tag{2.33}$$

In terms of these tunes then, the first order transport matrix for a dipole magnet in which the central ray enters and exits normal to the pole faces is given by

$$\begin{pmatrix} \cos(\nu_x\theta) & (\rho/\nu_x)\sin(\nu_x\theta) & 0.0 & 0.0 \\ -(\nu_x/\rho)\sin(\nu_x\theta) & \cos(\nu_x\theta) & 0.0 & 0.0 \\ 0.0 & 0.0 & \cos(\nu_y\theta) & (\rho/\nu_y)\sin(\nu_y\theta) \\ 0.0 & 0.0 & -(\nu_y/\rho)\sin(\nu_y\theta) & \cos(\nu_y\theta) \end{pmatrix}. \tag{2.34}$$

Note that further first order focusing and defocusing effects can be introduced if the central ray does not enter or exit the dipole magnet normal to the pole faces. Refer to [57,61,69] for further reading on dipole optics.

2.2.2.2 Quadrupole Magnet

A quadrupole magnet is used for focusing a charged particle beam. However, unlike a lens used in the optics of light, a quadrupole magnet focuses in one plane while defocusing in the other plane. Fortunately, quadrupole magnets can be used in combination to produce an overall focusing effect in both planes. One such combination is the quadrupole doublet. A quadrupole doublet is a grouping of two quadrupoles in which, for example, one focuses in the horizontal plane and the other focuses in the vertical plane. Figure 2.14 illustrates the quadrupole magnet structure and the field lines used in vertically focusing a positively charged particle. In addition, the forces exerted on a positively charged particle moving into the magnet are shown.

The magnetic field for a quadrupole magnet is given by [61, 69]

$$B_x = gy, \tag{2.35}$$
$$B_y = gx, \tag{2.36}$$
$$B_z = 0. \tag{2.37}$$

The field gradient g is equal to (B_0/a) where B_0 is the pole tip magnetic field strength and a is the aperture radius of the magnet. The first order transport matrix for a vertically focusing quadrupole magnet is given by

$$\begin{pmatrix} \cosh(kL) & k^{-1}\sinh(kL) & 0 & 0 \\ k\sinh(kL) & \cosh(kL) & 0 & 0 \\ 0 & 0 & \cos(kL) & k^{-1}\sin(kL) \\ 0 & 0 & -k\sin(kL) & \cos(kL) \end{pmatrix}, \tag{2.38}$$

where k^2 is equal to $g/(p/q)$ and L is the effective length of the quadrupole magnet.

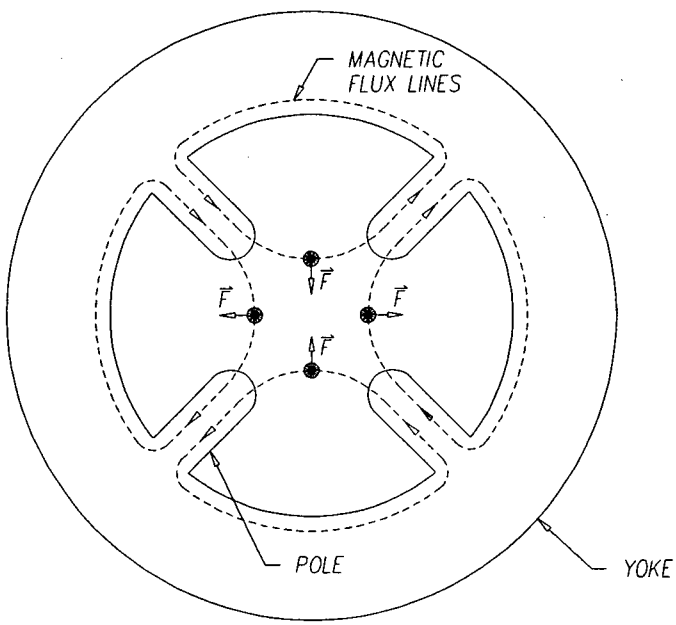

Figure 2.14: *The field lines for a quadrupole magnet which vertically focuses positively charged particles. The forces experienced by positively charged particles along each axis are also shown.*

2.2.2.3 Solenoid Magnet

The magnetic field lines for a solenoid magnet are shown in Figure 2.15. There are three optically important regions in a solenoid magnet. At the entrance and exit regions the magnetic field has a radial and an axial component, except on the magnet axis, whereas in the central region of the solenoid the field is strictly axial. The overall effect of the solenoid is to provide focusing, however, it also causes charged particles to rotate about the axial axis as they are transported through the magnet. This is useful if one wants to couple the (x, x') phase space of the beam to the (y, y') phase space.

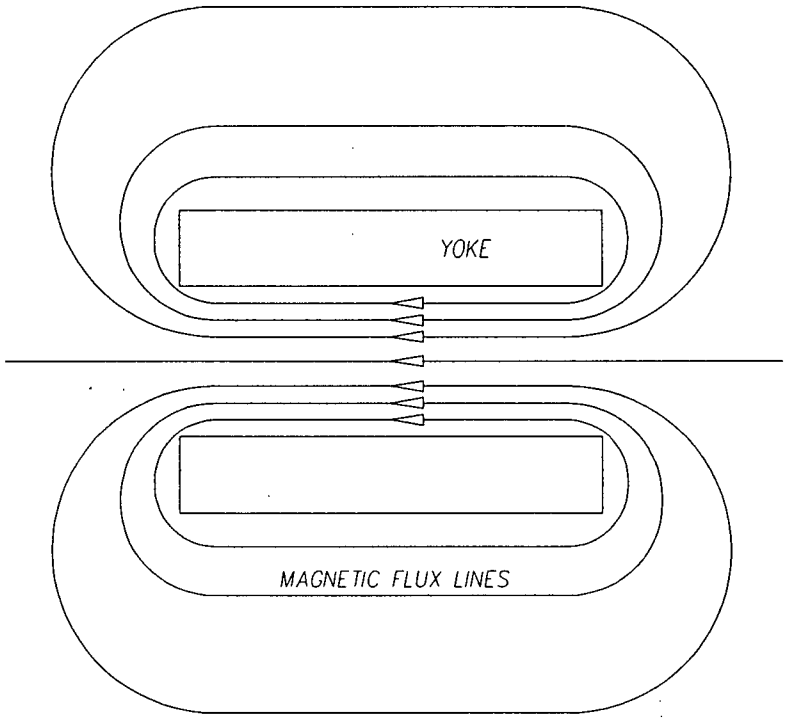

Figure 2.15: *The magnetic field lines of a solenoid magnet.*

The overall first order transport matrix for a solenoid magnet is [57, 69]

$$\begin{pmatrix} \cos^2(\theta/2) & K^{-1}\sin(\theta/2)\cos(\theta/2) & \sin(\theta/2)\cos(\theta/2) & K^{-1}\sin^2(\theta/2) \\ -K\sin(\theta/2)\cos(\theta/2) & \cos^2(\theta/2) & -K\sin^2(\theta/2) & \sin(\theta/2)\cos(\theta/2) \\ -\sin(\theta/2)\cos(\theta/2) & -K^{-1}\sin^2(\theta/2) & \cos^2(\theta/2) & K^{-1}\sin(\theta/2)\cos(\theta/2) \\ K\sin^2(\theta/2) & -\sin(\theta/2)\cos(\theta/2) & -K\sin(\theta/2)\cos(\theta/2) & \cos^2(\theta/2) \end{pmatrix}. \quad (2.39)$$

The angle θ is equal to $B_0L/(p/q)$ with B_0 being the peak axial field, and the factor K is equal to $\theta/2L$.

2.2.2.4 Circular Aperture Electrostatic Lens

The ion source extraction electrodes accelerate and focus the beam. These electrodes are circular aperture electrostatic lenses. Figure 2.16 shows a sketch of such a lens. The focal length for this lens is given by [83]

$$f = \frac{4V}{E_2 - E_1}. \quad (2.40)$$

The electrostatic potential of the lens plate is V, the magnitude of the upstream electric field is E_1 and the downstream electric field magnitude is E_2.

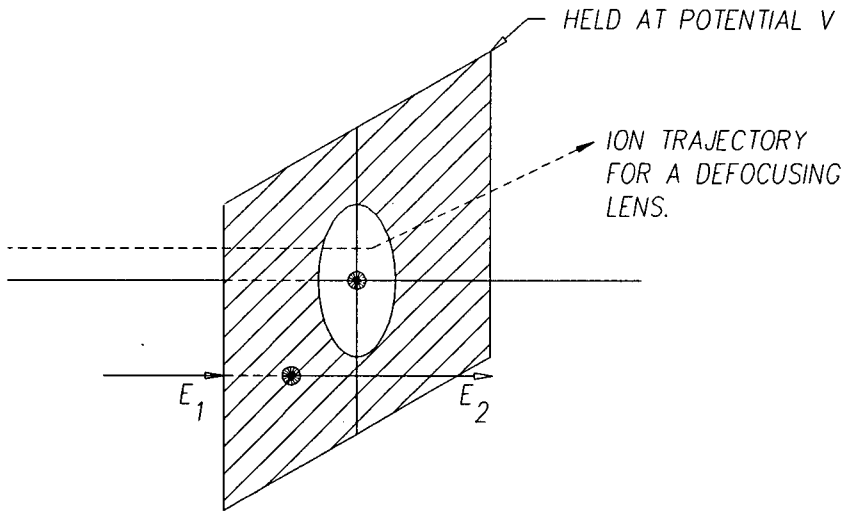

Figure 2.16: *An electrostatic lens with a circular aperture [83].*

The first order transport matrix for an electrostatic lens with a circular aperture is

$$\begin{pmatrix} 1 & 0 & 0 & 0 \\ -1/f & 1 & 0 & 0 \\ 0 & 0 & 1 & 0 \\ 0 & 0 & -1/f & 1 \end{pmatrix}. \tag{2.41}$$

2.2.2.5 Rotation Matrix

Standard optical components are sometimes rotated with respect to the lab horizontal and vertical axes. In order to avoid introducing complicated transport matrices for rotated components, optics codes usually rotate the particle coordinate vector or the beam sigma matrix while leaving the component's transport matrix in the usual unrotated form. Thus, the action of the rotated optical component is properly represented by the multiplication of three transport matrices. The first matrix represents a rotation of the curvilinear coordinate system by an angle θ, the second matrix is just the usual unrotated transport matrix of the optical component, and the third matrix represents a rotation of the curvilinear coordinate system by an angle $-\theta$ to bring the system back to the lab coordinates.

The rotation matrix used in this multiplication process is given by

$$\begin{pmatrix} \cos\theta & 0 & -\sin\theta & 0 \\ 0 & \cos\theta & 0 & -\sin\theta \\ \sin\theta & 0 & \cos\theta & 0 \\ 0 & \sin\theta & 0 & \cos\theta \end{pmatrix}. \tag{2.42}$$

2.2.2.6 Drift Space

The transport matrix for a field free drift of length L was derived in section 2.1.2.2. and is given in equation 2.8.

2.2.3 THE INFLECTOR

The injection axis of the H^- beam is perpendicular to the median plane, or, in other words, to the acceleration plane of the cyclotron. This implies that some mechanism or device is employed to bend the beam onto the median plane of the cyclotron. A number of such devices can accomplish the required bending, such as the electrostatic mirror, the hyperbolic inflector, the parabolic inflector and the spiral inflector. The interested reader can refer to [34, 38] for a description of these devices.

There are a number of important considerations to be kept in mind when designing an inflector system. The inflector must force the injected ion beam to have the correct position and momentum components at its exit for proper acceleration by the RF. The inflector must be kept small so that its physical presence does not affect other parts of the machine, yet it must be designed to have a reasonably large acceptance. Furthermore, its optical properties should be such that emittance growth is minimized, and it should be insensitive to slight fabrication imperfections and perturbations of the associated electromagnetic fields. Lastly, consideration should be given to minimizing the electrode potentials, the complexity of the machining requirements, and the overall cost of the device [34].

The design team for the TR30 cyclotron chose the spiral inflector of Belmont, Pabot and Root [37, 39, 40] as documented in [28, 86–88]. The very same inflector design was also chosen for the TR13 [24]. This type of inflector causes coupling between the (x, x') and (y, y') phase spaces which leads to emittance growth in these sub-spaces. However, this inflector has design parameters which can be used to position the beam optimally for further acceleration, which helps to reduce emittance growth during acceleration. In addition, the acceptance of the TR30 type inflector was found to be quite large [28].

2.2.3.1 Description of the TR30/TR13 Spiral Inflector

A number of coordinate systems are required to describe the path of the beam through the inflector. Figure 2.17 illustrates the four optical coordinate systems that come into play at the inflector entrance. The curvilinear optical system of the injection line (x, y, z) terminates at the inflector entrance. A fixed cyclotron coordinate system (x_c, y_c, z_c) is oriented such that the z_c axis points in the direction opposite z and has its origin at the median plane. The coordinate x_c points in the direction of the electric force at the inflector entrance, which, for the case of negative ions, points in the direction of the positive electrode. The y_c coordinate axis is defined by $x_c \times y_c = z_c$. For ease of computation, CASINO uses two coordinate systems, an unrotated curvilinear optical coordinate system (u, h, v) and a rotated system (u_r, h_r, v_r), which move along the central ray starting at the inflector entrance. In this coordinate system v and v_r point in the direction of the primary ray velocity vector. u points in the direction of the electric force in an untilted inflector and u_r points in the direction of the electric force in a tilted inflector. h and h_r are defined by $u \times h = v$ and $u_r \times h_r = v_r$, respectively. At the inflector entrance, the rotated and unrotated coordinate systems coincide. However, at the inflector exit the two systems are oriented as shown in Figure 2.18. For a more detailed description of these coordinate systems refer to [33]. Refer to Figure 5.4a for a sketch of a spiral inflector.

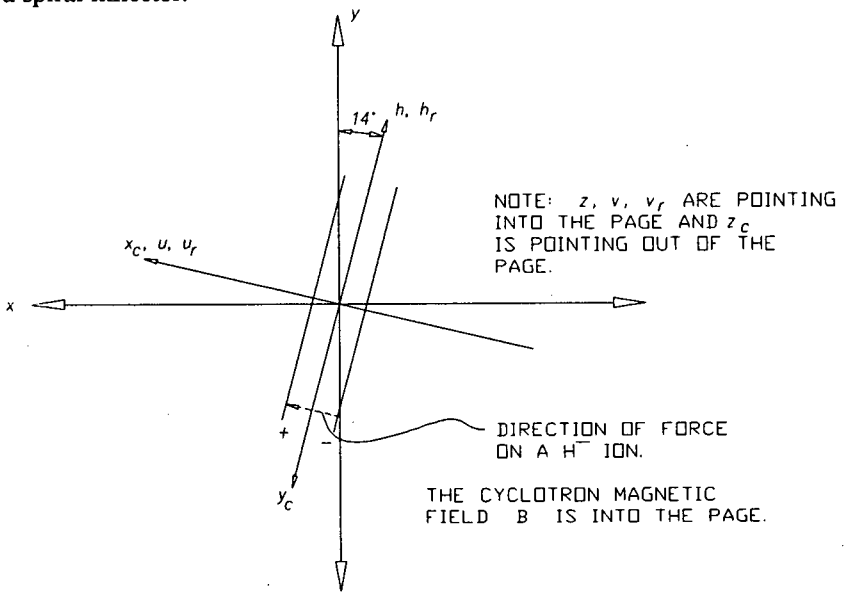

Figure 2.17: *Optical coordinate systems at the spiral inflector entrance. The beam is traveling into the page. The lab vertical axis points in the (y) direction, and the lab horizontal axis points in the (-x) direction.*

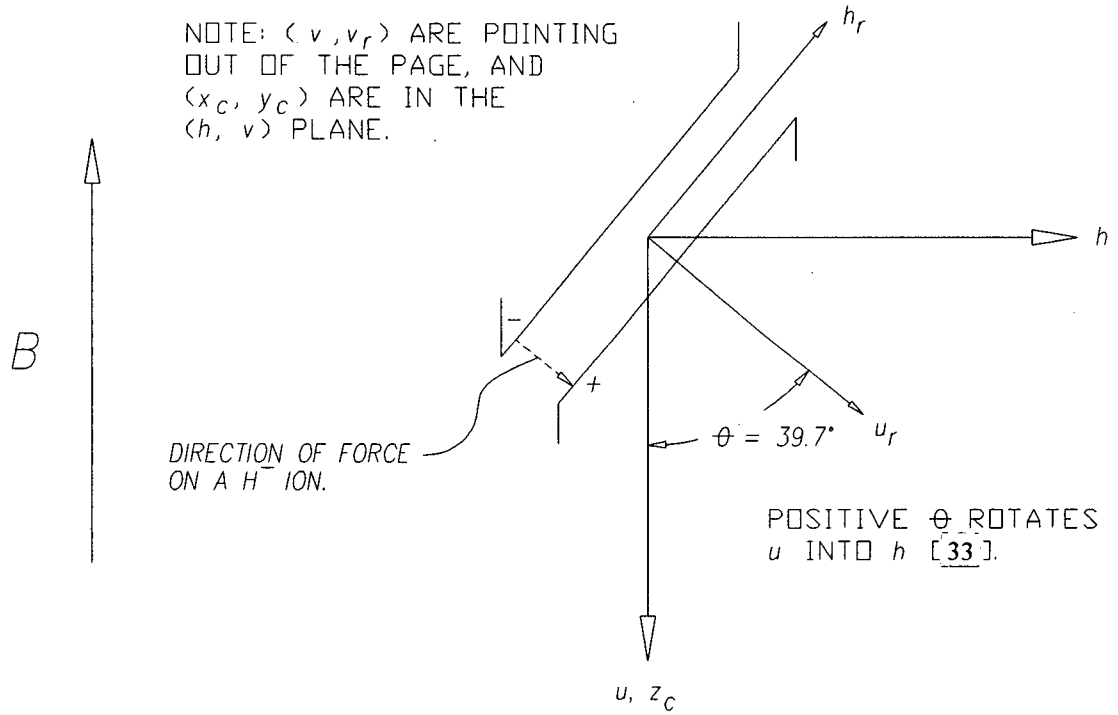

Figure 2.18: *Optical coordinate systems at the spiral inflector exit. The beam is traveling out of the page. The curvilinear coordinate system of Figure 2.1 is used in transport calculations after the beam exits the inflector, where (h corresponds to x) and (-u corresponds to y).*

Parametric equations describing the central ray motion through the inflector can be obtained if the following assumptions are made [39]:

- The magnetic field throughout the volume of the inflector is constant and is directed along the z_c axis.
- The *h* component of the electric field at any point along the central trajectory is proportional to the horizontal (x_c, y_c) component of the ion velocity at that point.
- The *u* component of the electric field is constant at all points along the central trajectory.
- The *v* component of the electric field is zero.

As used in CASINO, these equations are

$$x_c(b) = \frac{A}{2}\left(\frac{2}{1-4K^2} + \frac{\cos(2K-1)b}{2K-1} - \frac{\cos(2K+1)b}{2K+1}\right), \tag{2.43}$$

$$y_c(b) = \frac{A}{2}\left(\frac{\sin(2K+1)b}{2K+1} - \frac{\sin(2K-1)b}{2K-1}\right), \tag{2.44}$$

$$z_c(b) = A - A\sin(b). \tag{2.45}$$

The parameter A is the electric bending radius, where $A = (2T/qE)$, T is the nominal kinetic energy of the beam, q is the charge, and E is the electric field. The variable b is the instantaneous angle between the

central ray velocity vector and z_c. b varies from a value of 0 at the inflector entrance to $\pi/2$ at the inflector exit. K is equal to $A/2\rho$, for the case of an inflector with no tilt, where the magnetic bending radius ρ is equal to (p/qB) with p being the beam momentum and B the cyclotron magnetic field magnitude.

For the case of an inflector with tilt, the equations 2.43–2.45 remain the same if the electrodes are tapered so that the gap between them decreases as the exit is approached. The gap is narrowed in order to maintain a constant electric field in the u direction. In this case $K = A/2\rho + k'/2$ where

$$k' = \frac{\tan\theta}{\sin b}, \tag{2.46}$$

and θ is the angle of tilt of the inflector exit with respect to the cyclotron median plane.

An untilted spiral inflector has the electric bending radius A as the only practical parameter which can be chosen to achieve the necessary trajectory at the inflector exit. This can cause problems if a physically small inflector is required (small A) while at the same time a large acceptance is needed, as is the case for the TR30/TR13 inflector. However, this can be alleviated by tilting the inflector. The extra tilt parameter k' allows the correct exit orbit to be attained, and at the same time allows A to be reasonably small without overly compromising the acceptance [28].

The nominal TR type spiral inflector design parameters are quoted from [27], and are:

- A = 2.5 cm.
- B = 12 kiloGauss.
- k' = –0.83*.
- q = –1.
- p = 6.853 MeV/c.
- T = 25 keV.
- R = 19 mm.

* During the course of preparing this thesis, it was found that the sign of the axial magnetic field of the C.R.M. field map and the sign of k' had to be reversed so that the actual physical C.R.M. was properly simulated within CASINO.

2.2.4 CENTER REGION

Upon exiting the inflector, the H^- ions of the beam begin the first critical stages of acceleration within what is known as the central region of the cyclotron. The central region warrants special attention, as the bulk of any emittance growth occurring during acceleration is likely to have its origins in this region. In addition, a number of specialized physical obstacles must be avoided by the beam in this region,

and the importance of RF and space charge focusing effects relative to magnetic focusing effects is distinctly different than in the higher energy regions of the acceleration process. Fortunately, the TR13's peak injected current of 2 mA will result in negligible space charge related emittance growth. That this is so is based on the work [48], where no significant space charge related effects were observed for a 5 mA beam current. Refer to [89] for further reading on space charge effects in TR type cyclotrons.

For the TR type cyclotron, the center region is considered to be the region within the first five turns, or, in other words, the region where the ions are below a kinetic energy of 1 MeV. The Center Region Model 1 MeV cyclotron (C.R.M.) [48] is a good copy of the center region of the TR type cyclotron and provides a useful tool for studying the interplay between the ion source, injection system and the center region.

2.2.4.1 The Basic Acceleration Process

Once the H^- ions of mass m leave the exit of the inflector, they are traveling in the median plane. The ions are moving within an axial magnetic field of flux density **B** with a median plane velocity **v**. Under these conditions the ions are subject to the Lorentz force of equation 2.2, and the ions describe a circular-like orbit with angular frequency

$$\omega = \frac{qB}{m}. \tag{2.47}$$

The main operating principle of the cyclotron was recognized by Lawrence and is based on the fact that the angular frequency ω is constant regardless of an ion's kinetic energy, until the relativistic mass increase is no longer negligible. For modest levels of total kinetic energy gain then, one can introduce an oscillating electric field, which is directed so as to accelerate the ions tangent to their orbits in the median plane, and which is synchronized with ω, without tailoring **B** to account for the relativistic mass increase. In the TR type cyclotrons **B** is modified so that the ion revolution frequency in the magnetic field, ω from (2.47), is isochronous with the oscillating electric field frequency.

2.2.4.2 Center Region Physical Description

The C.R.M. cyclotron magnetic field is primarily that of a dipole magnet producing a large axial magnetic field. Therefore, one cyclotron magnet pole is above the median plane, and the other is below

the median plane. These poles, however, are divided into four hill regions that are separated by four valley regions, as indicated in Figure 2.19. These symmetrically placed segmented poles cause an ion, which travels through one revolution of the cyclotron, to experience an azimuthally varying magnetic field which looks similar to a square wave. The azimuthal variation of the magnetic field is termed flutter, and it gives rise to focusing forces which constrain the transverse extent of the beam to reasonable dimensions [56].

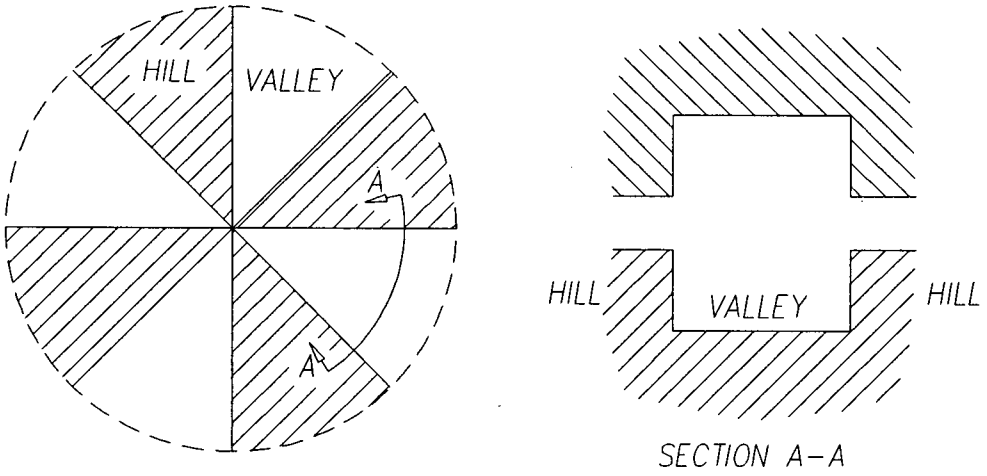

Figure 2.19: *Plan and cross-sectional views of the TR type cyclotron pole structure.*

Figure 2.20 shows a plan view of the median plane of the C.R.M. cyclotron. The central trajectory of the beam is depicted emanating from the inflector exit and proceeding along its path through the first turns of acceleration. As can be seen, there are a number of electrodes and/or support posts which must be cleared by the beam during the acceleration process. The beam ions require accelerations from the oscillating radio-frequency (RF) electric field at specific points along the trajectories to ensure that an appropriate increase in radius of curvature is attained so that all obstacles are missed.

The C.R.M. cyclotron accelerates the H^- ions with two RF dees which each span a pie shaped region in the median plane covering 45° of azimuthal angle. These dees are mounted in opposite valleys and operate at an angular frequency $\omega_{RF} = 4\omega$, which corresponds to $f_{RF} \approx 73$ MHz. These dees are separated by a small distance from ground plane liners that are mounted to the edges of the hills. Figure 2.21 illustrates schematically the electric field lines in the gap region between the dee and the liner. When

the RF voltage is at a peak on the dee the electric field lines extend across the gap as shown. This provides a large accelerating force in the median plane and small but significant forces perpendicular to the median plane. Each accelerated ion crosses four such gaps per full turn around the cyclotron. One gap is at the entrance of each dee, and another gap is at the exit of each dee. The peak RF potential is ≈50 kV, so any ion that is in phase with the peak of the RF will receive ≈200 keV of kinetic energy per revolution.

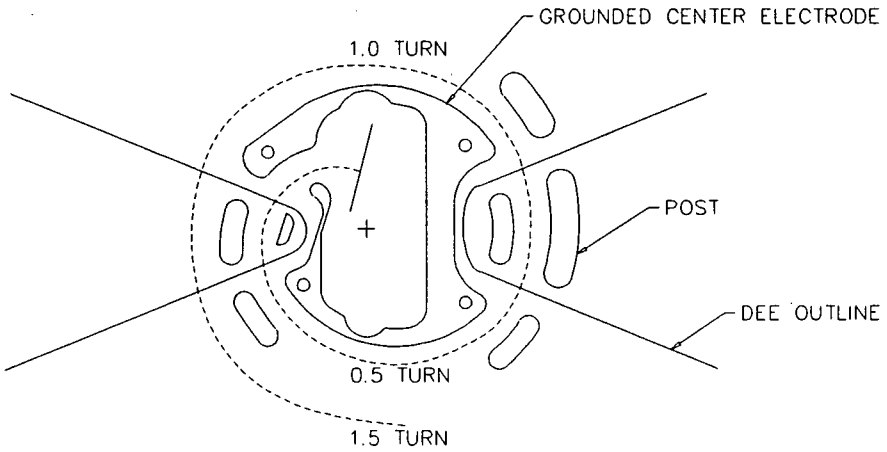

Figure 2.20: *Plan view schematic of TR type central region showing the central trajectory and posts.*

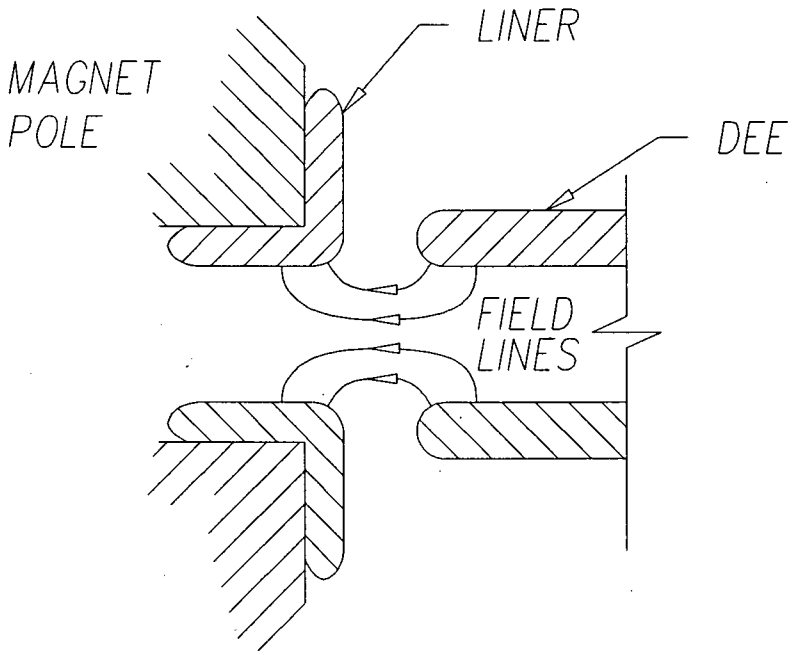

Figure 2.21: *An illustration of the electric field lines across the first accelerating gap.*

The aperture at the first accelerating gap is shown in Figure 2.22. It is essential that the beam is centered within this 1 cm wide by 2 cm high gap, so that the beam does not scrape against the electrodes or become distorted in phase space due to non-linear focusing near the electrode edges.

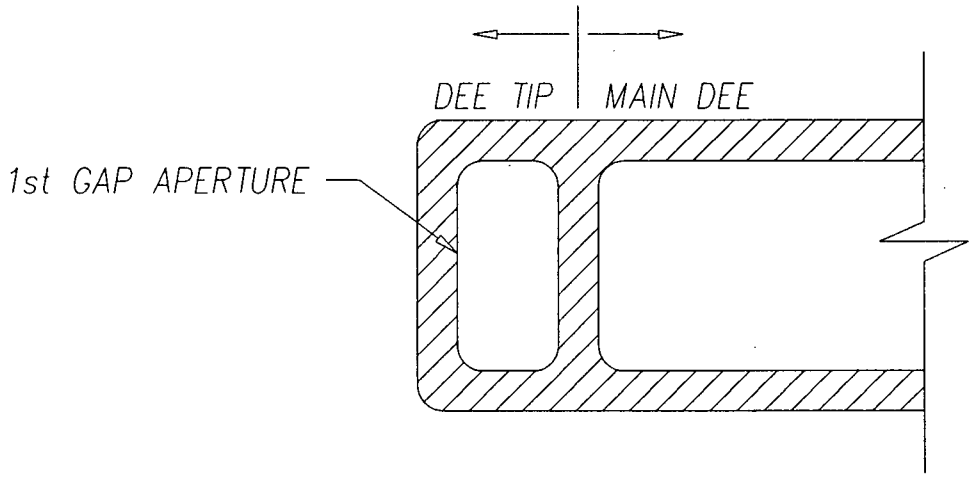

Figure 2.22: *Aperture of the first accelerating gap in the TR type cyclotron.*

2.2.4.3 Axial Phase Space

The axial and radial motions of the accelerated ions can be considered to be independent to a first approximation [90]. With respect to the axial phase space in the central region there are four effects to consider. These effects are those due to magnetic forces, RF electric forces, space charge electric forces and collimation.

The magnetic forces are due to the field index *n*, the flutter F and the spiral component of the magnetic field. The TR type cyclotrons have straight edged hill and valley sectors, so there is no spiral component of the magnetic field for these machines. The field index gives a measure of the change in the magnetic field as a function of radius and is defined in equation (2.31). The magnetic flutter is a measure of the azimuthal variation of the magnetic field and is given by [91]

$$F \approx \frac{(B_{hill} - \overline{B})(\overline{B} - B_{valley})}{\overline{B}^2}. \qquad (2.48)$$

For the case where magnetic spiral is zero, the leading terms in an expansion for the square of the axial tune in terms of the magnetic field are given by [91]

$$\nu_y^2 = n + F\frac{N^2}{N^2 - 1} + \cdots, \tag{2.49}$$

where N is the number of sectors. Using equation (2.34) one can easily formulate the first order dipole transport matrix.

The phase dependent focusing due to the RF electric forces in the central region is indeed important in that it contributes to emittance growth, however, in this thesis such focusing is not investigated in detail. The interested reader can refer to [44, 90] for a detailed discussion of these forces.

As mentioned previously, space charge forces in the center region are not of concern in this thesis, and the interested reader can refer to [89] for further information.

Collimation in the axial direction is due to ions being removed from the beam by striking the dees. The axial dee apertures in the center region are relatively wide to maximize beam current transmission. In addition, wide axial apertures minimize non-linear focusing effects.

It was mentioned above that the bulk of emittance growth would have its origins in the central region. In terms of the axial phase space, the main means by which emittance growth occurs is by mismatch of the injected beam ellipse with respect to the cyclotron machine ellipse as discussed in section 2.1.6. The concept of matching to a particular machine ellipse becomes somewhat hazy, however, when one considers that there is a different machine ellipse for each phase of the RF. Non-linear focusing forces introduced by either the magnetic or electric fields also contribute to effective emittance growth. Since the ions are moving relatively slowly in the center region, any unwanted electric effects can have a large impact on the ion beam. Also note that emittance growth can occur due to resonance conditions during the acceleration process. These resonance conditions arise when the sum of integer multiples of the radial and axial tunes results in an integer. The interested reader can refer to [56, 92] for further reading on resonances.

2.2.4.4 Radial Phase Space

RF focusing and space charge effects are relatively minor compared to the strong magnetic focusing in the radial phase space. Recall from equation (2.33) that the square of υ_x goes as $(1 - n)$, so that in a strict dipole field, with $n = 0$, the radial tune is much larger than the axial tune. Other phenomena in the radial phase space are usually much more important considerations than the radial focusing. The positioning of the support posts is critical in permitting ions to be accelerated over a wide RF phase band. The centering of the beam and the matching of the injected beam to the radial machine ellipse are both important with respect to minimizing emittance growth.

The positioning of the inflector and dee tip support posts is complicated by the fact that each longitudinal portion of the beam is accelerated by a different phase of the RF. Since the energy gain acquired by ions at each phase is different, they each have different radii of curvature. This implies that there will be a widening of the beam, and the posts must be placed appropriately in order to accelerate as large an RF phase band as possible. In the TR type cyclotron, 10% to 15% of the injected beam is transmitted through the center region. This corresponds to an RF phase band of about 40 to 50 degrees. The beam that is not transmitted is dumped into the electrically grounded and water cooled center electrode. This constitutes a heating load of over 45 watts in the TR13.

A primary goal at extraction is to have the outer turns of the beam radially centered with respect to the cyclotron center, so that the energy spread of the extracted beam is minimized. Such a centering at extraction requires an appropriate mis-centering of the beam in the center region. The appropriately mis-centered ion in the center region oscillates its center of curvature with each RF acceleration, and, as more energy is gained, the center of curvature converges to the center of the machine. The center region acceleration gaps and the inflector exit location must be appropriately designed and positioned to achieve proper centering. As well, flexibility must be provided for adjusting the centering through variations of the magnetic field, the inflector electrode voltages and the initial ion energy.

As usual, the emittance growth due to mismatching the injected beam with respect to the radial acceptance, non-linear focusing, and resonance conditions must be avoided.

3.0 INJECTION LINE DESIGN FOR THE TR13 CYCLOTRON

In this chapter a synopsis of the injection line design for the TR13 cyclotron is discussed. A detailed description of the design is given in [24, 47, 93–95]. The design of this injection line proceeded in an atypical manner for a number of reasons. First of all, the design of many of the TR13 sub-systems, including the injection line, proceeded in parallel with the cyclotron design to facilitate the expeditious completion of the overall project. This meant that full knowledge of the optical character of the cyclotron was not available during the design process, and approximate injection line design techniques had to be implemented [47]. The existence of a TR type 1 MeV test cyclotron, the C.R.M., at TRIUMF also affected the injection line design. The C.R.M. facility enabled prototype injection line testing to be undertaken. As a result, the definitive injection line did not have to be designed up front. Candidate systems could be proposed, designed and tested, and the final system could then be experimentally selected. Lastly, an effort was made to design the injection line in concert with the entire ion source and injection system (I.S.I.S.) including the center region. This philosophy was adopted to avoid common but sub-optimal practices, such as designing the injection line with respect to an ion source with static output beam characteristics. In essence, then, the injection line was designed within the context of optimizing the whole of I.S.I.S..

This chapter proceeds from general design considerations through the optical computations and optimizations to the final listing of the engineering specifications and measured component characteristics. The general design considerations include the up front design requirements as well as fundamental decisions as to the type of injection line to pursue. The optical calculations involve determining an adequate match between the ion source emittances and the cyclotron acceptances while maintaining high transmission through the injection line itself. The engineering specifications provide sufficient information to build the injection line components, and the measured characteristics are tabulated or illustrated.

3.1 GENERAL DESIGN CONSIDERATIONS

The injection line requirements were driven by the overall TR13 cyclotron system specifications. The TR13 was required to be a cost-effective, automated and compact 100 μA H^- cyclotron capable of radioisotope production in a hospital environment. Consequently, the aim of the injection line design process was to yield a compact, modular and cost-effective system capable of supplying a matched H^- direct current (DC) beam to the center region of the TR13. Of course, as for any system of this complexity, there are trade-offs between performance, cost, ease of operation, and maintenance etc..

In an effort to take advantage of efficiencies of manufacture, identical (modular) focusing elements were specified for the injection system. Three basic choices were available: electrostatic quadrupoles, solenoid magnets and quadrupole magnets. Solenoid magnets are reliable but are bulky, expensive and inefficient users of power. Electrostatic quadrupoles can be made to be inexpensive and compact, but they are prone to sparking. In addition, residual gas that is ionized by the beam is attracted to electrostatic devices and is not available for neutralizing the beam space charge [96]. Quadrupole magnets are intermediate in cost between electrostatic quadrupoles and solenoid magnets and they can be made to be quite compact. Power supply costs and power usage for this device are more akin to the electrostatic quadrupole than to the solenoid magnet. In addition, quadrupole magnets are reliable, they facilitate space charge neutralization and Ebco Technologies has experience building such devices. Consequently, the focusing elements for the TR13 injection line were chosen to be quadrupole magnets.

In order for the TR13 to be sufficiently compact for the hospital environment, the cyclotron design staff specified the injection line length to be at least 0.3 m shorter than the 1.8 m long solenoid and two quadrupole magnet (SQQ) [49] injection line of the TR30. The approach taken to achieve this specification was to utilize short, tightly spaced quadrupole magnets and a short initial drift length downstream of the ion source. The short initial drift length was made possible, in part, by eliminating one of two sets of (x, y) steering magnets normally found in an injection line. This was acceptable because operational experience with the TR30 cyclotron indicated that one of the two sets of injection line steering

magnets was often not used, and because, on a short injection line, a single (x', y') correction near the source waist can correct the central trajectory before it is irretrievably misaligned.

The following list summarizes the basic design parameters that were used to constrain the optical computations.

- Source Particle: H^-
- Injection Energy: 25 keV
- Source Current: 1 – 2 mA (expected)
- Source Emittance: 0.15 – 0.45 mm-mrad normalized (symmetric beam)
- Source Waist Radius: 2 – 5 mm
- Initial System Drift: 20 – 120 cm
- Spot Size on Target: 10 mm
- Maximum Extracted Current: 100 μA (protons)
- Maximum I.S.I.S. Length: 1.5 m
- Focusing Element: Quadrupole Magnet
- Quadrupole Magnet Length: 10 cm
- Quadrupole Magnet Aperture: 5 cm

The target spot size and the maximum required current on target were listed because they both affect the injection line design. The target beamspot size was a factor because beam sizes are normally much smaller than 10 mm in diameter in the first half meter downstream of the extraction point. For example, the TR30 beam sizes are approximately 3 mm in diameter at the same position. In order to achieve the relatively large beamspot sizes for the TR13, a machine which was not specified to utilize focusing elements between the extraction point and the target, emittance growth within the machine was not necessarily minimized, as is usually done. On the other hand, emittance growth had to be kept under control by appropriate injection line beam matching to avoid beam spill. The maximum beam current on target (100 μA) was listed above so that a minimum ion source output current could be determined. For a typical cyclotron beam transmission rate of about 10%, a minimum source output current of 1 mA is required.

The quadrupole magnet parameters were chosen from one of two existing quadrupole magnet designs. One quadrupole magnet design had a 6 cm length and a 5 cm aperture diameter. Such a geometry would result in a field which is entirely composed of edge effects. Therefore, the other quadrupole magnet design, with a 10 cm length and a 5 cm aperture diameter, was chosen as the standard.

3.2 OPTICAL COMPUTATIONS

In chapter 2 it was mentioned that emittance growth occurs if the injected (x, x') and (y, y') phase space ellipses of the beam are not similar to and aligned with the cyclotron machine ellipses. Such emittance growth results in what are known as large *circulating emittances* in the cyclotron. As well, emittance growth can occur due to the cross-plane coupling introduced by the inflector. The usual goals of axial injection are to contain and transport the ion source beam to the first RF accelerating gap with minimal beam loss and to manipulate the phase space character of the ion source beam in such a way as to minimize the circulating emittances within the cyclotron. These goals were initially adhered to, although, as already mentioned, the large spot size on target required a controlled emittance growth.

Since the design of the injection line proceeded concurrently with the cyclotron magnet design, the TR13's phase space machine ellipses were not available. However, the highly effective TR30 center region was specified for the TR13. This meant that it was reasonable to do beam matching computations using TR30 models. Note that the cyclotron community often calls the machine ellipse an acceptance ellipse. In this thesis, the latter phrase will be predominantly used.

3.2.1 BEAM MATCHING USING THE SMOOTH FOCUSING APPROXIMATION

The original TR30–SQQ injection line was designed using a beam matching technique [26, 49] which is approximate in nature, but useful for concurrent design. This technique is also useful for constraining the cross-plane coupling portion of the emittance growth. The technique assumes the cyclotron focusing to be smooth and uniform producing upright acceptance ellipses. This approximation yields a very simple expression for the normalized cyclotron circulating emittance in the radial plane

$$\varepsilon_{cnx} = \frac{\beta\gamma(\nu_x x_{max}^2)}{R_{cyc}}, \tag{3.1}$$

where ε_{cnx} (mm·rad) is the cyclotron circulating emittance, R_{cyc} (mm) is the radius of curvature of the circulating beam's central trajectory in the cyclotron, β and γ are the usual relativistic parameters, ν_x is the radial cyclotron tune and x_{max} (mm) refers to the largest radial beam half-size seen over one betatron oscillation. The equation is also valid if y, the axial beam half-size, is substituted for x. With the

normalized circulating emittance described in this manner, it can be minimized in each phase plane by simply minimizing the maximum x and y displacements over a betatron oscillation. This is easily accomplished using TRANSOPTR [72]. Note that ε_{cnx} must be multiplied by 1000 to convert to mm·mrad.

TRANSOPTR based beam transport systems are represented through a user specified subroutine and a data file which are linked to the program. The original TRANSOPTR based SQQ representation defines the beam at the ion source waist and then specifies the transport system as being composed of an initial drift, a section of focusing elements, an axial rotation element, an axial bore plus analytical inflector element and finally a weak focusing dipole element. This original TRANSOPTR based system is no longer the definitive representation of the TR30 injection system, however, it is a well known baseline which can be used as a first step in the comparison of the Q based systems to the SQQ system.

When the Q based systems were compared to the SQQ system, a number of factors were taken into account. The summed circulating emittances and the ratio of the circulating emittances were assessed, and results comparable to the SQQ were looked upon favourably. The beam size in the injection line and the length of the injection line were also noted and systems that were too long or which yielded overly large beams were not considered as potential prototype systems.

The original SQQ injection line design had an initial drift of 120 cm and a source waist radius of 4 mm [49]. The assumed cyclotron characteristics were R_{cyc} = 19 mm, $\beta\gamma$ = 0.0073, ν_x = 0.954 and ν_y = 0.3 [49]. Under these conditions the radial, x, and axial, y, circulating emittances were balanced ($\varepsilon_{cny}/\varepsilon_{cnx} \approx 1$) with a sum total $\varepsilon_{cnx} + \varepsilon_{cny}$ of 1.4 mm-mrad for initial normalized source emittances of 0.365 mm-mrad in each phase plane.

Since a range of source emittances, source waist radii, and initial drift lengths were to be eventually experimentally tested using a Q based system in the C.R.M., matching computations were conducted for which these initial conditions were incrementally varied over a representative region of parameter space. The summed minimized circulating emittances and the ratio of the minimized circulating emittances were plotted as a function of the initial conditions as a tool for analyzing various Q based scenarios. Examples of such plots are given in Figures 3.1, 3.2, 3.3 and 3.4.

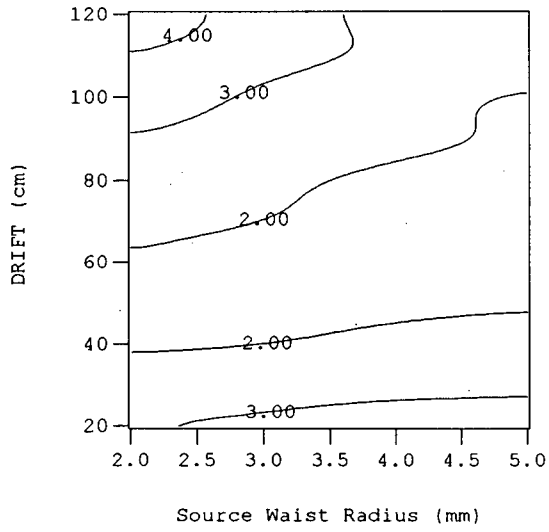

Figure 3.1: *Contours of minimized $\varepsilon_{cnx}+\varepsilon_{cny}$ (mm-mrad) for a range of source waist radii and initial drift lengths at fixed normalized source emittances of $\varepsilon_{cnx} = \varepsilon_{cny}$ = 0.365 mm-mrad for a 3Q injection line using approximate upright acceptance ellipses.*

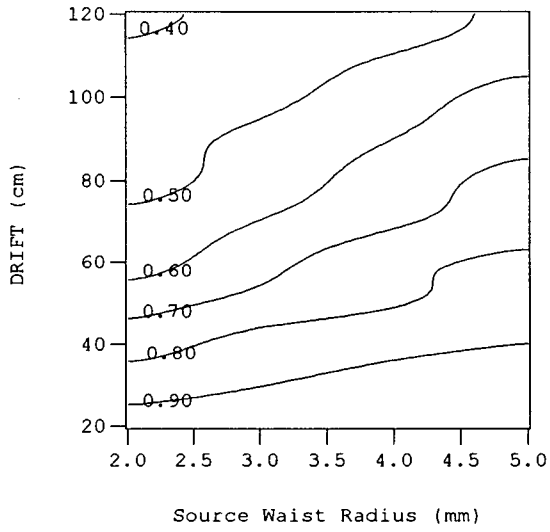

Figure 3.2: *Contours of $\varepsilon_{cny}/\varepsilon_{cnx}$ for a range of source waist radii and initial drift lengths at fixed normalized source emittances of $\varepsilon_{cnx} = \varepsilon_{cny}$ = 0.365 mm-mrad for a 3Q injection line using approximate upright acceptance ellipses.*

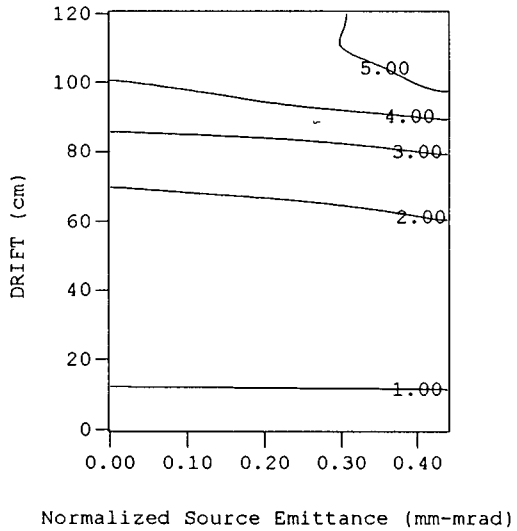

Figure 3.3: *Contours of minimized $\varepsilon_{cnx}+\varepsilon_{cny}$ (mm-mrad) for a range of source emittances and initial drift lengths at a fixed source waist radius of 2 mm for a 3Q injection line using approximate upright acceptance ellipses.*

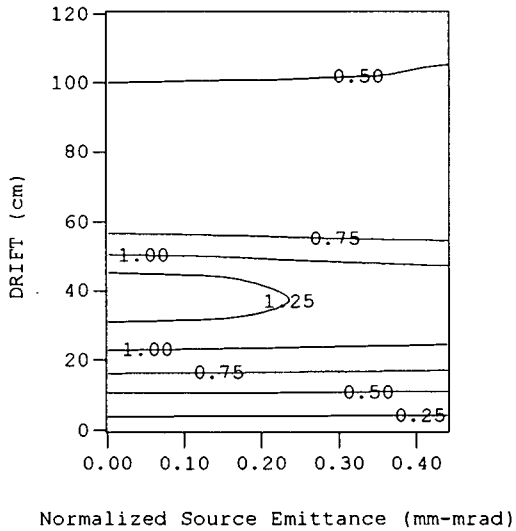

Figure 3.4: *Contours of $\varepsilon_{cny}/\varepsilon_{cnx}$ for a range of source emittances and initial drift lengths at a fixed source waist radius of 2 mm for a 3Q injection line using approximate upright acceptance ellipses.*

Many reference plots were produced and used during the design and testing stages. These plots helped to establish the optimal source beam characteristics for a particular drift length. For example, to achieve the required short injection line needed for the TR13, short initial drifts between 40 cm and 60 cm were of interest. From plot 3.1 one can see that for typical source emittances of 0.365 mm-mrad a small source waist radius of about 2 mm is required to minimize the circulating emittances. Figure 3.2 shows that for a 40 cm to 60 cm initial drift and a 2 mm source waist radius, the circulating emittances are reasonably balanced ($\varepsilon_{cny}/\varepsilon_{cnx} \approx 0.7$). Figure 3.3 shows that under these conditions the circulating emittances remain more or less minimized even if the source emittances are varied.

For a given source emittance, a small waist radius corresponds to a large maximum beam divergence. As the initial drift length is shortened, the maximum beam divergence increases (source waist radius gets smaller), so that the quadrupole lenses remain filled. Of course, if the maximum divergence increases too much the lenses become overfilled and beam loss results.

The minimum summed circulating emittances for 3Q injection line scenarios were on the order of the 1.4 mm-mrad obtained for the SQQ, and the ratio of the circulating emittances could be made to be approximately one. 4Q injection systems were also found to achieve equivalent matching results to the SQQ. The 2Q system on the other hand could only achieve minimized summed circulating emittances which were double those of the SQQ. The ratio of the emittances for the 2Q system could be made to be approximately one.

3.2.2 BEAM MATCHING USING TR30 ACCEPTANCE ELLIPSES

The next step in the preliminary testing of the various injection line scenarios was to determine how well the Q based systems could match the source emittances to the proper TR30 acceptance ellipses. An exhaustive set of matching calculations using these ellipses was not undertaken because they were yet again only approximations to the unknown TR13 acceptance ellipses. A brief investigation was warranted, though, to determine whether short Q based systems compared favourably to the SQQ system. The technique for doing so is described in [27] and is briefly re-iterated here.

The cyclotron acceptance ellipse in one phase plane is usually defined using the Twiss parameters α, β, and γ [67], which are not to be confused with the relativistic parameters. The Twiss parameters for an ellipse are defined in terms of its extreme points, as given by

$$x_{max} = \sqrt{\beta\varepsilon},\ x'_{max} = \sqrt{\gamma\varepsilon} \text{ and } \beta\gamma - \alpha^2 = 1, \tag{3.2}$$

where ε is the emittance. Within this formalism the acceptance ellipse can be written

$$\gamma_{ax}\, x^2 + 2\alpha_{ax}\, xx' + \beta_{ax}\, x'^2 = \varepsilon_{ax}, \tag{3.3}$$

where (x, x') are the beam half widths and half-divergence's, ε_{ax} is the emittance and α_{ax}, β_{ax}, and γ_{ax} are the Twiss parameters for the *acceptance ellipse* in the radial phase plane. A similar expression can be written for the axial phase plane. The phase space ellipse equation describing the particle beam, equation 2.12, can also be written using the Twiss parameter formalism. In this case the Twiss parameters describing the *beam ellipse* in the radial phase plane are ε_{bx}, α_{bx}, β_{bx}, and γ_{bx}.

As described in chapter 2, if the beam ellipse in a particular phase plane is not similar to the cyclotron acceptance ellipse in the same phase plane, it will eventually fill an ellipse which is similar to the cyclotron acceptance ellipse. This filled ellipse will have an area $\pi\varepsilon_{cx}$ in the radial phase plane, for example, where ε_{cx} is the radial circulating emittance. The circulating emittance in a particular phase plane can be computed knowing the beam ellipse Twiss parameters and the acceptance ellipse Twiss parameters as is shown in equations 3.4 and 3.5 below [97]:

$$D = \frac{1}{2}(\beta_{ax}\gamma_{bx} + \gamma_{ax}\beta_{bx} - 2\alpha_{ax}\alpha_{bx}), \tag{3.4}$$

$$\varepsilon_{cx} = (D + \sqrt{D^2 - 1})\varepsilon_{bx}. \tag{3.5}$$

The TR30 acceptance ellipses are described in [27], and matching computations were done using these ellipses. The emittance growth calculated using these TR30 acceptance ellipses was generally between 15% and 40% larger than was calculated using the technique of section 3.2.1. As well, the ratio of the axial to radial circulating emittances was often substantially different than the section 3.2.1 results, for a particular system. Interestingly enough, the summed circulating emittances for the SQQ system remained about 1.4 mm-mrad with the ratio of the axial to radial circulating emittances shifting to about

0.8. Selected short 4Q and 3Q systems were found which could achieve matching results equivalent to those obtained by the SQQ system.

3.2.3 FINAL OPTICAL DESIGN COMPUTATIONS

The 4Q and 3Q injection systems were found to be comparable in matching capability to the SQQ system using TR30 models. This result was sufficient justification to initiate the final optical design of the prototype systems to be tested on the C.R.M.. In addition to 4Q and 3Q systems, 2Q systems were considered for testing because their beam matching capabilities, albeit worse than the 4Q and 3Q, were potentially sufficient for the TR13.

The final optical design of the Q based injection systems was done in a more pragmatic manner than the initial design work in sections 3.2.1 and 3.2.2. First of all, the minimum initial drift length which could accommodate the required I.S.I.S. vacuum pumps, diagnostic devices and the (x, y) steering magnet was determined to be 50 cm. As well, the physical set-up of the C.R.M. test facility was most amenable to studying the 4Q system and only those 3Q and 2Q systems which could be energized as a subset of the 4Q configuration. Lastly, the axial bore of the cyclotron and the inflector were optically represented by linear transport matrices computed from equation 2.9 using paraxial ray data generated from CASINO, as opposed to the strictly analytical representation used in [26, 27, 49].

Table 3.1 presents the final optical layout which was proposed, prior to the start of detailed design and drafting work, in May 1992. The TRANSOPTR command file OPTR.LNK, 4Q system subroutine file 4Q_B9200G_ANA.FOR, and data file 4QSK.DAT which were used to formulate the system listed in Table 3.1 are listed in Appendix I. The axial bore and inflector matrices were computed using the magnetic field map MAP29_9200.ZFLD. This field map is identical to the map shown in Figure 5.11, except that the magnitude of the magnetic field is scaled down to 94% of the original. This was done because the TR13 field was expected to be about 5% to 10% lower in the central region than in the TR30.

The horizontal and vertical beam profiles (half-sizes) for the system described in Table 3.1 are shown in Figures 3.5 and 3.6, respectively. These profiles fit comfortably within the injection line beampipe, whose inside radius was to be between 20 mm and 22.5 mm depending on the availability of appropriate pipes or tubes. The oscillations in the beam profile at beam path lengths greater than

approximately 110 cm illustrates the beam focusing within the cyclotron. Note that the beam half-sizes in the cyclotron are on the order of 2.5 mm which is comfortably smaller than the 5 and 10 mm half-apertures seen by the beam in the first few turns.

Table 3.1: *The charged particle optics layout for the proposed TR13 4Q injection system. Note that positive quadrupole magnetic fields indicate horizontal focusing.*

COMPONENT	SETTINGS	LENGTH (mm)/BORE (mm)
Initial System Drift Space	–	500/200
Q0	189 Gauss	100/50
Drift Space	–	23/45
Q1	–561 Gauss	100/50
Drift Space	–	23/45
Q2	600 Gauss	100/50
Drift Space	–	23/45
Q3	–249 Gauss	100/50
Beam Rotation Angle *	37°	0/45
Axial Bore Optical Representation **	Matrices A, B, C	140/50
Inflector Optical Representation **	Matrices D, E, F	25/(8 tapering to 6)
Rotation to Cyclotron Coordinates **	Matrix G	0/20

* More specifically, the Q0 de-focusing axis is rotated to be at 37° counter clockwise of the inflector entrance electrode edges.
** These matrices were computed using CASINO and are listed in Appendix I.

The emittance matching technique of section 3.2.1 established the system in Table 3.1. The summed circulating emittance for this system was 3.7 mm-mrad. This corresponds to a realistic emittance growth factor of 5 for summed source emittances of 0.73 mm-mrad. The measured emittance growth factor in the C.R.M. is given as 5 in [48]. The ratio of the radial and axial circulating emittances was 3 to 1, which was of practical interest, as it corresponded to equivalent beam sizes in each phase plane.

The 4Q system was the most likely system to meet the TR13 requirements, as it was the most flexible injection system. Thus, the most detailed optical computations were done for this system. These computations gave the details required for the engineering design of the system and for reasonable initial field settings. No detailed calculations of 3Q or 2Q systems were attempted because the work described in sections 3.2.1 and 3.2.2 indicated that the 3Q and 2Q systems could potentially meet the TR13 requirements, and it was left to the prototype testing stage to experimentally determine their performance.

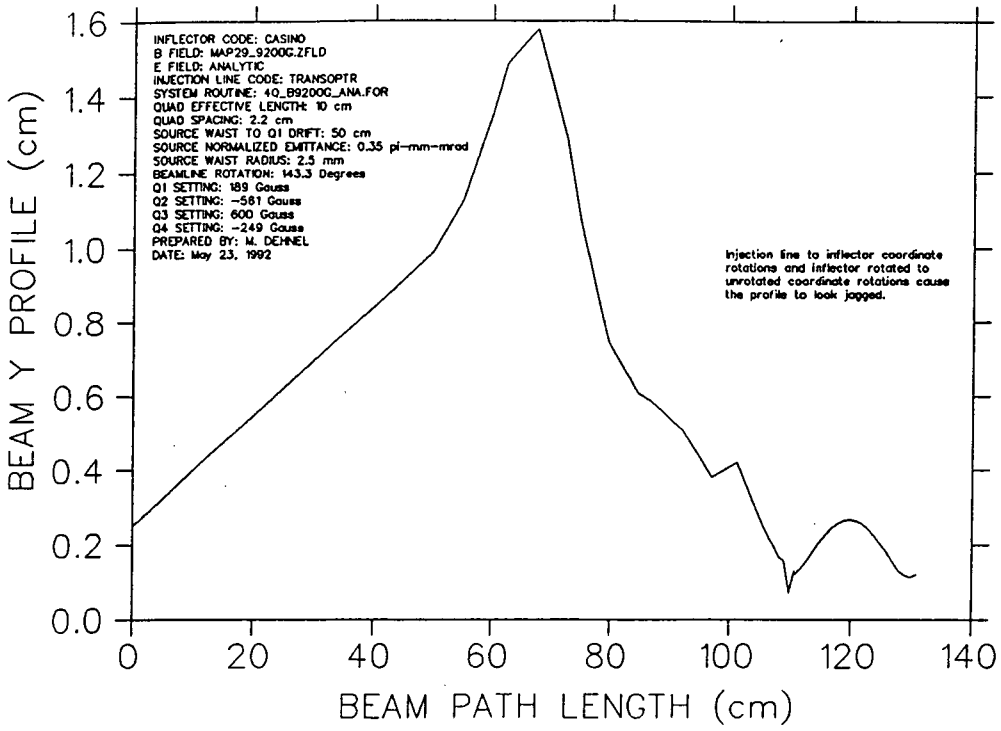

Figure 3.5: *The vertical (axial) beam profile for the TR13 4Q system.*

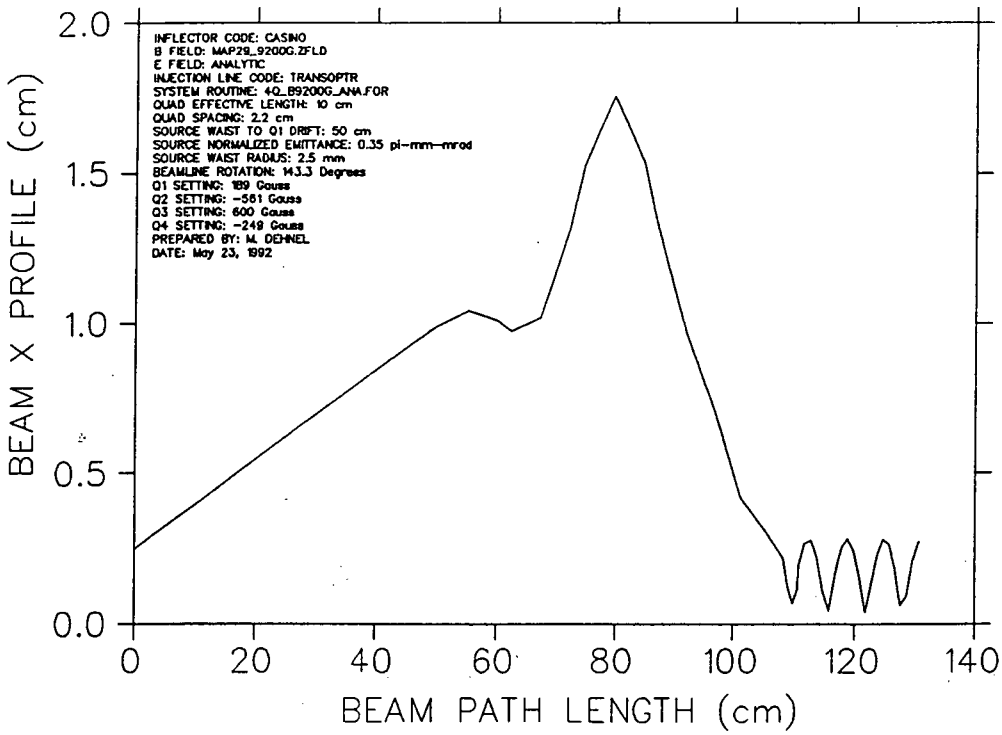

Figure 3.6: *The horizontal (radial) beam profile for the TR13 4Q system.*

The 143.3° beamline rotation angle listed in Figures 3.5 and 3.6 is a clockwise rotation of the defocusing axis, as reported by TRANSOPTR. This, of course, corresponds to a 36.7° counter-clockwise rotation of the defocusing axis. The 36.7° angle has been rounded off and listed as 37° in Table 3.1.

3.3 ENGINEERING SPECIFICATIONS

The complete specification of the 4Q injection line is recorded in [93, 94] and in Ebco Technologies assembly drawing IS–0182. A brief summary of the design considerations for each element of the injection line design are discussed in the following sub-sections.

3.3.1 QUADRUPOLE MAGNETS

As recorded in Table 3.1, the primary design parameters for the injection line quadrupole magnets were a 10 cm effective length, a 5 cm bore and a peak pole tip field on the order of 1000 Gauss. As mentioned in section 3.1, the magnet design originated from an existing magnet design [98]. This original magnet design had to be re-assessed because it was originally intended for peak pole-tip fields of only 500 Gauss. The new quadrupole design was undertaken by a summer student under the supervision of the author [93].

The work of [93] resulted in the following specifications for the quadrupole magnets:

- Pole: 8.0 cm long, 4.0 cm wide, 28.75 cm tall.
- Yoke: 14 cm long, 12.0 cm outside diameter, 0.6 cm thickness.
- Conductor: 16 AWG polythermaleze conductor.
- Maximum Current: 10 amps, Maximum Voltage (per coil): 6 volts.
- Power Supply: Xantrex HPD 30–10 with M5A Control Option.
- Water Cooling: 0.5 litre/min.

One quadrupole magnet was field mapped by the TRIUMF Magnet Group. Only one magnet, designated Q0, was chosen for comprehensive field mapping due to cost constraints. All the magnets were visually inspected, and electrical coil resistance measurements and Hall probe measurements were taken to ensure that all magnets were equivalent to within ±1%. Comparisons between the Q0 measurements and measurements made on the other magnets (Q1, Q2 & Q3) verified that they all behaved in the same manner. Consequently, the field map for Q0 was judged to be an acceptable representative field map for all the injection line quadrupole magnets.

The field map for Q0 determined the actual effective length of the magnet, the pole tip magnetic field magnitude as a function of excitation current, the pole tip magnetic field magnitude profile as a function of axial position, and the Fourier coefficients for the series expansion of the magnetic field. These experimentally determined results were typically somewhat different than those theoretically predicted, and, thus, they were used in the improved simulation runs described in chapter 5.

Figure 3.7 gives the pole tip magnetic field magnitude as a function of coil excitation current (B-I curve). The plot is linear and the slope is 131 gauss/ampere. This slope was necessary for converting between power supply current settings and the actual pole tip magnetic field magnitude during the prototype testing stage.

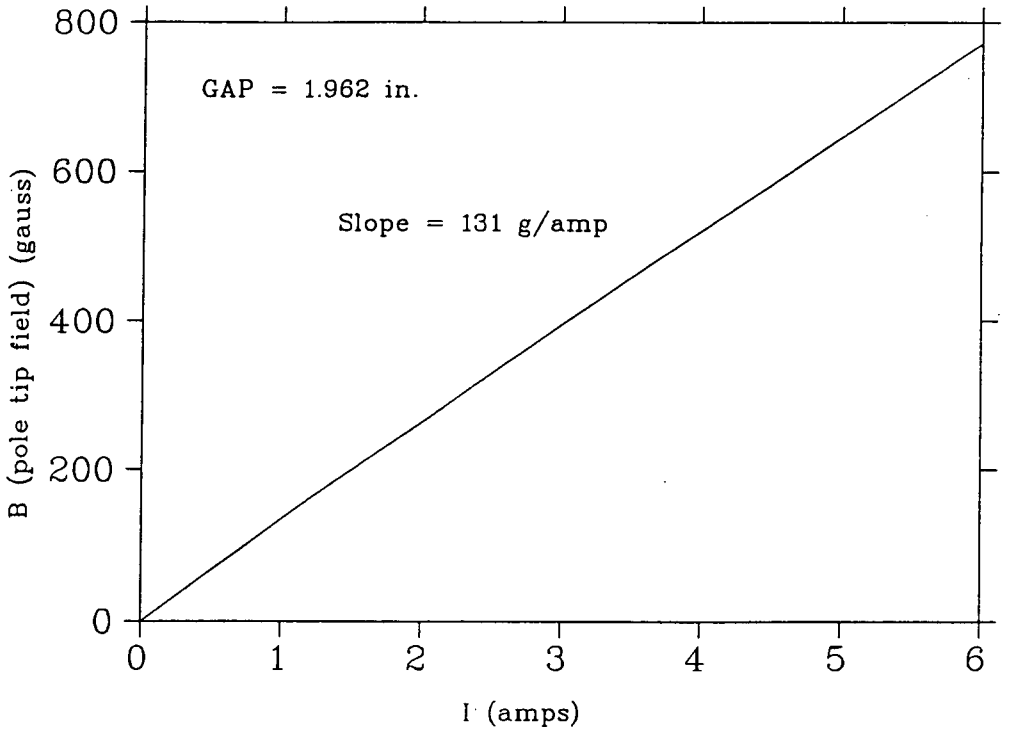

Figure 3.7: *The pole tip magnetic field magnitude as a function of the coil excitation current for Q0.*

The pole tip field as a function of axial position is given in Figure 3.8. Two separate cases are shown. Case 2 is without a field clamp installed and case 1 is with a field clamp installed on one end of the magnet. The graph shows that the field clamp does in fact limit the axial extent of the magnetic field. Note that the 4Q injection line uses field clamps between each of the quadrupole magnets. The effective length of Q0 was determined to be 9.7 cm without the field clamp. The design effective length was 10 cm.

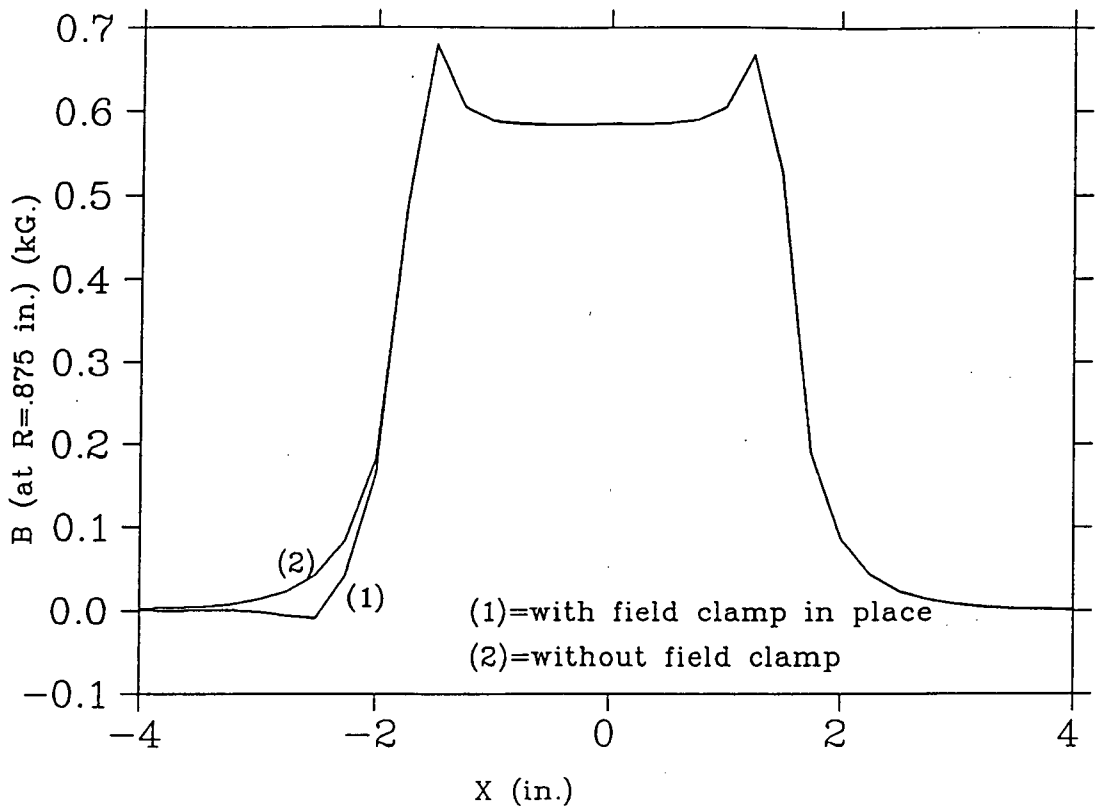

Figure 3.8: *The pole tip magnetic field as a function of axial position along Q0.*

The Fourier coefficients for the Q0 magnetic field listed in Table 3.2 indicate that the magnet is dominated by the second harmonic as it should be. The magnet group indicated that the relatively high first harmonic was probably due to a slight off-centering of the Hall probe.

Table 3.2: *The Fourier coefficients for the Q0 magnetic field.*

HARMONIC	**1**	**2**	**3**	**4**	**5**	**6**	**7**	**8**	**9**	**10**
Point:	0.90	100.0	0.26	0.25	0.05	0.14	0.04	0.14	0.10	0.17
Integrated:	0.84	100.0	0.26	0.27	0.10	0.72	0.03	0.12	0.12	0.13

3.3.2 STEERING MAGNETS

Only one set of (x, y) steering magnets was required for the injection line. The standard steering magnet design, Ebco Technologies drawing IS–0167, was satisfactory for the prototype experiments.

3.3.3 VACUUM CONSIDERATIONS

The existing C.R.M. diagnostic box with its associated cryo-pump, turbo pump and vacuum gate valve was an acceptable injection line vacuum system assembly for the prototype experiments. The

injection line beampipe was made according to standard vacuum practice, with non-magnetic stainless steel SS316. The outer diameter of the beampipe was specified to be no larger than 49 mm, and the specified inner diameter of 42 mm was sufficient (refer to Figures 3.5 and 3.6). The beampipe mated to the cyclotron through a double O-ring seal, and to the diagnostic box via a standard gate valve.

3.3.4 DIAGNOSTICS

The existing C.R.M. diagnostic devices were acceptable injection line diagnostic devices. These included a beamstop with a ring collimator and a secondary electron trapping screen, and a 6 mm by 14 mm rectangular collimator at the inflector entrance (refer to Appendix II). Each of these devices had a current readback. In addition to these diagnostic devices, it was recognized that a four-way collimator with current readbacks would be required for initial beam alignment within the injection line.

3.3.5 MECHANICAL SUPPORT

The 4Q injection line utilized a friction fit between the downstream quadrupole magnet, Q3, and the cyclotron bore to register and align the downstream portion of the line. An aluminum collar, which permitted quadrupole magnet rotation, supported and centered the injection line at the outer edge of the magnet yoke. A steel collar was used to compress the gate valve, the beampipe flange and the ion source diagnostic box flange against the upstream quadrupole magnet, Q0. In addition to making a vacuum seal this made the whole system rigid. The ion source and diagnostic box were supported on a rail system.

3.4 SUMMARY

The goal was to design a compact modular injection system capable of providing an appropriate injected beam for the TR13. Because the injection system design was done in parallel with the cyclotron design, a proper design using the actual TR13 optical characteristics was not possible. A reasonable approach to the design problem was to ensure that any proposed injection system for the TR13 was equivalent in terms of matching and beam transport to the established SQQ injection system of the TR30. This course of action determined that 4Q and 3Q injection systems were both capable of equivalent

matching to the SQQ. The 2Q injection system was not equivalent to the SQQ, however, the relatively large emittance growth associated with this system was possibly still acceptable for use in the TR13.

The 4Q system had the largest number of variable parameters available for beam transport and matching. Therefore, it was the most likely system to succeed during prototype testing. Consequently this system was designed in detail and built. Only 3Q and 2Q systems which could be energized within the 4Q configuration were available for prototype testing.

The initial constraints were all met by the 4Q injection system. In particular, the total system length of 1.5 m is 0.3 m shorter than the SQQ injection line, and the system was designed with modular components. Beam transport, as shown in Figures 3.5 and 3.6, was acceptable. If either the 3Q or, preferably, the 2Q were to exhibit acceptable beam transport during testing, they would be the most cost effective systems. The injection line components were built in late 1992 and assembled into the C.R.M. facility, as shown in Figure 3.9, in early 1993. A description of the prototype ion source and injection line testing which took place through the winter months of 1993 is described in the following chapter.

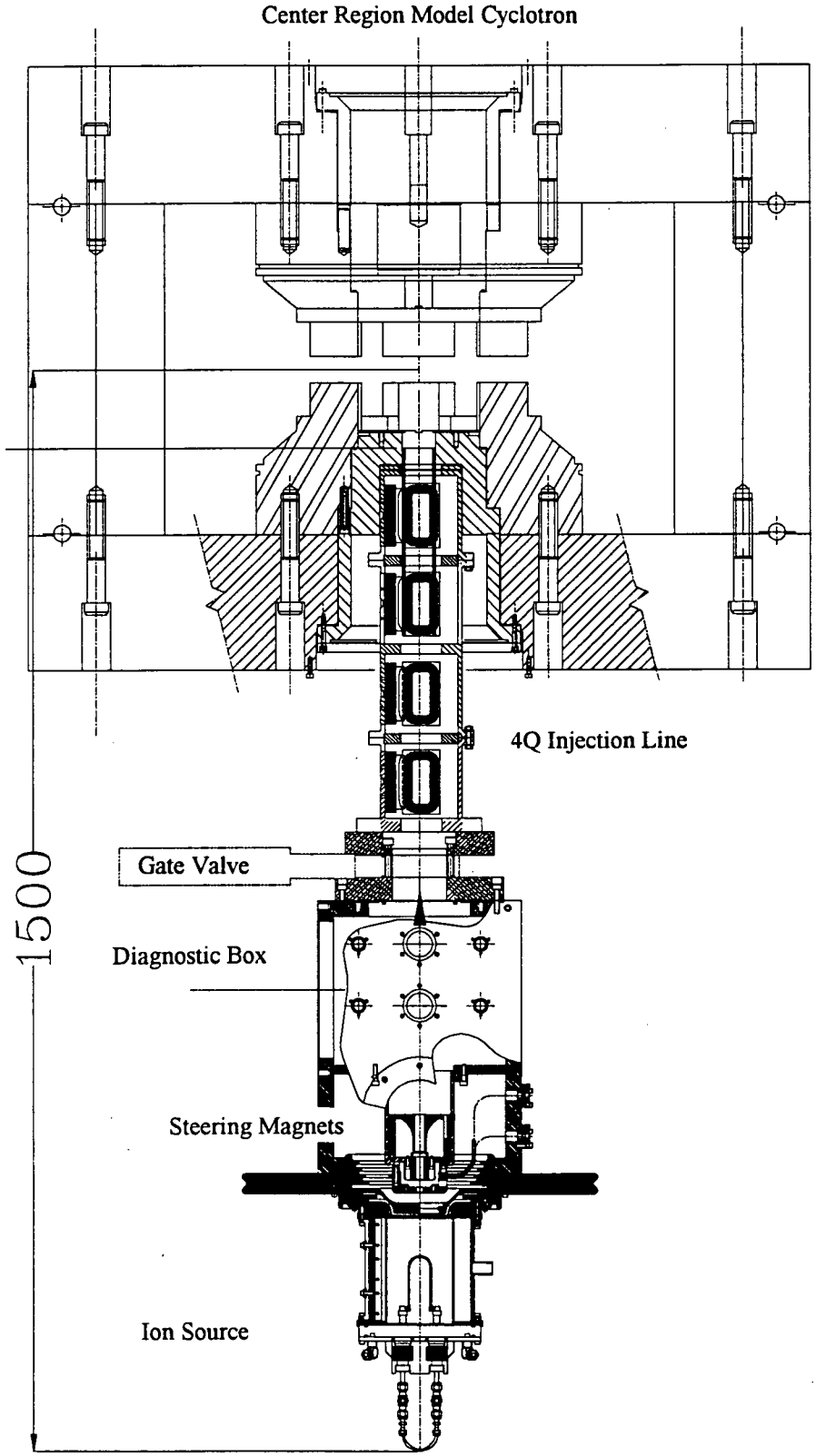

Figure 3.9: *The 4Q injection line assembly drawing. Dimensions are in millimetres. Scale is ≈ 10:1.*

4.0 INJECTION SYSTEM TESTING AND OPTIMIZATION

The C.R.M. cyclotron system is a full-scale working model of the center region of the TR30 cyclotron [48], and therefore it is a useful tool for providing information pertaining to the TR13 cyclotron. This was verified when the final beam measurements were carried out on the TR13 cyclotron and compared to the C.R.M. results. The only difference between the TR13 and the TR30/C.R.M. cyclotrons was a slight difference in their central region magnetic field profiles. The TR13 cyclotron's final magnetic field magnitude was up to 2.5% less than that of the TR30/C.R.M. cyclotrons' out to a radius of 4 cm [99].

This chapter describes how the C.R.M. was used to test the prototype Q based injection systems designed for the TR13 cyclotron system. The chapter begins with a description of the basic system set-up and the initial equipment calibrations. Subsequent to this, baseline transmission measurements made with the TR30 cyclotron's solenoid/quadrupole/quadrupole magnet (SQQ) based injection system are discussed. A series of ion source experiments are then analyzed to determine the relationship between the output beam characteristics and various configurations of the ion source. The transmission characteristics of the Q based injection systems with respect to the various ion source configurations and other system variations are then compared to the SQQ baseline results. The beam character in the center region of the C.R.M. for the 4Q injection system is then analyzed. The emittance growth, RF phase band, and sensitivity of the system are documented at this stage. Lastly, a summary of the chapter is given and the best commercial injection line is specified.

4.1 GENERAL: EQUIPMENT CALIBRATIONS AND THE C.R.M. CYCLOTRON SYSTEM

The C.R.M. is a general purpose test cyclotron with a TR type center region. It is well suited to test ion source and injection systems, and it has a wealth of diagnostic capabilities for assessing the character of the beam in the center region of the cyclotron. This cyclotron system is well described in [48]. In addition, a general description of the sub-systems utilized by the C.R.M. are given in section 2.2, and a brief but more technical description is given in Appendix II. For reference purposes, the following list

names the major C.R.M. sub-systems and components in the order seen by the beam as it proceeds from the ion source to the 1.125 MeV beamstop.

C.R.M. Sub-Systems and Components

- H^- ion source complete with extraction lenses.
- Diagnostic box complete with differential vacuum pumping, an emittance scanner, a Faraday cup and a collimator/beamstop assembly.
- Gate valve.
- Injection line lens assembly: SQQ, 4Q, 3Q or 2Q.
- Injection line and inflector entrance collimators.
- Spiral inflector combined with the C.R.M. main magnet field.
- Inflector exit beamstop.
- RF accelerating structures combined with the C.R.M. main magnet field in a high vacuum environment.
- Differential and integral beam current probes.
- 1.125 MeV beamstop.

Prior to testing the prototype Q based injection systems, the C.R.M. cyclotron system had to be re-commissioned, as it had been dormant for 4 years, and the various meters, probes and beamstops had to be calibrated. Approximately, two months were taken to refurbish and re-commission the system, and a further two months were taken to ensure that the instrumentation was well calibrated. A detailed description of the calibration work is given in Appendix II. The following list summarizes the calibrations that were performed.

Calibrated C.R.M. Devices

- Filament power supply current readback.
- Arc power supply current and voltage readbacks.
- Plasma lens power supply current and voltage readbacks.
- Extraction lens power supply voltage readback.
- Hydrogen flow rate meter.
- Beam current meters.
- Faraday cup.
- Ion source beamstop and collimator assembly.
- Emittance scanner.
- Injection line collimators.
- C.R.M. internal beamstops and probes.

The level of care taken to calibrate the instrumentation is notable in that the parameter setting readbacks and beam current readbacks were known, in the worst case, to within 2 or 3 percent, where, for example, it is quite often the case in this field that such readbacks would only be known to within about

10%. Particular attention was paid to the beam current readbacks, where careful voltage biasing was required to properly account for the secondary electrons generated by beam bombardment.

4.2 THE SQQ INJECTION SYSTEM

The nominal arrangement of the C.R.M. cyclotron system includes a TR30 type SQQ injection line and H^- ion source. This nominal system was re-commissioned and its beam transmission performance was investigated. This was done in an effort to become acquainted with the operation of the overall C.R.M. facility, and to verify that a fallback injection system was available for the TR13. In addition, the SQQ results were expected to provide a useful baseline to aid in the assessment of the prototype Q based injection systems.

The TR13's extracted beam current requirement is 100 μA @ 13 MeV. Therefore, a successful ion source and injection system should be capable of transporting at least 110 μA to the 1.125 MeV beamstop. This overhead is necessary to comfortably offset gas stripping losses between 1.125 MeV and 13 MeV. Stripping losses can be as high as 5% of the total low energy beam current.

The original SQQ system was designed by Baartman, and his reference design as given in his design note [49] follows.

Baartman Reference Tune

The assumed source beam full waist radius = 8 mm, its full divergence = 26 mrad and its normalized emittance = 0.36 mm·mrad.

1. Source waist to solenoid centre distance = 1.3 m. This parameter is not rigid because the source waist is not yet known. For a 2 mm source waist, this parameter becomes 0.65 m.
2. Solenoid field = 1.4 kG nominal, 2.0 kG design maximum; for an effective length of 23 cm and an aperture diameter = 10.0 cm.
3. Solenoid centre to first quadrupole centre distance = 20.3 cm.
4. First quadrupole pole tip field = -363 gauss nominal, -500 gauss maximum for an effective length of 6 cm and an aperture diameter = 5.0 cm.
5. First quadrupole to second quadrupole centre distance = 11.3 cm.
6. Second quadrupole pole tip field = 383 gauss nominal, 500 gauss maximum for an effective length of 10 cm and an aperture diameter = 5.0 cm.
7. Second quadrupole centre to median plane distance = 21.4 cm.

The SQQ system installed in the C.R.M. is somewhat different than that described in the Baartman Reference Tune. Figure 4.1 is a schematic of the SQQ injection system which gives the actual device to device distances. The main difference is that the drift between the source waist and the centre of

the solenoid magnet is 0.9633 m for the actual physical system, and 1.3 m for the Baartman Reference Tune. However, this is explained by point 1 of the Baartman Reference Tune which acknowledges that the characteristics of the input ion beam have some bearing on the initial drift space. Previous experimenters undoubtedly found the 0.9633 m initial drift more appropriate for their particular ion source beam.

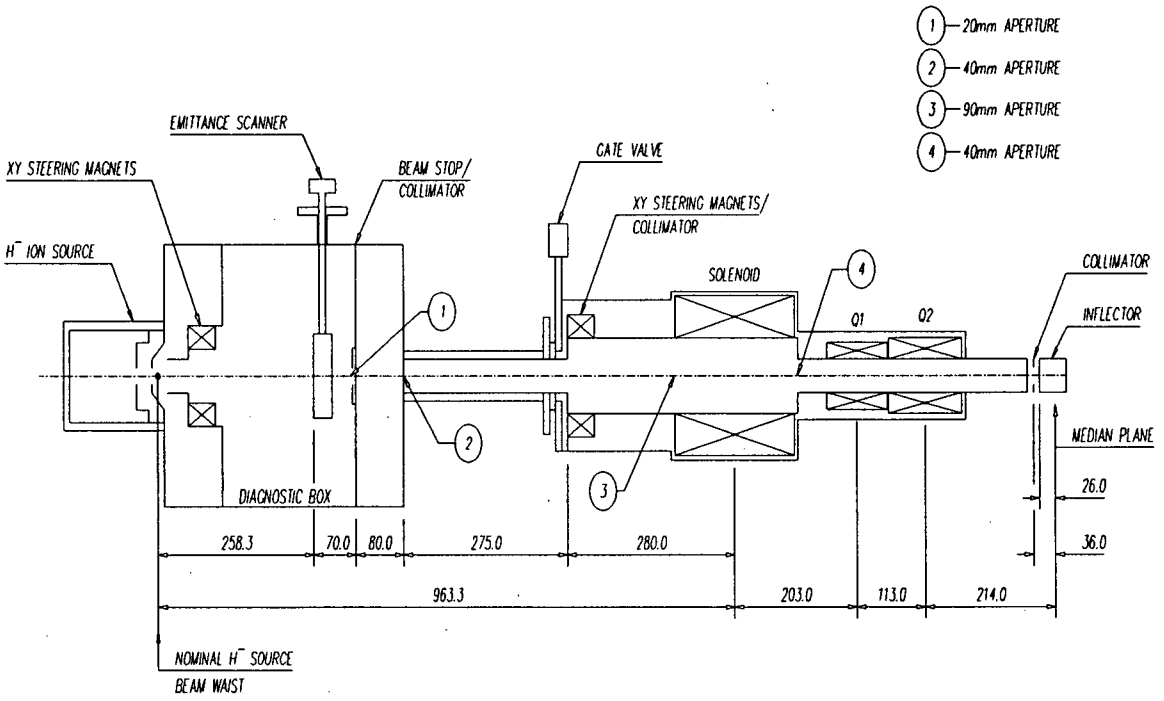

Figure 4.1: *The SQQ injection system layout. Dimensions are in millimetres.*

4.2.1 SQQ INJECTION SYSTEM COMMISSIONING

Prior to performing the SQQ injection line transmission measurements, system commissioning took place. The commissioning process involved achieving stable and repeatable ion source operation, centering the beam through the injection line, and confirming that the injection line, main magnet and RF systems were functioning properly.

4.2.1.1 Ion Source Commissioning

The TR30 type H^- ion source used for the SQQ injection line measurements had a chamber length of 155 mm and used the lens arrangement illustrated in Figure 4.2. For this lens arrangement, ion source parameters were varied and the output current was peaked on the ion source beamstop (IBS) for a number of arc current settings. The output current was shown to be stable over many hours of operation,

and, once nominal source tunes had been established, output current levels were repeatable to within ± 2% using nominal tunes. It was also determined that the ion source required a 15 minute warm up period for stable operation. Changes in arc current setting or in gas flow rate necessitated a wait period of at least a minute before the output current stabilized. Other power supply setpoint changes required a wait period of only a few seconds before output current stability was attained.

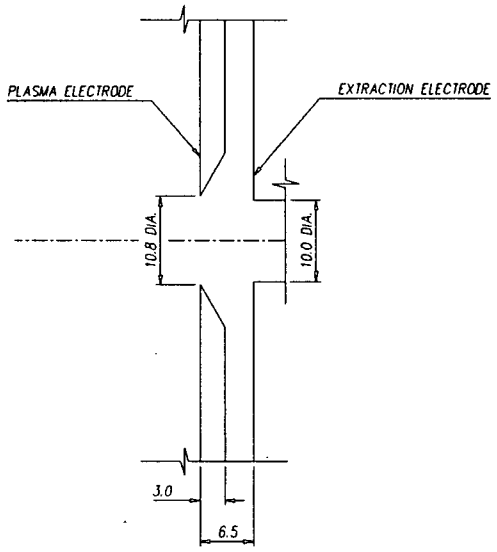

Figure 4.2: *Ion source lens geometry for SQQ tests. Dimensions are in millimetres.*

Table 4.1 lists the ion source tunes for three arc current settings, and the corresponding characteristics of the output current. The error in the last digit of each entry is 1, except for the beam current entries. The relative error for the beam current entries is ±2%, and the absolute error is ±4%. This applies to all beam current readings encountered in this thesis unless otherwise stated. This table shows that the hydrogen flow rate must increase as the arc current increases to obtain the appropriate plasma conditions for peak output currents at the ion source beamstop (IBS). The plasma electrode and the extraction electrode voltages were adjusted iteratively to obtain peak output beam currents at the IBS. The plasma electrode and the extraction electrode currents simply vary as necessitated by their respective voltage settings.

It is interesting to note that the emittance of the low current beam is much larger than for the high current beams. Also of note is that the increased emittance of the low current beam manifests itself

Table 4.1: *Ion source settings are shown which attained the maximum beam at the IBS for three different arc current settings. In addition, the corresponding beam characteristics are shown. The lens configuration in Figure 4.2 was used for these measurements.*

SETTINGS & READINGS	RUN 1	RUN 2	RUN 3
Arc Current (A)	2.7	4.8	6.4
Hydrogen Flow Rate (cc/min)	4.6	8.0	8.9
Plasma Electrode Current (A)	1.7	3.7	5.0
Plasma Electrode Voltage (V)	2.8	2.9	3.1
Extraction Electrode Current (mA)	11	13	17
Extraction Electrode Voltage (kV)	2.18	2.04	2.13
Source Bias Voltage (kV)	25.0	25.0	25.0
Extraction Region Vacuum (Torr)	9.8×10^{-5}	1.7×10^{-4}	1.8×10^{-4}
IBS Beamstop Current (μA)	647	994	1194
IBS Collimator Current (μA)	139	406	480
IBS Total Current (μA)	786	1400	1674
Normalized 4rms Emittance* (mm·mrad)	0.49	0.32	0.31
Beam Waist Diameter* (mm)	4.4	2.2	2.1
Maximum Beam Divergence* (mrad)	60	80	82

* Measurements are for the (x, x') sub-space.

in a spatially large waist with a relatively low divergence, relative to the high current beams. Thus, the low current beam of poor emittance is more compact at the beamstop, spilling only 20% of the total current on the collimator, whereas about 30% of the beam is spilled for the high current beams. Typically, a low emittance beam yields the best beam transmission through a system, however, in this case there is a danger that the low emittance but divergent high-current beams will be limited by the acceptance of the beampipe (40 mm I.D.) between the diagnostic box and the solenoid magnet.

4.2.1.2. SQQ Injection Line Commissioning

Injection line commissioning consisted of ensuring that the steering, solenoid and quadrupole magnets were in working order, and aligning the beam within the injection line. Aligning the beam within the injection line was achieved by first placing a four-jaw collimator at the downstream end of the diagnostic box. Then the steering magnet current settings were adjusted so that the beam spilled on the collimators was minimized while beam dumped on the inflector, which was biased and metered as a beamstop, was maximized. Subsequent to this, the four-jaw collimator was mounted immediately in front of the inflector, and the centering optimization was repeated. This optimization revealed that the upstream

steering magnet setpoints which maximized the beam on the IBS were slightly different than those required to center the beam within the injection line.

4.2.1.3 C.R.M. Cyclotron Commissioning

The first stage of C.R.M. cyclotron commissioning was to verify that the main magnet and the inflector were operational. Once this was ascertained, beam was run to the inflector exit beamstop. System settings were then adjusted until the inflector exit beam current reading was maximized.

Once sufficient confidence was achieved in transporting the beam to the inflector exit, the RF was re-commissioned and the beam was accelerated to 1.125 MeV. The RF system commissioning was accomplished by ensuring that the RF equipment was operational and by then "conditioning" the system. This entailed the following procedure. With the main magnet off, the system was conditioned by first driving the system with a Hewlett Packard 8656 signal generator set at 74.6 MHz. Then the frequency was adjusted to minimize the reflected power while the amplitude of the driving voltage was slowly increased. Once the system was stabilized at the operating point of 50 kV, the system was switched into self-excited mode. The input power was then slowly increased until the forward power was about 7.5 kW and the reflected power was about 0.1 kW. At these power levels the system was stable, and sufficient power was available to accelerate the beam.

4.2.2 SQQ INJECTION LINE TRANSMISSION MEASUREMENTS

Measurements of the total beam current were made at the IBS, the inflector exit beamstop, and the 1.125 MeV beamstop. The total beam current output by the ion source was considered to be the total current intercepted by the IBS.

The initial attempt at maximizing the beam to the inflector exit beamstop with the SQQ system resulted in beam currents and approximate transmission rates described in Table 4.2.

Table 4.2: *Nominal SQQ injection line beam currents and transmission rates to the inflector exit.*

READINGS	RUN 1	RUN 2	RUN 3
Arc Current (A)	2.7	4.8	6.4
Inflector Exit Beamstop Current (μA)	570	756	972
Inflector Collimator Current (μA)	15	38	45
Transmission IBS to Inflector Exit (%)	**73**	**54**	**58**

The beam transmission between any two points in the system was considered to be the total current at the downstream point divided by the current at the upstream point multiplied by 100%. The beam transmission to the inflector exit given in Table 4.2 confirms the suspicions of section 4.2.1.1. The low current beam transmission is much higher than that of the high current beams. Overriding this interesting phenomenon, though, is that under ideal conditions the injection line should be a high transmission region (at least 95%) over all current levels. Since a conservative estimate of the RF phase acceptance is about 10%, the system as described so far will likely only transport about 100 μA to 1.125 MeV. Thus, some optimization of the SQQ set-up was required to enable the system to transport 110 μA of beam or more to 1.125 MeV.

A number of options were available for increasing the transmission efficiency of the SQQ system. These included tailoring the ion source lenses to produce a less divergent beam, reducing the initial system drift length, introducing additional focusing upstream of the nominal focusing elements, and/or increasing the inner diameter of the beampipe. Since the optimal SQQ transmission results were already available from [48], and since the need to achieve a beam current reading of over 110 μA at the 1.125 MeV beamstop with the physical SQQ system was intended as more of a proof of principle experiment than a detailed study, the simplest and least expensive option was chosen for optimizing the SQQ system. This was the option which advocated additional focusing elements (Figure 4.3). The focusing elements chosen were permanent magnet solenoids, which had a peak axial magnetic field strength of 1250 gauss.

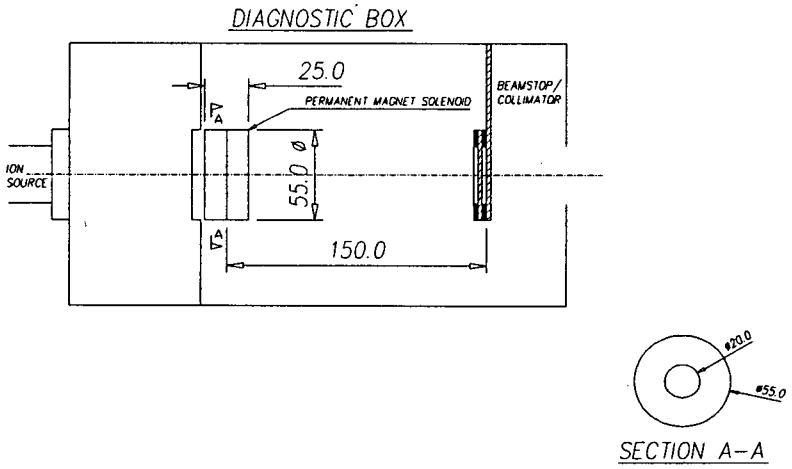

Figure 4.3: *Permanent magnet solenoid arrangement within the diagnostic box. Dimensions are in millimetres.*

Table 4.3 gives the system tune that maximized the beam current at the inflector exit beamstop for the SQQ injection line outfitted with permanent magnet solenoids. Beam was also sent through, using these settings, to the 1.125 MeV beamstop, and a total beam current of 130 μA was obtained. As expected, Table 4.3 illustrates that the beam did become narrower downstream of the permanent magnet solenoid. For example, the IBS beamstop current reading increased while the IBS collimator current reading decreased relative to the readings given in Table 4.1. It is interesting to note that the total IBS current decreased in Table 4.3, however, one should keep in mind that the tune was intended to maximize current at the inflector exit and not at the IBS. It is often the case that the highest beam intensities at downstream points in an accelerating system are achieved by sacrificing some ion source beam intensity for an ion source beam with a better phase space shape. A comparison of Tables 4.1 and 4.3 reveals that the source tunes are indeed slightly different, as expected when two different optimizations are undertaken. The main magnet and inflector setpoints required substantial changes in order to best match the beam to the cyclotron acceptance. The injection line settings changed somewhat to compensate for the new source tune and the effect of the permanent magnet solenoids. Note also that the settings required from run 1 to run 3 in Table 4.3 were very consistent. This is useful, as an injection line tune that does not vary with arc current is very desirable in terms of implementing automatic computer control.

Table 4.4 lists the beam transmission rates achieved between various points in the SQQ injection system. These transmission rates indicate that the effect of the permanent magnet solenoids was to focus the beam enough to gain about 5% to 8% more beam at the inflector exit beamstop. In addition, the peak current attained to 1.125 MeV was 130 μA, well above the 110 μA required. For the record, the peak beam current attained to 1.125 MeV using the modified SQQ system was 134 μA. This was achieved with an arc current of 7.3 amps, a hydrogen flow rate of 8 cc/min and an RF forward power of 7.5 kW, and the system settings were optimized for maximizing the current at 1.125 MeV.

The physical SQQ system, with some modifications, was shown to be a capable substitute injection system for the TR13. In addition, the transmission from the inflector exit beamstop to the 1.125 MeV beamstop, of approximately 12%, matches the maximum transmission obtained in [48]. It is also

apparent that, if necessary, the source lenses could be adjusted or the initial system drift could be reduced to increase the transmission between the IBS and the inflector exit beamstop.

Table 4.3: *C.R.M. & SQQ injection system setpoints and beam current readings for the case where permanent magnet solenoids are used and maximum beam current was obtained at the inflector exit beamstop. Using these settings beam was also transported to 1.125 MeV.*

SETTINGS & READINGS	RUN 1	RUN 2	RUN 3
Arc Current (A)	2.7	4.7	6.5
Hydrogen Flow Rate (cc/min)	4.6	7.8	8.9
Plasma Electrode Current (A)	1.9	3.3	4.9
Plasma Electrode Voltage (V)	3.1	2.6	2.9
Extraction Electrode Current (mA)	4	12	16
Extraction Electrode Voltage (kV)	1.7	2.0	2.3
Source Bias Voltage (kV)	25.0	25.0	25.0
Extraction Region Vacuum (Torr)	9.8×10^{-5}	1.6×10^{-4}	1.8×10^{-4}
1st Steering Magnet [x,y] (A)	[1.6, 0.9]	[1.4, 0.4]	[1.2, 0.0]
2nd Steering Magnet [x,y] (A)	[0.5, 0.4]	[0.5, 0.4]	[0.5, 0.4]
Solenoid Magnet (A)	200	200	200
Q1 Magnet (A)	2.2	2.2	2.2
Q2 Magnet (A)	2.1	2.1	2.1
Main Magnet (A)	448	448	448
Inflector (kV)	±7.7	±7.7	±7.7
RF (kW)	7.5	7.5	7.5
Cyclotron Vacuum (Torr)	1.3×10^{-6}	1.3×10^{-6}	1.3×10^{-6}
IBS Beamstop Current (μA)	691	1026	1328
IBS Collimator Current (μA)	80	298	333
IBS Total Current (μA)	771	1324	1661
Inflector Exit Beamstop Current (μA)	583	826	1096
Inflector Collimator Current (μA)	13	10	8
1.125 MeV Beamstop (μA)	67	102	130

Table 4.4: *SQQ system beam transmission rates for the case where permanent magnet solenoids were used and the tune was optimized for obtaining maximum beam current at the inflector exit beamstop.*

TRANSMISSION ENDPOINTS	RUN 1	RUN 2	RUN 3
IBS to Inflector Exit Beamstop	76	62	66
IBS to 1.125 MeV Beamstop	8.7	7.7	7.8
Inflector Exit to 1.125 MeV Beamstop	11.5	12.3	11.9

4.3 AN INVESTIGATION OF ION SOURCE PERFORMANCE

The SQQ injection line transmission experiments high-lighted the importance of having the beam well matched to the injection line and/or the injection line well matched to the beam for maximum beam transmission. The Q-based injection system simulations shown in Figures 3.5 and 3.6 used a normalized source emittance of 0.35 mm-mrad and a source waist radius of 2.5 mm. These parameter choices result in a full (not half) beam divergence of approximately 40 mrad. Unfortunately, the full beam divergence's listed for the ion source in Table 4.1 are 60 – 80 mrad. These divergence's were too large for the nominal Q based system configuration. One possible solution would have been to make the diagnostic box shorter, however, this would have resulted in insufficient space for the vacuum pumps. Monetary and time constraints negated the possibility of creating a Q-based system with a larger acceptance. Ad hoc solutions such as mounting permanent magnet solenoids in the diagnostic box were not considered long term solutions, as such techniques were contrary to the original design philosophy of building a simple, compact and modular injection line composed of identical focusing elements. Consequently, the only optimization avenue available was to investigate the performance of the ion source to determine whether any configuration changes could provide a less divergent beam that would be more appropriate to the initial drift space and to the acceptance of the Q-based system.

The TR13 extracted beam current requirement is about a factor of five smaller than that required for the TR30 (100 μA versus 500 μA). Since less extracted beam current is required by the TR13, the arc power supply current rating was reduced from about 30 amps to 7 amps. This resulted in a significant cost saving (less expensive power supply), but it placed the ion source in an unfamiliar operating regime. Typically, H^- ion source researchers expend little or no time investigating source performance in the low arc current ranges. Thus, source performance investigations were necessary for providing a better beam match to the Q based injection systems, and for providing some new data to the scientific community [50].

The main goal of the ion source experiments was to investigate a sufficient number of source configurations and parameter variations to confidently select the best ion source scenario for the Q based injection system. This was accomplished, in part, by tuning for the highest output beam current possible at

selected arc current settings for each configuration tested, and then by measuring the phase space characteristics of these maximum current beams. Each configuration tested consisted of a standard TR30 H^- ion source with any number of the geometric parameters listed in Figure 4.4 changed from their nominal values. The compilation of ion source tunes and measured beam characteristics provided an opportunity to determine relationships between the parameters, and to deduce which configuration would likely produce the best overall beam transmission results. The ion source experiments also provided an opportunity to assess other characteristics such as the axial symmetry of the beam and the character of the beam in phase space as a function of its kinetic energy.

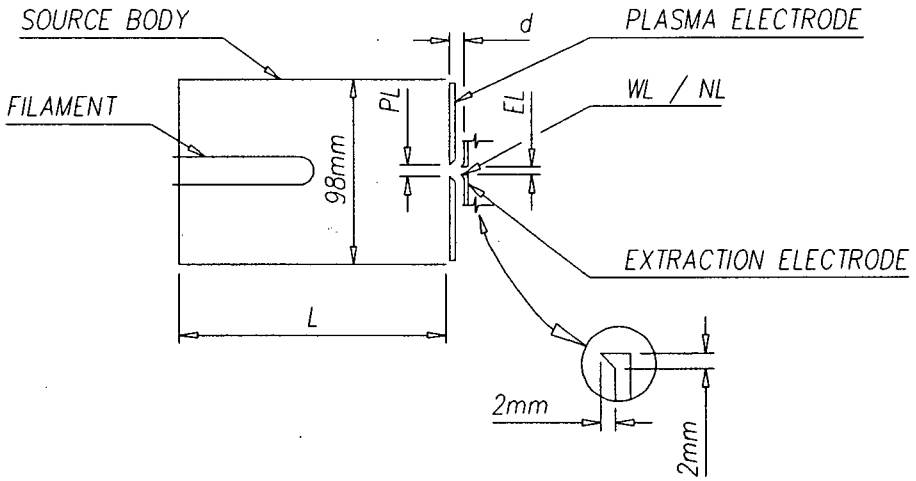

Figure 4.4: *The variable geometric parameters of the ion source. Refer to Appendix II for further details.*

4.3.1 ION SOURCE MEASUREMENTS

Note that all parameters which are not explicitly discussed in any given measurement should be assumed to be held constant.

4.3.1.1 Hydrogen Flow Rate

The plasma density varies, in part, as a function of the hydrogen flow rate. The plasma density, in turn, has a bearing on the output current level. The relationship between the hydrogen flow rate and the output current for a given arc current was found to be a fairly flat curve for all source configurations.

Figure 4.5 illustrates the change in output current as a function of the hydrogen flow rate for an ion source with geometric parameters L = 105 mm, PL = 8 mm, and EL = 8 mm with a lip (WL = with lip). Such an ion source is typically specified as L105/PL8/EL8/WL for brevity. All other parameters in Figure 4.5 were adjusted for peak performance at an arc current of 7.3 amps. The broad peak indicates that the hydrogen flow rate can vary by ± 0.5 cc/min without affecting the total output current significantly.

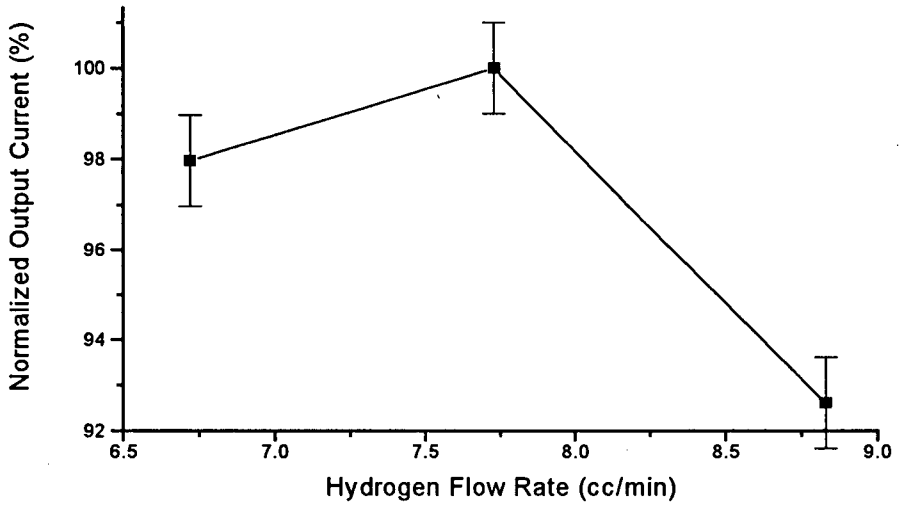

Figure 4.5: *Percentage change in ion source output current as a function of the hydrogen flow rate.*

Recall from section 2.2.1.4 that the output beam current increases as the arc current increases. In order to maximize the output beam current at a particular arc current setting, however, requires an optimized hydrogen flow rate. The hydrogen flow rates which maximize the output current over a range of arc current settings are shown in Figure 4.6, for two ion source configurations. The relationship between the hydrogen flow rate and the arc current which produce the highest output current is shown to be roughly linear, and the long ion source is shown to require a higher flow rate than the short ion source for optimal performance. This plot is representative of all the ion source configurations tested.

The hydrogen flow rate necessary to peak the output current was found to increase only slightly as a function of the plasma electrode aperture area. For example, the overall increase in flow rate from an

8 mm diameter aperture with area 210 mm^2 to a 10.8 mm aperture with area 366 mm^2 was found to be about 1.2 cc/min for any particular arc current setting.

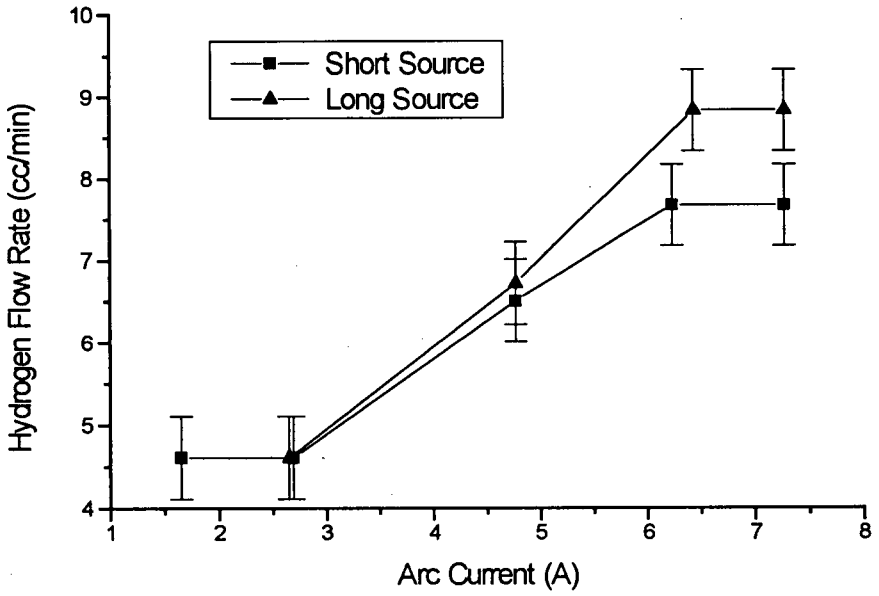

Figure 4.6: *Hydrogen flow rates required to maximize the output current for a given arc current for two ion source configurations: Long Source = L155/PL9/EL10/WL and Short Source = L105/PL9/EL10/WL.*

4.3.1.2 Plasma and Extraction Electrode Apertures

An obvious ion source configuration change to investigate was the maximum ion source output current as a function of plasma and extraction electrode aperture sizes. The current density which can be extracted from a plasma will remain constant if the plasma conditions remain constant. Therefore, the extracted beam current should be proportional to the area of the plasma and extraction electrode apertures if the plasma conditions do not change. However, since optimizations will be performed to maximize the output beam current of the ion source as a function of the aperture sizes, the plasma conditions may change causing the direct proportionality to be affected. Figure 4.7 gives the maximum ion source output current as a function of the plasma electrode aperture area for four different extraction electrode configurations. In all cases L was 155 mm, the arc current was 6.4 amperes, and PL was either 6, 8, 9, 10 or 10.8 mm. All other parameters were optimized to achieve the maximum output beam current.

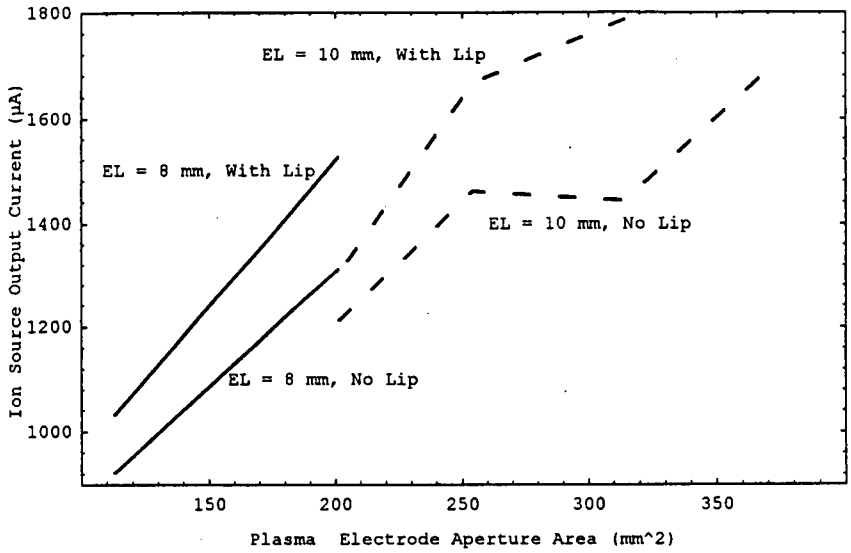

Figure 4.7: *Ion source output current as a function of the plasma electrode aperture area for four different extraction electrode aperture sizes.*

Figure 4.7 illustrates that the output current does increase approximately linearly as the plasma electrode aperture increases. Also note that significant gains in output current are obtained by adding a lip to the extraction lens aperture. This increase in beam current, when the lip is present, likely occurs due to a better plasma meniscus shape and/or due to better focusing, which causes more of the extracted beam to actually make it through the third electrode to the IBS. The addition of the extraction electrode lip necessitated a reduction of the plasma electrode voltage by about 10% in order to obtain maximum output current. This implies that the new arrangement required a new set of plasma parameters. This, then, suggests another reason for the increased output current; the new plasma parameters may have permitted more beam to be extracted through the meniscus.

Figure 4.7 also shows that at a plasma electrode aperture area of 201 mm^2 (PL = 8 mm), the output current can be increased by reducing the extraction electrode aperture from a diameter of 10 mm to 8 mm for both the lip and no lip cases. This change also affects the focusing forces, the meniscus shape and the plasma conditions near extraction. It is difficult to clearly determine which effect dominates in producing the higher output currents.

Figures 4.8 and 4.9 depict the changes in the output beam emittance and maximum divergence, respectively, as a function of the plasma electrode aperture area for the four extraction electrode configurations. It is interesting to note that the extraction electrode configurations that had the highest output beam currents also had the smallest beam divergence's and the largest beam emittances for a given plasma electrode aperture area. This suggests that higher output beam currents are probably more related to better transport through the third electrode than to a higher current yield from the plasma. In particular, for a given plasma electrode aperture area, the extraction electrode with lip tends to disrupt the curvature of the meniscus causing a larger beam emittance (refer to section 2.2.1.4.), but in doing so it reduces the maximum beam divergence, which keeps the beam size small as it passes through the third electrode and reduces beam loss due to collimation.

Figure 4.8 also shows that the beam emittance increases as the plasma electrode aperture area increases for all extraction electrode configurations. This is likely caused, for a given extraction electrode configuration, because the larger plasma electrode apertures cannot contain the plasma as well as the smaller plasma electrode apertures. This tends to allow the meniscus to flatten or bulge which causes emittance growth in the manner described in section 2.2.1.4.

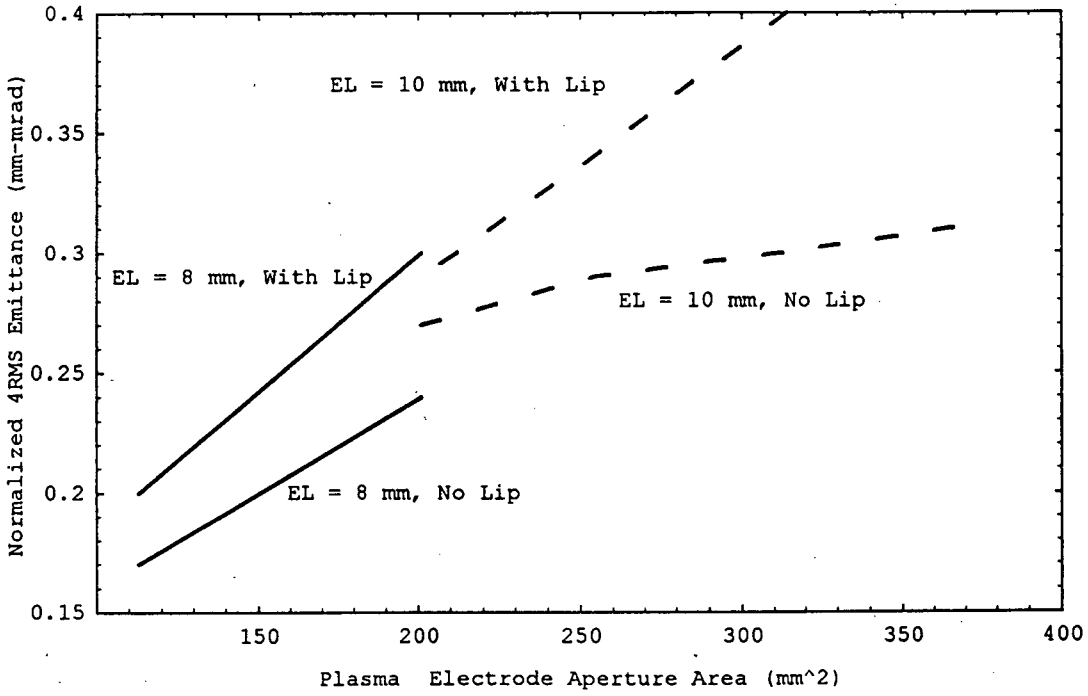

Figure 4.8: *Ion source emittance as a function of the plasma electrode aperture for four different extraction electrode aperture sizes.*

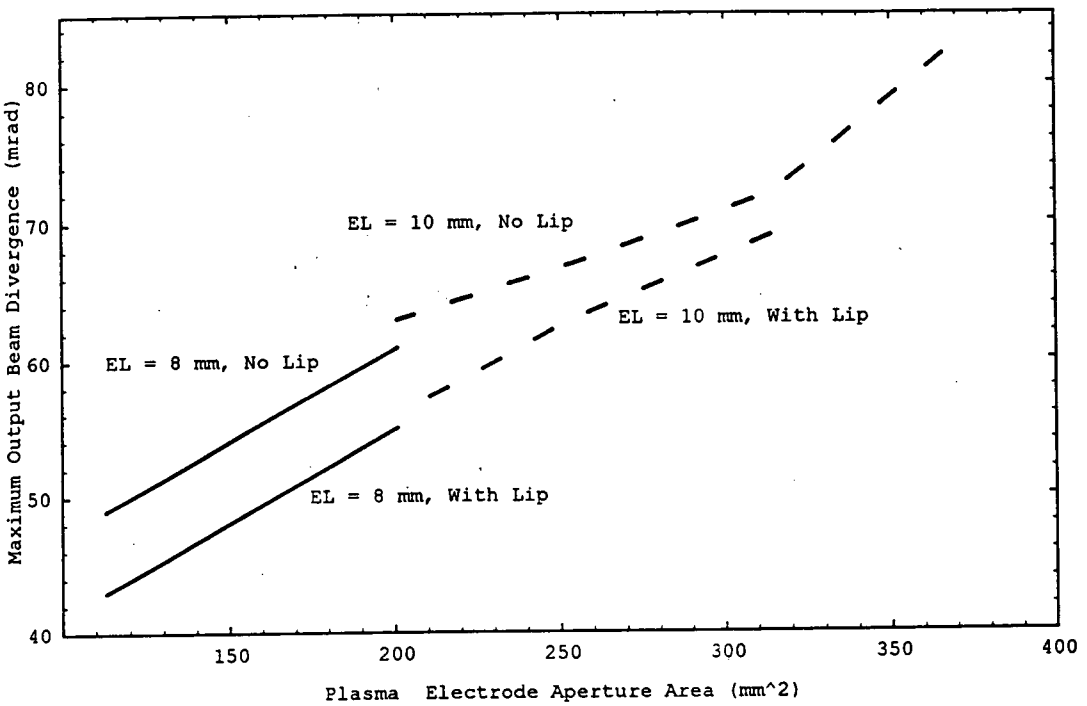

Figure 4.9: *The ion source maximum beam divergence as a function of the plasma electrode aperture for four different extraction electrode aperture sizes.*

4.3.1.3 Source Volume

The nominal TR30 ion source has an ion source chamber length of L = 155 mm, and typically produces 5 mA of output current at an arc current of approximately 25 A with PL = 11 mm and EL = 10 mm. Since the TR13 arc current is limited to 7 A, it was felt that the source volume might be too large to yield the optimal plasma densities and temperatures for this arc current. Luckily, events conspired to permit an ion source of L = 105 mm to be available for testing (68% of the volume of the long source). Figure 4.10 compares the maximum output beam current of the short source configurations L105/PL9/EL10/WL and L105/PL8/EL8/WL to the long source configuration which produced the highest output current, L155/PL10/EL10/WL. In addition, a representative set of long source configurations are also plotted. In each case all the adjustable parameters have been varied to obtain the maximum possible output current.

It is clear from Figure 4.10 that the smaller source volume of the L = 105 mm source configuration yields significantly higher output beam currents over the 0 to 7 amp arc current range than the long source for any of its lens configurations. As suspected, the lower arc current regime is much

better suited to a smaller volume ion source in terms of producing the most output current. Also note that the ion source configurations with an extraction electrode lip (WL) consistently out perform their counterpart configurations with no such lip (NL).

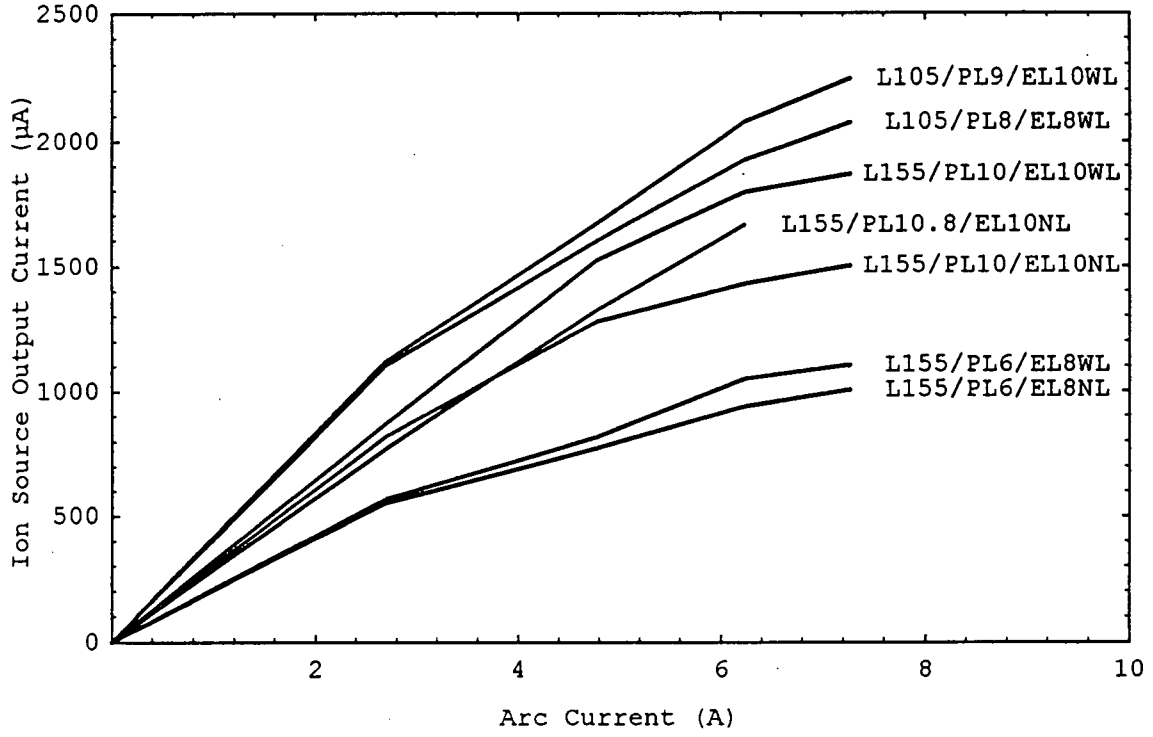

Figure 4.10: *Output beam current as a function of arc current for a number of representative ion source configurations.*

4.3.1.4 Phase Space Characteristics as a Function of Arc Current

Another important consideration in matching an ion source beam to the acceptance of the cyclotron is the variation of ion source beam characteristics as a function of arc current. The variation in the beam characteristics occur for two main reasons. First, the plasma parameters vary as a function of the arc current, and second the extraction optics settings change in relation to the magnitude of the space charge associated with the output current. Figures 4.11, 4.12, 4.13 and 4.14 show the (x, x') phase space contour plots and the horizontal (x) intensity profiles of the output beams from the L155/PL6/EL8/WL source configuration for arc current settings of 2.7, 4.8, 6.4, and 7.3 amps, respectively. The improvement in beam emittance as a function of arc current depicted in these figures is representative of the improvement seen for the other ion source configurations tested, as shown in Figure 4.15.

As an aside, it is interesting to note that the bulk shape of the beam in phase space is indeed elliptical in shape. This validates the use of beam ellipses when simulating real physical beams during beam transport exercises, as suggested in Chapter 2.

The phase space plot which represents the beam produced with the lowest arc current, Figure 4.11, looks as if it is the superposition of two different beams. The origin of this effect may have arisen from two different curvatures existing in the meniscus, one near the center and a different one near the perimeter. Another possibility is that non-linear focusing may have been imposed on the outermost ions, in one of the accelerating lens apertures, but not on the innermost ions.

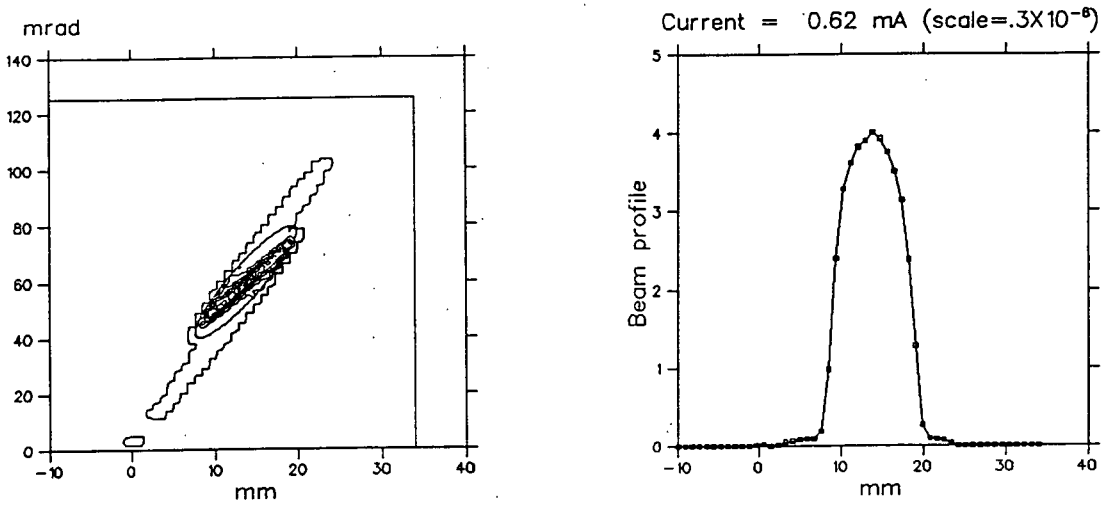

Figure 4.11: The *(x, x') phase space contour plot and intensity profile for the L155/PL6/EL8/WL ion source at 2.7 amperes of arc current. The normalized 4rms emittance is 0.37 mm-mrad.*

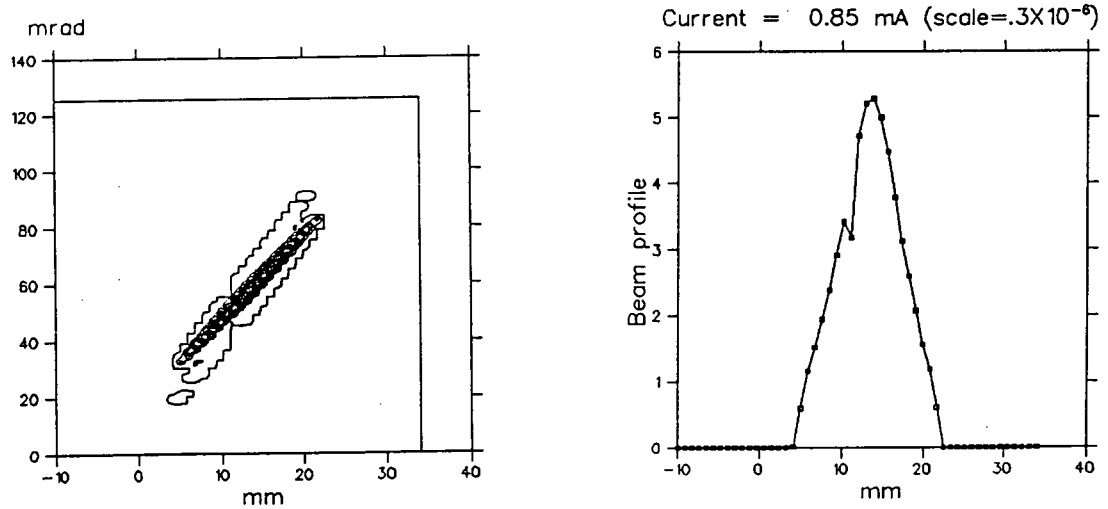

Figure 4.12: The *(x, x') phase space contour plot and intensity profile for the L155/PL6/EL8/WL ion source at 4.8 amperes of arc current. The normalized 4rms emittance is 0.24 mm-mrad.*

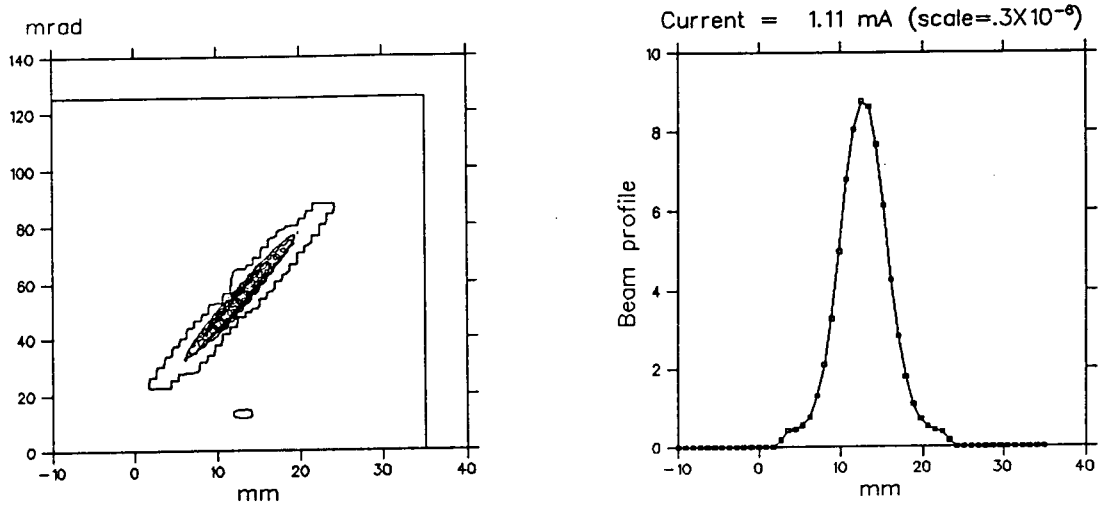

Figure 4.13: The *(x, x') phase space contour plot and intensity profile for the L155/PL6/EL8/WL ion source at 6.4 amperes of arc current. The normalized 4rms emittance is 0.20 mm-mrad.*

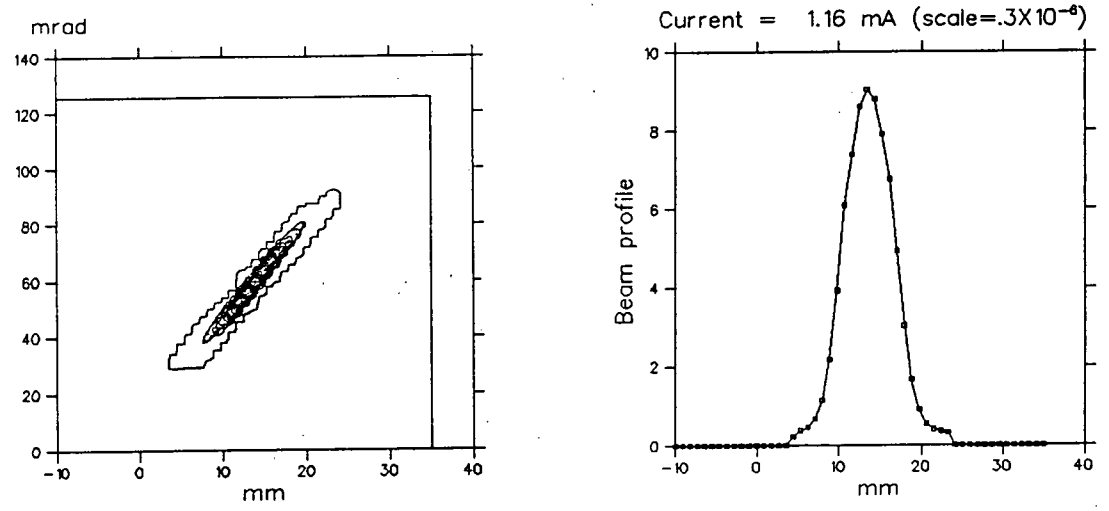

Figure 4.14: The *(x, x') phase space contour plot and intensity profile for the L155/PL6/EL8/WL ion source at 7.3 amperes of arc current. The normalized 4rms emittance is 0.19 mm-mrad.*

In each of the figures, the 4rms emittance ellipse has been overlaid on the plots. In all the figures except 4.11, the 4rms emittance ellipses line up so well with the phase space contours that they are not noticeable. With the "second" beam causing problems in Figure 4.11, the 4rms emittance ellipse is noticeable because it must be rotated and enlarged to adequately represent the oddly distributed low arc current beam. Refer to equation 2.23 for a reminder of how the 4rms emittance is calculated.

Recall that beams of low emittance are preferred in charged particle transport. Figure 4.15 makes it clear that the ion source configurations with no lip on the extraction lens (NL) consistently out perform their counterpart configurations with the lip (WL). This is interesting because it is contrary to the WL/NL relationship found in Figure 4.10. This underscores the need to determine some method of weighing the various beam parameters when comparing ion source configurations.

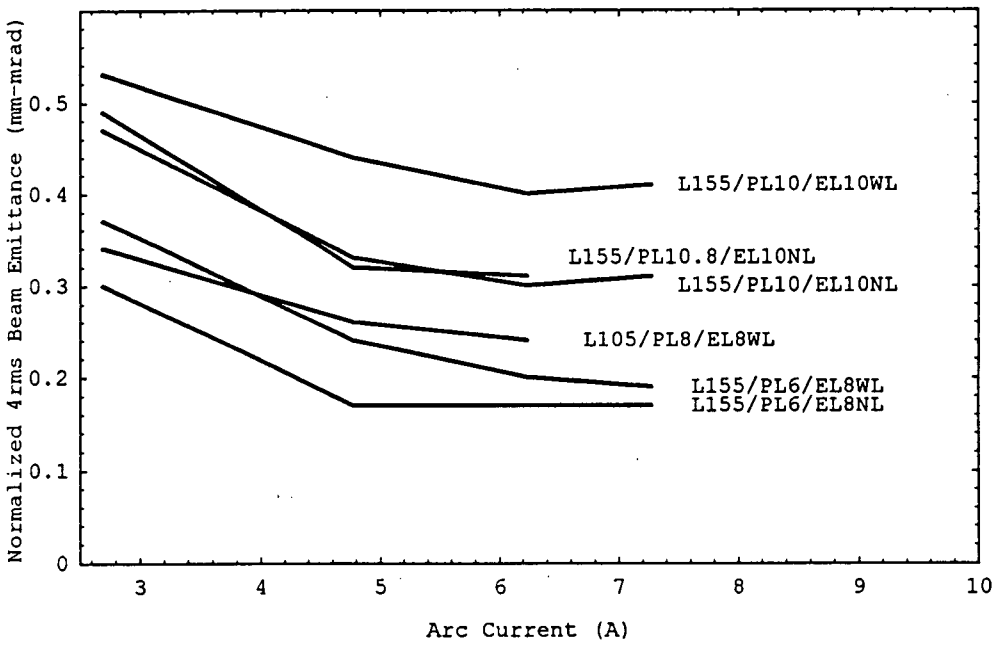

Figure 4.15: *The normalized 4rms beam emittance as a function of arc current for a number of representative ion source configurations.*

4.3.1.5 Selection of the Best Source Configurations for the Q Based Injection Line

Recall that one of the purposes of pursuing ion source measurements and optimizations was to find ion source parameters that produced a beam well suited to the fixed initial drift length and aperture size of the Q based injection systems. Beams of relatively small cross-sectional area that just fill the quadrupole magnet apertures are favoured. Also beams with the smallest emittance are preferred, and, of course, beams with more current, all other beam characteristics being equal, are desirable. A number (η) can be computed using equation 4.1, for each of the ion source configurations, which embodies these requirements. Larger values of η correspond to source configurations which will be best matched to the Q based injection system. Equation 4.1 is given by

$$\eta = \frac{I/A}{\varepsilon} = \frac{J}{\varepsilon}, \tag{4.1}$$

where the parameters I, A and ε are all measured at the emittance scanner (Figure 4.1), which is of type [100]. The current I is the H^- beam current in μA, the normalized 4rms emittance of the beam, ε, is measured in (mm-mrad), the area of the 4rms emittance beam, A, is measured in mm^2, and J is just the current density in $\mu A/mm^2$.

Table 4.5 lists the values of η obtained for each of the source configurations that were fully tested. Note that η was not explicitly maximized during experimentation. Typically, beam currents were only maximized, and, therefore, Table 4.5 only approximately represents the capability of each ion source configuration. Also note that external time constraints permitted only one short ion source configuration to be fully tested. Based on the results obtained from the short ion source, it would have been very interesting to have further explored the characteristics of this ion source.

Table 4.5: *η as a function of ion source configuration and arc current. Recall that the ion source configuration designations can be read as follows: L155/PL10.8/EL10/NL corresponds to L = 155 mm, PL = 10.8 mm, EL = 10 mm and NL = no lip in terms of the Figure 4.4 designations.*

Source Configurations	Arc = 2.7 A	Arc = 4.8 A	Arc = 6.4 A	Arc = 7.3 A
L155/PL10.8/EL10/NL	5.7	9.7	12.7	–
L155/PL10/EL10/NL	6.4	9.8	13.3	14.8
L155/PL9/EL10/NL	8.1	11.2	18.2	–
L155/PL8/EL10/NL	10.7	14.3	15.6	17.8
L155/PL10/EL10/WL	8.1	8.9	13.7	14.5
L155/PL9/EL10/WL	8.3	8.7	16.7	18.1
L155/PL8/EL10/WL	11.1	16.2	19.9	20.6
L155/PL8/EL8/NL	12.9	11.1	22.1	23.2
L155/PL6/EL8/NL	**8.5**	**22.7**	**35.9**	**40.7**
L155/PL8/EL8/WL	13.4	25.1	25.4	27.9
L155/PL6/EL8/WL	**13.4**	**18.2**	**39.1**	**49.6**
L105/PL8/EL8/WL	**11.6**	**18.8**	**24.0**	**35.1**

The two highest rated ion sources in terms of η were the long source configurations with 6 mm diameter plasma electrode apertures and 8 mm diameter extraction electrode apertures. These two source configurations, therefore, were most capable of producing beam which could be transported from the IBS to the inflector exit without loss. However, the total output current of these configurations was only about 1000 μA, which meant, for a typical RF phase acceptance of approximately 10%, that just over 100 μA of

beam would make it to the 1.125 MeV beamstop. The short source configuration which came in at third place overall, could produce about 2000 μA in output current. Therefore, this configuration could still lose some beam in the injection line and yield well over 100 μA of beam at the 1.125 MeV beamstop.

Table 4.5 makes it clear that source configurations with EL = 8 mm were preferred over configurations with EL = 10 mm, and, in general, smaller plasma electrode apertures were also preferred.

In summary, it was expected that the beam transmission rates from the IBS to the inflector exit beamstop would be highest for those configurations with the largest η values. The short source configuration looked particularly favourable as its η number was quite high, and its output current was well above the rough threshold of 1000 μA needed to achieve 100 μA at the 1.125 MeV beamstop.

4.3.1.6 Injection Line Pressure

Ion source performance as a function of the injection line pressure was not extensively studied. Only two injection line pressure scenarios were studied, and this was done on only the short source configuration. The only variable in the experiment was the pressure at the upstream end of the diagnostic box.

The nominal pressure at the downstream end of the diagnostic box for the L105/PL8/EL8/WL source configuration, and a 6.4 A arc setting with a gas flow of 7.8 cc/min was 1.6×10^{-4} Torr. Under these conditions, with all other source settings at their nominal positions for producing maximum output current, the output current was 1925 μA, the 4rms emittance was 0.35 mm-mrad, the 4rms beam diameter at the scanner was 17.1 mm, and η was 24.0 $\mu A/mm^{-2}/mm\text{-}mrad$.

The second pressure condition was 4.4×10^{-4} Torr. Under this scenario the output current was 1916 μA, the 4rms emittance was 0.24 mm-mrad, the 4rms beam diameter at the scanner was 13.6 mm, and η was 55.0 $\mu A/mm^{-2}/mm\text{-}mrad$. Under these conditions the η value tops all those listed in Table 4.5.

The second pressure condition was forced upon the experiments by a change in the state of the vacuum system. Unfortunately, the nominal pressure condition could not be regained during the remainder of the experiments, so the beam characteristics for this condition could not be re-checked.

However, the beam characteristics for the second pressure condition were re-confirmed several times. All of the experiments in Chapter 5 were performed with the higher than nominal injection line pressure.

The improved emittance of the beam under higher than normal injection line pressures has been documented by Baartman and Yuan in [96]. An injection line held at a higher pressure than normal tends to lose some beam due to gas stripping, but the benefit is that any resultant positive ions become trapped in the negative potential well of the beam causing a cancellation of net charge. This reduces the repulsive space charge forces between the particles of the beam, which, in turn, reduces emittance growth. In this case the reduced emittance growth probably occurred in the extraction region, as the injection line is already highly space charge neutralized.

4.3.1.7 Bias Voltage

The ion source bias voltage determines the kinetic energy of the beam. The nominal value of the bias voltage is 25 kV. A number of injection line and center region experiments were expected to involve beams with non-nominal kinetic energies. Therefore, it was important, at this stage, to determine whether any changes in the ion source beam characteristics would occur as a function of a change in bias voltage.

For the L105/PL8/EL8/WL source configuration with all parameters at their nominal settings except for the injection line vacuum, which was at 4.4 x 10^{-4} Torr, the bias voltage was varied and the beam characteristics were measured. Table 4.6 lists the results.

Table 4.6: *The (x, x') beam characteristics as a function of the ion source bias voltage for the L105/PL8/EL8/WL ion source configuration set at an arc current of 6.4 amperes. The injection line vacuum was recorded as 4.4 x 10^{-4} Torr.*

Bias Voltage (kV)	4RMS ε (mm-mrad)	Waist Diameter (mm)	Maximum Divergence (mrad)	Scanner Beam Diameter (mm)	Scanner to Waist Distance (mm)	Output Beam Current (μA)
28	.27	2.9	47	14.5	246	1897
26	.25	2.9	47	14.7	253	1897
25	**.24**	**2.9**	**45**	**14.1**	**246**	**1860**
25	**.23**	**3.0**	**43**	**13.1**	**239**	**1907**
25	**.24**	**3.0**	**44**	**13.6**	**243**	**1916**
24	.23	2.9	45	14.0	251	1879
22	.22	2.6	48	15.5	268	1785
19	.23	2.5	59	19.4	286	1766

The differences between the three rows of 25 keV beam measurements in Table 4.6 give an indication of the error bars associated with any particular measurement in the table. Based on this then, one can see that the 24 kV through to 28 kV measurements are essentially equal. The 22 kV beam characteristics are only different in that the waist is farther upstream, which results in a larger beam at the scanner. In addition, the 22 kV measurement exhibits some beam loss, which possibly occurs on the third electrode lens. The 19 kV beam characteristics accentuate those already being exhibited by the 22 kV beam. As well, the 19 kV beam has a much larger maximum beam divergence than the other beams. The focusing of the ion source lenses are undoubtedly far from optimum once the beam energy is as low as 19 kV.

The (x, x') phase space contours and horizontal intensity profiles for the 22 through 28 kV beams look very similar. A representative example is given in Figure 4.16a which gives the profiles for the third 25 kV beam listed in Table 4.6. Figure 4.16b gives the profiles for the 19 kV beam. Notice that the 25 kV beam, which is preferred relative to the 19 kV beam, has a nice intense core that is not spatially spread out.

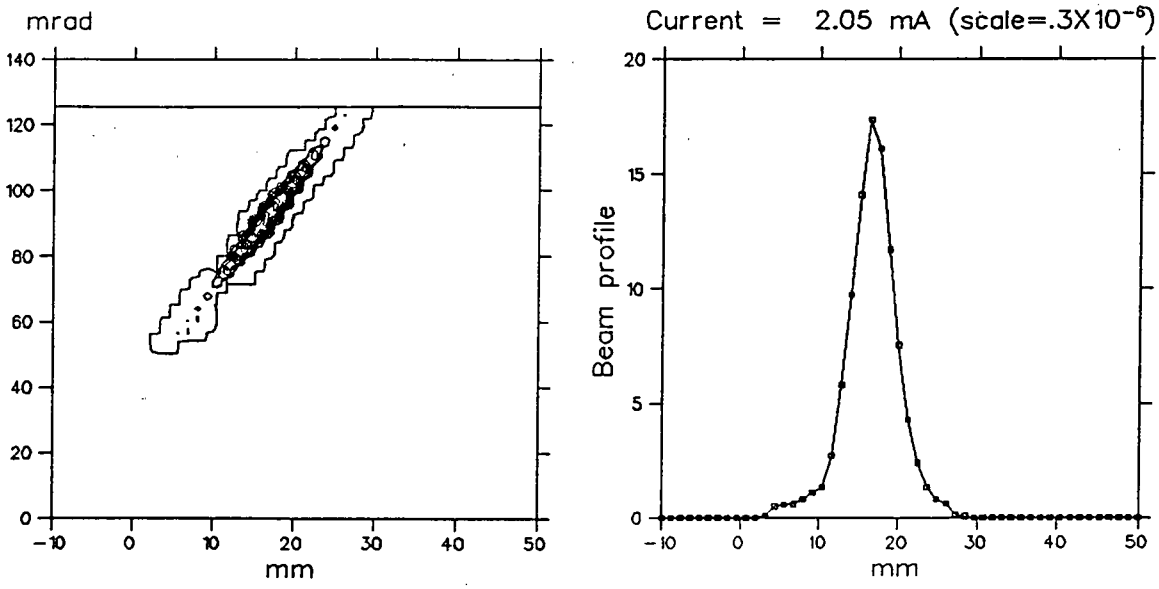

Figure 4.16a: *The (x, x') phase space contours and the horizontal intensity profile for a representative 25 kV beam from Table 4.6.*

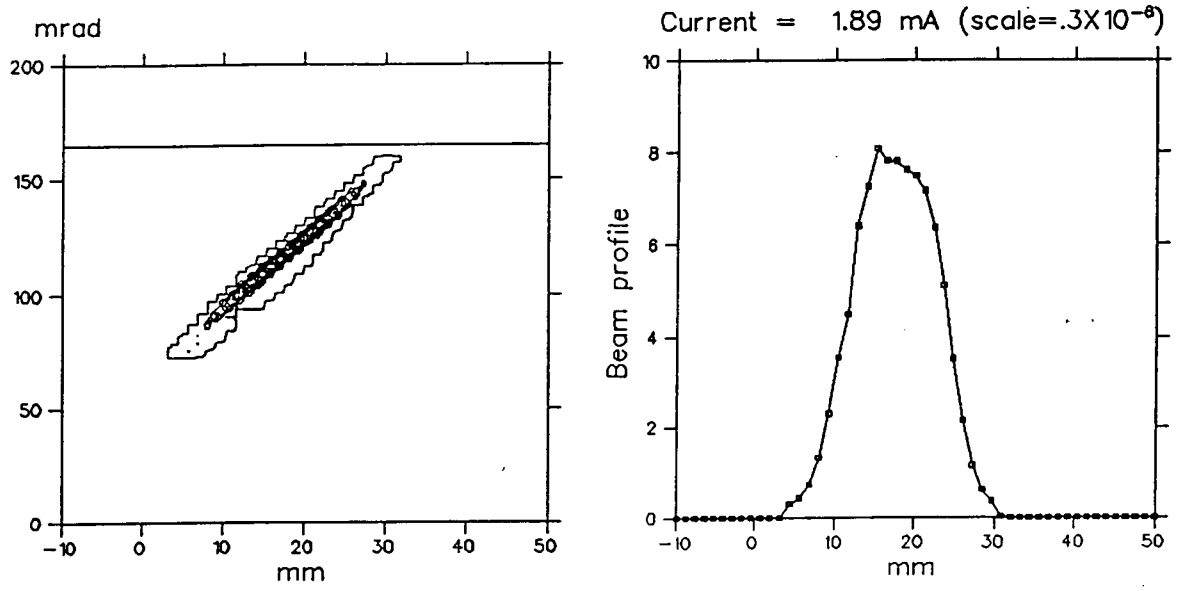

Figure 4.16b: *The (x, x') phase space contours and the horizontal intensity profile for the 19 kV beam from Table 4.6.*

4.3.1.8 Vertical Phase Space Characteristics

A common assumption is that the (x, x') phase space characteristics of the ion source's output beam are the same as those in the (y, y') phase space. However, various factors could cause this assumption to be false. One such factor is the transverse magnetic field which sweeps the unwanted electrons out of the beam at the extraction electrode. The space charge force associated with these electrons may affect one side of the beam more than the other. Another possible factor could be slight asymmetries in lens placement during assembly.

Table 4.7 lists the (y, y') characteristics of the beam for the same ion source conditions used for the 25 kV beam in Table 4.6. The differences between the two measurements shown in Table 4.7 give an indication of the error in repeated measurements. Unfortunately, the difference between the two measurements is fairly large. In retrospect, it is obvious that it would have been useful if these measurements had been repeated several more times. However, a comparison of the 25 kV measurements from Tables 4.6 and 4.7 reveals that the variation of characteristics overlap, and therefore the beams are deemed to be equivalent, within experimental error, in the (x, x') and (y, y') phase planes.

Table 4.7: *The (y, y') beam characteristics as a function of the ion source bias voltage for the L105/PL8/EL8/WL ion source configuration set at an arc current of 6.4 amperes. The injection line vacuum was recorded as 4.4 x 10^{-4} Torr.*

Bias Voltage (kV)	4RMS ε (mm-mrad)	Waist Diameter (mm)	Maximum Divergence (mrad)	Scanner Beam Diameter (mm)	Scanner to Waist Distance (mm)	Output Beam Current (μA)
25	.26	3.4	41	13.2	238	1916
25	.23	2.9	43	14.1	263	1832

Figure 4.17 gives the phase space contours and intensity profiles for the first 25 kV beam listed in Table 4.7. Comparison with Figure 4.16a reveals that the two beam intensity profiles look very similar except for their low intensity phase space contours, which are oriented and shaped somewhat differently. The low intensity contours are of little importance, however. The two beams can be considered to be equivalent, since their high intensity cores are very similar.

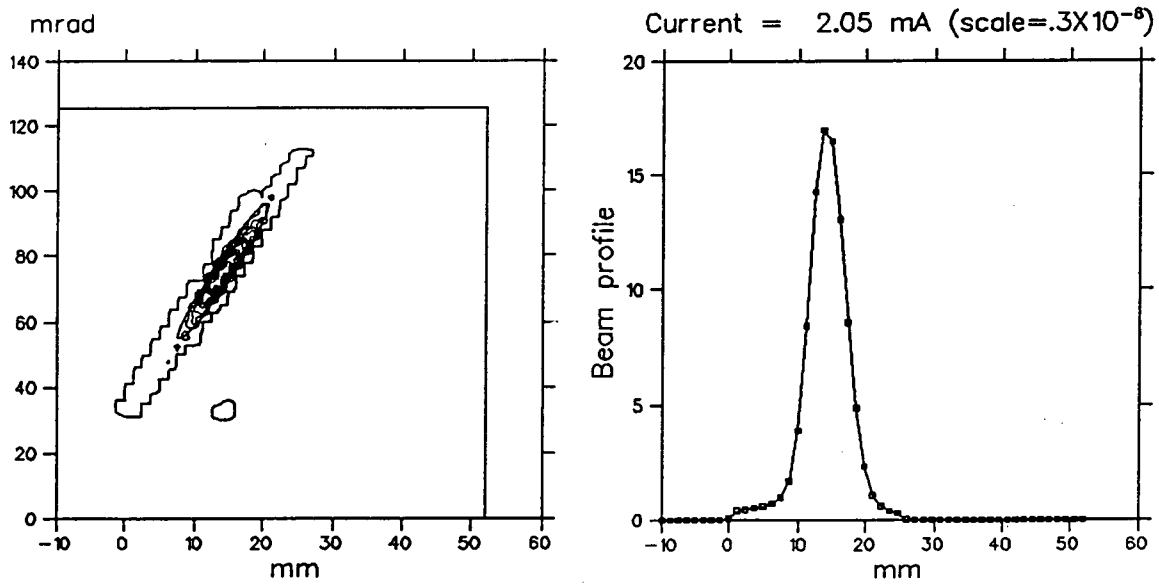

Figure 4.17: *The (y, y') phase space contours and the vertical intensity profile for a representative 25 kV beam from Table 4.7.*

As a consequence of these comparisons, the assumption that the two phase planes are identical will be accepted in subsequent computations and analysis.

4.4 THE 4Q INJECTION SYSTEM

The 4Q injection system design parameters were derived in section 3.2.3. In this section of the thesis the first general tests of the 4Q injection system are described. Commissioning tests and the system set-up are first discussed briefly. Following this the beam transmission measurements are documented. The transmission measurements for all the ion source configurations discussed in section 4.3 are studied. As well, the 4Q transmission measurements are used to compare the 4Q and the SQQ systems in terms of performance. Lastly, the beam transmission as a function of the injection line axial rotation angle is presented.

4.4.1 4Q SYSTEM COMMISSIONING

4.4.1.1 System Layout

After removing the SQQ injection line, the 4Q injection line was installed. The 4Q magnets were each aligned to have the same pole orientation. Once the 4 magnets were bolted together, the whole set of magnets was rotated so that the Q0 defocusing axis, for a negative ion beam, was at 37° counter clockwise from the inflector entrance electrode edges as viewed looking in the direction of beam travel. Unfortunately, the entrance electrode was not easily accessible, so a best estimate for the inflector entrance angle was used. This angle was estimated to be 10° clockwise from vertical, as viewed in the direction of beam travel. Therefore, the defocusing axis for a negative ion beam on Q0 was fixed at 27° counterclockwise from vertical as viewed looking in the direction of beam travel (refer to Figure 4.18).

The quadrupole magnets were wired so that Q1 and Q3 were oppositely powered to Q0 and Q2. A Hall probe was used to verify that the magnetic field directions were correct.

The sensitivity of the beam transmission to 4Q rotation angle was not expected to be too high, and transmission as a function of rotation angle was to be tested as part of the experimental process, so having a potentially off-nominal starting angle for the injection system was not deemed a problem. After the experiments were completed, the inflector was removed and the angle of the electrode edges to the vertical was found to be 14°.

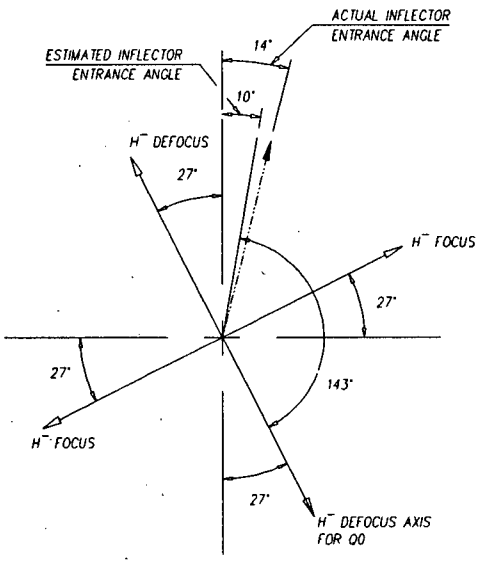

Figure 4.18: *Q0 orientation with respect to the lab axes and the inflector entrance angle.*

The 4Q system layout is given in Figure 4.19. The 4Q system is 33 cm shorter than the C.R.M. SQQ system. Note also that the second set of xy steering magnets shown in Figure 4.1 was removed from the 4Q system, as prescribed in Chapter 3.

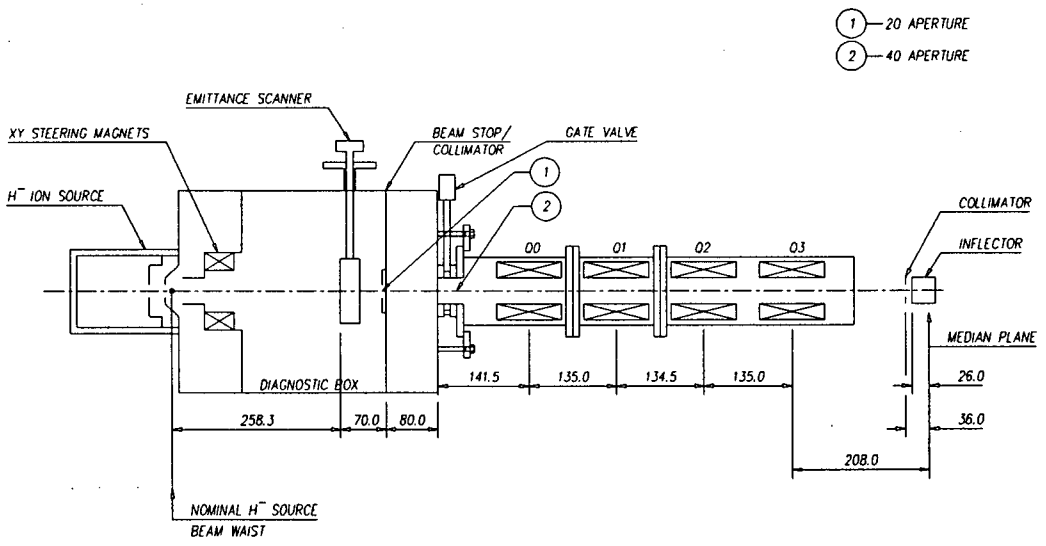

Figure 4.19: *The 4Q injection system layout. All dimensions are in millimetres.*

4.4.1.2 Initial Operation

The L155/PL10.8/EL10/NL source configuration used with the SQQ system was initially used to test the 4Q system. As was done with the SQQ system, the four-jawed collimator was installed

immediately upstream of the inflector entrance to facilitate initial beam centering. Subsequent to this, the four-jawed collimator was removed and beam was run to the inflector exit beamstop.

The initial quadrupole settings were those determined in Chapter 3. They are listed in Table 4.8 along with the experimentally determined nominal settings. It is evident that two of four settings are substantially different than predicted. These differences can be partly attributed to having a different source beam than hoped for in Chapter 3. As well, the cyclotron magnetic field magnitude used in the calculations of Chapter 3 was smaller than the magnitude of the C.R.M. central field in an effort to better approximate the conditions in the TR13. Lastly, the inherent limitations in modeling the cyclotron as a weak focusing dipole magnet in the center region also affect the quadrupole magnet settings. However, the concurrent design techniques used in Chapter 3 were realistic enough to yield a system design which was robust enough to accommodate any perturbations to the initial requirements.

Table 4.8: *The 4Q design settings and measured settings.*

QUADRUPOLE	DESIGN CURRENT (A)	MEASURED CURRENT (A)
Q0	1.44	2.24
Q1	4.28	4.1 *
Q2	4.58	4.4 *
Q3	1.90	3.90

* The Q1 and Q2 power supplies gave readbacks at 0.1 amp resolution only.

4.4.2 THE 4Q INJECTION LINE TRANSMISSION MEASUREMENTS

The first major series of experiments with the 4Q injection line were designed to compare its performance with that of the SQQ system. Subsequent to this, the 4Q transmission results for the ion source configurations of section 4.3.1.5 were tested.

4.4.2.1 4Q Transmission Versus SQQ Transmission

The 4Q injection system did not require the use of permanent magnet solenoids in order to compete with the SQQ system. Table 4.9 gives the ion source and injection line tune that maximized beam to the inflector exit beamstop for the 4Q system. The beam current readings at the IBS and at the inflector collimator are given in Table 4.10. One should note that the ion source tune in Table 4.9 yields about 5% less current to the IBS than the maximum possible, which is listed in Table 4.1.

The ion source tune listed in Table 4.9 is optimized for maximum beam at the inflector exit beamstop using the 4Q injection system. It is interesting to note that the settings are somewhat different than those given in Table 4.1 where the ion source was tuned to maximize beam to the IBS. This reveals that the source tune which maximizes output current at an upstream point in the system does not necessarily yield the most beam at downstream points. Notice also that the ion source tune of Table 4.9 resembles more closely the ion source tune of Table 4.2 where the object was to maximize beam to the inflector exit beamstop for the SQQ system. One can see that the 4Q injection line is better matched to the ion source beam characteristics, since its inflector exit beamstop readings average 10% higher than those for the SQQ injection line. This is largely due to the shorter initial drift space in the 4Q injection line.

Table 4.9: *C.R.M. & 4Q injection system setpoints for the case where maximum beam current is achieved at the inflector exit beamstop using the L155/PL10.8/EL10/NL ion source configuration.*

SETTINGS	RUN 1	RUN 2	RUN 3
Arc Current (A)	2.6	4.8	6.4
Hydrogen Flow Rate (cc/min)	4.6	7.8	8.9
Plasma Electrode Current (A)	2.0	3.4	5.0
Plasma Electrode Voltage (V)	3.1	3.0	3.3
Extraction Electrode Current (mA)	5	11	16
Extraction Electrode Voltage (kV)	1.78	2.06	2.28
Source Bias Voltage (kV)	25.0	25.0	25.0
1st Steering Magnet [x,y] (A)	[0.53,1.94]	[0.38,1.37]	[0.26,1.06]
Q0 (A)	2.22	2.28	2.31
Q1 (A)	4.1	4.2	4.2
Q2 (A)	4.5	4.5	4.5
Q3 (A)	3.59	3.79	3.88
Main Magnet (A)	447	447	447
Inflector (kV)	±7.5	±7.5	±7.5
Cyclotron Vacuum (Torr)	1.6×10^{-6}	1.6×10^{-6}	1.6×10^{-6}

Table 4.10: *Beam current readings for the tune of Table 4.9.*

DEVICE	RUN 1	RUN 2	RUN 3
IBS Beamstop Current (μA)	670	967	1354
IBS Collimator Current (μA)	74	344	276
IBS Total Current (μA)	**744**	**1311**	**1630**
Inflector Exit Beamstop Current (μA)	**617**	**963**	**1210**
Inflector Collimator Current (μA)	22	21	24

Table 4.11 lists the system settings for the case where maximum beam is achieved at the 1.125 MeV beamstop using the 4Q injection line. Note that the ion source tune is different again from those

where the beam was maximized to either the IBS (Table 4.1) or the inflector exit (Table 4.9). Similarly, the C.R.M. and injection line settings are slightly different between Table 4.9 and Table 4.11. This again emphasizes the point that the system tune which maximizes the beam to a particular upstream point in the system is not necessarily the tune which maximizes the beam to a point further downstream in the system. Having said this, it should be noted that the tunes do not, in general, change by very much when optimizing at different points in the system. In fact, using the tune which maximizes the beam current to the inflector exit as a starting point for maximizing the beam current to 1.125 MeV yields a beam current within a few percent of the maximum.

The most important aspect of Table 4.11 is the 162 μA of total beam current measured at the 1.125 MeV beamstop. This level of beam current is significantly higher than that reported for the SQQ system in Table 4.3, and it is certainly enough total beam current for use in the TR13 cyclotron.

Table 4.11: *C.R.M. & 4Q injection system setpoints and beam current readings for the case where maximum beam current is achieved at the 1.125 MeV beamstop using the L155/PL10.8/EL10/NL ion source configuration.*

SETTINGS AND READINGS	RUN 1	RUN 2	RUN 3
Arc Current (A)	2.6	4.8	6.5
Hydrogen Flow Rate (cc/min)	4.6	7.8	8.9
Plasma Electrode Current (A)	1.8	3.5	4.9
Plasma Electrode Voltage (V)	2.8	2.9	3.1
Extractor Electrode Current (mA)	9	11	17
Extractor Electrode Voltage (kV)	1.73	2.06	2.26
Source Bias Voltage (kV)	25.0	25.0	25.0
1st Steering Magnet [x,y] (A)	[0.58,1.10]	[0.19,0.78]	[0.34,0.69]
Q0 (A)	2.16	2.22	2.25
Q1 (A)	4.1	4.0	4.0
Q2 (A)	4.4	4.4	4.4
Q3 (A)	3.93	4.05	4.13
Main Magnet (A)	446	446	446
Inflector (kV)	±7.6	±7.6	±7.6
Cyclotron Vacuum (Torr)	1.6×10^{-6}	1.6×10^{-6}	1.6×10^{-6}
RF (kW)	7.6	7.2	7.2
1.125 MeV Beamstop (μA)	**76**	**119**	**162**

Unfortunately the inflector exit beamstop was a device which could not be automatically placed in and out of the beam. In fact, it required one to purge and open the cyclotron tank to install or remove it. As a result of this inconvenience, inflector exit beam current measurements were not undertaken using the

exact system tunes which maximized the beam current at 1.125 MeV. Therefore, transmission rates between these two points are somewhat more uncertain than they could be. However, using separate system tunes, which maximize the beam current at the inflector exit and at the 1.125 MeV beamstop for a particular arc current, in fact, will yield a conservative estimate of the transmission between these points.

Table 4.12 lists the conservative 4Q system percent transmission rates. Note that in all categories the transmission rates are higher than for the SQQ system with permanent magnet solenoids (Table 4.4). The transmission improvement from the IBS to the inflector exit is understandable as the initial drift for the 4Q system is shorter than for the SQQ system. In fact, both systems could achieve near to 100% transmission to the inflector exit if the ion source was better matched to the respective injection lines, as discussed previously. The most important factor in Table 4.12 is the 12% to 13% transmission rates from the inflector exit to the 1.125 MeV beamstop. These rates indicate an RF phase acceptance of at least 12% to 13%, which is higher than expected.

Table 4.12: *The 4Q system beam transmission rates for the cases where the maximum beam currents were obtained at the inflector exit beamstop and at the 1.125 MeV beamstop.*

TRANSMISSION ENDPOINTS	RUN 1	RUN 2	RUN 3
	Transmission (%)	Transmission (%)	Transmission (%)
IBS to Inflector Exit Beamstop	83	74	74
IBS to 1.125 MeV Beamstop	10.2	9.1	9.9
Inflector Exit to 1.125 MeV Beamstop	12.3	12.4	13.4

For the record, the peak beam current attained at 1.125 MeV with the L155/PL10.8/EL10/NL ion source configuration was **177 μA**. This was achieved at an arc current of 7.3 ampere, a hydrogen gas flow rate of 9.5 cc/min and RF forward power of 7.3 kW.

4.4.2.2 4Q Transmission for Various Ion Source Configurations

It was recognized during the SQQ tests that one of the main constraints in transporting all the beam to the C.R.M. center region was the poor match between the ion source's beam divergence, the initial system drift and the injection line lens apertures. This concern was partly addressed in Section 4.3, where it was realized that the best way to improve the situation was to find ion source lens configurations which would provide output beams that were better matched to the two injection systems. The final test of

the performance of the various ion source configurations in terms of beam transported to the inflector exit or to the 1.125 MeV beamstop is revealed in this section.

These tests were not completed to the point where beam current was measured at both the inflector exit and the 1.125 MeV beamstops for the various ion source configurations. This occurred for several reasons. First of all, the RF system malfunctioned from time to time. This meant that significant portions of the available window of opportunity were used to repair the RF. Second, the long ion source was taken by Ebco Technologies for a higher priority industrial project before the experiments were finished. Third, as mentioned before, swapping the inflector exit beam stop in or out of the system was a time consuming process, so it could not be done very often. Lastly, the time window available for performing all the experiments was limited. As a result, certain experiments were partially sacrificed in an effort to maximize the knowledge gained over all possible experiments.

Table 4.13 reveals the beam transmission characteristics to the inflector exit for four of the ion source configurations. Table 4.14 gives the characteristics to the 1.125 MeV beamstop for the eight other configurations. Almost all of the transmission rates in these two tables are better than the nominal ion source transmission rates in Table 4.12. This links nicely with the η numbers of Table 4.5, which indicated that the nominal ion source configuration (L155/PL10.8/EL10/NL) would likely be the weakest in terms of beam transmission.

Table 4.14 shows that the 110 μA of beam current required at 1.125 MeV by the TR13 was achievable using any of the ion source configurations in the table with the 4Q system. The two short ion source configurations resulted in, by far, the highest levels of beam current to 1.125 MeV.

Table 4.13*: Beam current readings at the IBS and at the inflector exit beamstop as a function of ion source configuration and arc current for the 4Q injection line.*

Source Configurations	**Arc = 2.7 A**			**Arc = 4.8 A**			**Arc = 6.4 A**			**Arc = 7.3 A**		
	IBS	INF	%	IBS	INF	%	IBS	INF	%	IBS	INF	%
L155/PL8/EL8NL	691	562	**81**	1019	794	**78**	1317	1062	**81**	1402	1155	**82**
L155/PL6/EL8NL	533	475	**89**	766	651	**85**	926	813	**88**	991	876	**88**
L155/PL8/EL8WL	823	737	**90**	1215	1058	**87**	1533	1253	**82**	1587	1367	**86**
L155/PL6/EL8WL	579	524	**91**	794	712	**90**	1038	907	**87**	1084	993	**92**

Table 4.14: *Beam current readings at the IBS and at the 1.125 MeV beamstop as a function of ion source configuration and arc current for the 4Q injection line.*

Source Configurations	Arc = 2.7 A			Arc = 4.8 A			Arc = 6.4 A			Arc = 7.3 A		
	IBS	1.125 MeV	%	IBS	1.125 MeV	%	IBS	1.125 MeV	%	IBS	1.125 MeV	%
L155/PL10/EL10NL	831	71	**8.5**	1298	116	**8.9**	1448	147	**10.2**	1542	-	-
L155/PL9/EL10NL	831	98	**11.8**	1214	149	**12.3**	1467	178	**12.1**	-	195	-
L155/PL8/EL10NL	663	84	**12.7**	1000	122	**12.2**	1215	154	**12.7**	1224	162	**13.2**
L155/PL10/EL10WL	869	112	**12.9**	1523	178	**11.7**	1794	206	**11.5**	1869	-	-
L155/PL9/EL10WL	888	110	**12.4**	1476	162	**11.0**	1673	205	**12.3**	1719	216	**12.6**
L155/PL8/EL10WL	720	100	**13.9**	1103	145	**13.1**	1308	178	**13.6**	1356	185	**13.6**
L105/PL8/EL8WL	1103	141	**12.8**	1598	197	**12.3**	1925	235	**12.2**	2075	255	**12.3**
L105/PL9/EL10WL	1119	124	**11.1**	1667	194	**11.6**	2076	246	**11.8**	2246	271	**12.1**

There were two main factors which contributed to better transmission rates between the IBS and either the inflector exit or the 1.125 MeV beamstop relative to the SQQ results reported in Tables 4.2 and 4.3. The first factor was the reduced initial drift space between the ion source and the injection line lenses which limited how big the beam could grow before being focused. The other important factor, of course, was the lessening of beam divergence through the use of the experimental ion source lens configurations. This also limited how big the beam could grow before being focused. These two improvements helped bring percent beam transmission rates from the ion source through to the inflector exit much closer to 100%.

Another, more subtle, factor that relates to improved transmission to 1.125 MeV is the match between the beam and the acceptance of the cyclotron. One can also think of this as how much of the beam the RF will actually accelerate. Table 4.4 shows that the SQQ system could achieve about 12% transmission between the inflector exit and 1.125 MeV. This will be considered a baseline result for the SQQ. To be fair, though, remember that 12% may not be the upper limit for the SQQ system, as the level to which it could be optimized was not under investigation in this thesis.

In Table 4.12 we found that a conservative estimate of the transmission between the inflector exit and 1.125 MeV for the nominal ion source configuration (L155/PL10.8/EL10/NL) mounted on the 4Q system was between 12% and 13%. This already indicates an improvement in matching over the SQQ system whose baseline transmission was 12%. For the new source configurations there were no direct measurements of the transmission between the inflector exit and 1.125 MeV. However, in Table 4.14

there are measurements between the IBS and 1.125 MeV, and these averaged 12% with standard error ± 0.2%. Table 4.13 gives an indication of the percent transmission that could be obtained between the IBS and the inflector exit, albeit for different configurations. Since the configurations in Table 4.13 had fair to good η values, their average transmission rate (86% with standard error ± 1%) will be considered slightly optimistic but representative for the configurations in Table 4.14. Now the percent transmission from IBS to 1.125 MeV (12%) equals the transmission rate from IBS to inflector exit (86%) multiplied by the transmission rate from the inflector exit to 1.125 MeV. Therefore, the transmission rate from the inflector exit to 1.125 MeV equals (0.12/0.86)·100% or 14% with standard error ± 0.4%. This level of transmission indicates a very good matching of the beam to the cyclotron acceptance. Typically reported percent transmission rates are on the order of 10% to 12% [14, 48]. Since 100% transmission from the IBS to the inflector exit is, in principle, possible then systems could be made with transmission rates between the ion source and 1.125 MeV of 14%.

There is also the question of total beam current to a particular point in the system. It is apparent from Tables 4.13 and 4.14 that the configurations which delivered the most beam current to the inflector exit or to 1.125 MeV did not necessarily have the highest transmission rates. These configurations more than made up for the fact that their beams lost ions from their outer halos by increasing the total amount of beam available. For these systems, there is room for improvement. In particular, the initial drift space could be reduced yet again. However, it is quite clear that the 4Q system configured with an ion source limited to 7 amps of arc current is more than capable of producing the required 110 μA of beam current to 1.125 MeV. Therefore, this system is certainly a capable candidate system for the TR13 cyclotron.

The absolute error in the total beam current measurements at any particular point in the system were estimated to be ± 4%. The errors in the measuring equipment have been discussed previously. An estimate of the error in the claimed peak current for a particular configuration basically requires some idea of whether the ion source and injection system parameters were locally or globally optimized. Since a large number of configurations were tested and parameters were optimized from a variety of starting points, it is the author's belief that the parameters were globally optimized.

4.4.3 THE 4Q SYSTEM AXIAL ROTATION TESTS

In section 4.4.1.1 it was noted that the Q0 defocusing axis for a negative ion beam was fixed at 27° counterclockwise (CCW) from the lab vertical axis as viewed looking in the direction of beam travel. In Chapter 3 it was noted that the match of the ion source beam to the cyclotron acceptance was a function of the axial rotation angle of the injection line. In an effort to observe this much discussed [26, 27, 51–54] but seldom attempted optimization, a measurement of the beam transmission as a function of rotation angle was undertaken. The transmission rate as a function of rotation angle does not directly correlate with changes in emittance growth as a function of rotation angle. For example, for a certain level of emittance growth no change in transmission will occur because the available acceptance is not used up. After the available acceptance is used up, however, emittance growth will result in a reduction in transmission. Although the transmission rate will not vary directly with the emittance as a function of rotation angle, it will indicate whether the changes in emittance growth were large enough to make a difference in transmission.

The first test undertaken was to rotate Q1 with respect to the rest of the quadrupole magnets. The results of this test are listed in Table 4.15 for the case of a 4.8 ampere arc current setting with the L105/PL8/EL8/WL ion source configuration. The beam currents at the 1.125 MeV beamstop for each rotation position are the peak currents obtained after optimizing all the variable ion source and injection system parameters. There is the possibility that some portion of parameter space was not sufficiently investigated and that a higher maximum current could have been obtained. To minimize this chance, each of the main parameters was purposely offset from nominal and all the parameters were then re-adjusted to maximize the peak beam current reading. This procedure was done repeatedly and it was found that the parameters would walk back to a consistent point in parameter space for each rotation position. Thus, there is a high level of confidence that the "peak" beam current readings are indeed at their peak.

One can see the beam current and beam transmission to 1.125 MeV fall off very sharply as a function of rotation angle in Table 4.15. The rotation angles are very slight, so the system definitely prefers Q1 to have the exact opposite polarity to its neighbours Q0 and Q2.

Table 4.15: *Maximum beam current at 1.125 MeV as a function of Q1 rotation angle for an arc current of 4.8 amps and ion source configuration L105/PL8/EL8/WL.*

Angle of focusing Axis CCW from Lab Vertical Axis (°)	Maximum Beam Current @ 1.125 MeV Beamstop (μA)	Percent Transmission IBS to 1.125 MeV Beamstop
28.9	92	5.8
27.1	138	8.6
27.8	173	10.8
27.4	173	10.8
27.0	201	12.6
26.6	190	11.9
26.2	188	11.8
25.9	146	9.1
25.1	92	5.8

The maximum beam current and beam transmission obtained to the 1.125 MeV beamstop at 4.8 amperes of arc current as a function of rotation of the 4Q injection line as a whole is given in Table 4.16. The same arc current setting and ion source configuration as was used for Table 4.15 was also used for these measurements. The listed rotation angle is for the position of the Q0 defocusing axis relative to the lab vertical axis. Remember that the whole injection line was rotated as a unit so that the Q0 defocusing axis angle was the same as the Q1 and Q3 focusing axes, and the defocusing axis of Q2. Table 4.16 reveals that there is a broad peak in the maximum beam current through the Q0 angles of 25° CCW through to 13° CCW and possibly beyond. The angles of rotation were limited to those shown due to the physical limitations of the injection system.

The final orientation of Q0 with respect to the vertical was 21.7° CCW. This choice was made because the position gave a maximum beam current in the broad peak, and it was physically convenient. By reversing the polarities of all the quadrupole magnets, the Q0 position of 111.7° CCW could be investigated (90° rotation). The beam current obtained at 111.7° CCW is that of the worst possible rotation angle for the 4Q injection line. At this rotation angle the beam current is approximately 20% less than at the 21.7° CCW position. A variation in peak beam current of only 20% over all possible rotation angles (180° covers all possible quadrupole angles due to symmetry) is quite moderate. The beam current peak is likely quite flat over a fairly large range of rotation angles because the beam's phase space area is smaller than the center region acceptance over this range of angles. Consequently, the transmission rate

does not change until the beam's phase space area is sufficiently perturbed by the injection line rotation angle to be larger than the acceptance.

Table 4.16: *Maximum beam current at 1.125 MeV as a function of the 4Q rotation angle for an arc current of 4.8 amps and ion source configuration L105/PL8/*EL8/WL.

Angle of Q0 Defocusing Axis CCW from Lab Vertical Axis (°)	**Maximum Beam Current @ 1.125 MeV Beamstop (μA)**	**Percent Transmission IBS to 1.125 MeV Beamstop**
29.7	202	12.6
27.0	202	12.6
24.7	211	13.2
22.0	212	13.3
21.7	212	13.3
19.4	211	13.2
14.0	212	13.3
12.9	212	13.3
111.7	175	11.0

Recall from section 4.4.1.1 that the 4Q injection line was rotated so that the initial Q0 defocusing axis angle was 37° CCW of the inflector entrance electrode edge angle, which was at 10° clockwise (CW) of vertical. Recall also that it was eventually determined that the inflector entrance electrode edge angle was 14° CW of vertical, which meant that the initial Q0 rotation angle should have been 23° CCW of vertical. If Q0 had been installed at 23° CCW of vertical, the beam transmission would have been within the broad beam current peak of Table 4.16. Note also that the eventual final Q0 rotation angle of 21.7° CCW of vertical is very close to the predicted angle of 23° CCW of vertical.

Table 4.17 compares the maximum beam currents and corresponding transmission rates obtained at various arc current settings for the 21.7° CCW and 111.7° CCW positions. The peak beam currents for the 111.7° case are consistently 20% less than for the 21.7° case. Also of interest is that a comparison of the 21.7° beam currents with the L105/PL8/EL8/WL beam currents of Table 4.14 reveals about a 7% beam current increase for the optimal rotation angle. This suggests that all the beam currents and percent transmissions of Table 4.13 and 4.14 are slightly sub-optimal. If the rotation angle was corrected and the various ion source configurations were re-tested, the already excellent transmission rates reported in these tables could be improved upon. Of particular interest, in Table 4.17, is that at the 21.7° rotation angle and

an arc current setting of 7.3 ampere, a beam current of 275 μA at 1.125 MeV was obtained. This was the highest current obtained to 1.125 MeV for any system tested.

Table 4.17: *The maximum beam current and transmission rates as a function of arc current and 4Q rotation angle for the L105/PL8/EL8/WL ion source configuration.*

	Arc = 2.7 A	Arc = 4.8 A	Arc = 6.4 A	Arc = 7.3 A
1.125 MeV Beam Current (4Q/21.7° CCW)	140	212	253	275
IBS to 1.125 MeV Percent Transmission	12.7	13.3	13.1	13.3
1.125 MeV Beam Current (4Q/111.7° CCW)	113	175	201	221
IBS to 1.125 MeV Percent Transmission	10.2	11.0	10.4	10.7

4.5 TESTS OF 3Q INJECTION ARRANGEMENTS WITHIN THE 4Q LAYOUT

Using a 4Q system as the nominal injection system provided the opportunity to investigate a limited number of 3Q injection systems. The likelihood of any of the 3Q systems performing spectacularly was thought to be low, as the various permissible arrangements within the 4Q layout were not optimal in terms of transport and matching. However, testing these 3Q arrangements would give some indication of general 3Q performance. If one of the 3Q arrangements had transmission characteristics which were sufficiently high, then it would also be considered a suitable candidate for the TR13, along with the 4Q system.

The 3Q arrangements were tested using the nominal L155/PL10.8/EL10/NL ion source configuration, and the original injection line rotation given in section 4.4.1.1. Table 4.18 gives the inflector exit beamstop current readings for three different 3Q arrangements, and the nominal 4Q results from Table 4.10 are also included for comparison.

Table 4.18: *The 3Q and the nominal 4Q inflector exit beam current readings as a function of arc current using the L155/PL10.8/EL10/NL ion source configuration.*

	Arc = 2.7 A	Arc = 4.8 A	Arc = 6.4 A
Nominal 4Q Beam Current @ Inflector Exit (μA)	617	963	1210
3Q: Q0 = 0, Beam Current @ Inflector Exit (μA)	483	670	858
3Q: Q2 = 0, Beam Current @ Inflector Exit (μA)	460	810	1026
3Q: Q3 = 0, Beam Current @ Inflector Exit (μA)	502	815	1040

The Table 4.18 results show that 3Q arrangements with the upstream quadrupoles powered are preferred. This is because, as we have already discovered, the source beam is overly divergent given the

initial drift length and the quadrupole bore size, so the closest two quadrupoles to the ion source must be powered to initiate the focusing process where the beam is as small as possible. Of the two configurations that powered Q0 and Q1, the one with Q3 not powered was best.

The 3Q configuration with Q3 not powered was tested with polarities reversed at an arc setting of 2.7 amperes. In this situation the beam current at the inflector exit was 465 μA, which was worse than at the original polarity. Thus, the original polarity was deemed best for this 3Q system.

The 3Q tune with Q3 not powered was with Q0 = 3.03 amperes, Q1 = 4.5 amperes and Q2 = 2.3 amperes. This setting also peaked the beam current at the 1.125 MeV beamstop at 48 μA for an arc current of 2.7 amperes. This compares with a 4Q beam current of 76 μA for the same circumstances.

The 3Q arrangements tested gave beam current results which were substantially worse than the nominal 4Q arrangement, but which were comparable to the results of the nominal SQQ arrangement (Table 4.2). In order to find a 3Q system with better transmission results, the initial drift space issue would have to be solved, as has been the case for all injection systems discussed so far, and the three quadrupole magnets would have to be optimally positioned with respect to the inflector entrance.

4.6 TESTS OF 2Q INJECTION ARRANGEMENTS WITHIN THE 4Q LAYOUT

Tests of the 2Q injection systems were limited in the same way that tests of the 3Q injection systems were. However, as was the case for the 3Q systems, the 2Q systems were tested to give an indication of general performance. The beam transmission rates for the various 2Q systems were of particular interest because if they were high enough, the 2Q system would be the most cost effective injection system meeting the TR13 requirements.

Since the source beam needs as small an initial drift as possible prior to being focused, it was thought to be essential for Q0 and Q1 to be the magnets which were powered. Table 4.19 shows that if the first two magnets were powered with nominal polarity (i.e. same polarity as for the nominal 4Q arrangement), the beam transmission was much better than for the cases where Q1 and Q2 were powered. In fact, the 2Q system performs as well as the 3Q systems described in Table 4.18, and the SQQ system

described in Table 4.2. The 2Q results shown in Table 4.19 were thought to be good enough to transport over 110 μA to 1.125 MeV.

Table 4.19: *The 2Q inflector exit beam current readings as a function of arc current using the L155/PL10.8/EL10/NL ion source configuration.*

	Arc = 2.7 A	Arc = 4.8 A	Arc = 6.4 A
2Q: Q2 = Q3 = 0, Beam Current @ Inflector Exit (μA)	475	840	1091
2Q: Q0 = Q3 = 0, Beam Current @ Inflector Exit (μA)	217	349	455
2Q: Q2 = Q3 = 0 Reversed Polarity, Current @ Inflector Exit (μA)	264	400	502

Although the Table 4.19 beam currents are not as good as the Table 4.11 beam current results, the 2Q system had sufficiently high transmission and matching capabilities to obtain 1188 μA of beam current at the inflector exit beamstop and 120 μA at the 1.125 MeV beamstop for the case where 7.3 amps of arc current was used in the L155/PL10.8/EL10/NL ion source configuration. The 2Q magnets were of nominal polarity with excitation currents: Q0 = 3.21 amps and Q1 = 3.4 amps. Obtaining 120 μA at 1.125 MeV was slightly worse than for the SQQ system with permanent solenoid magnets, which obtained 130 μA (Table 4.3). Nevertheless, the 2Q system performance is sufficient for the TR13 cyclotron.

Since the 2Q performance was good enough for the TR13 system, and because it was the most cost effective system, it was further tested with respect to other ion source configurations and axial rotation. The 3Q system, on the other hand, was deemed uninteresting and was not further tested.

One test of the 2Q system was with the L155/PL6/EL8/NL ion source configuration. At 7.3 amperes of arc current, the beam current obtained to the inflector exit was 810 μA, which is remarkably close to the 876 μA current obtained with the 4Q system (from Table 4.13). This indicates that if the source beam is less divergent, then the 2Q system approaches the 4Q system in terms of transporting the beam through the inflector. Table 4.20 reveals the beam transmission rate from the IBS to the 1.125 MeV beamstop, as well as the peak beam currents for several arc current settings (L105/PL8/EL8/WL) for the nominal 2Q system (Q2 = Q3 = 0). Again the transmission rates are not as good as for the 4Q system (Table 4.14), however, the minimum beam current requirement for the TR13 system is certainly achieved.

Table 4.20: *Beam current readings at the IBS and at the 1.125 MeV beamstop as a function of arc current for the 2Q injection line configured with the L105/PL8/EL8/WL ion source.*

Source Configurations	Arc = 2.7 A			Arc = 4.8 A			Arc = 6.4 A			Arc = 7.3 A		
	IBS	1.125 MeV	%	IBS	1.125 MeV	%	IBS	1.125 MeV	%	IBS	1.125 MeV	%
L105/PL8/EL8/WL	1103	91	8.3	1598	149	9.3	1925	179	9.3	2075	-	-

The 2Q peak beam current at 1.125 MeV as a function of axial rotation angle was also tested. Note that the injection system was rotated as a whole, but that the rotation angle was referenced to Q0. Figure 4.20 reveals that there is a strong correlation between 2Q axial rotation angle and beam transmission. The correlation is likely strong for the 2Q case because the 2Q beam's elliptical phase space areas do not necessarily all fit through the center region acceptances, so beam transmission varies significantly as a function of the size of these phase space areas and their alignment with the acceptance region.

Unfortunately, the 4Q final position of 21.7° CCW of the lab vertical for the Q0 defocusing axis does not place the 2Q system at its optimal rotation. However, the 4Q system was the nominal system for the Chapter 5 experiments, and thus the rotation angle was peaked for the 4Q arrangement.

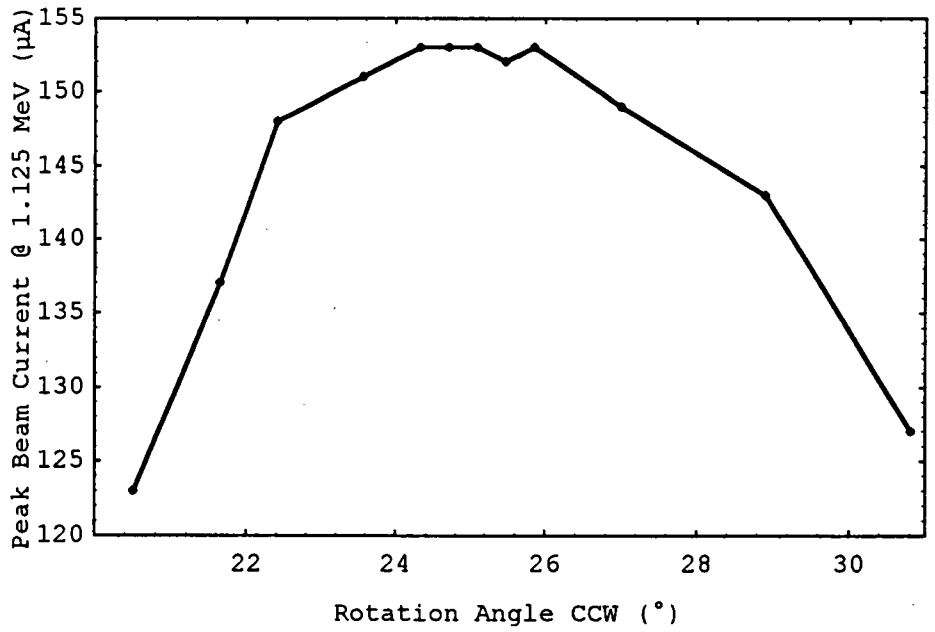

Figure 4.20: *The peak beam current @ 1.125 MeV for the 2Q system and L105/PL8/EL8/WL source configuration at 4.8 amps of arc as a function of the axial rotation angle of the Q0 defocusing axis.*

4.7 CENTER REGION MEASUREMENTS WITH THE 4Q, 3Q AND 2Q INJECTION SYSTEMS

The C.R.M. cyclotron system comes complete with a number of diagnostic probes for performing detailed beam studies in the center region. Altogether there are four such probes. The 1.125 MeV beamstop has been discussed previously. The three other probes will be described in the following sub-section. These probes were used to quantitatively measure the radial and/or axial beam intensity profiles under a variety of operating conditions. Consequently, this section of the thesis will report on the location of the radial and axial orbit centers for the 4Q system, beam intensity profiles as a function of the injection system type (2Q, 3Q, 4Q), and the axial and radial circulating emittances for the 4Q system. In addition, the variation in transmission as a function of the main magnet current setting, the inflector electrode potential settings and the injection quadrupole magnet current settings will be described. Note that all measurements discussed in this section were made with the L155/PL10.8/EL10/NL ion source configuration with the original 4Q injection line axial rotation angle of 27° CCW of vertical for the Q0 defocusing axis specified in sub-section 4.4.1.1. All 2Q, 3Q and 4Q system tunes (including the ion source) utilized in this section were those used to produce maximum beam to 1.125 MeV for a given arc current. Although, it would have been interesting to have performed center region measurements for other ion source configurations, it was felt that more useful information per unit time could be determined by performing the inflector experiments of Chapter 5 instead.

4.7.1 THE C.R.M. DIAGNOSTIC SYSTEM LAYOUT

The four C.R.M. diagnostic probes are shown in Figure 4.21. Probes #3, #5 and #6 can be moved radially by typing commands processed by an automated control system. The probes have ranges of 75 mm, 84 mm, and 88 mm, respectively. The position readbacks for these probes were output on a computer terminal. The readback systematic error was ± 0.30 mm, and the random error was ± 0.05 mm. The 1.125 MeV probe remained fixed at a particular radius through any particular series of measurements, but it could be re-adjusted, if necessary. The nominal radius for the tip of this probe was 118.0 ± 0.3 mm from the C.R.M. center. The nominal axial centering of the other probes was to within ± 0.2 mm of the median plane (90.0 mm from the valley floor), and the axial widths of the probes were 15.0 mm, except for probe

#5 whose axial width was as pictured in view AA of Figure 4.21. The head of probe #3 contained an axial slit (0.5 mm wide) for scanning vertical slices of the beam. During experiments this probe seriously malfunctioned invalidating measurements taken with it. As a result, measurements made with probe #3 are not presented.

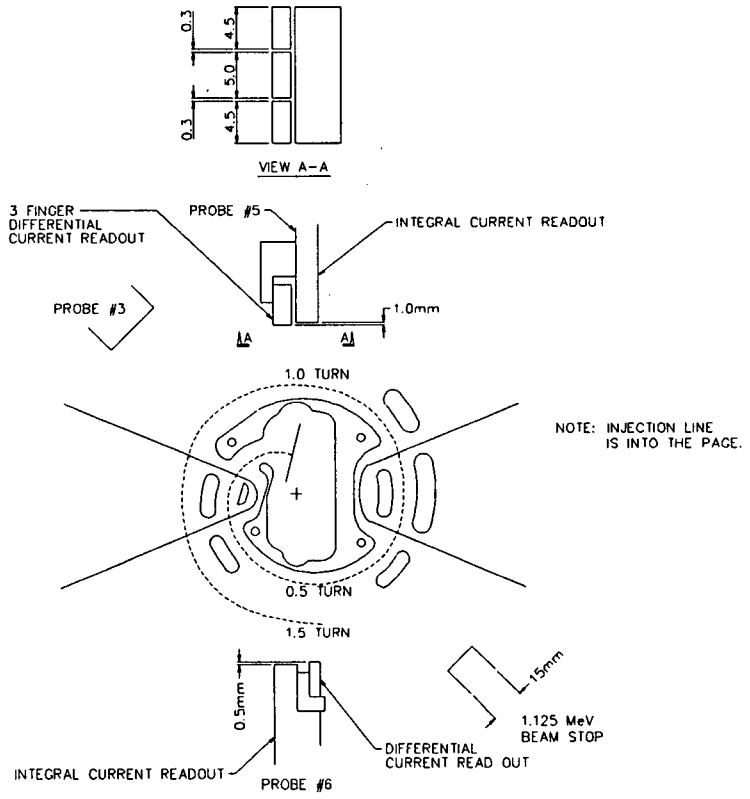

Figure 4.21: *A schematic layout of the C.R.M. central region and its probes.*

The current readbacks from the integral current portion of probes #5 and #6, and the 1.125 MeV beamstop were observed on the standard current meters discussed in Appendix II. The differential portions of probes #5 and #6 had their current readbacks read from Keithley current meters. The integral current probe components were biased at 300 volts, and the differential probe components were biased at 45 volts.

4.7.2 RADIAL BEAM MEASUREMENTS IN THE CENTER REGION

Probes #5 and #6 were used to obtain beam centering and beam profile information as a function of radius in the C.R.M. center region. The injection line configuration for these tests was the 4Q set-up with the ion source set at a nominal arc current of 2.6 amperes. As described in sub-section 4.3.1.4., the

emittance of a beam produced at this arc current will be larger than that of a beam produced at a higher arc current, however, the diagnostic probes are only indirectly cooled through boron nitride insulators, so it was important that a relatively low beam current was used to avoid melting the probe heads.

Figures 4.22 and 4.23 show the differential probe scans produced from probes #6 and #5, respectively. The beam intensities (dI/dR) are given in arbitrary units (a.u.). The measurements were done with a system tune as described in Table 4.21. A few general comments can be made at this stage. First, the intensity distributions of turns #0.5, #1.0, and #1.5 are not to be taken too seriously because, for these turns, the probe heads come in close proximity to the center ground electrode. This causes the secondary electron capturing conditions to change, which alters the measurements in an unpredictable manner.

Figures 4.22 and 4.23 clearly indicate the radial locations of the peak beam intensity points at each half-turn. In addition, a characteristic beam intensity profile shape that has a steep slope on the outer radius side of a given turn and a milder slope on the inner radius side is evident. This shape can be understood in terms of the acceleration process which the beam experiences. First of all, consider that the RF voltage placed upon the dees has a sinusoidal variation in time. This means that if each accelerated beam pulse was divided up into infinitesimal slices in time, each of these would cross the dee gap at a different phase of the RF. Consequently, each time slice of the beam would be accelerated by a different voltage. For example, the accelerating voltage seen by an infinitesimal time slice of the beam that arrives at the dee gap when the RF waveform has already passed its peak by 10° (i.e. $\phi_{RF} = -10°$) is at 50·Cos(−10°) kilovolts. Furthermore, if the cyclotron magnetic field is isochronous, this particular time slice of the beam will always cross the dee gaps at $\phi_{RF} = -10°$. This has serious implications on each accelerated beam pulse because each time slice of the beam will always be accelerated by a consistent energy increment unique to its phase. This causes each time slice of a beam pulse to travel at a different radius of curvature. Those beam slices not too far out of phase with the peak of the RF wave form will pile intensity into the outer radius side of the peak of the beam pulse (steep slope), and those which are fairly far out of phase will spread intensity over the inner radius side of the peak of the beam pulse (mild slope).

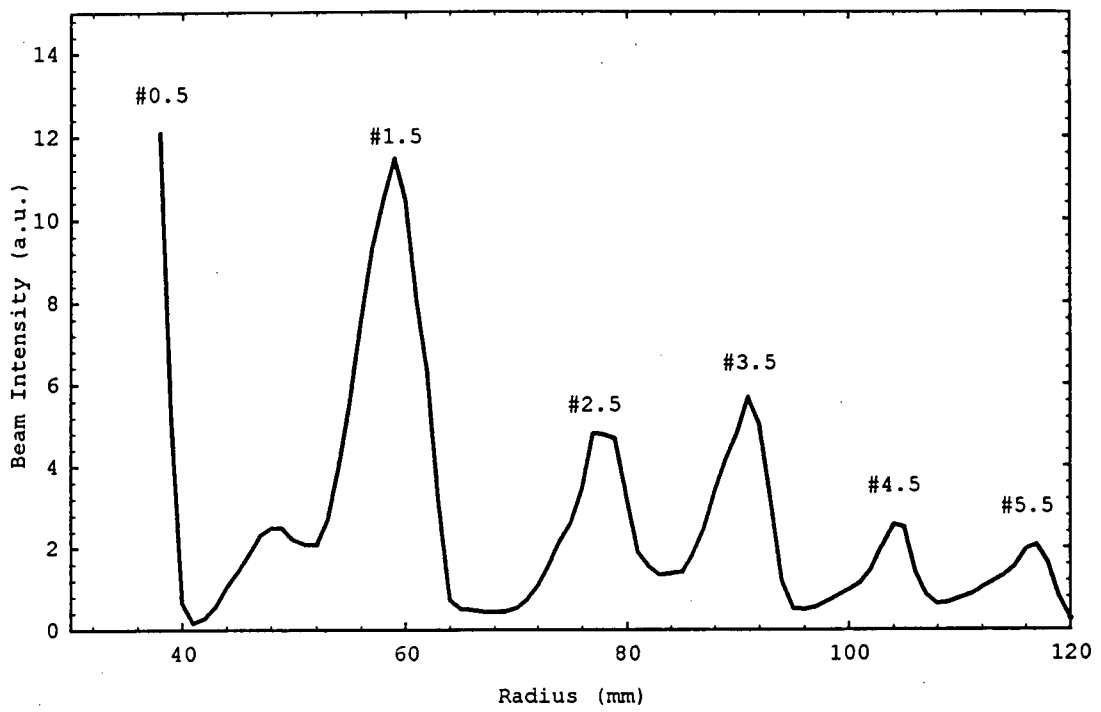

Figure 4.22: *A radial beam intensity scan with a single finger differential probe head on probe #6.*

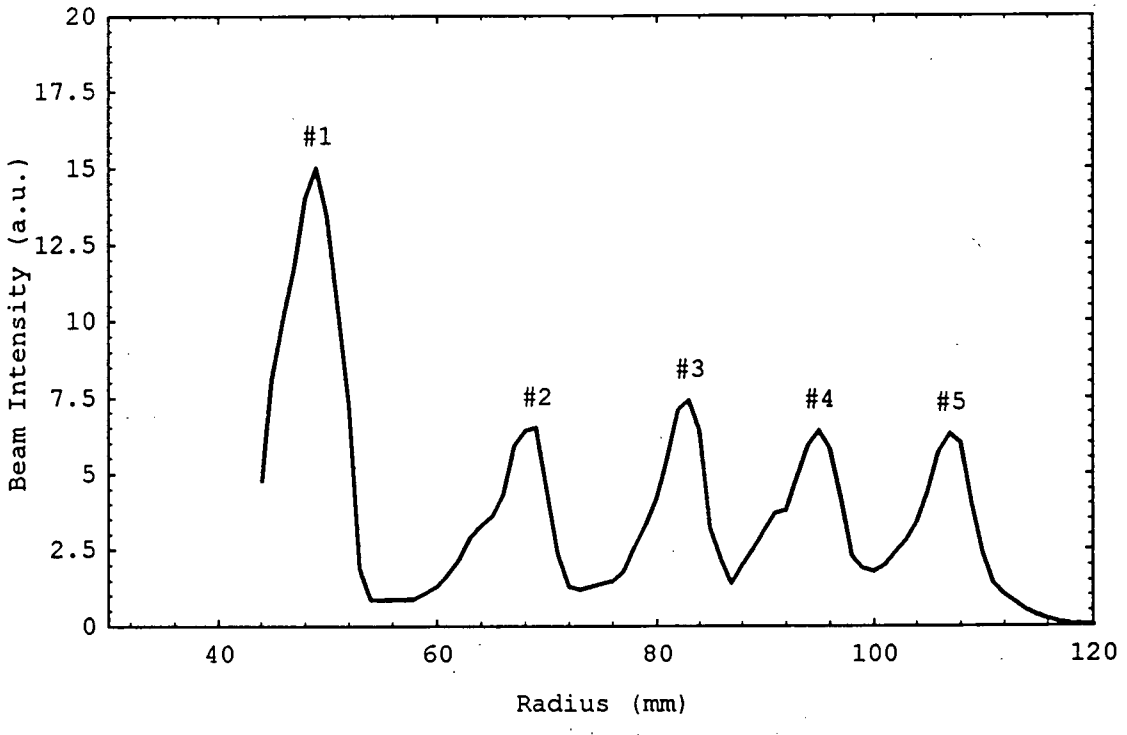

Figure 4.23: *A radial beam intensity scan with a single finger differential probe head on probe #5.*

Table 4.21: *The C.R.M. & 4Q/L155/PL10.8/EL10/NL injection system setpoints for probe #5 and probe #6 center region radial beam intensity scans.*

SETTINGS AND READINGS	PROBE #6 & #5 RUN
Arc Current (A)	2.6
Hydrogen Flow Rate (cc/min)	4.6
Plasma Electrode Current (A)	1.8
Plasma Electrode Voltage (V)	2.8
Extractor Electrode Current (mA)	9
Extractor Electrode Voltage (kV)	1.73
Source Bias Voltage (kV)	25.0
1st Steering Magnet [x,y] (A)	[0.61,0.68]
Q0 (A)	2.11
Q1 (A)	4.1
Q2 (A)	4.4
Q3 (A)	3.92
Main Magnet (A)	446
Inflector (kV)	±7.6
Cyclotron Vacuum (Torr)	1.8×10^{-6}
RF (kW)	7.5
1.125 MeV Beamstop (μA)	69

Recall from section 4.4.2.2 that up to 14% of the continuous beam current provided to the RF can be accelerated. This corresponds to totally populating the RF phases between ±25°. However, if it is assumed that all of the accelerated phases have lost some intensity due to collimation in the axial plane, then a larger RF phase band will be required to transmit 14% of the original beam, say the phase band between ±32° for sake of argument. Figure 4.24 illustrates the azimuthal and radial distribution of such a beam at turn #5.5 and at turn #4.5. The nominal radial width of each time slice in these beam pulses was chosen to be 3 mm for purposes of illustration.

The RF frequency is at four times the cyclotron frequency, so the azimuthal extent of the two beam pulses is only ±8° in Figure 4.24. As expected, the leading and trailing edges of the two beam pulses are traveling at substantially smaller radii than the pulse centers which have received the full 50 kilovolts of acceleration at each dee gap. Figure 4.24 also makes it apparent that the radial location of the leading and trailing edges of the turn #5.5 beam pulse (positive and negative RF phases) overlap with the radial location of the center of the turn #4.5 beam pulse (0° RF phase). This explains why the radial beam

intensities from different turns in Figures 4.22 and 4.23 overlap, indicating that, for cyclotrons with large RF phase acceptances, the turns may not be separated even in the center region.

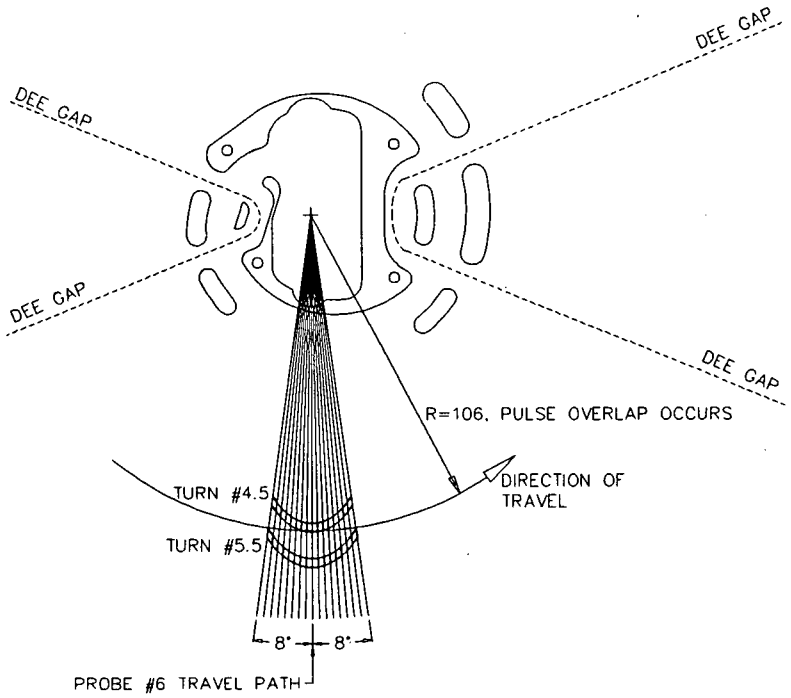

Figure 4.24: *A schematic of the beam pulse spatial distribution at turns #4.5 and #5.5.*

Now consider probe #6 when it radially scans through a continuous stream of the turn #5.5 beam pulses depicted in Figure 4.24. As this probe traverses the beam from the outer radius side to the inner radius side, the measured intensity will rapidly climb to a peak because the center ¼ of the time slices in the boomerang shaped pulse (ϕ_{RF} between ±8°) will have almost identical radii because each will have received accelerating voltage kicks which vary by only about ±0.5%. However, as the probe moves toward smaller radii each beam time slice is spread through a range of radii. Due to this smearing of time slices across the inner radii, the beam intensity falls off gradually on the inner radius side of the beam pulse. But, as already discussed, from the perspective of a radial probe, the beam intensity on the inner radius side of turn #5.5 will not reach zero before it rises sharply as a result of the overlap of the turn #5.5 and the turn #4.5 intensity distributions.

A simple model can be constructed which can approximate the measured intensity distribution quite well. The modeling procedure, as implemented within Mathematica [101] is as follows:

- Divide the RF phase band of the beam pulse into beam slices at 2° intervals.
- Assume each beam slice has an identical radial gaussian intensity distribution.
- Discretize the radial intensity distribution of each beam slice using 0.1 mm increments.
- Center the radial intensity distribution of each beam slice @ radius ($R_{\varphi = 0°} - \Delta R_{\varphi = \text{beam slice}°}$).
- Sum the radial intensity distributions of each beam slice as a function of radius.
- Iteratively adjust σ, $R_{\varphi = 0°}$ and the size of the RF phase band until the summed radial intensity curve approximates the measured intensity curve (Figures 4.22 and 4.23) reasonably well.

Using this prescription the measured radial intensity distribution for turn #5.5 was approximated. The results are shown in Figure 4.25. The parameters used to achieve this fit were σ = 1.4 mm, $R_{\varphi = 0°}$ = 117.8 mm and an RF phase band of ±32°. As can be seen the model simulates the measured intensity distribution very well. This model is also very useful in that one can quickly obtain the important beam related quantities (σ, $R_{\varphi = 0°}$ & the RF phase band) and verify that they represent the measured results well. Although this simple model is useful, be aware that it assumes that the cyclotron is isochronous, that a gaussian distribution is appropriate for an individual phase slice, that all the phases are radially identical at the azimuth of the measurement probe, and that no partly filled phases exist.

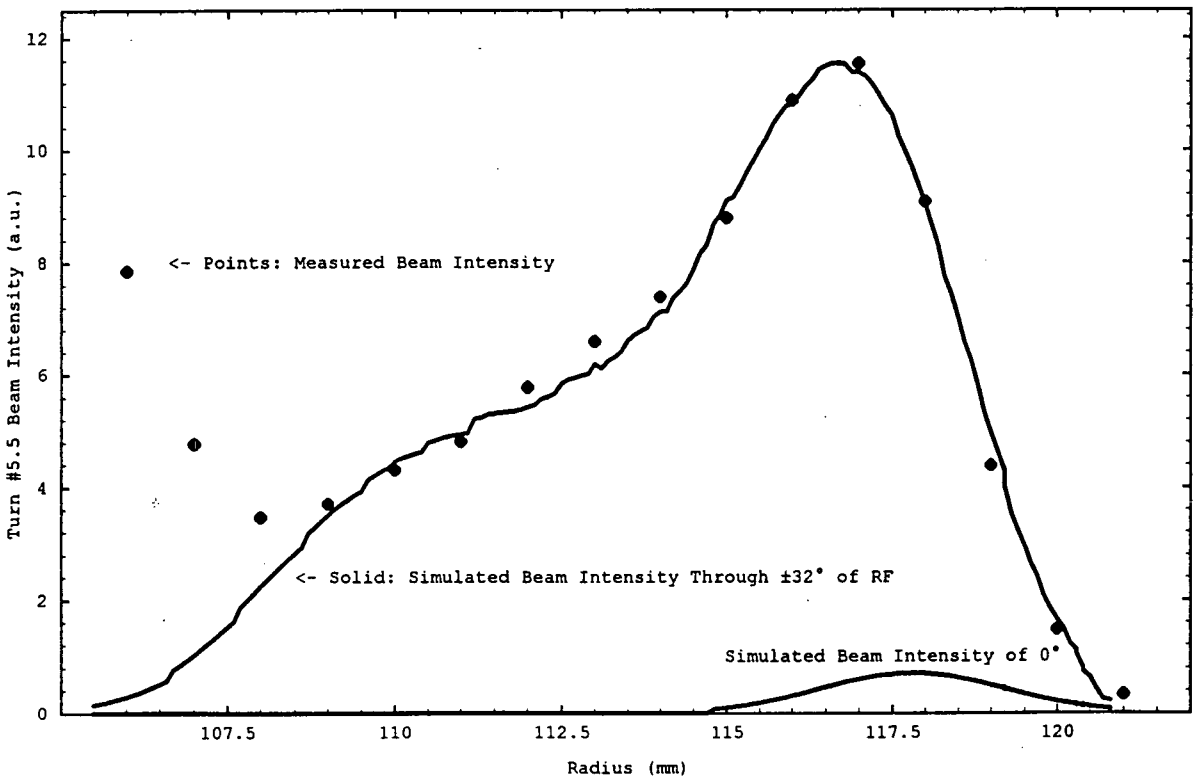

Figure 4.25: *The measured and simulated turn #5.5 radial beam intensity distributions, and the radial beam intensity distribution of the $\varphi_{RF} = 0°$ beam slice.*

The magnitude of σ is important because one can use it to directly estimate the circulating emittance of the cyclotron at turn #5.5. First, however, note that the phase ellipse of each beam slice in a given beam pulse will actually be at a different stage of phase space evolution due to phase dependent focusing in the center region [44]. This indicates that each phase slice should have had its own gaussian distribution. The fact that a single gaussian distribution was used for each phase slice with a good result implies that this single gaussian distribution is acting as an average distribution across all phase slices. In other words, the single gaussian distribution is a good candidate for being the distribution which represents the circulating emittance phase space region. Now given that the circulating emittance is constructed as a composite of many individual phase spaces smeared across each other, a reasonable approximation for the shape of this region in radial phase space is that of an upright ellipse. Since this phase space shape corresponds to the matched ellipse of a dipole, one can use the relationship for the normalized emittance given in equation 3.1 to calculate the normalized emittance at turn #5.5. All the parameters needed to evaluate equation 3.1 are available. For example, a 2σ beam half-width is a good approximation to the x_{max} dimension of a 4rms ellipse ($x_{max} = 2\sigma = 2.8$ mm). The radial tune υ_x is equal to 1.03 at this radius [92]. The cyclotron radius for the average magnetic field of 12 kG (refer to Figure 5.10) and a beam kinetic energy of 1.125 MeV is 127.7 mm. Lastly, the value of $\beta\gamma$ is 0.049. This results in a normalized radial emittance $\varepsilon_{n\_rad\_circ} \approx 0.003$ mm·rad = 3 mm·mrad. Under column heading RUN 1 in Table 4.1, the 4rms emittance for the L155/PL10.8/EL10/NL ion source configuration used here was given as 0.49 mm·mrad. This gives a value for the emittance growth in the radial phase space of $3/0.49 \approx 6$, which is comparable to the factor of 5 computed in section 3.2.3. With an emittance growth factor of 6, a normalized radial circulating emittance of about 1.5 mm·mrad can be expected for the favoured L105/PL8/EL8/WL ion source configuration.

The summed intensity distribution peak radius is less than 1 mm lower than the $\varphi_{RF} = 0°$ intensity distribution peak radius (refer to Figure 4.25). Knowing that this is also true for lower energy turns, provides a means for establishing whether the beam has been injected into the center region properly. With the magnetic field varying as a function of azimuthal angle, it was difficult to establish the

ideal beam path using a simple model, so computer simulations were used. Figure 4.26 illustrates the beam path for the $\varphi_{RF} = 0°$ beam slice through the first 3.5 turns in the C.R.M. [102]. Verifying whether the radial peak intensity points of Figures 4.22 and 4.23 were less than 1 mm smaller than the $\varphi_{RF} = 0°$ beam center will give a good indication of whether the real beam had been correctly injected by the inflector and the injection system. Table 4.22 lists the radial peak beam intensity points and the $\varphi_{RF} = 0°$ beam centers at the same azimuthal positions. The table verifies that the real beam was indeed traveling as expected (i.e. within 1 mm) with respect to the calculated beam. This indicates that the beam was properly injected into the center region.

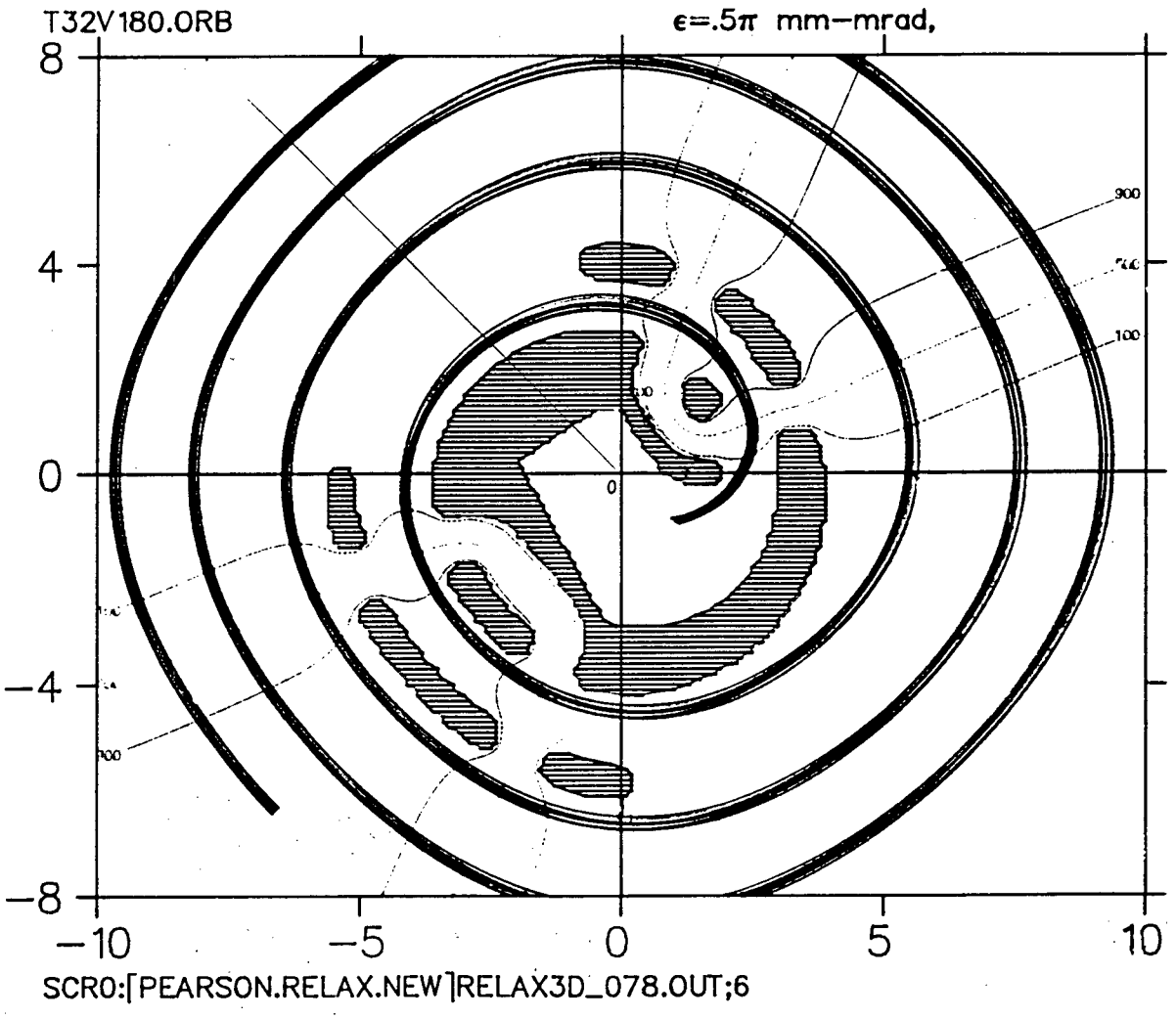

Figure 4.26: *The radial trajectory and beam envelope of a beam accelerated at $\phi_{RF} = 0°$ within the C.R.M.. Dimensions are in centimetres.*

Table 4.22: *The radial locations of the beam intensity peaks as determined by the probe #5 and #6 scans in Figures 4.22 and 4.23 and the calculated ϕ_{RF} = 0° beam slice's radial centers along the probe #5 and #6 azimuthal insertion paths as measured from Figure 4.26**.

PROBE #	TURN #	PEAK INTENSITY RADIUS (mm)	0° PHASE BEAM CENTER RADIUS (mm)
6	0.5	36 ± 1	36.5
5	1.0	49.0	48.5
6	1.5	59.0	60.0
5	2.0	69.0	68.5
6	2.5	78.0	77.0
5	3.0	83.0	83.5
6	3.5	91.0	91.0
5	4.0	95.0	–
6	4.5	104.5	–
5	5.0	107.0	–
6	5.5	117.0	–

* Error on radii is ± 0.5 mm except where stated.

Another radial beam experiment, which was done to help confirm the modeling results, involved measuring the beam current fall-off on the 1.125 MeV beamstop as probe #6 moved radially inward. By doing so, the 2σ beam width established above was checked, and the full beam size at the 1.125 MeV beamstop was ascertained.

Figure 4.27 shows the fall-off of the 1.125 MeV beamstop current as a function of the position of the #6 and #5 probe tip positions, and Figure 4.28 shows dI/dR as a function of radius at the 1.125 MeV beamstop, where I is beam current and R is radius. The differential beam intensity profile shape has basically the same non-gaussian differential beam intensity distribution as is shown in Figure 4.25. This means that if the beam intercepted by the 1.125 MeV probe was actually extracted, it would also have this same non-gaussian shape. This shape is observed in the extracted beam of the TR30 as is shown in Figure 4.29 [103], although the extracted shape in the TR30 case is complicated by the effects of multi-turn extraction.

Although the differential beam intensity distribution at 1.125 MeV is not a gaussian distribution, where the intensity falls to a value of e^{-2} times the peak intensity will be considered to be the boundary of the ±2σ beam. This gives a beam size of about 13.5 ± 1 mm. Using the formula of [104] for the beam width at an extraction point, the equation:

$$\text{Width} = \frac{dR}{dn} + x_{max} \cdot \sin(2\pi\nu_x) \tag{4.2}$$

with dR/dn (radius gain per turn) = 12.5 mm (refer to Table 4.22), x_{max} = 2.8 mm, and υ_x = 1.03 yields a beam width of 13 mm, which is in good agreement with the measured beam size.

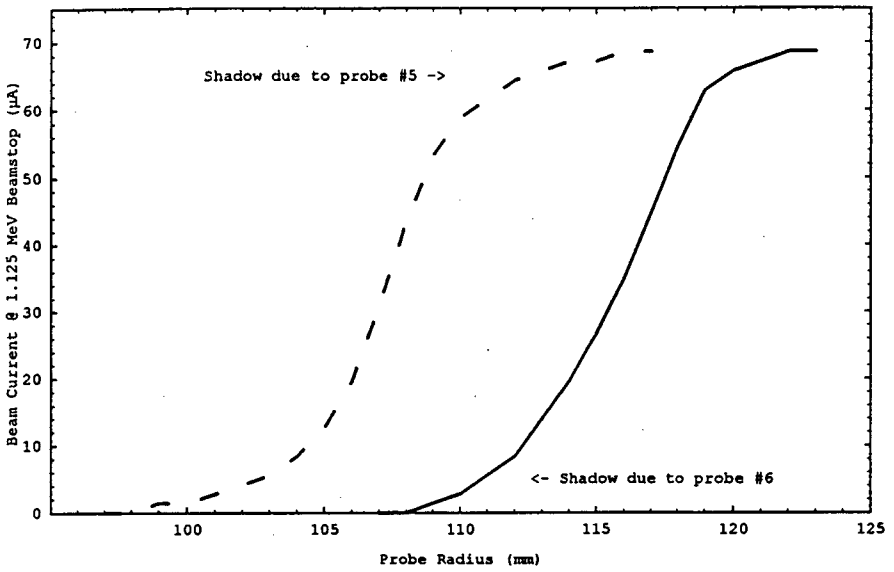

Figure 4.27: *Beam current @ the 1.125 MeV beamstop as a function of probe #6 and probe #5 radial positions.*

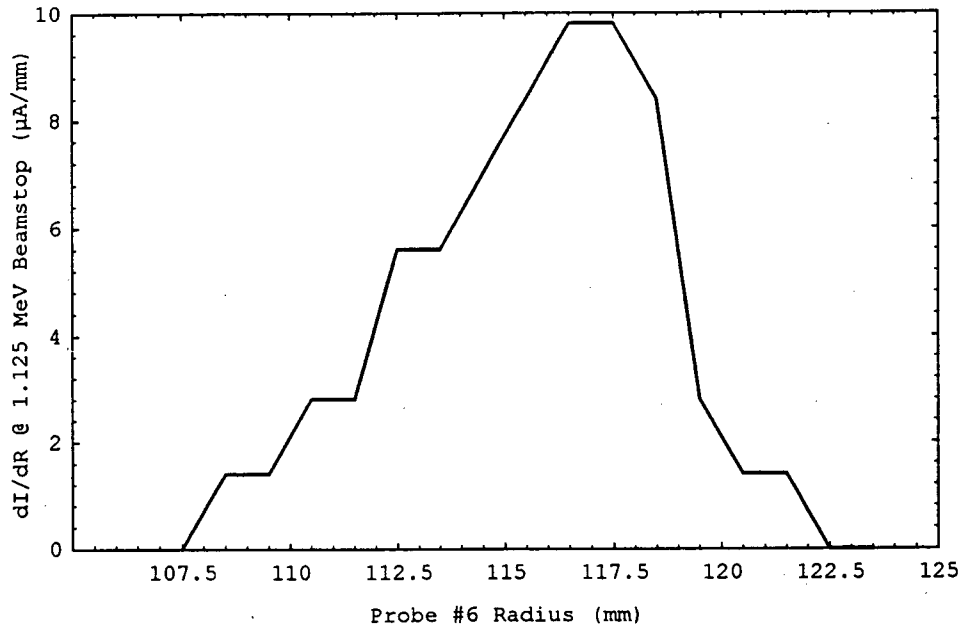

Figure 4.28: *The differential beam intensity @ the 1.125 MeV beamstop as a function of the position of probe #6.*

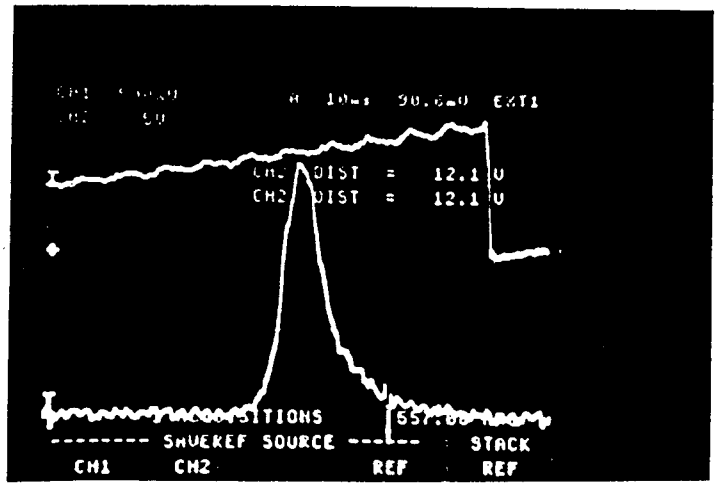

Figure 4.29: *The horizontal intensity profile of a 30 MeV proton beam extracted from the TR30 cyclotron.*

The value for x_{max} can be obtained by another method. According to [104], $2 \cdot x_{max}$ is equal to the difference in the lengths of the probe #5 and probe #6 shadow regions in Figure 4.27. The length of the probe #5 shadow region is 18 ± 1 mm, and the length of the probe #6 shadow region is 13 ± 1 mm. Therefore, the value of x_{max} according to this scheme is 2.5 ± 1 mm. This is in agreement with our previous estimates.

4.7.3 VERTICAL BEAM MEASUREMENTS IN THE CENTER REGION

Vertical beam intensity information was obtained using probe #5 outfitted with a differential three-finger probe head (refer to Figure 4.21). The measured differential beam intensity as a function of probe tip radius and axial height is given in Figure 4.30. Information must be gleaned very carefully from this figure, as a number of approximations and smoothing operations were performed to obtain the image.

The axial beam intensity distribution was assumed to fall-off in a gaussian like manner. Assuming a value for σ of approximately 1.4 mm (i.e. conforming to the expected emittance growth as per [48], one can see that it would be unfair to place the outer finger intensity values at axial coordinates ± 5.05 mm, which is where the outer finger centers were located. In a somewhat arbitrary manner, the outer finger intensity values were located at the axial locations of ± 3.0 mm. These locations are 0.2 mm within the inner axial boundaries of the outer fingers.

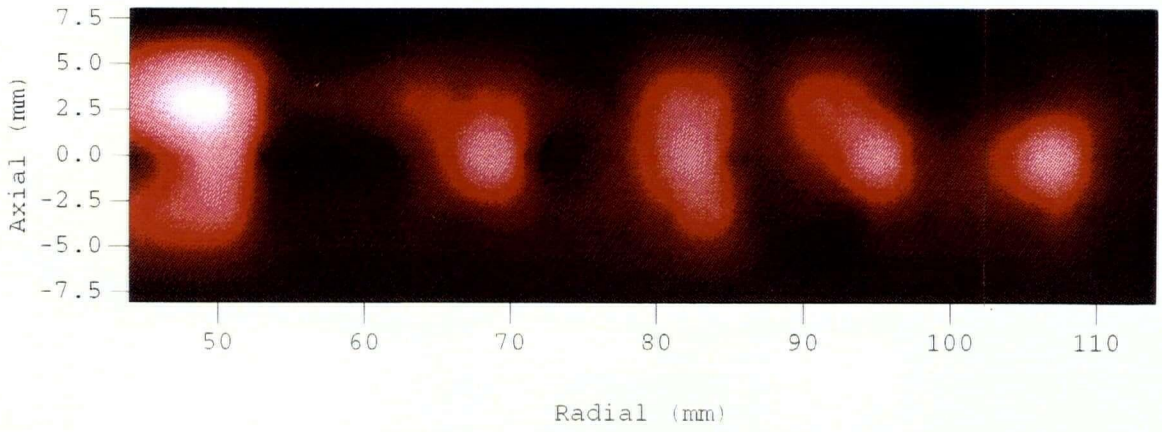

Figure 4.30: *Differential beam intensity as a function of radius and axial height. This data was obtained using probe #5.*

The first warning to be made concerning the image is that the high intensity and off-median plane position of the first turn beamspot might have been due to improper secondary electron capture at this position.

As one might expect with only three data points in the axial direction for every radial increment of the probe, the data was too sparse to be directly converted into a contour plot. Therefore, the program Transform [105] was used to fill in and smooth the data according to a statistical process known as kriging. Kriging replaces each missing data value with a weighted calculation that minimizes the variance of the whole data array. The weighting function assigns weights to those intensities neighbouring the missing intensity value. The weighting function used for the data displayed in Figure 4.30 was $1/R^2$.

In terms of observations based on Figure 4.30, note that the outermost turns of the beam are centered on the median plane (axial height of zero). One can also see the overlap of the RF phases between turns. Consider the outermost turn (#5). The intensity peak is due, as discussed previously, to roughly the center ±8° of RF phase whereas the diminishing intensity between the 5th and 4th turns is due to the RF phases between roughly ±8° and ±32°. A final observation is that the intensity peaks of Figure 4.30 are at the same radii as shown in Figure 4.23 and listed in Table 4.22. This repeatability confirms

that the probe readbacks were calibrated in the same manner for the two figures, and that the same tune can be reliably achieved in the C.R.M. on different experiment days.

For those readers that are not particularly familiar with accelerator physics, the following discussion provides a simplistic, but roughly accurate explanation of the axial beam size changes over the first five turns as illustrated in Figure 4.30. An average value of the axial tune ν_y over the first five turns is 0.333 [92]. This indicates that three full turns are required to achieve one axial oscillation. Figure 4.31 shows a schematic representation of two axial rays executing betatron oscillations overlaid on the ray's rotation cycle around the cyclotron. Given that turn #5 in Figure 4.30 appears to be at a waist, the two rays in Figure 4.31 were shown to be focused to a point at turn #5. Traversing the two rays backwards from turn #5 and noting the axial separation of the rays (i.e. indicating axial defocusing or focusing) shows a rough correspondence to the beam sizes at turns #4, #3, #2, #1 as illustrated in Figure 4.30. For example, turns #4 and #3 appear to be defocused in Figure 4.30, and then turn #2 appears to be at a waist again, in correspondence with the ray trajectories of Figure 4.31. This gives some reassurance that ν_y is indeed approximately 0.333.

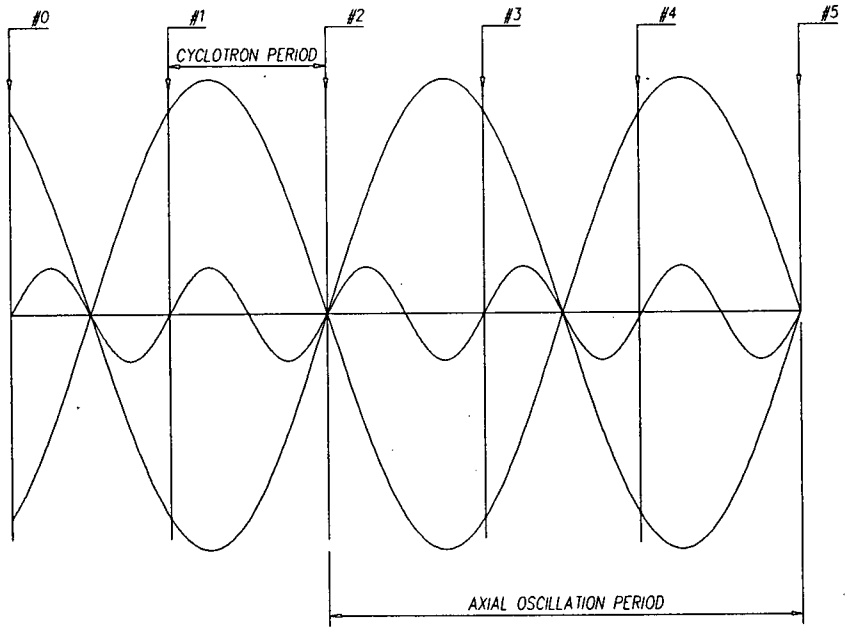

Figure 4.31: *Axial betatron oscillations for ν_y equal to 0.333.*

Recall that the inflector will couple the radial and axial phase spaces. This means that at the inflector exit one would expect to see the elliptical beam intensity profile to be rotated with respect to the radial and axial axes. Once acceleration takes place, though, the smearing of phases with radius and the gradual process of phase mixing will begin to hide this coupling. However, this radial/axial beam coupling does appear to still be visible in Figure 4.30 at turn #4, for example.

An estimate of the effective axial circulating emittance can be made using equation 3.1, if the radial parameters are replaced with axial parameters. Since the axial width is oscillating, as discussed above, the overall effective circulating emittance can be estimated by using the largest axial beam size attained between turns #2 and #5. Turn #3 has the largest axial width ($2 \cdot y_{max}$), and it is 10 ± 2 mm. Thus, y_{max} is equal to 5 ± 1 mm. With an axial tune υ_y equal to 0.333, a cyclotron radius, for the average magnetic field of 12 kG and beam kinetic energy of 0.625 MeV, of 95 mm, and a value of $\beta\gamma$ equal to 0.037, an estimate of the axial circulating emittance $\varepsilon_{n\_ax\_circ} = 0.003$ mm·rad = 3 mm·mrad can be given. This again corresponds to an emittance growth of approximately 6.

4.7.4 A COMPARISON OF 2Q, 3Q AND 4Q BEAM PROFILES AT TURN #5

Probe #5 three finger differential intensity scans at turn #5 were obtained for the nominal 2Q (Q0 and Q1 powered), 3Q (Q0, Q1 and Q2 powered) and 4Q injection line scenarios. Each injection line scenario was tuned to maximize the beam current at the 1.125 MeV beamstop using the L155/PL10.8/EL10/NL ion source configuration @ 2.6 amperes of arc current under the original injection line axial rotation angle where the Q0 defocusing axis was set at 27° CCW to the lab vertical axis. Also, one 4Q profile was taken with the arc current set to 4.8 amperes. The three former profiles were taken to determine the manner in which beams from different injection line scenarios differ after having been accelerated through several turns. The latter profile was measured to see whether the substantially smaller emittance of the 4.8 ampere arc current beam was still evident after several turns of acceleration.

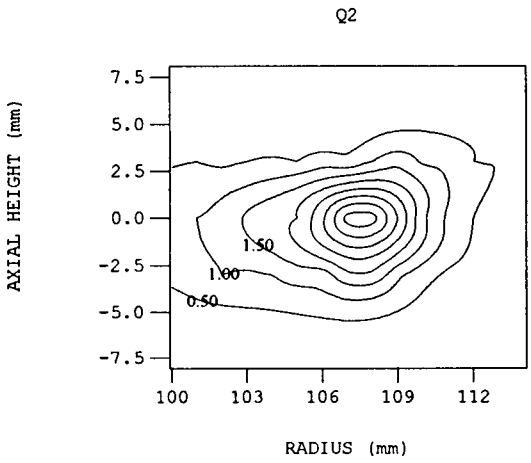

Figure 4.32: *The turn #5 beam intensity contours for the nominal 2Q injection line scenario @ an arc current of 2.6 amps. The integrated beam current was 46 μA.*

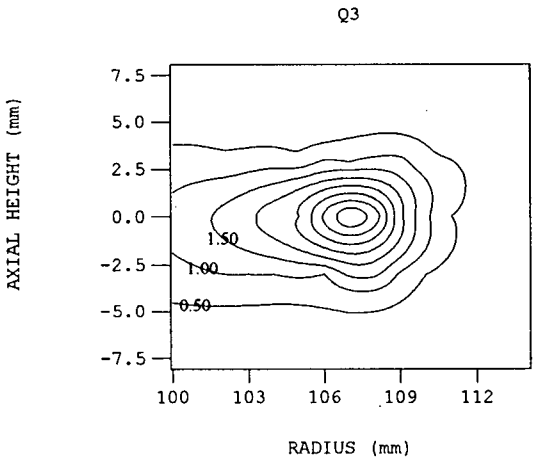

Figure 4.33: *The turn #5 beam intensity contours for the nominal 3Q injection line scenario @ an arc current of 2.6 amps. The integrated beam current was 42 μA.*

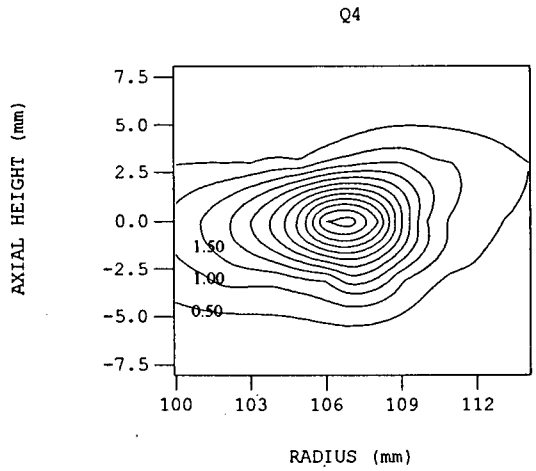

Figure 4.34: *The turn #5 beam intensity contours for the nominal 4Q injection line scenario @ an arc current of 2.6 amps. The integrated beam current was 69 μA.*

Figures 4.32, 4.33 and 4.34 contain contour plots of the beam intensity distributions for the 2Q, 3Q and 4Q scenarios. The spacing of the three finger data and the use of kriging to fill in the sparse data in a smooth manner was done as described in the previous sub-section and in Appendix II. The three contour plots look very similar to each other. Their radial and axial centers are located at very nearly the same points, and their general contour shapes are similar, as well. This illustrates that the cyclotron heavily dominates the shaping of the beam regardless of which system injects the beam.

Certain differences between plots do exist, however. In particular, the lower level contour lines of the 2Q scenario extend out to larger radii, while the same low level 3Q contour lines extend out more towards inner radii. This could indicate that the 2Q system places more beam in the central RF phases while the 3Q system places more beam in the very positive or negative RF phases.

The 4Q system, on the other hand, populates all phases more densely. In fact, the total beam current at the 1.125 MeV beamstop for the 4Q system was 69 μA, whereas the 3Q and 2Q systems were able to put 42 μA and 46 μA, respectively, onto the 1.125 MeV beamstop. The difference in total beam current between the 4Q system and the other two can be partially accounted for by the relatively low 3Q and 2Q beam transmission rates through the injection line. The rest of the beam loss for these two systems arose due to their poorer beam matching capabilities.

Lastly, note the mild axial/radial coupling on the outer radius side of each of the contour plots (Figures 4.32, 4.33 and 4.34). It is interesting to note that this injected asymmetry still persists out to the fifth turn.

Figure 4.35 illustrates the beam intensity contours for the 4Q scenario where the arc current setting has been increased to 4.8 amps. The magnitude of the normalized emittance of the beam for this arc current setting is 65% that of the 2.7 amp arc current case, as shown in Table 4.1. This corresponds to a 2σ radial beam width of about 80% that of the 2.7 ampere arc current case. A shorter radial 2σ width means that the RF phase slices that almost add on top of each other (i.e. those between $\pm 8°$) will cause the radial intensity distribution to have a very steep slope between the peak intensity and the outer radius side. Also, of course, the 4.8 ampere arc current case will have a higher peak intensity point because the total

extracted ion source current is higher. The total beam current for Figure 4.35 was 108 μA at the 1.125 MeV beamstop.

Qualitatively speaking, Figure 4.35 shows a very steep radial slope on the outer radius side, and the overall area of the beam as defined by the lowest contour level is about the same size as the Figure 4.34 beam. These observations tend to support the argument that the Figure 4.35 beam is of a lower emittance than the Figure 4.34 beam.

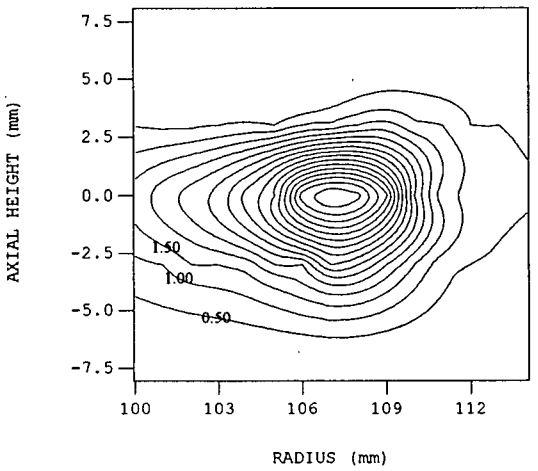

Figure 4.35: *The turn #5 beam intensity contours for the nominal 4Q injection line scenario and an ion source arc current of 4.8 amps. The integrated beam current was 108 μA.*

4.7.5 C.R.M. MAGNETIC FIELD VARIATION AND ITS EFFECT ON BEAM TRANSMISSION

A change in the C.R.M. magnetic field magnitude can affect the radial position of the beam at the inflector exit, the axial position (due to cross-plane coupling) at the inflector exit, the radius of curvature of the beam and the synchronization of the ion cyclotron frequency with the RF frequency. Observing the transmitted beam current at the 1.125 MeV beamstop as a function of the average magnetic field magnitude or the magnet excitation current will not discern between these various effects. However, it will provide clues as to whether positive or negative RF phases are preferred, as to the manner in which different RF phase bands are selected, and as to the general sensitivity of the beam transmission to perturbations in the magnitude of the magnetic field.

Figure 4.36 shows a plot of the beam current at 1.125 MeV as a function of the C.R.M. magnet excitation current. The peak current transmission occurs at 445.5 ± 0.5 amps. The C.R.M. is insensitive to

changes in the excitation current over a 2 amp region denoted as region 3. In general, a larger and flatter peak region is preferred for tuning flexibility and beam stability.

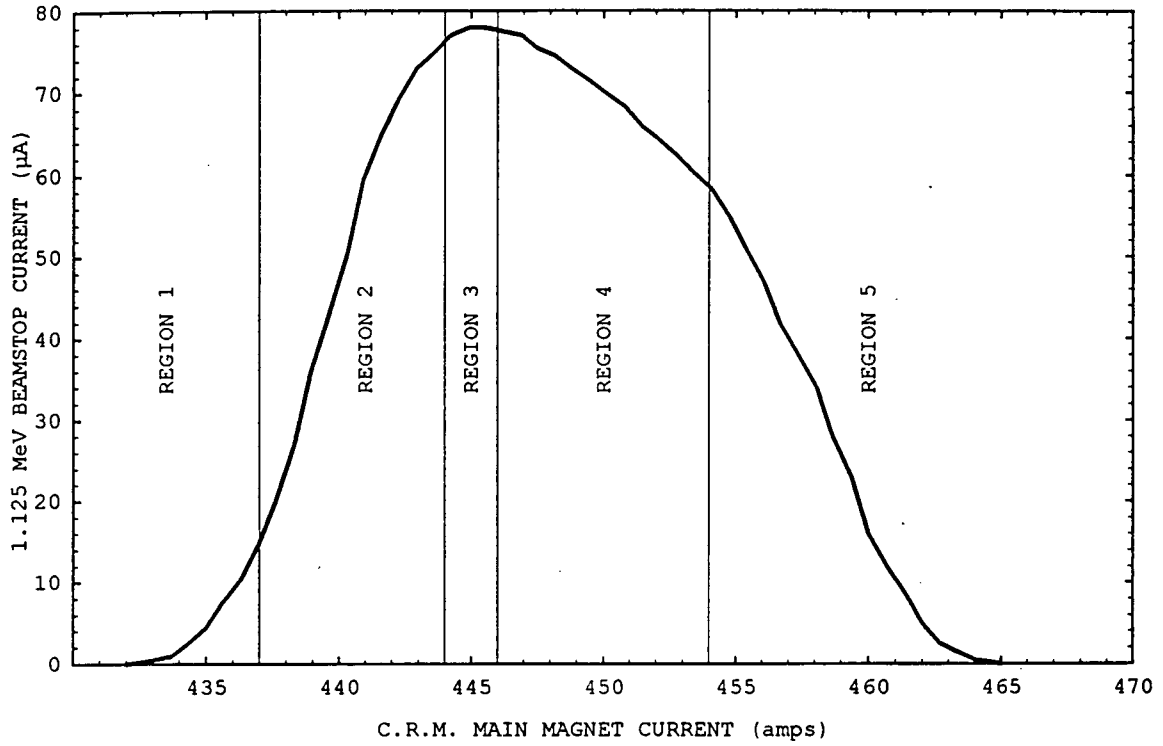

Figure 4.36: *Beam current at the 1.125 MeV beamstop as a function of the C.R.M. excitation current.*

Note that as the excitation current increases, the magnitude of the average magnetic field also increases. Consequently, the radius of curvature of the beam decreases. As the radius of curvature decreases in region 4, the slope of the beam current curve falls off fairly gently. This corresponds to removing the, radially spread out and, therefore, less intense, large positive and negative RF phase slices first. The removed beam has likely been skimmed off on ground posts and/or the dee gaps on the inner radius side of the beam over the course of the first and possibly the second turn. As the radius of curvature decreases even further, the steep sloped region 5 is entered. The steep slope is a result of starting to remove the intense central RF phases (roughly between ±8°).

Note that the magnitude of the average magnetic field increases by only 4.5% over regions 3, 4 and 5. This corresponds to a reduction in the radius of curvature of only 1.8 mm at turn #0.5 and 3.0 mm at turn #1.5. This is not enough of a radial change to eradicate the full extent of the beam in the central

region, where the beam is spread over about 5 mm. Three other effects moderate the way in which beam is lost. First, the centering of the beam is affected by an increase in the magnetic field strength. This could cause the beam to be intercepted on either the low or high intensity side of each beam pulse. Second, an increase in the magnetic field strength couples into the axial plane due to the inflector, so axial beam losses could occur over all phases of the beam pulse. Third, the cyclotron frequency of the beam's pulses increase with the magnetic field strength. This causes each beam pulse to shift intensity into phases which lead the RF voltage peak. This contributes to axial defocusing and to losing beam phases which lead the RF voltage peak by so much as to be out of synchronization.

As the magnetic field strength is decreased, the radius of curvature of the beam increases. This means that the central RF phases will be removed from the beam first. The loss of the concentrated central phases explains the sudden steepness of the curve in region 2. As the excitation current is dropped further and region 1 is entered, a distinct mellowing of the slope of the curve in a similar manner to region 4 is not clearly seen. This is due to the same three moderating effects mentioned above: changes in centering, coupling to the axial plane and loss of synchronization.

4.7.6 INFLECTOR ELECTRIC POTENTIAL VARIATION AND ITS EFFECT ON BEAM TRANSMISSION

The spiral inflector is comprised of two electrodes; one held at a negative electric potential and the other held at a positive electric potential. The two electrodes are parallel at the inflector exit but are rotated to an angle of 39.7° with respect to the median plane. If the electric potential difference between the electrodes change, the beam shifts both axially and radially. Therefore, it is not a simple matter to correct either radial or axial centering with the inflector electrode voltage settings.

Figure 4.37 shows a plot where the contours correspond to the total current transmitted to the 1.125 MeV beamstop, and the axes of the plot correspond to the electric potential placed on the inflector electrodes. This plot shows that the beam transmission remains peaked if the total potential difference is kept at 15.3 ± 0.1 kV. Given that the inflector electrode power supplies can be easily set to better than ± 0.03 kV, the current transmission can be considered to be sufficiently insensitive to changes in the total potential difference to be acceptable for typical cyclotron operation.

The transmitted current, in Figure 4.37, falls off faster if the total potential difference is less than 15.3 kV. If one refers to Figure 5.37, it is apparent that the beam is shifted to positions where the axial height is greater than zero ($y > 0$) and the radial position is closer to the machine center ($x > 0$) as a result of the lower electrode voltages. A beam with initial radial coordinates that were too small would be expected to lose the less intense positive and negative phases first. However, since beam loss was quite rapid as the potential difference decreased another effect must have been dominating. In particular, miscentering the beam to a higher initial axial position and a lower initial radius in combination with the beam's natural betatron evolution was obviously less compatible with the aperture spacings and positions than a beam miscentered to a lower initial axial position and a larger initial radius.

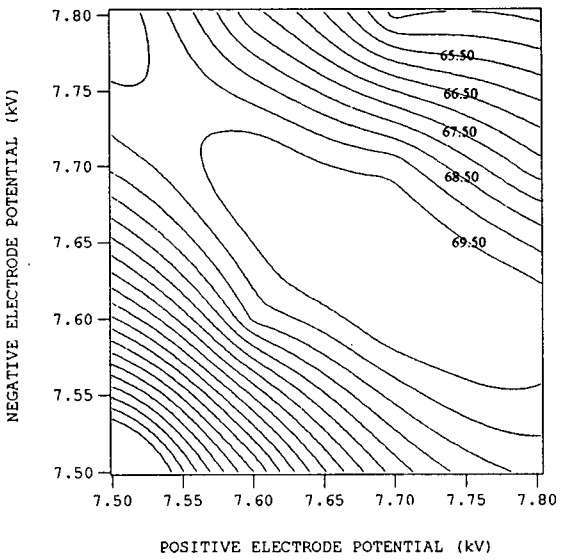

Figure 4.37: *Beam current transmitted to the 1.125 MeV beamstop as a function of the inflector electrode electric potentials. Current contours are in (μA).*

4.7.7 INJECTION LINE QUADRUPOLE MAGNET CURRENT VARIATION AND ITS EFFECT ON BEAM TRANSMISSION

The 4Q injection system tune was found to be stable and repeatable throughout the four month test period. However, it was noted that the quadrupole magnet currents did not have to be adjusted by very much to significantly affect the beam transmission. As an example of this consider Table 4.23 which demonstrates the sensitivity of the current transmission to quadrupole magnet field strength changes.

From this table it is clear that substantial decreases in transmitted beam current result from variations in the quadrupole magnet current settings.

Table 4.23: *Beam current transmission as a function of Q0 and Q3 field strength variation within the 4Q system.*

MAGNET	% FIELD CHANGE	% CURRENT CHANGE @ 1.125 MeV
Q0	−4.5	−16.7
Q0	+11.3	−27.5
Q3	−8.8	−27.5
Q3	+5.2	−23.5

4.8 SUMMARY

This chapter began with a description of the beam transmission tests performed on the SQQ based injection line installed within the C.R.M. facility. This was done to establish baseline beam transmission measurements with which to compare the Q based injection line measurements, and to establish a back-up injection line scenario for the TR13 cyclotron. The divergence of the beam emanating from the nominal ion source configuration coupled with the rather long initial drift space of this system resulted in modest transmission rates from the ion source to the 1.125 MeV beamstop of about 8% (Table 4.4). The highest beam current recorded at the 1.125 MeV beamstop was 134 μA.

The large beam divergence's produced by the nominal ion source configuration and the resultant modest transmission rates for the SQQ system prompted a serious investigation of the ion source's output beam characteristics as a function of a number of geometrical and tunable variables. These investigations were also valuable for establishing the ion source performance in an arc current range (0 to 7 amps) which had not been extensively studied before. The ion source investigations culminated in the selection of the L105/PL8/EL8/WL ion source configuration as the best choice for the Q based injection line tests.

The Q based injection line tests established that the 4Q injection line was of interest with respect to the TR13 because it could transmit the highest levels of beam current to 1.125 MeV. With the injection line orientation angle optimized, a current of 275 μA could be obtained at the 1.125 MeV beamstop. However, the 2Q injection line, which is considerably less expensive than the 4Q, 3Q and SQQ injection

lines, could transmit a current of 179 μA to the 1.125 MeV beamstop, which was well above the 110 μA minimum required at 1.125 MeV to ensure 100 μA of extracted protons from the TR13 cyclotron. Therefore, the 2Q injection line was considered to be the best choice for the TR13 cyclotron system.

The Q based injection line tests also revealed other useful information. The beam current transmission rates from the ion source to 1.125 MeV were as high as 13% for the 4Q system, whereas the previous highest rate was 12% [48]. In addition, the beam current transmission from the inflector exit to 1.125 MeV was found to be 14%. This corresponds to a RF phase band of at least ±25°. Novel injection line orientation angle experiments showed that the 4Q injection line's beam transmission was relatively insensitive to orientation angle changes, whereas the 2Q injection line was quite sensitive.

Center region experiments were undertaken primarily with the 4Q injection system, but also with the 3Q and 2Q, to verify that the beam had been properly injected. As well, a number of important beam related parameters were measured. The beam was found to be of a reasonable size and properly centered in the center region. The emittance growth was found to be approximately a factor of 6 in both phase planes which corresponds well with the factor of 5 reported in [48]. A useful method was obtained for simulating the radial beam intensity distribution in the center region, and it revealed that remnants of phase slices as large as 32° on either side of the RF voltage peak may be present in the beam at 1.125 MeV. The beam current transmission sensitivity as a function of the C.R.M. excitation current, the inflector electrode potential difference and the injection line quadrupole magnet field strengths were investigated and the results were tabulated or plotted.

After a number of months of investigating the beam character within the 4Q injection line and the C.R.M., the combined 4Q/C.R.M. system became quite well understood. This provided a unique opportunity to use the system as a "tool" to study the character of the beam immediately prior to entering and immediately after exiting the inflector. This work is described in the following chapter.

5.0 INFLECTOR EXPERIMENTS

The detailed experimental characterization of the ion source, injection line and center region in Chapter 4 combined with the flexibility of the C.R.M. as a test cyclotron resulted in a unique opportunity to perform ground breaking measurements of the injected ion beam in the vicinity of the inflector. A review of the various cyclotron journals and accelerator conference proceedings [26–46] revealed that virtually all papers concerned with cyclotron inflectors were based on theoretical or numerical calculations, and not on measured data. An understanding of the optical behaviour of the inflector and of the beam in the neighbourhood of the inflector is very important, as the literature makes clear. The fact that measured data is rarely used to advance the state of the art is surprising, but can be understood in terms of the extreme inaccessibility of the inflector within a typical cyclotron. As a consequence, there exists a need for the development of an experimental technique for measuring the optical character of the inflector. This chapter describes a comprehensive original technique for making such measurements. This technique requires a well understood injection system, a collimation system to produce beamlets for ray-tracing, a specially re-configured center region to expose the inflector to view, a system of scintillators in close proximity to the inflector for producing visible beamspots, a TV camera and frame grabber to record images [106], and a set of image analysis procedures.

Again as a consequence of the lack of inflector related experimental data, even relatively basic measurements are significant. Gross features, such as the beam size, shape, orientation and centering, fit into this category and are presented. These measured characteristics are compared to simulations.

Detailed original measurements of the optical properties of the injection system and the inflector, in particular, are made possible by generating test beamlets with a small aperture translatable collimator. Measured changes in the beamlet position on scintillators immediately before and after the inflector as a function of the phase space characteristics of the initial beamlets are then recorded. This data yields quantitative constraints which must be met by the simulations if they are to be judged as correctly representing the system. This permits, for the first time, the output from an inflector modeling code, CASINO, to be tested with respect to measured data.

With this more precise inflector and injection system transport characterization, the definitive assessment of the emittance growth due to cross-plane coupling from the ion source to the inflector exit can be made. The injected beam match to the cyclotron acceptance ellipses is also evaluated. These numbers are compared to the radial and axial circulating emittance measurements made in Chapter 4. A novel technique for measuring the (x, x', y, y') phase space coordinates for the central ray of each beamlet is introduced, and the measured phase space region occupied by the beamlets is compared to the simulated system phase space ellipses.

The experimental set-up also permitted a detailed study of measured beam displacements at the inflector exit as a function of changes in the cyclotron magnetic field, the inflector potential and the beam energy which have never been done before. This data was also compared to computer simulations.

5.1 GENERAL EXPERIMENTAL SET-UP

The C.R.M. facility had to be brought into a state where scintillator images of beams or beamlets could be viewed at the inflector entrance, exit or at a half-turn. In order to do this, a number of technical details had to be sorted out. The technical areas of concern were divided up into the following 7 different topics: collimation, inflector support, scintillator arrangement, optical considerations, frame grabbing, image analysis, and general system set-up. One can get a feel for how these areas were addressed within the C.R.M. facility in Figure 5.1. These topics are discussed in more detail in succeeding sub-sections.

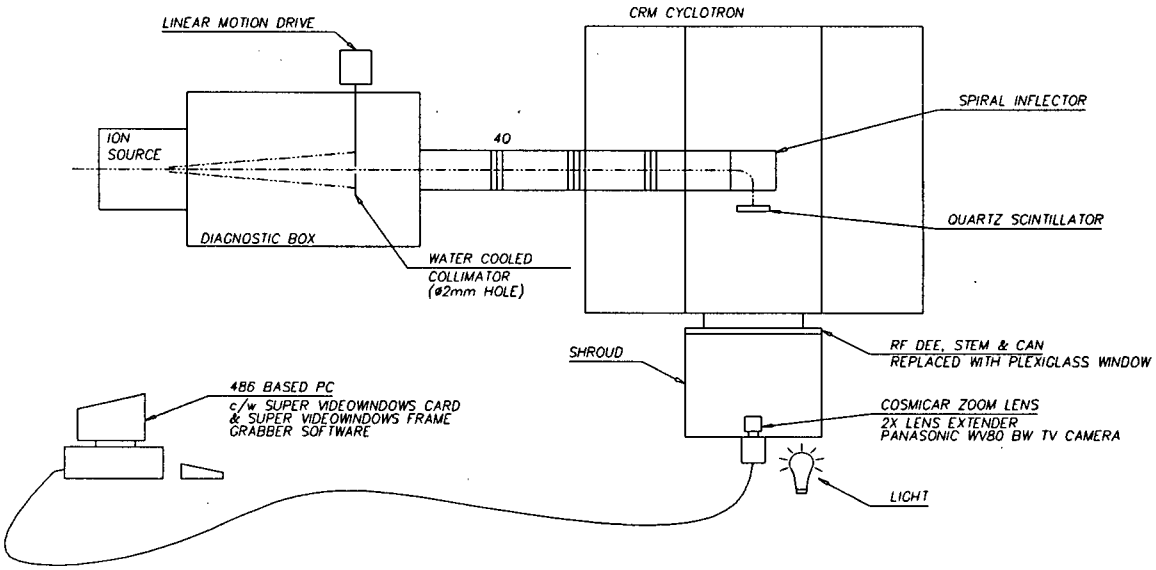

Figure 5.1: *Layout of the inflector experiment equipment within the C.R.M. facility.*

5.1.1 COLLIMATION CONSIDERATIONS

It was known that both the entire beam and individual collimated beamlets would be required for the scintillator experiments. For the experiments in which the entire beam was required, the collimating device(s) were removed. For beamlet experiments, provision was made to use two independent collimating devices that were separated by a drift distance. Using both of these devices would have permitted the selection of beamlets with phase space centroids located at any desired location within the beam's full (x, x', y, y') phase space. However, after the commencement of experimentation, it was found that the beamlet intensity, after being collimated twice, was not sufficient to provide adequate scintillation. Consequently, the experiments were continued using only one collimation device. This resulted in a reduction in the amount of useful information that could be obtained, but the experimental goals were still achieved.

The beam diameter at the collimation point was approximately 30 mm. Therefore, a 50 mm range was specified for the linear motion drive which was used to position the collimator. The translation accuracy of the drive was ±0.05 mm. A water-cooled collimating plate with a vertical beamlet selection piece was mounted to the linear drive which was in turn mounted to the diagnostic box as shown in Figure 5.2. Five knife-edged beamlet holes with 2.00 ± 0.05 mm diameters were aligned vertically and spaced on 5.00 ± 0.05 mm centers. The beamlet holes were counter-sunk so that the collimation was performed by the knife-edge. Smaller beamlet holes were tested as well (1.00 mm diameter), however, the resultant beamlet intensity was not sufficient for an adequate scintillation signal.

Collimators used to produce beamlets of positive ions often require a voltage bias to prevent backstreaming of secondary electrons along the positive potential well of the beam. Eliminating the backstreaming ensures that the beam does not become artificially narrow due to space charge neutralization [107]. Since negative ions form the beam in this investigation, no voltage bias was applied to the collimator, and the secondary electrons were dissipated by the negative potential well of the beam.

A continuous sequence of horizontal beamlets was produced for each vertical beamlet hole position using the linear drive. This was facilitated by having flexible water lines attached to the collimator. Only five vertical positions could be chosen for the beamlets, however, this provided sufficient

information in the (y, y') plane. In order to switch between vertical positions on the collimator, the diagnostic box had to be vented, so that the selection plate could be adjusted. During each venting period the vertical distance between the top surface of the collimator plate and the bottom surface of the diagnostic box was measured with digital calipers. This distance was found to be 108.4 ± 0.2 mm over the range of the linear drive and over all venting period measurements. The drift distance between the ion source waist and the collimation plane was 335 mm.

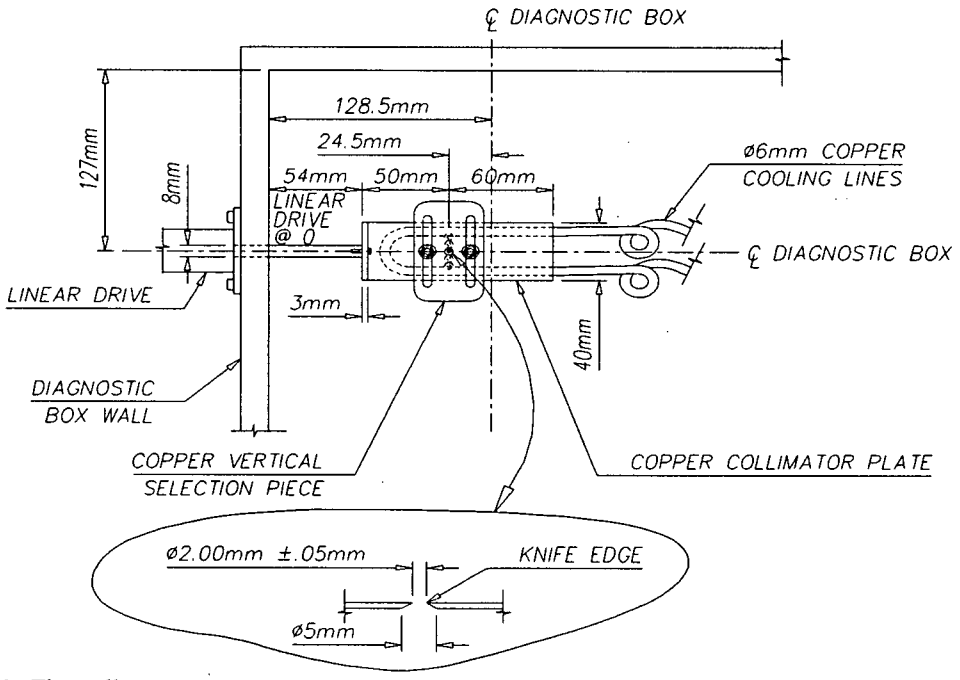

Figure 5.2: *The collimator apparatus*

The diagnostic box was also fitted with a special flanging arrangement through which the cooling lines were brought in. As well, the flanging arrangement contained a 50 mm diameter plexi-glass window so that the collimator apparatus could be observed during the experiments.

5.1.2 INFLECTOR SUPPORT

As is the case with other cyclotrons containing inflectors, the C.R.M. inflector is fairly inaccessible. In fact, the spiral inflector in the C.R.M. is completely enclosed by a clam shell shaped center ground electrode. To further complicate matters, the RF dee structures obscure the whole region near the inflector exit.

The solution to these problems was two-fold. First the interfering dee structure and accompanying resonator stub were removed. This left a clear view of the centre region, and provided a convenient port for a plexi-glass viewing window on the C.R.M. main vacuum tank. Second, the technical staff at Ebco Technologies was instructed to construct a replacement center ground electrode that had a portion of its side removed so that the inflector would no longer be obscured from view. The resulting minimalist central electrode design opened up the inflector region to the camera's view and was completely functional. The installed inflector with this new center electrode design is shown in Figure 5.3. The inflector is mounted directly below the long narrow copper support bar which has two white insulators on top, and it is completely open to view on the left where the viewing port is located.

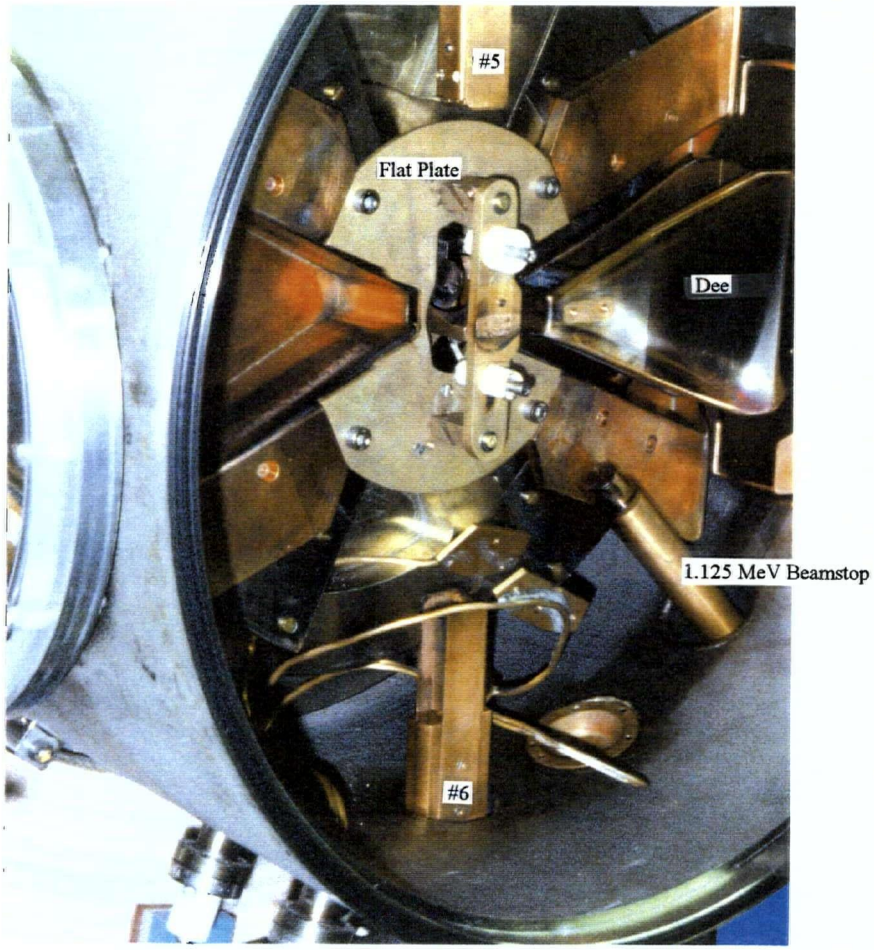

Figure 5.3: *The minimalist center electrode is comprised of a flat plate with two posts mounted to hold the inflector and its support bar in place. The flat plate is fastened to the pole tips with four prominent silver-coloured bolts, and the support bar has two white insulators affixed to it. The left hand dee has been removed. Probe #5 is at the 12 o-clock position, probe #6 is at the 6 o'clock position and the 1.125 MeV beamstop is at the 4 o'clock position. Refer to Figure 4.21 for a schematic representation of the nominal C.R.M. center region.*

5.1.3 SCINTILLATOR ARRANGEMENT

Recall that three scintillator locations were required; at the inflector entrance, at the inflector exit and after the first half-turn. Each of the three scintillator set-ups required solutions to different problems, and, therefore, they are considered separately.

In order for the inflector exit scintillator to reveal beam characteristics at the "inflector exit", it had to be positioned as close to the exit as possible. On the other hand, the scintillator could not be too close to the inflector as the secondary electrons generated from beam bombardment would cause the inflector to continuously spark. A distance of 6.0 ± 0.2 mm between the nearest edge of the inflector exit and the back of the scintillator, and a distance of 9.0 ± 0.2 mm between the farthest edge of the inflector exit and the back of the scintillator were found to eliminate sparking during the experiments.

The inflector exit scintillator was mounted on a copper piece that was attached to probe #5. This arrangement permitted the inflector exit scintillator to be removed from the inflector exit region so that the beam could then pass to the half-turn scintillator without altering the system operating conditions. This eliminated the need to vent the cyclotron between inflector exit experiments and half-turn experiments. Figures 5.4a and 5.4b show the inflector exit scintillator arrangement on the left hand side. The scintillator radial width was 25 mm, the axial height was 20 mm, and the thickness was 1.4 mm.

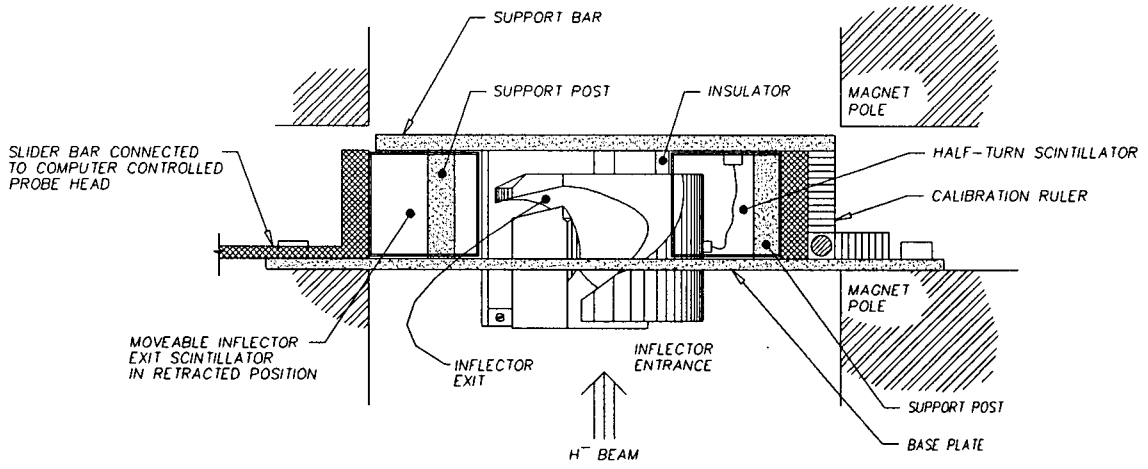

NOTE: THE SCINTILLATORS ARE TRANSPARENT, AND THEY ARE IN THE FOREGROUND. POSTS AND INFLECTOR PARAPHERNALIA ARE BEHIND THE SCINTILLATORS.

Figure 5.4a: *A schematic representation of the inflector exit and half-turn scintillator set-up.*

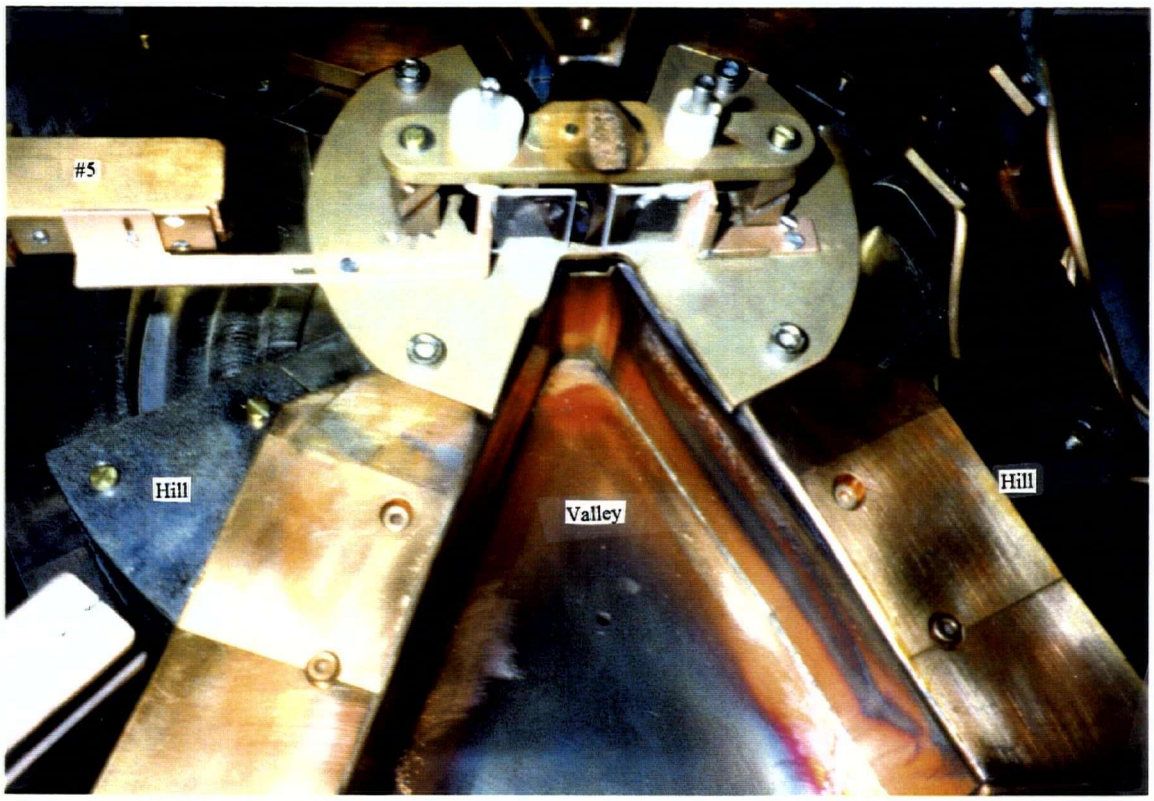

Figure 5.4b: *The inflector exit and half-turn scintillator set-up. The inflector exit scintillator is attached to probe #5 on the left and the half-turn scintillator is located on the right. Note that the images in this figure and in Figure 5.4a have been rotated by 90° for ease of illustration. The left hand side, therefore, corresponds to the upwards direction in the lab.*

The stationary half-turn scintillator was positioned vertically below the inflector exit scintillator with respect to the lab axes (i.e. on the right hand side in Figures 5.4 a & b). It was aligned so that a beam with a radius of curvature of approximately 19 mm would strike it in the center. The dimensions of the half-turn scintillator piece were the same as for the inflector exit scintillator.

The inflector entrance scintillator was mounted at the position normally occupied by the inflector entrance collimator, as illustrated in Figure 5.5. The difficulty with this arrangement was that the scintillator could not be directly viewed by the TV camera. This problem was solved by removing the inflector and its support bar and then mounting a mirror on the inflector support posts angled at 45°. This provided a clear view of the inflector entrance scintillator to the camera. Unfortunately, visible light from the ion source illuminated the inflector entrance scintillator which caused contamination of the beamspot images. Special software based techniques were developed to remove this background light.

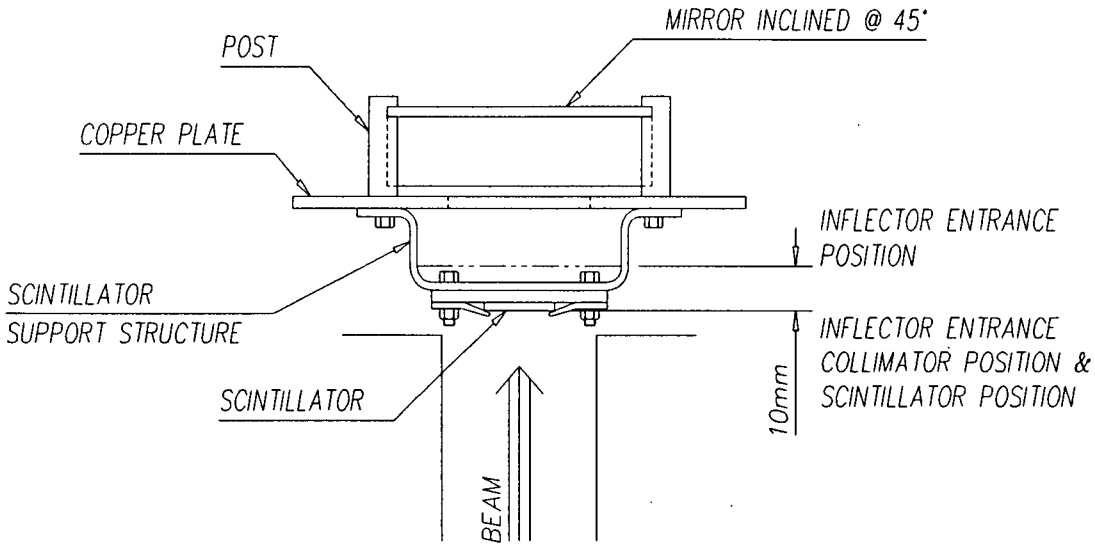

Figure 5.5: *The inflector entrance scintillator set-up. Note that this figure has been rotated by 90° for ease of illustration. The left hand side, therefore, corresponds to the upwards direction in the lab.*

Choosing the appropriate scintillating material for these experiments involved some experimentation. Four types of scintillating materials were tested: aluminum oxide, zinc sulfide, quartz glass, and NE102. The zinc sulfide was eliminated as a choice because it came as a powder which was difficult to affix homogeneously to a glass plate. The TRIUMF staff who had used zinc sulfide had used it as a very qualitative diagnostic tool, where homogeneity of light output was not essential, so techniques for using this material were very limited. The NE102 material was a plastic which meant that the beam power that could be absorbed by it was quite small. Estimates indicated that a total current of 0.1 $\mu A/mm^2$ @ 25 keV would be the very maximum which could be sustained. Besides the fact that this level of current was much too small for some of the experiments, the risk of melting plastic in and around the inflector precluded using this material. The aluminum oxide material was tested, but even at relatively low current levels this material would darken after a few minutes. This changed the light intensity level at the camera as a function of time even when the beam parameters were held constant. Another drawback of the aluminum oxide material was that it was opaque which meant that the beamspot always had to strike the same side of the scintillator as the camera was viewing. The quartz glass scintillator had the best characteristics, and was chosen for use in the experiments. It was transparent which meant that the beam spot could strike the front or the back of the scintillator and the camera would still be able to see it. As

well, the collimated beamlets (≈10 μA/mm^2 max. @ 25 keV) could strike the quartz glass indefinitely without any change in the light output. As well, the full 2 mA beam current (beamspot ≈ 16 mm^2) could strike quartz glass for brief periods (less than 5 seconds) without causing damage.

Quartz plate scintillators are electrical insulators and, thus, there was some concern that the charge from the beam would not dissipate to the grounded holders. If this was so, the accumulation of charge on the scintillator might have affected the beam spot size. To verify whether a problem existed the quartz plate scintillators were coated with 25 ± 5 Å of aluminum. This made them semi-transparent and electrically conductive. Beam spot images produced by the coated scintillators were no different than those produced by non-coated scintillators. Therefore, non-coated scintillators were used throughout the experiments.

5.1.4 OPTICAL CONSIDERATIONS

As already mentioned, one of the dee structures and its resonator stub were removed from the C.R.M., and a Plexiglas window was mounted in the vacated vacuum port. The window was chosen to be thick (1") to minimize on window distortion when the C.R.M. was under vacuum. Although some attenuation of the light from the beam spot images occurred, the optical transmission was acceptable.

The scintillators, as illustrated in Figures 5.4a, 5.4b and 5.5, were situated to be in full view of the camera without altering the camera position. The beam spot planes were set up to be perpendicular to the camera's light sensitive imaging area. A small right angle ruler with vertical and horizontal scribe marks on 1.00 ± 0.02 mm centers was attached to the side of the half-turn scintillator. This position was in the field of view of the camera, and was used to provide dimensional calibrations within the image analysis software.

The camera had to be placed approximately 1 metre from the scintillators to avoid the effects of the C.R.M. magnetic field. If the camera was too close, the image became skewed or even obliterated. The region between the camera and the viewing window was shrouded with black non-glossy construction paper to eliminate background light. The camera was mounted to a sturdy Burndy bar support frame.

Behind the camera, the shroud could be lifted and a light could be turned on and directed at the center region so that the scintillator set-up and the inflector could be viewed (refer to Figure 5.1).

The Panasonic WV-80 black and white TV camera was outfitted with a zoom lens. With the lens apparatus set for the best focus, the picture resolution was approximately 7 pixels/mm. This resolution was sufficient for the inflector experiments. For example, a particularly small beamlet would have an area of 1 mm^2, and would have about 49 pixel intensities in the image. This density of data provided enough information to calculate area centroids for the beamlets accurate to ± 0.1 mm. The resolution could have been improved if the whole scintillator set-up and the calibration ruler did not have to be viewed at once, but it was felt that it was essential to view the whole measurement region so that all images could easily be referenced to each other.

5.1.5 FRAME GRABBING

The camera was connected to a video digitizing board within a 486 based personal computer. The name of this board was the Super Video Windows board. The board came with software entitled Veditor [108]. It permits live images from the camera to be viewed on the computer screen. The software is also capable of freezing an image when desired and it can be saved to disk in a standard image format such as targa (*.tga) or as a windows bitmap (*.bmp). In this way images of scintillating beam spots can be viewed, perturbed (i.e. a system setting could be varied), frozen and saved to disk. The images were viewed and saved as gray scale images with 0 to 255 levels of gray.

5.1.6 IMAGE ANALYSIS PROCEDURES

The image analysis procedure involved a data extraction process, a data analysis process and a visualization process. The data extraction process involved obtaining quantitative measurements such as beam size, location and average gray level. A software package called Optimetric [109] was used to perform this function. The analysis of the relationships between these quantitative measurements was performed using, *Mathematica*. Visualization of the data for qualitative assessment utilized both Optimetric and *Mathematica* as well as Transform. The data extraction process followed a number of set rules. These rules were laid out so that quantitative data could be extracted from each image in a

consistent manner, and in a manner which permitted the data to be accurately compared. The general data analysis and visualization techniques were applied on a data set to data set basis, so they will be discussed in subsequent sections of this chapter. The remainder of this sub-section will be devoted to a description of the data extraction process.

Knowing the general data taking sequence will help to understand certain parts of the data extraction process. Therefore, note that the scintillator experiments were done in sessions. Typically, no more than two such sessions were finished in a given day. A particular, experimental session involved, for example, obtaining and saving all the beamlet images at the inflector exit and at a half-turn for the case where the collimator had the center aperture selected and its position was advanced horizontally in 2 mm increments. The first image that was obtained and saved to disk in each session was a calibration image in which no beam spot was present but the region around the scintillators was illuminated. After this image was saved, the shroud was closed up and the beam spot images for the experiment were obtained and saved to disk. For the case of inflector entrance scintillator experiments, an associated background light image was obtained and saved to disk for each beamlet image that was saved to disk. This background image was obtained after turning off the 25 kV ion source bias supply. Once this had been done, the beam was not accelerated, but the contaminating background light was still projected throughout the injection line by the ion source. Lastly, after all the experiment's images had been saved, a second calibration image was always obtained and saved to disk.

Recall that the whole data extraction process was done from within Optimetric. The data extraction steps from a particular experimental session were to:

- check the ***aspect ratio*** for each of the calibration images. For example, a 5 millimetre vertical section should have been equivalent to a 5 millimetre horizontal section on the calibration ruler image. This was checked with a measuring stick tool within the program. If the aspect ratio needed to be changed, the program permitted this parameter to be adjusted.
- check the ***dimensional calibration*** for each of the calibration images. A 10.0 mm section of the calibration ruler, within the calibration image, was measured for the case of inflector exit or half-turn experiments. For inflector entrance experiments, the length of a feature located at the inflector entrance with a known length was measured. Confirmation that the program agreed with the known length was then obtained. The measurement units were re-calibrated, if necessary.
- locate ***standard points*** for each of the calibration images. Standard points were located so that any rotational or translational deviations between the images of different experimental sessions could be corrected for. Figures 5.6 and 5.7 schematically illustrate the locations of the standard points. Note that some of the standard points were located on features for which well defined (x, y) coordinates

could be obtained, whereas others were located, in conjunction with a partner point, anywhere along line like features. For these latter standard points, the issue was to establish the orientation of the line.

- perform a ***background light correction*** to each of the images obtained in the experimental session. First one had to check whether the beamspot was riding on a background gray level or not. If the pixels neighbouring the beamspot were primarily at a gray level of zero, with perhaps random regions with gray levels between 0 and 3, then no background light correction was performed. However, if the beamspot was surrounded by a non-zero background gray level, then a correction was performed. Typically, background light correction was only needed for inflector entrance images because the light emitted by the ion source shone directly down the injection line. Luckily, however, the ion source light was also collimated by the beam collimator, which greatly reduced the contamination of the beamlet images. The correction procedure involved subtracting the image which contained strictly background light from the images which contained both the beamlet image plus the background light.
- set a ***gray level threshold*** for each of the images obtained in the experimental session. A threshold was needed to define the area which was occupied by the beam. The standard threshold was at a gray level of 5. On rare occasions the threshold would have to be set up to a gray level of 8 in order to differentiate the beamlet image from residual background light. Peak beamlet or beam gray levels varied from a low of 8 to a maximum of 255. The beamlet images were never saturated, however, full beam images were sometimes saturated.
- perform a ***search for all regions in the image at a gray level above the threshold***. The beamlet region was then isolated from the other regions and selected.
- execute ***data extraction*** from beam or beamlet images. The data extraction was performed on the region defined for the beamlet by the threshold. Dimensional data was computed based on the aspect ratio and dimensional calibrations. The types of data extracted from the beamlet region were the following: beamlet area, beamlet perimeter, (x,y) coordinates of the area centroid, length of the major axis, length of the minor axis, the mean gray level, the peak gray level, and the (x,y) coordinates of the peak gray level.
- standardize the coordinate systems for each experimental session through ***data pre-processing***. Using the standard points from the calibration images from each experimental session, a check was performed to determine whether the calibration images were translated, rotated or scaled with respect to each other. In all cases lengths were preserved, so no scaling was required. However, typically the calibration images were somewhat rotated and/or translated with respect to each other. An average translation in both (x) and (y), and an average rotation correction were determined for each experimental session. Lastly, a standard coordinate system was chosen, and all the data from each session was translationally and/or rotationally adjusted to the standard coordinate system.
- perform a ***coordinate correction on the dimensional data of the beams or beamlets*** which struck the inflector exit or half-turn scintillators. This accounted for the slightly non-normal incidence of these beams or beamlets.

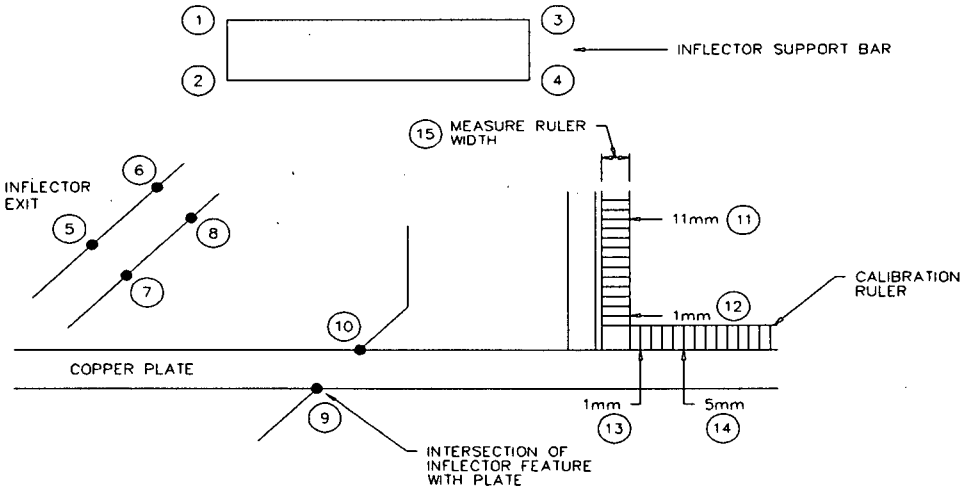

Figure 5.6: *A schematic of the standard point locations for the inflector exit and half-turn measurements.*

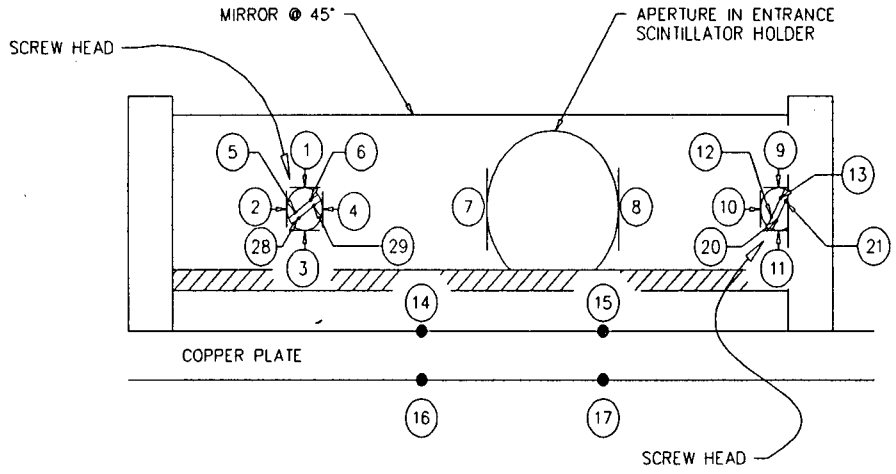

Figure 5.7: *A schematic of the standard point locations for the inflector entrance measurements.*

5.1.7 GENERAL SYSTEM SET-UP

The L105/PL8/EL8/WL ion source configuration was used for all of the scintillator experiments. The injection system which was used was the 4Q system set at the new axial rotation angle, where the defocusing axis of Q0 was oriented at 21.7° CCW with respect to the lab vertical axis.

The experiments of Chapter 4 illustrated that when consistent system settings were used, the beam current readings and the phase space characteristics of the beam were repeatable to within a few percent. Thus, the majority of the experiments were conducted with the system settings used to obtain the 1.125 MeV beamstop beam current of 253 μA at an arc current of 6.4 amperes (Table 4.17), except that the RF was turned off. Table 4.14 indicates that the ion source output beam current for this arc current is approximately 1.9 mA, and Table 5.1 gives the system settings for this nominal experimental tune. Situations which required a different tune will be explicitly described in the text.

Before any measurements were taken the whole system was run for approximately one half hour in order for each component to settle into its steady operating state. From time to time, IBS current readings and emittance scans would be taken to confirm that the beam currents and phase space characteristics of the ion source beam did not change.

Table 5.1: *Nominal L105/PL8/EL8/WL ion source, 4Q injection system and C.R.M. settings for the scintillator experiments.*

SETTINGS AND READINGS	Values
Arc Current (A)	6.4
Hydrogen Flow Rate (cc/min)	7.6
Plasma Electrode Current (A)	3.1
Plasma Electrode Voltage (V)	2.3
Extractor Electrode Current (mA)	10 ± 2
Extractor Electrode Voltage (kV)	2.0
Source Bias Voltage (kV)	25.0
1st Steering Magnet [x,y] (A)	[0.18,1.10]
Q0 (A)	2.2
Q1 (A)	3.9
Q2 (A)	4.3
Q3 (A)	4.0
Main Magnet (A)	446
Inflector (kV)	+7.6/–7.65
Cyclotron Vacuum (Torr)	1×10^{-6}

5.2 INITIAL OBSERVATIONS

It is important to understand the measured characteristics of the full beam before discussing the collimated beamlet measurements, since the full beam scenario provides a general framework with which to reference the detailed beamlet investigations. As well, the full beam measurements provide answers to often asked questions such as: "What is the size, shape and orientation of the beam at the inflector entrance and exit?", or "What is the axial and radial beam centering at the inflector entrance and exit?".

5.2.1 INFLECTOR EXIT AND HALF–TURN SCINTILLATOR POSITIONS

A few precautionary points must first be made before discussing the characteristics of the full beam scintillator images. The full beam, as discussed in sub-section 5.1.7, is at a current of 1.9 mA, which, for a 25 keV beam, corresponds to 47.5 Watts of power that must be dissipated by the quartz scintillator. The quartz was not cooled in any manner so the scintillator heated up rapidly. To avoid melting the scintillator, the beam was typically shut off within about 5 seconds. As well, the inflector sparked every second or so under these conditions (due to the copious quantities of secondary electrons liberated), which would momentarily stop the beam from striking the scintillator. The light produced from the scintillators under these conditions resulted in beam spot images saturated at gray level 255.

Obviously, these conditions conspired to degrade the quantitative value of the captured images. Consequently, the full beam images are to be viewed with caution, and only in terms of their gross characteristics, such as: the general location of the radial and axial center positions of the images, and the general orientation, shape and size of the images.

Figure 5.8 shows the contour of the inflector exit and half-turn scintillator beamspot images at a gray level of 200. This contour was chosen because it bounded the very distinct high intensity regions of both of the beams. The background gray level for these beamspot images was relatively high at approximately 80. The background level was high because the experiment was done with the lights on, so that the various calibration reference points were visible. The benefit of having visible reference points, which helped to confirm exactly where the beam spots were located, outweighed the negative aspects of having relatively high background light levels. It is also important to note that the physical inflector exit was not perpendicular to the camera's viewing axis (refer to Figure 5.9). This fact must be taken into account when comparing the inflector exit scintillator image to the inflector exit markings that have been included in Figure 5.8. Another concern is that the beam central trajectory was not perpendicular to the scintillator surfaces, however, for the simulated trajectories in Figure 5.9 and the beam sizes of Figure 5.8, the estimated additional beam spread on the scintillator was only 0.2 mm. This small level of beam spread can be ignored given that only the gross beam characteristics are under discussion.

The inflector exit scintillator beamspot has a major axis length of 4.5 mm and a minor axis width of 2.5 mm, and, even though the percentage of the total current which is contained within the beamspot is not well defined, it appears that the beam is comfortably smaller than the 6 mm gap between the inflector electrodes at the exit. The (x, y) coupling of the beam induced by the rotated injection quadrupole magnets, the axial bore of the cyclotron and the inflector is very apparent. The major axis angle of the beam with respect to the radial axis is $50° \pm 10°$, and the beam centroid is located at (−20.6 mm, −0.4 mm).

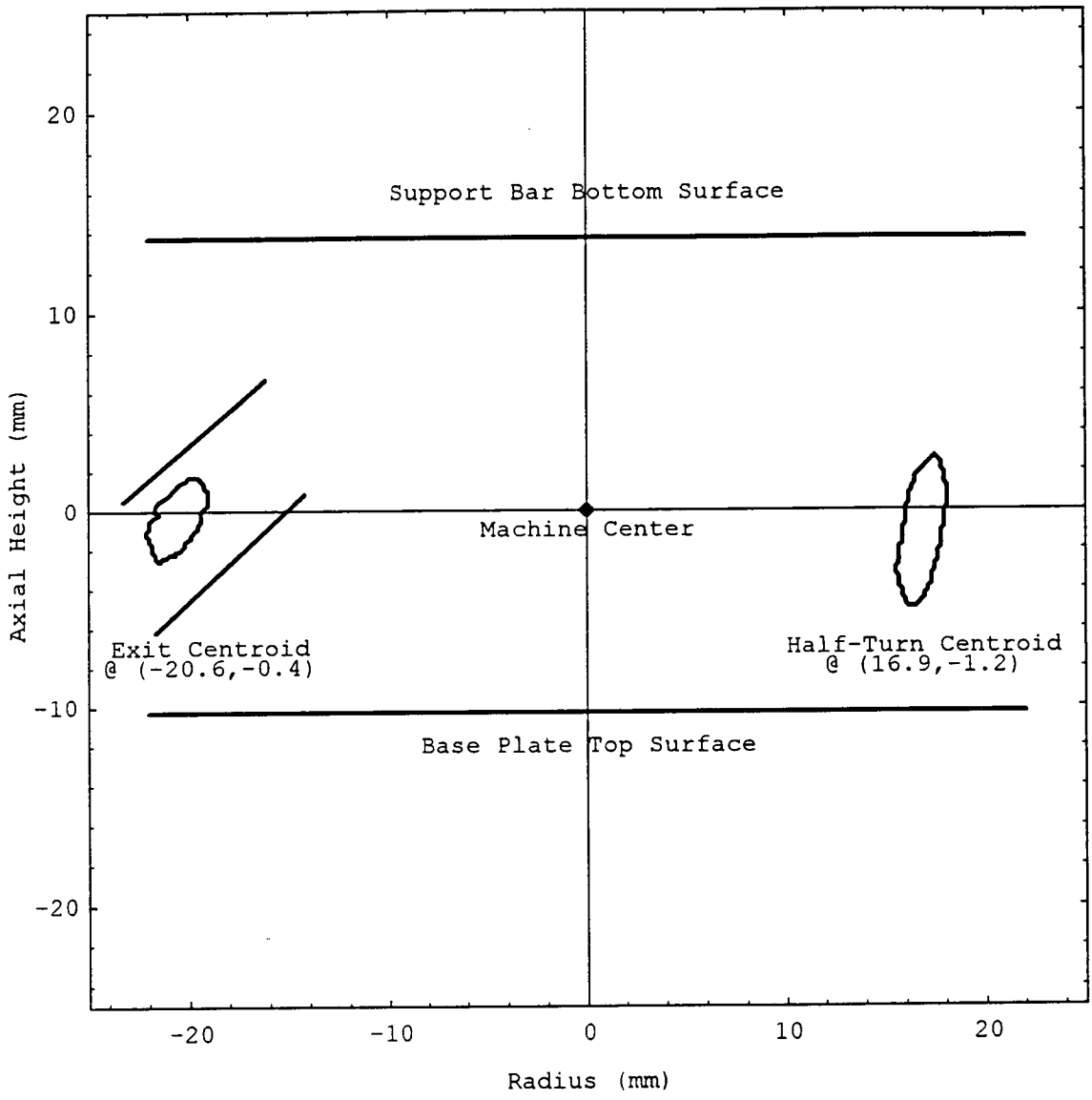

Figure 5.8: *The inflector exit and half-turn scintillator beamspot images for a 1.9 mA H^- beam produced by the L105/PL8/EL8/WL ion source and injected by the 4Q injection system rotated at 21.7° counter clockwise.*

The half-turn scintillator beamspot has a major axis length of 7.5 mm and a minor axis width of 2 mm. The axially elongated image illustrates the axial defocusing which occurs over the first half-turn (with the RF off). To appreciate the origin of the beam defocusing in this region consider Figure 5.10

which illustrates the azimuthally averaged magnetic field in the C.R.M.. The magnetic field rises from about 9.7 kiloGauss at the machine center to about 12.0 kiloGauss at a radius of about 3 cm where it levels off. The low central field is caused by the axial bore of the magnet, through which the beam is injected. The first half turn, with the RF off, resides entirely within a radius of 3 cm from the machine center where, because of the rising field, the field index (equation 2.31) is negative. This yields very strong radial focusing with $\nu_x > 1$ (equation 2.33) and a very unstable axial defocusing situation with ν_y becoming an imaginary number (equation 2.32). Under this situation the axial components of the dipole transport matrix in equation 2.34 become hyperbolic sines and cosines.

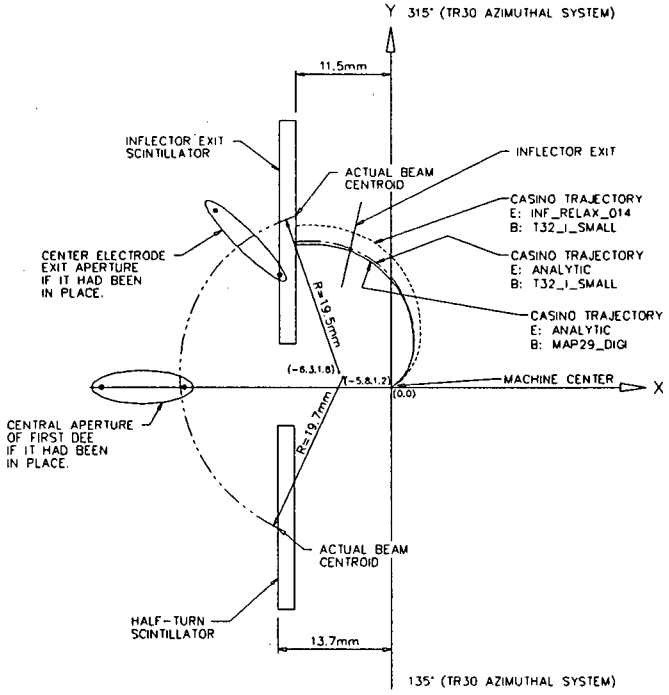

Figure 5.9: *The location of the inflector exit, the locations of the points where the radial centroid of the beam intersects the inflector exit scintillator and the half-turn scintillator, the CYCLONE calculated trajectory of a 25 keV H^- beam which connects the two scintillator/beam intersection points, and standard CASINO calculated trajectories of the injected beam traveling through the inflector are shown.*

The major axis angle of the half-turn beam with respect to the radial axis is 81° ± 3°. Because of the axial defocusing near the very center of the machine, it is obvious that the first RF acceleration during normal cyclotron operation should occur as soon as possible, and with enough energy to bring the beam to a radius greater than 3 cm. In the C.R.M. the first acceleration occurs midway between the center electrode aperture and the first dee central aperture, as shown in Figure 5.9. The beam radius, under

normal operation with the RF on, is greater than 3 cm by the time it is midway between the first dee central aperture and the half-turn scintillator position, as can be confirmed by looking at the beam trajectory in Figure 4.26.

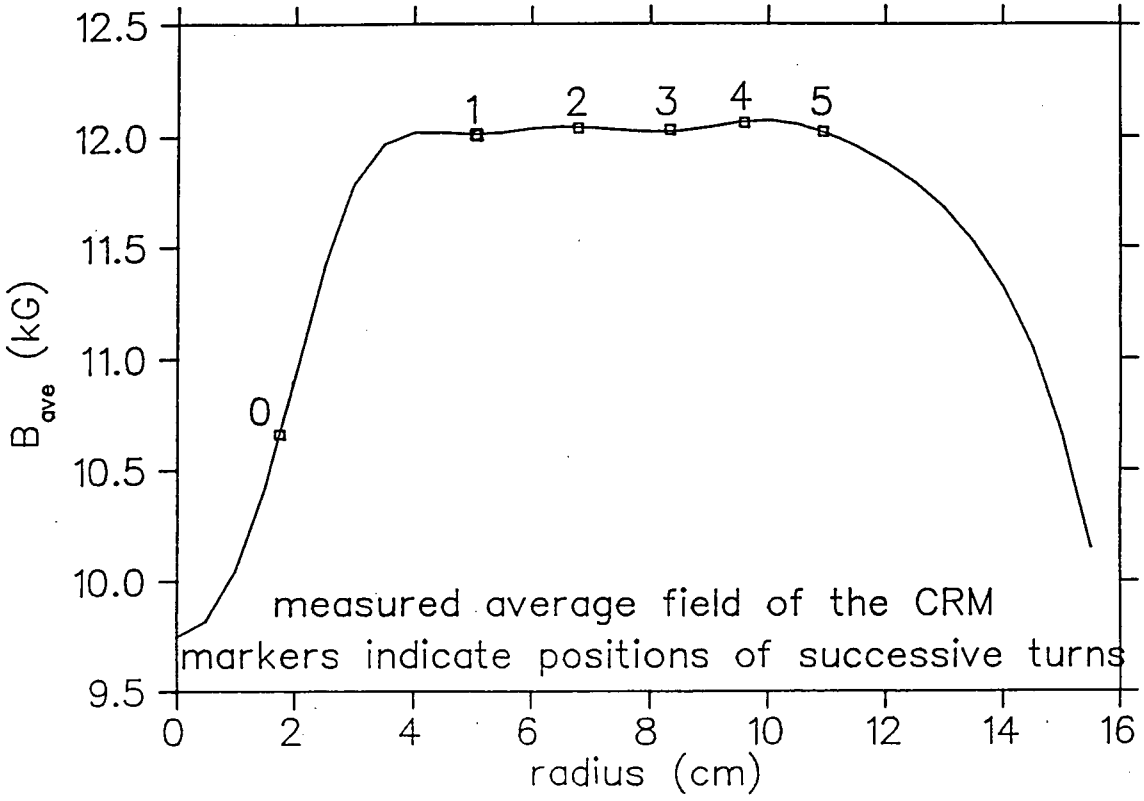

Figure 5.10: *The measured average magnetic field of the C.R.M. in the median plane @ 445 ampere excitation current [110].*

The half-turn beamspot's centroid is located at (16.9 mm, −1.2 mm). The total radial separation between the two scintillator beamspot centroids is, thus, 37.5 mm and the error is estimated to be ± 0.4 mm. An axial drop of 0.8 mm with an estimated error of ± 0.4 mm occurs from the inflector exit scintillator to the half-turn scintillator.

Using the code CYCLONE, a central trajectory for a 25 keV H^- beam was found which connected the centroids of the inflector exit and half-turn beamspots, as shown in Figure 5.9. The radius of curvature of the beam at the inflector exit scintillator is 19.5 mm and the center of curvature is located at (−6.3 mm, 1.8 mm). The radius of curvature at the half-turn scintillator is 19.7 mm and the center of curvature is at (−5.8 mm, 1.2 mm). Note that this trajectory is well centered with respect to the center

electrode exit, and, since the RF is off, the beam trajectory is not centered with respect to the central aperture of the first dee. The azimuthal travel between the two scintillator interception points is 145° ± 5°. Now that the location of the beam centroid at the inflector exit scintillator has been measured and a trajectory has been found which lands the beam on the half-turn scintillator centroid, future simulations can be performed from the inflector outwards to extraction with more confidence. Table 5.2 gives the central trajectory coordinates, which were derived from the measurements, for reference.

Table 5.2: *The central trajectory coordinates of the beam at the inflector exit scintillator position in CYCLONE coordinates.*

Coordinate Name	Coordinate Value
R (cm)	2.4
θ (°)	344.2
Pr (cm)*	0.46
Z (cm)**	-0.04
Pz (cm)***	-0.02
E (MeV)	0.025

* Defined as Px, ** defined as (y), *** defined as Py in this thesis.

Figure 5.9 also shows three standard CASINO trajectories (refer to Appendix III for command files) which have been used over the years to represent the trajectory of the beam through the inflector. These trajectories do not intercept the inflector exit beamspot centroid. The variability's in inflector manufacture, the centering of the beam at the entrance to the inflector, and small differences between simulated and actual field settings account for differences between the actual and simulated locations of the beam at the scintillator.

The CASINO run which used the RELAX3D electric field map computed the axial centroid at the exit scintillator to be –0.8 mm. The run which used an analytic electric field and the magnetic field file T32_I_SMALL.ZFLD computed the centroid to be at –0.3 mm, and the run which used an analytic electric field and the magnetic field file MAP29_DIGI.ZFLD (Figure 5.11) computed the centroid to be –0.2 mm. The measured axial centroid position was –0.4 mm with an estimated error of ±0.4 mm. Therefore reasonable agreement between the simulated and the measured values exists. With the axial centroid slightly below the median plane, and with a slight negative axial momentum (Table 5.2) at the

inflector exit scintillator position, it is not surprising, given the strong axial defocusing, that the half-turn axial centroid is substantially below the median plane, at 1.2 ± 0.4 mm.

Due to the low optical contrast in the images used to generate Figure 5.8, they were not of sufficient quality to be used for publication. Fortunately, a set of images of sufficient optical quality for publication were obtained using a 1.1 mA input beam from the L105/PL8/EL8/WL ion source configuration using a 2.7 ampere arc current. These images are shown in Figure 5.12. The images are shown so that the reader can develop an appreciation for what a full beam spot image looks like. They do not correspond to the 1.9 mA experiments that are performed throughout this chapter. In fact, the images are expected to be somewhat different than those from the 1.9 mA experiments. Recall from Figure 4.15 that the emittance of the beam becomes larger as the arc current drops. This meant that the injection system tune had to be adjusted from a 1.9 mA tune (6.4 A arc) to a 1.1 mA tune (2.7 A arc), and, thus, the beamspot sizes and orientations at the inflector exit and half-turn scintillator positions were somewhat different for these two beam tunes.

As described in the first paragraph of this section, the full beam spot images produced from high current beams were difficult to capture due to inflector sparking and scintillator overheating. In addition, the light output from the beamspots was sufficiently high to cause the camera's light sensitive area to become saturated. Therefore, remember to view the full beam scintillator images with a certain degree of caution. Despite this warning, the images do indicate that the 1.1 mA beam is substantially smaller than the inflector exit aperture, the beam is axially lower at the half-turn scintillator than at the inflector exit scintillator, and the radial focusing and axial defocusing is evident at the half-turn scintillator.

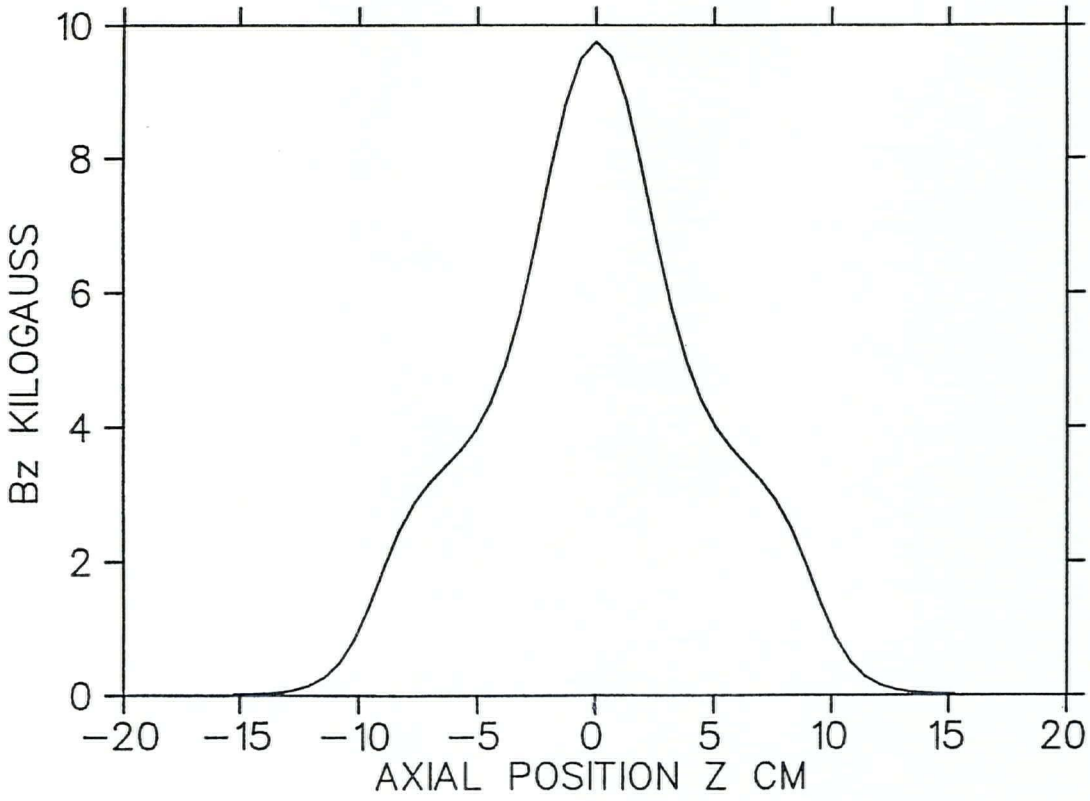

Figure 5.11: *The measured axial magnetic field of the C.R.M. at an excitation current of 445 amps [110].*

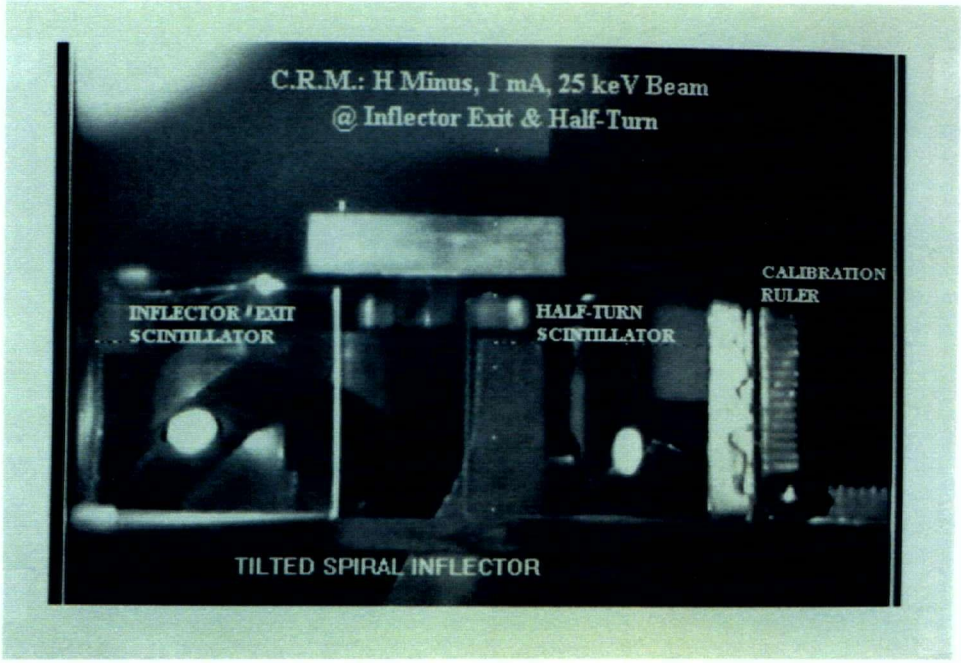

Figure 5.12: *The inflector exit and half-turn scintillator beamspot image for a 1.1 mA H^- beam produced by the L105/PL8/EL8/WL ion source and injected by the 4Q injection system rotated at 21.7° CCW from the lab vertical.*

5.2.2 INFLECTOR ENTRANCE SCINTILLATOR POSITION

Only beamlet data were determined at the inflector entrance. The full beam was not measured at the inflector entrance because background illumination from the ion source obliterated the beam spot image. Luckily, the beamlet collimator limited the amount of light which reached the inflector entrance from the ion source, so that background light subtraction (section 5.1.6) was feasible for the inflector entrance beamlet experiments.

Figure 5.13 shows the (x, y) centroid locations of the beamlets at the inflector entrance scintillator position. Nine measured points along the perimeter of the aperture are also shown, and a circle representing the full aperture has been fitted to these points. The center of this aperture is the center of the inflector entrance. The edges of the inflector entrance electrodes, which are 10 mm downstream of the entrance scintillator position, were, thus, positioned with respect to this origin. Recall that the electrodes are inclined at 14° to the lab vertical, and that the gap is 8.0 ± 0.1 mm. The positive direction of the x axis in the beam transport optical system is in the negative direction of the lab horizontal axis.

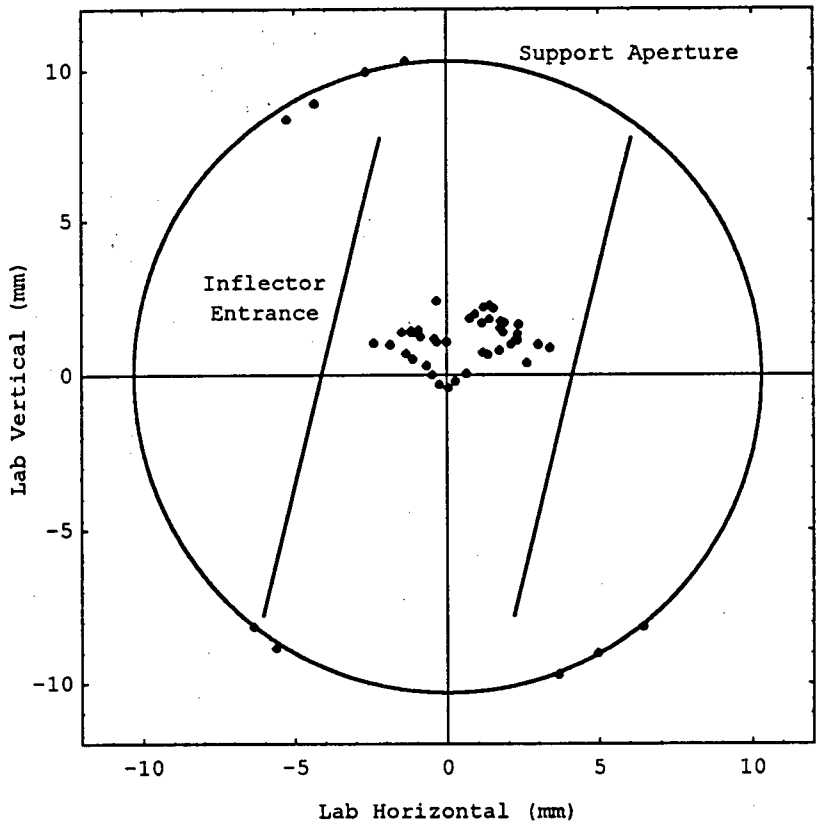

Figure 5.13: *The beamlet centroid locations at the inflector entrance scintillator position. The beam is traveling into the page.*

The (x, y) central ray coordinates for the full beam are estimated to be (0.6 ± 0.3 mm, 1.0 ± 0.3 mm) in the lab system of coordinates. These full beam coordinates were obtained using the average position of the beamlet centroids corrected for the initial vertical offset imposed upon the beamlets by the collimator (refer to Figure 5.15). Recall that the system tune used for this beam was the one which transported the most beam to 1.125 MeV. This implies that a slight miscentering of the beam at the inflector entrance is necessary to minimize beam loss further on in the acceleration process. In reference [28] it was observed that fringe fields push the central ray off the axis of the inflector, so an initial miscentering as shown in Figure 5.14 is necessary to compensate for the fringe field effect, in particular.

In order to obtain a better estimate for the extent of the full beam than can be achieved using Figure 5.13, the beamlet outlines, at the minimum gray level threshold for each beamlet, were overlaid on the inflector entrance plot in Figure 5.14. This plot illustrates that the full beam size is approximately 7.5 mm horizontally and 5.0 mm vertically. The assembled beamspot in Figure 5.14 shows no obvious tilt. This indicates that the solenoid effect of the axial bore, at least with respect to the approximate full beam envelope shown, has compensated for the tilt of the quadrupole magnets.

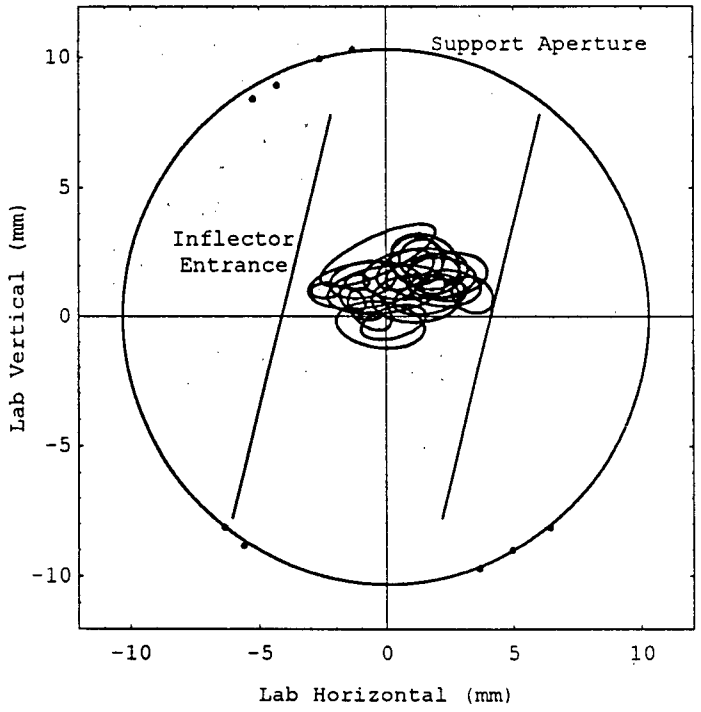

Figure 5.14: *Beamlet perimeter outlines at the inflector entrance scintillator position. The beam is traveling into the page.*

5.3 PHASE SPACE SELECTION USING THE BEAMLET COLLIMATOR

One of the fundamental concepts of linear charged particle beam transport is that the central ray of a beam, which experiences no losses, will remain the central ray of the beam throughout the system. In particular, this central ray will be located at the center of the four dimensional phase space hypervolume as well as being located at the area centroid of any two dimensional projection of the beam. With respect to beam collimation this means that the central ray for a beamlet passes through the center or area centroid of the collimation hole which forms the beamlet. Similarly, the central ray for the beamlet must pass through the area centroid of the beamlet image at a scintillator. This is useful for two reasons. First, a mapping can be established between the input central rays from each collimated beamlet and the central rays of each beamlet at each scintillator position, enabling one to study the optical effects imparted to the rays by the system. Second, this study of the central rays can be accomplished without requiring the scintillator light output to be linear with respect to the beam intensity.

The vertical collimator aperture positions were vertically centered at 8.0 mm, 3.0 mm, −2.0 mm, −7.0 mm, and −12.0 mm with respect to the beam vertical axis. It would have been aesthetically pleasing to have had the collimator apertures centered about the vertical origin of the beam, however, this would not have gained any additional information and would have been very time consuming to achieve. Figure 5.15 illustrates the locations of the collimator apertures from which beam could actually be transported to the scintillators. The centers of the apertures define the (x, y) phase space coordinates of the central ray of each beamlet at the collimation point. Note that no useful beamspots were obtained using the y = −12.0 mm row of beamlets.

Although the beam was actually axially symmetric at the collimation point, the aperture positions shown in Figure 5.15 define a tilted elliptical region through which beam was transported to the system. The reason for this was that the quadrupoles were tilted with respect to the lab axes, and even very divergent particles aligned with the focusing axis of the first quadrupole Q0 passed through the system. However, those particles that were fairly divergent and aligned with the defocusing axis of Q0 were lost on the injection system beampipe. Note that the 4rms beam envelope safely passes through the system.

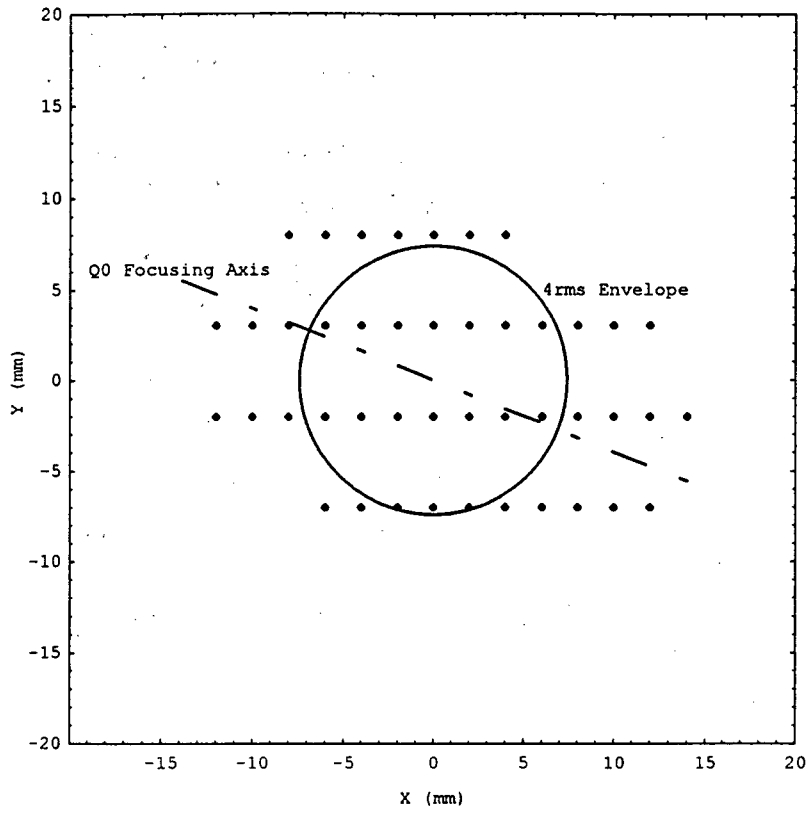

Figure 5.15: *The (x, y) beamlet central ray coordinates selected by the collimator. Figure 5.2 shows the collimation device which selected the beamlets in this figure. The beamlets are traveling out of the page.*

The (x', y') coordinates of the central rays of each beamlet are more difficult to determine than the (x, y) coordinates. However, a reasonable estimation of these coordinates can be obtained by noting that at the left, right, top and bottom extremum of each of the 2.0 mm diameter collimator apertures, two of the four phase space parameters are fixed, namely x and y, and that x' and y' can each be individually maximized or minimized within the four dimensional beam ellipse. The four dimensional beam ellipse at the collimator position is given by

$$1 = \frac{x^2 - 2Lxx'}{\sigma_{11}} + (x')^2\left(\frac{L^2}{\sigma_{11}} + \frac{1}{\sigma_{22}}\right) + \frac{y^2 - 2Lyy'}{\sigma_{33}} + (y')^2\left(\frac{L^2}{\sigma_{33}} + \frac{1}{\sigma_{44}}\right) \qquad (5.1)$$

where L is the 335 mm drift length from the ion source waist to the collimator, $\sigma_{11} = \sigma_{33} = 6.25$ mm^2 are the squares of the beam half sizes containing 95% of the beam at the ion source waist, and $\sigma_{22} = \sigma_{44} =$ 2025 mrad^2 are the squares of the beam divergence half angles containing 95% of the beam at the ion

source waist. With x and y already given at the aperture extremum points, equation 5.1 becomes a quadratic equation in x' and y' from which the minimum or maximum x' and y' can be determined. By finding y'_{max} at the top of the aperture and y'_{min} at the bottom of the aperture, y' for the central ray can be found by averaging these values. A similar calculation yields x' for the central ray. Following this procedure for each collimator aperture position yields a full set of central ray coordinates (x, x', y, y') for the collimator apertures. This calculation depends on reasonable values for L, σ_{11}, σ_{22}, σ_{33} and σ_{44}, which were obtained from the emittance scanner outputs associated with Figures 4.16a and 4.17.

Figures 5.16 and 5.17 depict the regions of phase space which the beamlet centroids occupy at the collimator. Plots containing either x' or y' data are actually very slightly non-linear. However, as can be seen , the curves are so close to linear that the data shall be described as being in lines, for purposes of discussion. Thus, if the injection system is a linear transport system, one would expect these phase space lines formed at the collimator to be transported into lines at the scintillator positions.

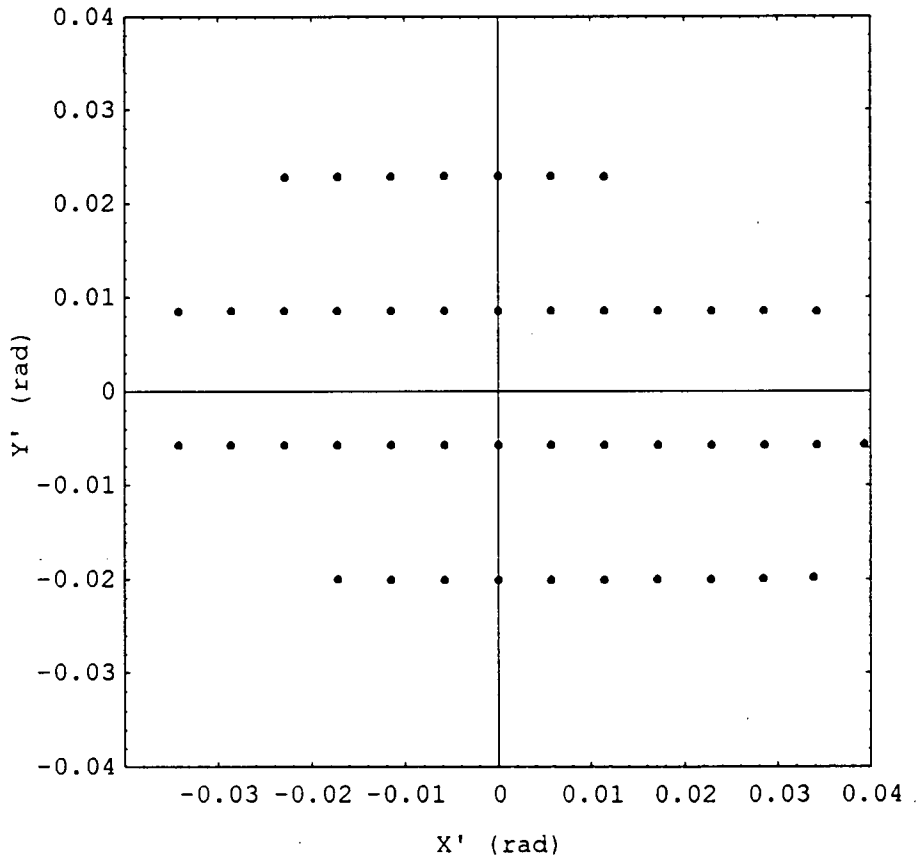

Figure 5.16: *The (x', y') beamlet central ray coordinates selected by the collimator.*

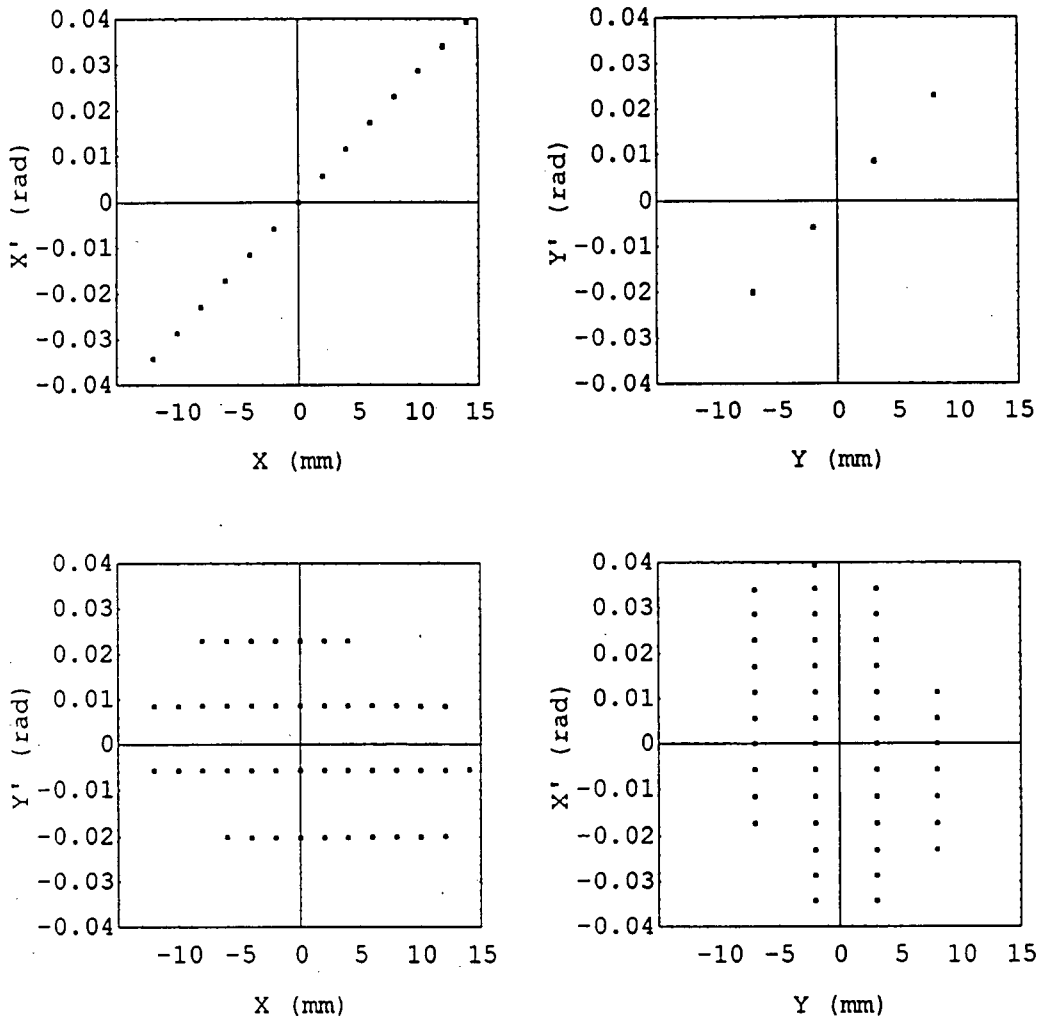

Figure 5.17: *The (x, x'), (y, y'), (x, y') and (y, x') beamlet central ray coordinates selected by the collimator.*

5.3.1 THE BEAM INTENSITY DISTRIBUTION AT THE BEAMLET COLLIMATOR

The beamlet scintillator experiments were not intended to study the intensity distribution of the beam. The experiments were designed to investigate phenomena related to the beamlet's area centroid coordinates. Nevertheless, beamlet intensity data was available from the scintillator experiments, and it can be used in a limited study of the beam's intensity distribution at the collimator position.

The relationship between the actual beam current intensity distribution and the captured scintillator output intensity is important to establish. Since these experiments were not designed to investigate this relationship, it must be determined in a circuitous manner. The only avenue available for

determining this relationship was to compare the beam's horizontal intensity profile measured by the emittance scanner to one deduced from the scintillator measurements. The procedure for this is as follows:

- optically transport the emittance scanner horizontal intensity profile of Figure 4.16b from the scanner position to the collimator position. Plot the resultant profile normalized with respect to its peak.
- associate the integrated gray level of each beamlet measured at the half-turn scintillator position with the beamlet's original coordinates at the collimator position (refer to Figure 5.15).
- fit a gaussian curve to the integrated gray level intensities associated with each (y) coordinate at a given (x) position, and then compute the area under this curve. This area corresponds to the empirically determined beam intensity at (x).
- plot the empirically determined intensity distribution from the scintillator data normalized with respect to the peak.
- compare the beam's horizontal intensity profile from the scanner to the one from the scintillator data.

Figure 5.18 shows the two intensity profiles. It is apparent that the two profiles compare favourably at the peak and at the tails. However, the intensities from the scintillator profile are up to a factor of three larger than the scanner based intensities between the peak and tail positions of the profile.

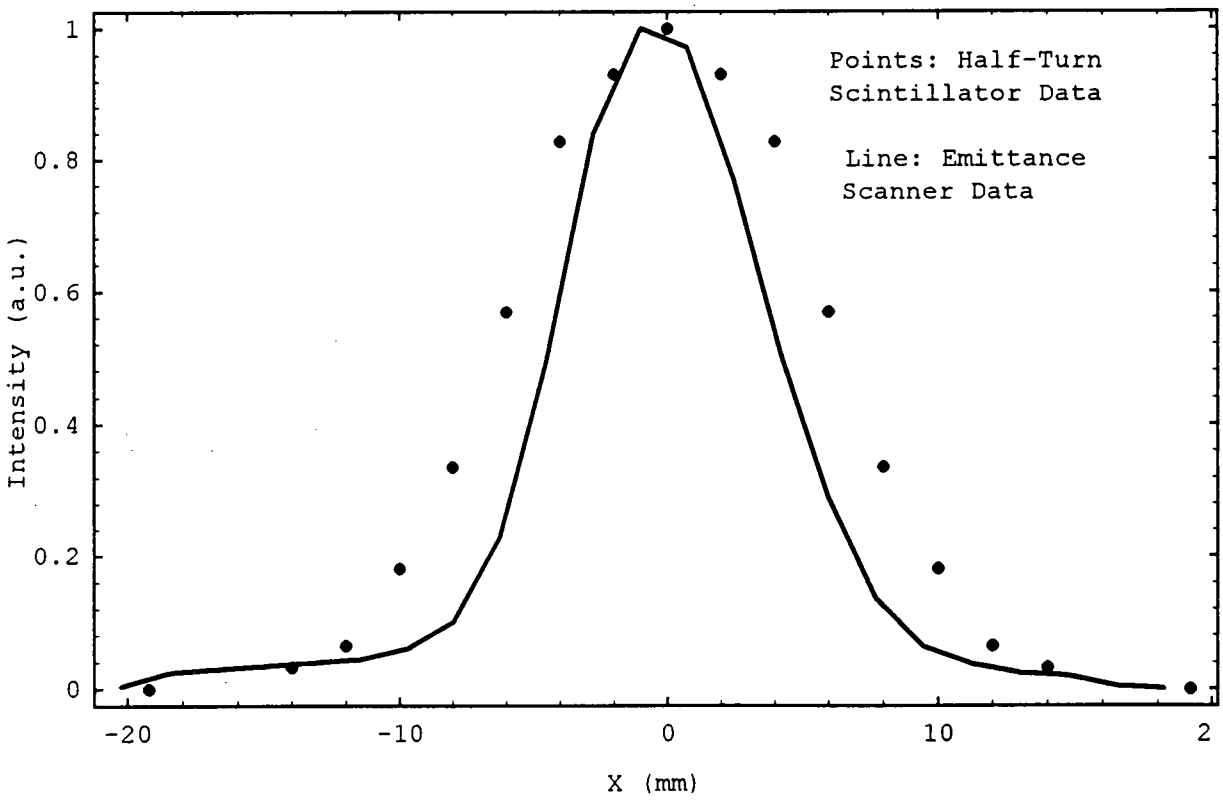

Figure 5.18: *Two normalized horizontal beam intensity profiles at the beamlet collimator. One based on emittance scanner data and the other based on the integrated gray level data associated with each beamlet at the half-turn scintillator position.*

There are a number of possible reasons for the differences between the profiles in Figure 5.18, such as:

- the actual intensity distribution was not sufficiently sampled by the scintillator method.
- the intensity distribution measured by the emittance scanner was uncollimated, whereas the intensity distribution measured by the scintillator method was partially collimated by the injection system.
- all the scintillator data were not measured at the same time. The data were measured over a period of days. Thus, slight tuning shifts could have caused the actual intensity profile to drift slightly with time.
- each beamlet was uniquely focused at the scintillator. Therefore, some beamlet images may have been tightly focused and saturated, whereas others may have had diffuse beamspots with some intensity lost in the background.
- the relationship between the scintillator data and the actual beam intensity may simply be non-linear in the current density regime investigated.

To properly assess the effectiveness of the scintillator method for deducing the beam intensity distribution, all of the beam's intensity should be sampled. This could be done through the use of closely spaced moveable slit collimators, or through the use of a pinhole collimator which is capable of sampling the whole beam. No collimation should be allowed between the sampling point and the scintillator. Immediately after measuring each beamlet with the scintillator, the scintillator should be retracted and the beamlet's current should be measured using a Faraday cup. A complete set of beam intensity measurements should be taken during one experimental session.

The intensity distribution constructed from the total integrated gray values obtained from beamlet images must be compared to the distribution constructed from the Faraday cup readings. A transfer function should be established relating the scintillator based intensity distribution to the one measured using the Faraday cup. If focusing elements were present between the sampling point (collimator location) and the measurement point (scintillator location), the effect of variations in beamlet focusing on the transfer function must be determined.

Using the scintillator output to produce beam intensity plots permits a rare opportunity to display the beam intensity distribution as a function of both x and y. Figure 5.19 illustrates such a plot at the beamlet collimator position based again on half-turn scintillator data. The data was smoothed using the Kriging procedure described in section 4.7.3. The beam appears axially asymmetric in agreement with Figure 5.15. The beam contours are centered reasonably well about the origin except for the very peak of

the beam intensity, which is off-centered. The beam is shown to have a reasonably uniform central core with no large valleys or other anomalies.

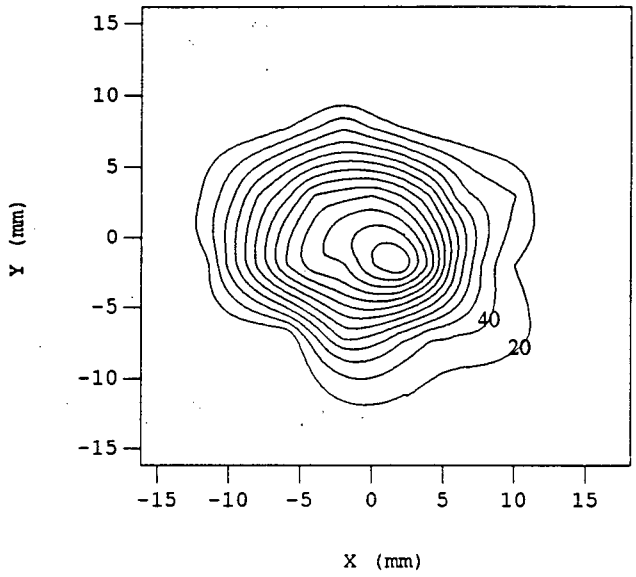

Figure 5.19: *A contour plot of the (x, y) intensity profile of the beam at the beamlet collimator position based on half-turn scintillator data. The intensity contour levels are given in arbitrary units.*

The beamspot size and the ion current density for a particular beamlet was different at each scintillator due to the optics of the injection system. This meant that if beam profiles generated from data obtained from different scintillators were the same, confirmation of a reasonably linear relationship between current density and captured light intensity would be established. Figures 5.20 and 5.21 show the beam intensity profiles generated from data from each of the three scintillators, respectively, as a function of the beamlet central ray (x, x') and (y, y') coordinates at the beamlet collimator position. The curves replicate the same shape fairly well. However, they certainly are not identical. The differences between these curves are similar to the differences seen in Figure 5.18.

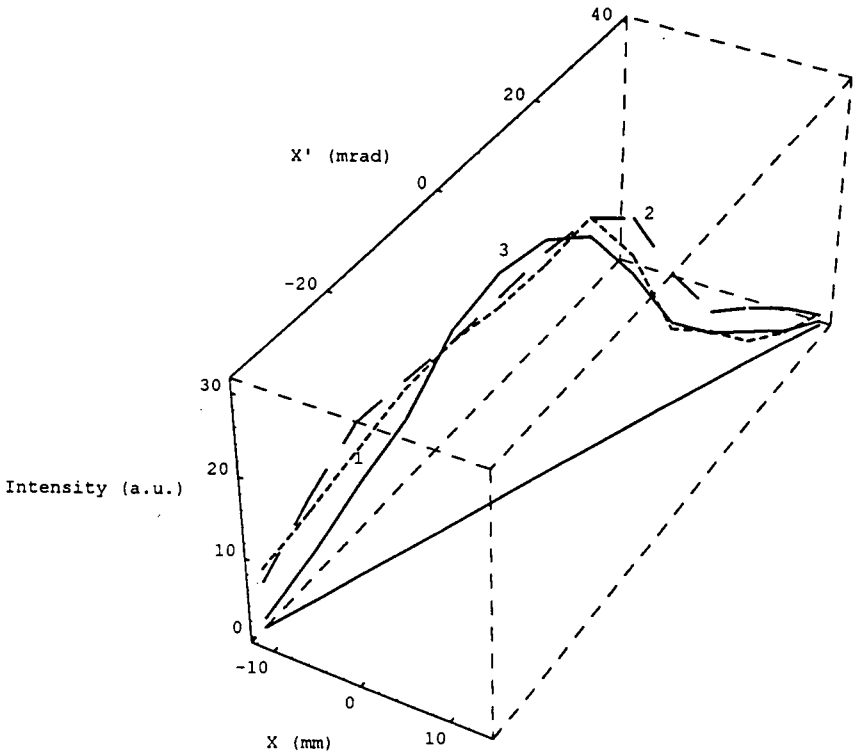

Figure 5.20: *A comparison of beam intensity profiles as a function of (x, x') at the beamlet collimator position. Curve 1 was constructed from the inflector entrance scintillator data, curve 2 was constructed from the inflector exit scintillator data, and curve 3 was constructed from the half-turn scintillator data. The intensity is given in arbitrary units.*

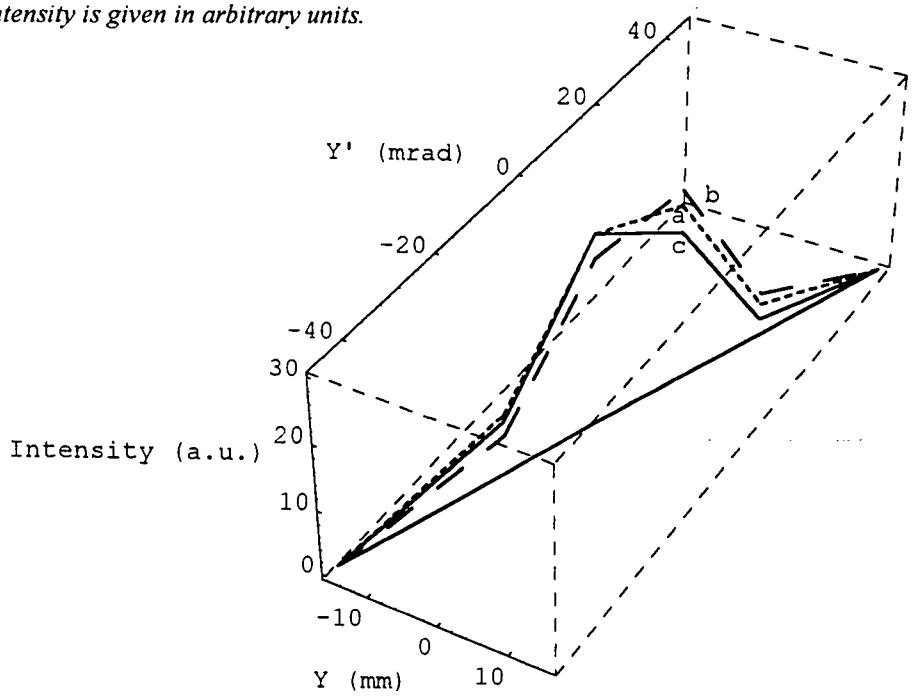

Figure 5.21: *A comparison of beam intensity profiles as a function of (y, y') at the beamlet collimator position. Curve (a) was constructed from the inflector entrance scintillator data, curve (b) was constructed from the inflector exit scintillator data, and curve (c) was constructed from the half-turn scintillator data. The intensity is given in arbitrary units.*

5.4 LINEAR INJECTION SYSTEM SPECIFICATION USING MEASURED CONSTRAINTS

5.4.1 BEAMLET CENTROID PLOTS AT EACH SCINTILLATOR

If beam transport for the system can be described as linear, the lines of (x, y) beamlet centroids selected by the beamlet collimator should remain as lines in (x, y) space after transport to downstream points. Similarly the equi-spacing and parallelism of the lines should also be preserved. Having said this, lines of beamlet centroids may not be observed at the scintillator positions, and the resultant curves that are measured may not be equi-spaced and parallel. There are four main reasons why the beamlet centroids could be shifted from a linear, equi-spaced and parallel arrangement. The centroids could be shifted due to

(a) non-linear effects.
(b) partial collimation of the beamlet by the injection system beampipe.
(c) measurement error.
(d) variations in the system tune over time.

Figures 5.22, 5.23 and 5.24 show the (x, y) centroid curves at the inflector entrance, the inflector exit and at the half-turn scintillator, respectively. The individual curves correspond to beamlets extracted from the Y = 8 mm, 3 mm, −2 mm or −7 mm rows of apertures on the beamlet collimator. The (x, y) coordinates are those of the optical transport coordinate system and may not correspond to the regular lab or camera coordinate systems. Recall that (x, y, z) is a right-handed coordinate system, and that (z) points in the direction of the velocity vector of the central ray as described in section 2.1.2.1.

The central stretch of each curve in 5.22, 5.23 and 5.24 is quite linear, and lines computed using linear regression have been included for comparison. Only the linear portions of each curve were used in the linear regression calculations. At first glance the non-linear centroid placement at the end of each beamlet curve is somewhat disturbing. However, this phenomenon is primarily due to (b) above, and when this occurs, the partially collimated beamlet travels with respect to a new central ray which can be substantially different than the original central ray of the beamlet.

Each measured line of centroid data for a particular scintillator has the same general slope. However, these slopes are certainly not identical. This indicates that the equi-spacing and parallelism of the curves was not perfectly preserved. This result was primarily due to the fact that each line of

experimental data was collected during different experimental sessions, in which the system parameters might have varied slightly from the nominal settings. Since the injection system tune was rather sensitive (refer to section 4.7.7), noticeable changes in the slope of the lines can be observed.

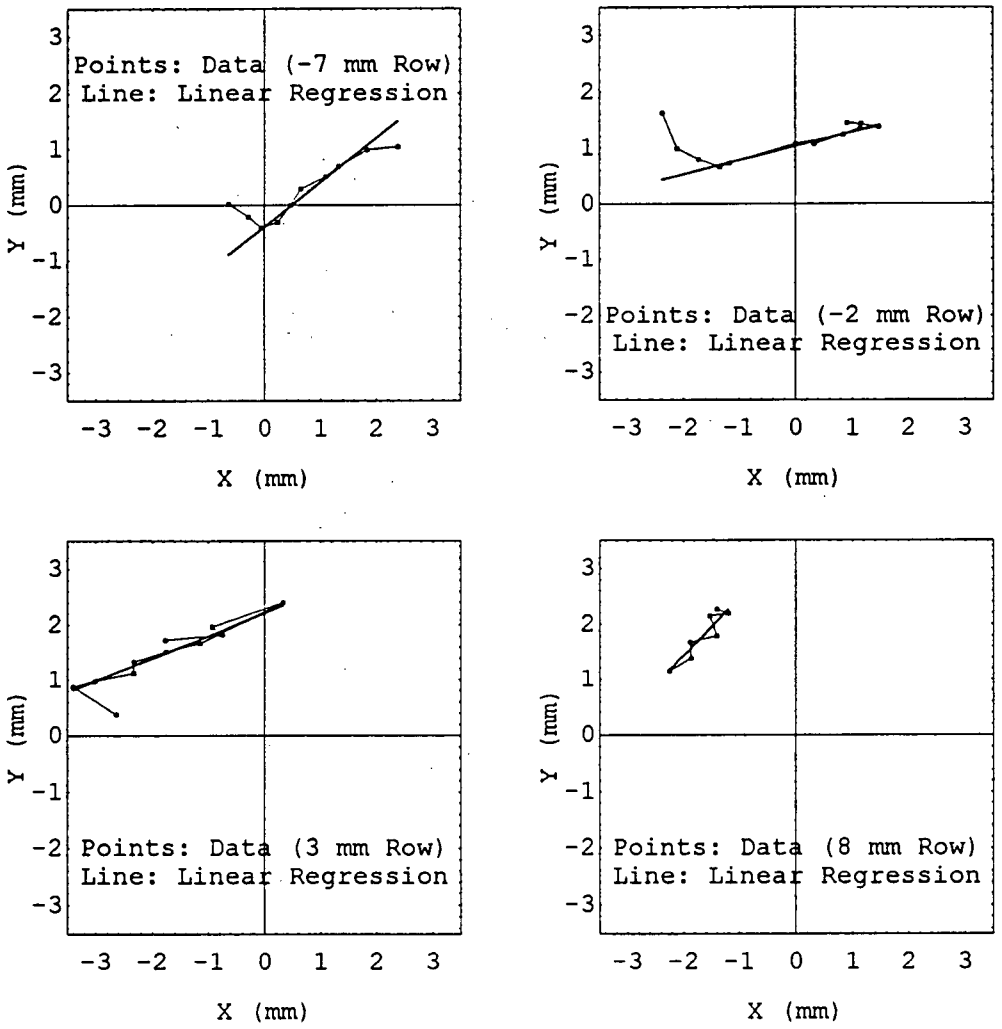

Figure 5.22: *Beamlet (x, y) centroid curves at the inflector entrance scintillator given in the beam optical coordinate system. Each curve corresponds to a horizontal row of beamlets generated at the beamlet collimator. The positive (x) end of each curve was generated on the positive (x) side of the beamlet collimator.*

In terms of using these curves to compute empirical constraints for the linear system simulations, the linear portions of the Y = 3 mm and −2 mm curves at each scintillator are the most trusted. Although the Y = 8 mm and −7 mm curves have linear sections as well, they were likely to have been uniformly

collimated by the injection system beampipe. The Y = 8 mm row of beamlets would likely have been nearly uniformly collimated along their upper edge with varying degrees of collimation on the left or right sides of the outer beamlets of the row. Whereas the Y = −7 mm row of beamlets would have been collimated in a similar manner except along the bottom edge instead of the top edge of the beamlets. The approximately uniform skimming of beam from the top or bottom of these lines of beamlets could have permitted the centroids to be aligned more or less in lines at the scintillators, however the equi-spacing of the lines would have been affected.

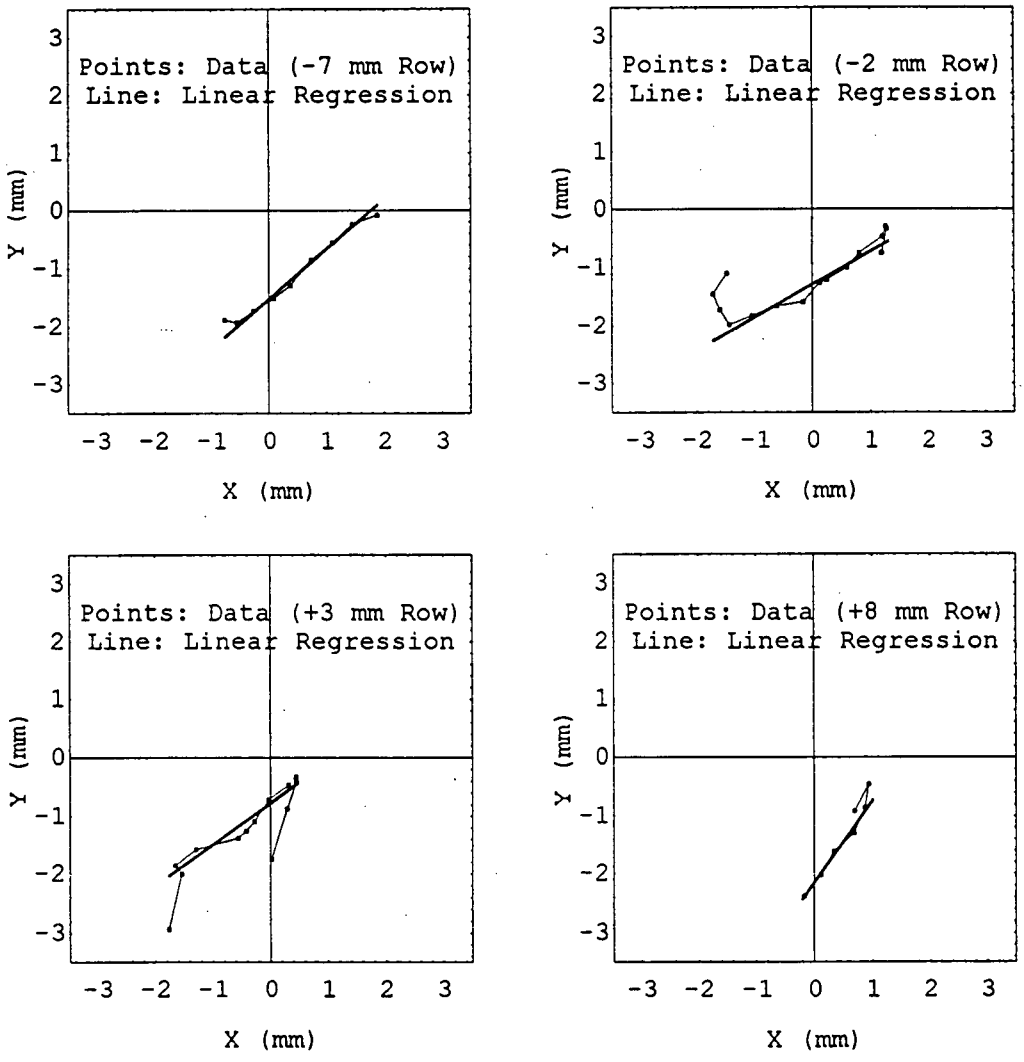

Figure 5.23: *Beamlet (x, y) centroid curves at the inflector exit scintillator given in the beam optical coordinate system. Each curve corresponds to a horizontal row of beamlets generated at the beamlet collimator. The positive (x) end of each curve was generated on the positive (x) side of the beamlet collimator.*

The 4 rms acceptance region of the Y = 3 mm and Y = –2 mm lines of centroids exhibit linear behaviour within the error bounds of this experiment. The error bounds for any given centroid is ±0.1 mm in either x or y. As well, no collimation effects are apparent for the 4 rms region. A last note of interest is that the shapes of the centroid curves defined at the inflector entrance, including the non-linear outer extremities, are largely preserved at the inflector exit and half-turn scintillators.

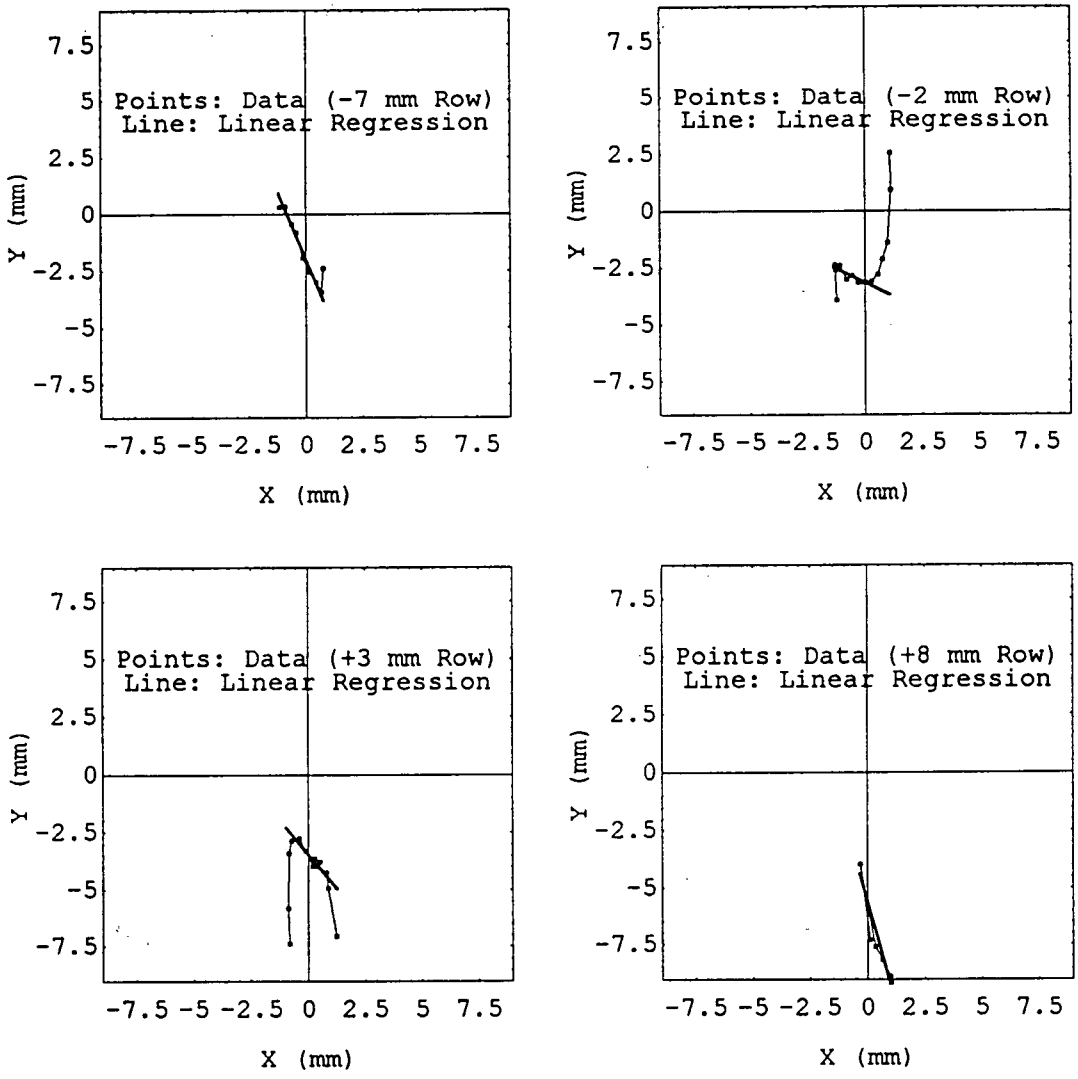

Figure 5.24: *Beamlet (x, y) centroid curves at the half-turn scintillator given in the beam optical coordinate system. Each curve corresponds to a horizontal row of beamlets generated at the beamlet collimator. The positive (x) end of each curve was generated on the negative (x) side of the beamlet collimator.*

5.4.2 LINEAR SYSTEM CONSTRAINTS AND SIMULATIONS

Most of the measured constraints to be met by linear transport modeling are given in terms of beamlet central ray positional or angular displacements at each scintillator location as a function of positional displacements of the beamlet central rays at the collimator position. Altogether 12 measured positional displacement constraints and 12 angular displacement constraints, which are computed from measured quantities, are determined. In addition the full beam major and minor axis lengths and orientation angles at each scintillator position provide another 9 constraints. The 33 constraints provide sufficient data to assign a high level of confidence to the linear transport model which meets them all.

5.4.2.1 Positional Displacement

The positional displacement constraints which can be measured from the beamlet central ray coordinates at each scintillator are $\Delta x_i/\Delta x_{coll}$, $\Delta y_i/\Delta x_{coll}$, $\Delta x_i/\Delta y_{coll}$ and $\Delta y_i/\Delta y_{coll}$. The subscript "i" denotes which scintillator position the displacements were measured at, and the subscript "coll" refers to displacements at the beamlet collimator.

The data from the linear portions of the Y = 3 mm and −2 mm centroid curves in Figures 5.22, 5.23 and 5.24 are considered to be the most reliable in terms of being unaffected by beampipe collimation and were, therefore, used for computing the displacement constraints. These curves are presented together in Figure 5.25 so that a sense of the spacing of the curves with respect to each other can be obtained. At the inflector entrance the linearity, spacing and parallelism between the two curves is quite good. At the inflector exit the linearity of the curves is fairly good but the lines appear to be partially rotated with respect to each other. The half-turn curves are not quite as obviously linear as the curves at the other scintillator positions, and the curves again appear to be somewhat rotated with respect to each other. The manner in which the curves overlap at the half-turn position suggests that under ideal identical conditions the linear curves would be quite close together but parallel.

The linear transport model of the system can be used to derive a computed version of the constraints. First, recall from Figure 5.17 that the (x, x') beamlet central ray coordinates are linearly related to each other at the beamlet collimator position, as are the (y, y') coordinates. The relationship

between these coordinates was deduced using equation 5.1, and at the beamlet collimator the relationship is given by

$$y = 349.5y'$$
$$x = 349.5x' \tag{5.2}$$

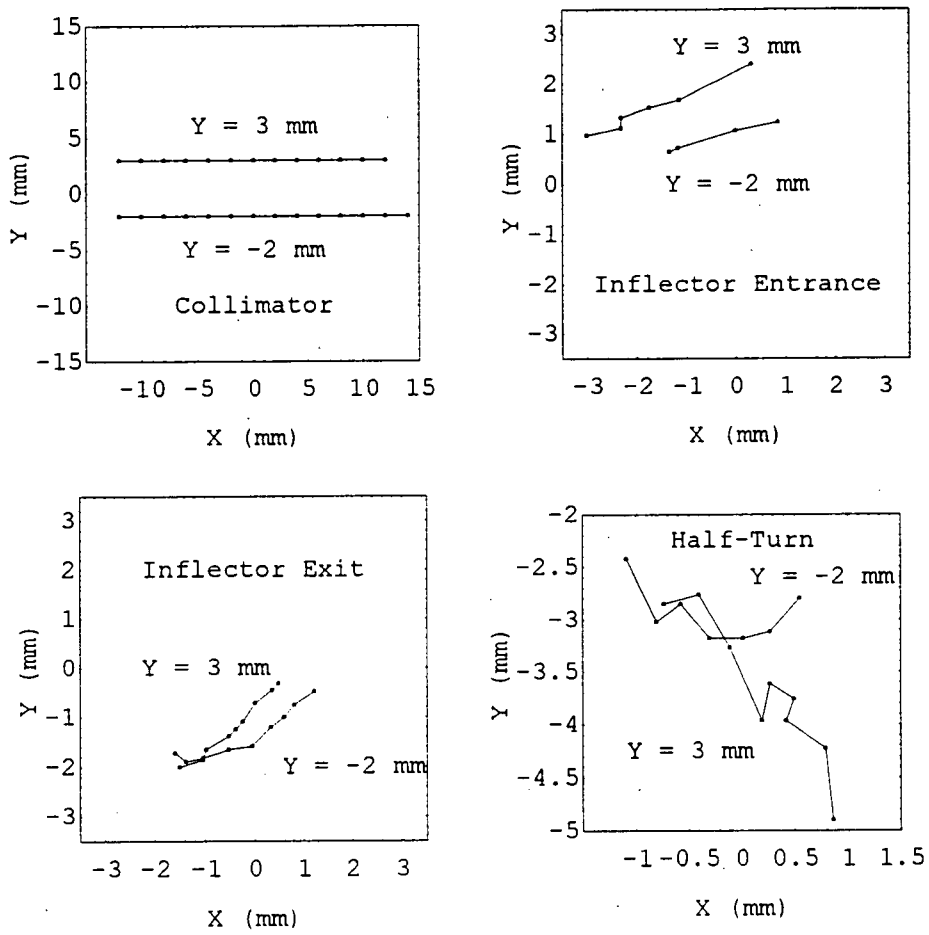

Figure 5.25: *Linear portion of the Y = 3 mm and –2 mm beamlet (x, y) centroid curves at the beamlet collimator, the inflector entrance, the inflector exit and at a half-turn in the beam optical coordinate system. Not all beamlet centroids could be extracted and plotted in the linear portion of the entrance scintillator curves due to background light contamination problems.*

The equations (5.2) can be combined with the linear matrix elements from the beamlet collimator to the inflector entrance, the inflector exit or the half-turn scintillator position to yield the linear transport model's computed positional displacement constraints:

$$\frac{\Delta x_i}{\Delta x_{coll}} = R_{11}^{coll\_i} + \frac{1}{349.5} R_{12}^{coll\_i} \tag{5.3}$$

$$\frac{\Delta y_i}{\Delta x_{coll}} = R_{31}^{coll\_i} + \frac{1}{349.5} R_{32}^{coll\_i} \tag{5.4}$$

$$\frac{\Delta x_i}{\Delta y_{coll}} = R_{13}^{coll\_i} + \frac{1}{349.5} R_{14}^{coll\_i} \tag{5.5}$$

$$\frac{\Delta y_i}{\Delta y_{coll}} = R_{33}^{coll\_i} + \frac{1}{349.5} R_{34}^{coll\_i} . \tag{5.6}$$

where the subscript "i" corresponds to the particular scintillator position of interest and the superscript "coll_i" indicates that the matrix element represents transport from the beamlet collimator to the scintillator position.

The linear simulations undertaken to match the measured constraints involved tweaking system parameters such as the field settings, effective lengths and the center region dipole parameters in order to obtain the best match. This tweaking was required because the system is fairly sensitive to variations in these parameters, and, although the parameters are known to a higher level of accuracy than had been attained by previous experimenters, many of the parameters were only known to within two or three percent.

The constraints extracted from curves in Figure 5.25 are presented in Table 5.3 complete with a listing of the linearly computed constraints. The error in the measured constraints is the statistical standard error, and the error in the linear simulation arises from uncertainty in the 349.5 coefficient in equation 5.2, which in turn comes from the uncertainty in the measured quantities in equation 5.1. The best fit linear system match to the average constraints is very good in all cases except for $\Delta y_{ha}/\Delta x_{coll}$. However, the linearly computed constraint is reasonably close to the measured value obtained from the curve generated from the Y = 3 mm line of centroid data and is, thus, considered acceptable.

The nominal and best fit linear 4Q/C.R.M. injection system representations are given in Table 5.4. The two representations are quite similar but evidence of the aforementioned system tweaking is apparent. The similarity between the representations combined with the good match between the simulated constraints and the measured constraints helps to confirm that the system is well understood.

During the simulation process all three inflector representations mentioned in Figure 5.9 were tested. It is interesting to note that the inflector matrix computed using the relatively simple axial magnetic field map in Figure 5.11 and an analytic electric field resulted in the best fit to the constraints of Table 5.3.

Table 5.3: *The measured positional displacement constraints at each scintillator position and the best fit linear system's estimation of these constraints. The measured constraints were obtained from the Y = 3 mm curve, the Y = –2 mm curve, and the combination of these two curves. The subscripts en, ex, ha and coll refer to entrance, exit, half-turn, and collimator.*

Parameter	**Measured Constraints** Curve Y = 3 mm	**Measured Constraints** Curve Y = –2 mm	**Measured Constraints** Y = 3 and –2 mm	**Best Fit System Value**
$\Delta x_{en}/\Delta x_{coll}$	0.25 ± 0.06	0.16 ± 0.09	0.20 ± 0.06	0.23 ± 0.04
$\Delta y_{en}/\Delta x_{coll}$	0.10 ± 0.02	0.02 ± 0.03	0.06 ± 0.03	0.10 ± 0.01
$\Delta x_{en}/\Delta y_{coll}$			–0.16 ± 0.06	–0.11 ± 0.02
$\Delta y_{en}/\Delta y_{coll}$			0.17 ± 0.07	0.19 ± 0.01
$\Delta x_{ex}/\Delta x_{coll}$	0.12 ± 0.03	0.18 ± 0.02	0.15 ± 0.02	0.14 ± 0.01
$\Delta y_{ex}/\Delta x_{coll}$	0.11 ± 0.02	0.09 ± 0.03	0.10 ± 0.02	0.11 ± 0.01
$\Delta x_{ex}/\Delta y_{coll}$			0.00 ± 0.03	0.03 ± 0.01
$\Delta y_{ex}/\Delta y_{coll}$			0.09 ± 0.01	0.11 ± 0.02
$\Delta x_{ha}/\Delta x_{coll}$	–0.09 ± 0.03	–0.13 ± 0.01	–0.11 ± 0.02	–0.08 ± 0.01
$\Delta y_{ha}/\Delta x_{coll}$	0.15 ± 0.08	0.03 ± 0.06	0.09 ± 0.05	0.24 ± 0.01
$\Delta x_{ha}/\Delta y_{coll}$			0.01 ± 0.02	0.01 ± 0.01
$\Delta y_{ha}/\Delta y_{coll}$			–0.11 ± 0.05	–0.17 ± 0.06

In order to complete the specification of the injection system, the non-standard transport matrices for the axial bore and the inflector must be given. These matrices were obtained using the technique of section 2.1.2.2. These matrices are

$$R_{BORE} = \begin{bmatrix} 0.82630 & 88.801 & -0.41681 & -45.432 \\ -0.007849 & 0.10830 & -0.008022 & -1.3574 \\ 0.41681 & 45.432 & 0.8263 & 88.801 \\ 0.008022 & 1.3574 & -0.007849 & 0.1083 \end{bmatrix} \quad (5.7)$$

and

$$R_{INF} = \begin{bmatrix} 0.211074 & -19.7347 & -0.111844 & 0.0685255 \\ 0.05888 & 1.08267 & 0.00166418 & -1.11298 \\ 0.0581361 & -17.6993 & 0.717573 & 7.08156 \\ -0.0174532 & -1.40525 & 0.062024 & 1.81794 \end{bmatrix} \quad (5.8)$$

where R_{BORE} represents transport through the axial bore of the C.R.M. and R_{INF} represents beam transport through the spiral inflector of the C.R.M.. These two matrices were formulated using the electric and magnetic field representations indicated in Table 5.4, and their dimensions are in millimeters and radians. In order to calculate off-axis magnetic field components from the axial magnetic field map, CASINO automatically invokes the solenoid approximation where

$$B_r = -\frac{r}{2} \cdot \frac{\partial B_z}{\partial z}. \tag{5.9}$$

Refer to Appendix IV for a discussion of the symplectic conditions which matrices (5.7) and (5.8) satisfy.

Note that the "best fit system" description shown in Table 5.4 contains sufficient optical information to allow any researcher to replicate the results of this thesis using standard codes such as TRANSPORT or TRANSOPTR.

Table 5.4: *The charged particle optics layout for the nominal 4Q/C.R.M. injection system and for the best fit 4Q/C.R.M. injection system.*

Optical Parameter	Measured System Values	Best Fit System Values
Initial System Drift Space (mm)	486 ± 5	486.(338)
Beam Rotation Angle (°) *	21.7 ± 0.2	21.7
Q0 Field (kG), Length (mm), Bore (mm)	0.287 ± 0.009 , 96.5 ± 2, 50.0 ± 0.1	0.278(0061), 95.9(238), 50.0
Drift Space (mm)	38.5 ± 4	40.5(769)
Q1 Field (kG), Length (mm), Bore (mm)	−0.51 ± 0.02, 96.5 ± 2, 50.0 ± 0.1	−0.49(35294), 93.1(224), 50.0
Drift Space (mm)	38 ± 4	41.(3327)
Q2 Field (kG), Length (mm), Bore (mm)	0.56 ± 0.02, 96.5 ± 2, 50.0 ± 0.1	0.55(09074), 93.4(122), 50.0
Drift Space (mm)	38.5 ± 4	40.5(769)
Q3 Field (kG), Length (mm), Bore (mm)	−0.53 ± 0.02, 96.5 ± 2, 50.0 ± 0.1	−0.50(99514), 95.6(340), 50.0
Beam Rotation Angle (°) *	−21.7 ± 0.2	−21.7
Drift Space(mm)	20.0 ± 2	20.4(83)
$\mathbf{R}_{BORE}$: B Field File	MAP29_DIGI.ZFLD	MAP29_DIGI.ZFLD
Beam Rotation Angle (°) **	−14.0 ± 0.1	−14.0
$\mathbf{R}_{INF}$: B Field File	T32_I_SMALL.ZFLD	MAP29_DIGI.ZFLD
$\mathbf{R}_{INF}$: E Field File	RELAX_014.DAT	Analytic
Dipole to Exit Scintillator: θ (°), ρ (mm), υ_x, υ_y ***	5 ± 2, 19.6 ± 0.3, 1.07 ± 0.02, 0.39 ± 0.02	3.0, 19.6, 1.07(2380), 0.37(41657)
Exit to Half-Turn Scintillator: θ (°), ρ (mm), υ_x, υ_y ***	145 ± 5, 19.6 ± 0.3 1.07 ± 0.02, 0.39 ± 0.02	152, 19.6, 1.07(2380), 0.37(41657)

* Beam rotation simulates entry and exit into rotated quadrupoles.
** Beam rotation simulates entry into the tilted inflector entrance.
*** Mild flutter is experienced at this radius.

5.4.2.2 Angular Displacement

In section 5.4.2.1 the best fit linear transport system for the 12 positional displacement constraints was determined. Thus, best fit transport matrices between each of the scintillator positions were determined. This provides a means for generating the 12 angular displacement constraints at each of the scintillator positions using measured displacements and the best fit transport matrices.

Suppose that the positional and angular displacement constraints with respect to a displacement change in x at the collimator were known at scintillator "i". The positional and angular displacement constraints with respect to a displacement change in x at the collimator could then be computed at scintillator "j" as described in equation 5.10. A similar equation can be constructed for displacement constraints that are a function of a displacement change in y at the collimator. Consider "i" to be the entrance scintillator position and "j" to be the exit scintillator position. In section 5.4.2.1 a best fit linear matrix between "i" and "j" was determined and the positional displacement constraints were presented. Substituting these quantities into 5.10 yields a linear system of four equations in four unknowns, namely the four angular displacement constraints, all of which can be solved for. Using this technique, a set of angular displacement constraints can be generated at each of the scintillator positions.

$$\begin{pmatrix} \Delta x_j / \Delta x_{coll} \\ \Delta x'_j / \Delta x_{coll} \\ \Delta y_j / \Delta x_{coll} \\ \Delta y'_j / \Delta x_{coll} \end{pmatrix} = \begin{pmatrix} R^{ij}_{11} & R^{ij}_{12} & R^{ij}_{13} & R^{ij}_{14} \\ R^{ij}_{21} & R^{ij}_{22} & R^{ij}_{23} & R^{ij}_{24} \\ R^{ij}_{31} & R^{ij}_{32} & R^{ij}_{33} & R^{ij}_{34} \\ R^{ij}_{41} & R^{ij}_{42} & R^{ij}_{43} & R^{ij}_{44} \end{pmatrix} \bullet \begin{pmatrix} \Delta x_i / \Delta x_{coll} \\ \Delta x'_i / \Delta x_{coll} \\ \Delta y_i / \Delta x_{coll} \\ \Delta y'_i / \Delta x_{coll} \end{pmatrix} \tag{5.10}$$

The linear transport system estimation of these constraints is done with the following set of equations

$$\frac{\Delta x'_i}{\Delta x_{coll}} = R^{coll\_i}_{21} + \frac{1}{349.5} R^{coll\_i}_{22} \tag{5.11}$$

$$\frac{\Delta y'_i}{\Delta x_{coll}} = R^{coll\_i}_{41} + \frac{1}{349.5} R^{coll\_i}_{42} \tag{5.12}$$

$$\frac{\Delta x'_i}{\Delta y_{coll}} = R^{coll\_i}_{23} + \frac{1}{349.5} R^{coll\_i}_{24} \tag{5.13}$$

$$\frac{\Delta y'_i}{\Delta y_{coll}} = R^{coll\_i}_{43} + \frac{1}{349.5} R^{coll\_i}_{44}, \tag{5.14}$$

where the subscript i corresponds to the particular scintillator position of interest and the superscript coll_i indicates that the matrix element represents transport from the beamlet collimator to the scintillator position.

Table 5.5 lists the angular displacement constraints computed from the positional displacement constraints of section 5.4.2.1, and the section 5.4.2.1 best fit linear system's estimation of these constraints. Again there is excellent agreement between the constraints and the linear system's estimation of the constraints. The uncertainties in the angular constraints are derived from the uncertainties in the positional constraints from which they were computed. The uncertainty in the linear system values arise from uncertainty in the 349.5 coefficient in equation 5.2.

Table 5.5: *The angular displacement constraints derived from measurements at each scintillator position and the best fit linear system's estimation of these constraints. The subscripts en, ex, ha and coll refer to entrance, exit, half-turn, and collimator.*

Parameter	**Constraints Computed Using R^{en_ex} (radians/mm)**	**Constraints Computed Using R^{en_ha} (radians/mm)**	**Constraints Computed Using R^{ex_ha} (radians/mm)**	**Best Fit System Value (radians/mm)**
$\Delta x'_{en}/\Delta x_{coll}$	-0.005 ± 0.002	-0.005 ± 0.001		-0.004 ± 0.001
$\Delta y'_{en}/\Delta x_{coll}$	-0.003 ± 0.009	-0.005 ± 0.004		-0.003 ± 0.001
$\Delta x'_{en}/\Delta y_{coll}$	0.001 ± 0.003	0.000 ± 0.001		0.0002 ± 0.0001
$\Delta y'_{en}/\Delta y_{coll}$	$-0.01(2) \pm 0.01$	-0.013 ± 0.007		-0.014 ± 0.001
$\Delta x'_{ex}/\Delta x_{coll}$	0.008 ± 0.008		0.006 ± 0.008	0.012 ± 0.002
$\Delta y'_{ex}/\Delta x_{coll}$	0.002 ± 0.009		-0.001 ± 0.002	0.001 ± 0.001
$\Delta x'_{ex}/\Delta y_{coll}$	$0.00(4) \pm 0.01$		0.002 ± 0.009	0.008 ± 0.001
$\Delta y'_{ex}/\Delta y_{coll}$	$-0.00(4) \pm 0.01$		-0.004 ± 0.001	-0.006 ± 0.001
$\Delta x'_{ha}/\Delta x_{coll}$		-0.012 ± 0.005	-0.008 ± 0.008	-0.013 ± 0.002
$\Delta y'_{ha}/\Delta x_{coll}$		0.001 ± 0.002	0.001 ± 0.002	0.004 ± 0.001
$\Delta x'_{ha}/\Delta y_{coll}$		-0.005 ± 0.007	-0.002 ± 0.009	-0.009 ± 0.001
$\Delta y'_{ha}/\Delta y_{coll}$		-0.004 ± 0.002	-0.004 ± 0.002	-0.006 ± 0.001

5.4.2.3 Full Beam

As a check on the validity of the "best fit" system, the 4rms beam envelope and a beam envelope encompassing 99% of the beam's particles were transported through to the inflector entrance, exit and

half-turn scintillator positions from the ion source waist. The term 99% is used as a synonym for "effectively all of the beam including halo". The specifications for the 4rms envelope at the ion source waist are given in Tables 4.6 and 4.7. The maximum half-width of 3.4 mm, and the maximum half-divergence of 50 mrad used for the 99% beam envelope comfortably contain the phase space region occupied by the beam in Figures 4.16a and 4.17.

Figure 5.26 shows the 4rms and 99% beam envelopes overlaid on the beamlet centroids at the inflector entrance scintillator. Beam transport for these envelopes assumed 100% transmission. The 99% beam envelope represents the outermost limits of the beam halo, and, therefore, it is reassuring that the measured extents of the beam from Figure 5.20 are contained within this envelope. It is also encouraging to note that the simulated beam envelopes show very little (x, y) coupling as observed in Figure 5.20.

The simulations make it clear that a fraction of the outer beam envelope would be intercepted by the inflector entrance electrodes if they were not protected by a collimator. This is noticed in practice where approximately 1% of the beam is intercepted by the inflector entrance collimator (refer to Table 4.10). The simulations also make it clear that the 86% of the beam that is contained within the 4rms envelope is comfortably smaller than the inflector entrance aperture.

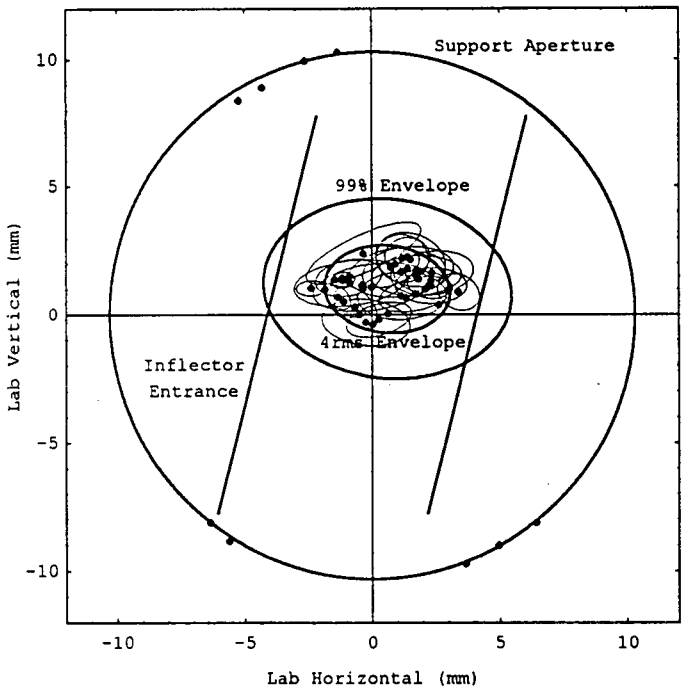

Figure 5.26: *Simulated beam envelopes overlaid on the beamlet centroid locations at the inflector entrance scintillator position. The beam is traveling into the page.*

To determine whether second order quadrupole effects or beampipe collimation affected the full beam envelope at the inflector entrance the beam transport code ZGOUBI [76] was used. Two runs were performed. One in which beampipe collimation was inactive, and one with beampipe collimation active. Both runs initiated an 8000 particle beam at the ion source waist position that had a gaussian intensity distribution. Figure 5.27 gives the scatter plot for the case where no collimation is present and Figure 5.28 gives the scatter plot where beampipe collimation is present. Both plots agree with Figure 5.26, and the main difference between Figures 5.27 and 5.28 is that the uncollimated beam is generally more intense. The collimated beam is slightly smaller, as well, but there are no distinct collimated edges to be seen. Obviously, sufficient blending of the beam has occurred to obscure any distinct edges imposed by collimation.

Figure 5.29 and 5.30 show the 4rms and 99% beam envelopes overlaid on the measured beam envelopes from Figure 5.8 at the inflector exit and half-turn scintillator positions, respectively. Although the measured beam envelopes contain an undetermined amount of the beam, they are nicely bound, at the proper orientation, by the simulated 99% beam envelope. Similarly, the measured envelopes contain the simulated 4rms envelopes which is also reassuring. The optical threshold used on the measured beam envelopes is, thus, shown to yield an optically useful beam spot that is midway between the 4rms and 99% beam envelopes. ZGOUBI computed scatter plots were also obtained at the inflector exit and half-turn scintillator positions. They did not illustrate any information beyond what Figure's 5.27 and 5.28 revealed for the inflector entrance, so they are not included.

The agreement between the measured full beam and simulated full beam plots is quite impressive. Considering that when the nominal system settings and CASINO representations were used, the resultant beam spots had major axis angles off by up to 90° and beam sizes that could be off by as much as 10 mm. In fact, a good match to the full beam sizes could not be obtained, through system tweaking, without first matching to the measured constraints. Once the constraints were met, the full beam match was automatic. This in itself helps to verify that the best fit simulated system provides a very good representation of reality.

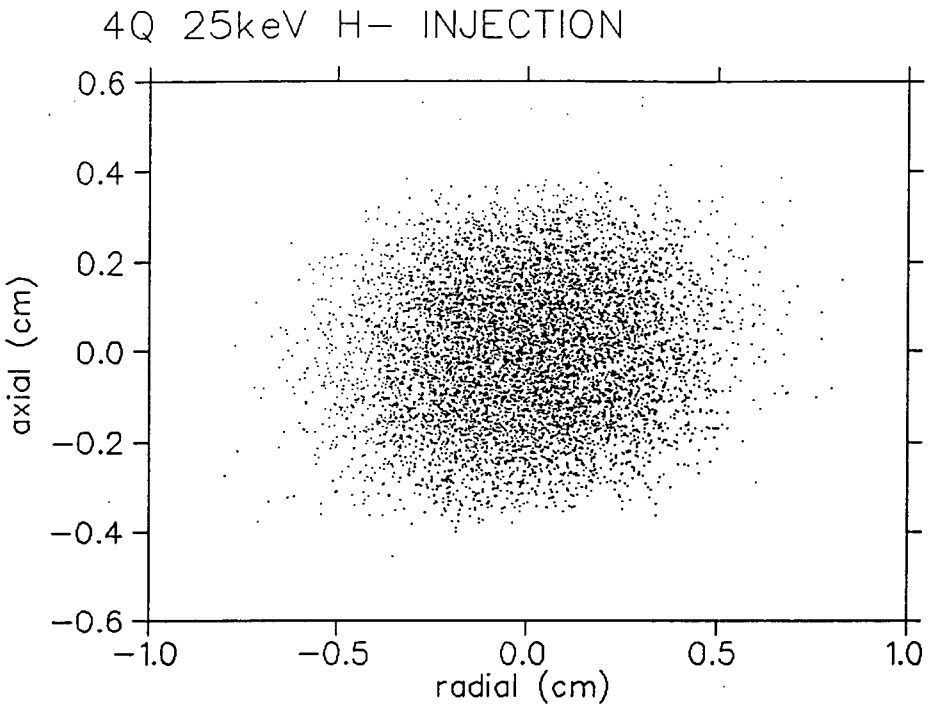

Figure 5.27: *ZGOUBI computed scatter plot of the beam at the inflector entrance. Second order quadrupole effects have been enabled but beampipe collimation has not. The beam is traveling out of the page. The radial and axial axes correspond to the curvilinear (x, y) axes.*

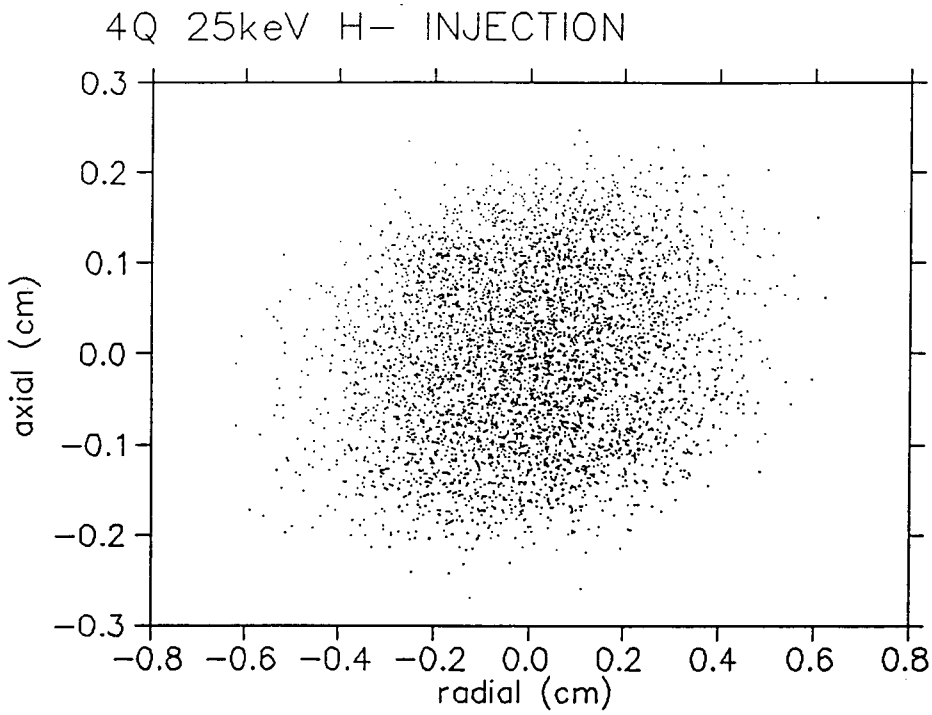

Figure 5.28: *ZGOUBI computed scatter plot of the beam at the inflector entrance. Second order and beampipe collimation effects have both been enabled. The beam is traveling out of the page. The radial and axial axes correspond to the curvilinear (x, y) axes.*

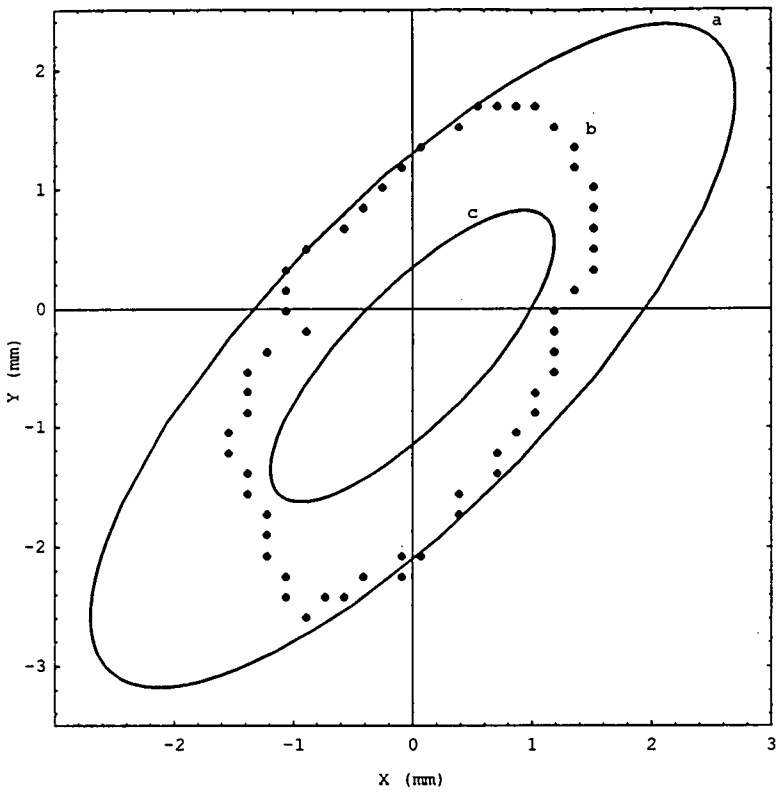

Figure 5.29: *Simulated beam envelopes overlaid on the measured full-beam outline at the inflector exit scintillator position. Curve (a) is the 99% beam envelope, curve (b) is the measured beam envelope, and curve (c) is the 4rms beam envelope. The beam is traveling out of the page.*

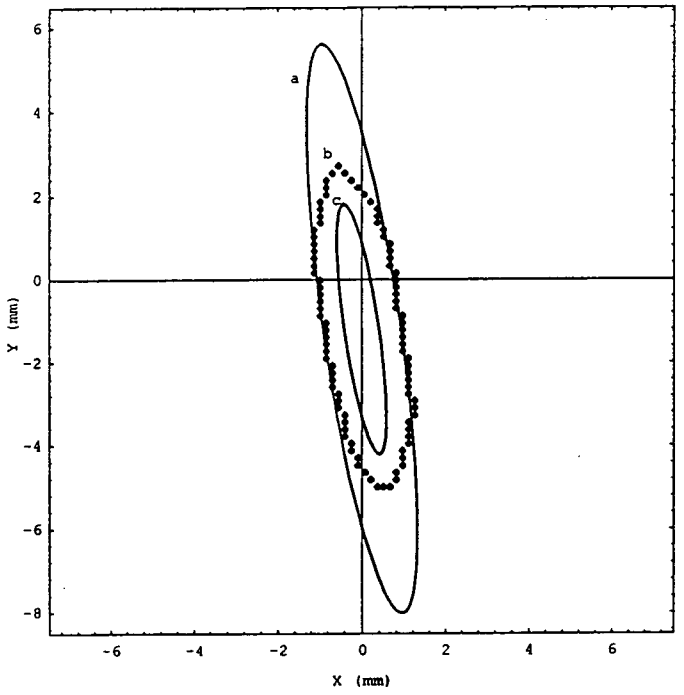

Figure 5.30: *Simulated beam envelopes overlaid on the measured full-beam outline at the half-turn scintillator position. Curve (a) is the 99% beam envelope, curve (b) is the measured beam envelope, and curve (c) is the 4rms beam envelope. The beam is traveling out of the page.*

Table 5.6 provides a listing of the measured and simulated beam dimensions and orientations for reference. The measured beam dimensions contain between 86% and 99% of the beam.

Table 5.6: *Measured and simulated full beam characteristics at the three scintillator positions.*

BEAM TYPE & POSITION	Minor Axis Length (mm)	Major Axis Length (mm)	Major Axis to X Axis Angle (°)
Measured Entrance Beam	5.0 ± 0.2	7.5 ± 0.2	0 ± 5
Simulated 4rms Entrance Beam	3.4	5.0	–6 *
Simulated 99% Entrance Beam	7.8	11.2	–6 *
Measured Exit Beam	2.5 ± 0.2	4.5 ± 0.2	55 ± 10
Simulated 4rms Exit Beam	1.1	3.2	46
Simulated 99% Exit Beam	2.5	7.3	46
Measured Half-Turn Beam	1.8 ± 0.2	7.5 ± 0.2	–81 ± 3
Simulated 4rms Half-Turn Beam	0.8	6.1	–82
Simulated 99% Half-Turn Beam	1.8	13.8	–82

* This angle is with respect to the Lab Horizontal axis as shown in Figure 5.26.

5.4.2.4 Summary

The linear matching of the simulated transport matrix constraints to the measured constraints was successful. The level of confidence associated with the resultant "best fit" system representation is much higher than has ever been attained by previous researchers including those at other laboratories. Under normal circumstances the original nominal system representation would have resulted in a poor representation of reality. This section of the thesis also showed that, within the limits of the experimental error, transport is linear for the 4rms beam envelope, and the 4rms envelope is free of collimation.

5.5 THE (X, X') AND (Y, Y') PHASE SPACE REGIONS AT EACH SCINTILLATOR POSITION

The constrained linear system representation of the injection system will provide an excellent approximation to the full beam phase space ellipse in the (x, x') and (y, y') planes at each of the scintillator positions. In addition, the technique of section 5.4.2.2 can be used to obtain the complete set of (x, x', y, y') central ray coordinates for each beamlet at each scintillator position. These measurement based coordinates can then be compared to the linearly simulated phase ellipses. If the comparison shows good agreement the emittance growth from the ion source waist to each of the scintillator positions due to

cross-plane coupling can be determined. Using these results, a good estimate of the accelerated circulating emittance can be made and subsequently compared to the measured emittances of Chapter 4.

5.5.1 MEASURING THE BEAM PHASE SPACE COORDINATES IN THE CENTRAL REGION

The cyclotron center region is a cramped place, even if RF structures and center ground electrodes are removed. The lack of space combined with the overwhelming influence of the cyclotron magnetic field precludes the use of a phase space scanner, such as is used in the injection line, for measuring the phase space characteristics of the beam in the vicinity of the inflector exit. However, a useful method has been formulated for making such measurements at the inflector exit.

This method is simply an extension of the technique developed in section 5.4.2.2 and has three requirements. First, the (x, y) central ray coordinates of a beamlet must be measurable at the inflector exit. Second, the (x, y) coordinates for these beamlets must be measurable at another location downstream of the inflector exit, say at the half-turn position. Third, the transport matrix between the inflector exit position and the half-turn position must be known. This matrix is known for most cyclotrons because the magnetic field must be very well known for the machine to function properly. If these conditions are met, a set of four equations with four unknowns can be solved to obtain the divergence components of the inflector exit beamlet central ray coordinates (x_{ex}, x'_{ex}, y_{ex}, y'_{ex}) and of the half-turn beamlet central ray coordinates (x_{ha}, x'_{ha}, y_{ha}, y'_{ha}). Since magnetic midplane symmetry is maintained through the first half-turn, the off-diagonal sub-matrices of the transport matrix are occupied by zeros yielding the following simple solution to the problem

$$\begin{pmatrix} x'_{ex} \\ x'_{ha} \\ y'_{ex} \\ y'_{ha} \end{pmatrix} = \begin{pmatrix} -R_{11}^{ex\_ha}/R_{12}^{ex\_ha} & 1.0/R_{12}^{ex\_ha} & 0.0 & 0.0 \\ R_{21}^{ex\_ha}-R_{11}^{ex\_ha}\cdot R_{22}^{ex\_ha}/R_{12}^{ex\_ha} & R_{22}^{ex\_ha}/R_{12}^{ex\_ha} & 0.0 & 0.0 \\ 0.0 & 0.0 & -R_{33}^{ex\_ha}/R_{34}^{ex\_ha} & 1.0/R_{34}^{ex\_ha} \\ 0.0 & 0.0 & R_{43}^{ex\_ha}-R_{33}^{ex\_ha}\cdot R_{44}^{ex\_ha}/R_{34}^{ex\_ha} & R_{44}^{ex\_ha}/R_{34}^{ex\_ha} \end{pmatrix} \bullet \begin{pmatrix} x_{ex} \\ x_{ha} \\ y_{ex} \\ y_{ha} \end{pmatrix} . \quad (5.15)$$

With respect to the first two requirements, the technique used to measure the beamlet (x, y) central ray coordinates discussed in section 5.1.6 can be used. Note that the exit scintillator can be withdrawn without altering any of the system parameters. This ensures that the radial and axial coordinates from the two scintillator positions truly correspond to each other. The third requirement can be met by computing the

transport matrix through the first half-turn using paraxial rays computed using a standard field map and the program CYCLONE. The sources of error for this technique originate from uncertainties in the axial and radial trajectory start and end points, the (x, y) centroid coordinates and the magnetic field map. The transport matrix can also be determined by calculating the field index seen by the beam over the first half-turn (use Figure 5.10) and by using equations 2.31, 2.32, 2.33 and 2.34. The sources of error for this technique arise from uncertainties in the azimuthal angle traveled by the beam, the (x, y) centroid coordinates, the field strength, the radius of curvature and the field index. The match between the matrices computed by these two techniques was quite good. Therefore, the latter analytical technique was used in practice as it was more amenable to being adjusted, which was necessary for obtaining the best linear system match to the constraints.

Figure 5.31 shows the measurement based (x, x') and (y, y') phase space coordinates at the inflector exit and half-turn scintillator positions with the full beam 4rms and 99% phase space ellipses overlaid for comparison. In addition, a polygon which bounds the outermost beamlet centroids from Figures 5.15, 5.16 and 5.17 was transported to the scintillator positions, and is also shown in Figure 5.31. Note that the individual coordinates of each beamlet are not expected to uniformly inhabit the whole of the 99% phase ellipses, as the original beamlets did not uniformly cover all of the beam's phase space region at the collimator in the first place. However, the beamlets are expected to uniformly cover the area within the bounding polygon, and this is the case within the limits of experimental error. Thus, the best fit linear system (Table 5.4) has again provided a reasonable simulation of the system.

As described previously, the determination of the measurement based phase space coordinates at the inflector exit and half-turn positions can be obtained without any knowledge of beam transport through the inflector. However, the same cannot be said for determining these coordinates at the inflector entrance. In this case the (x, y) coordinates of the beamlets at both the inflector entrance and exit must be known, as well as the transport matrix through the inflector. Fortunately, all of these conditions were satisfied in section 5.4. This permits measurement based phase space coordinates to also be determined for the inflector entrance. Figure 5.32 shows the inflector entrance phase space coordinates with the 4rms and 99% phase space beam envelopes and the beamlet's bounding polygon overlaid. The match between the

polygon and the beamlet phase space coordinates coordinates is fairly good, and the beam envelopes encompass the polygon and the beamlet centroids reasonably well.

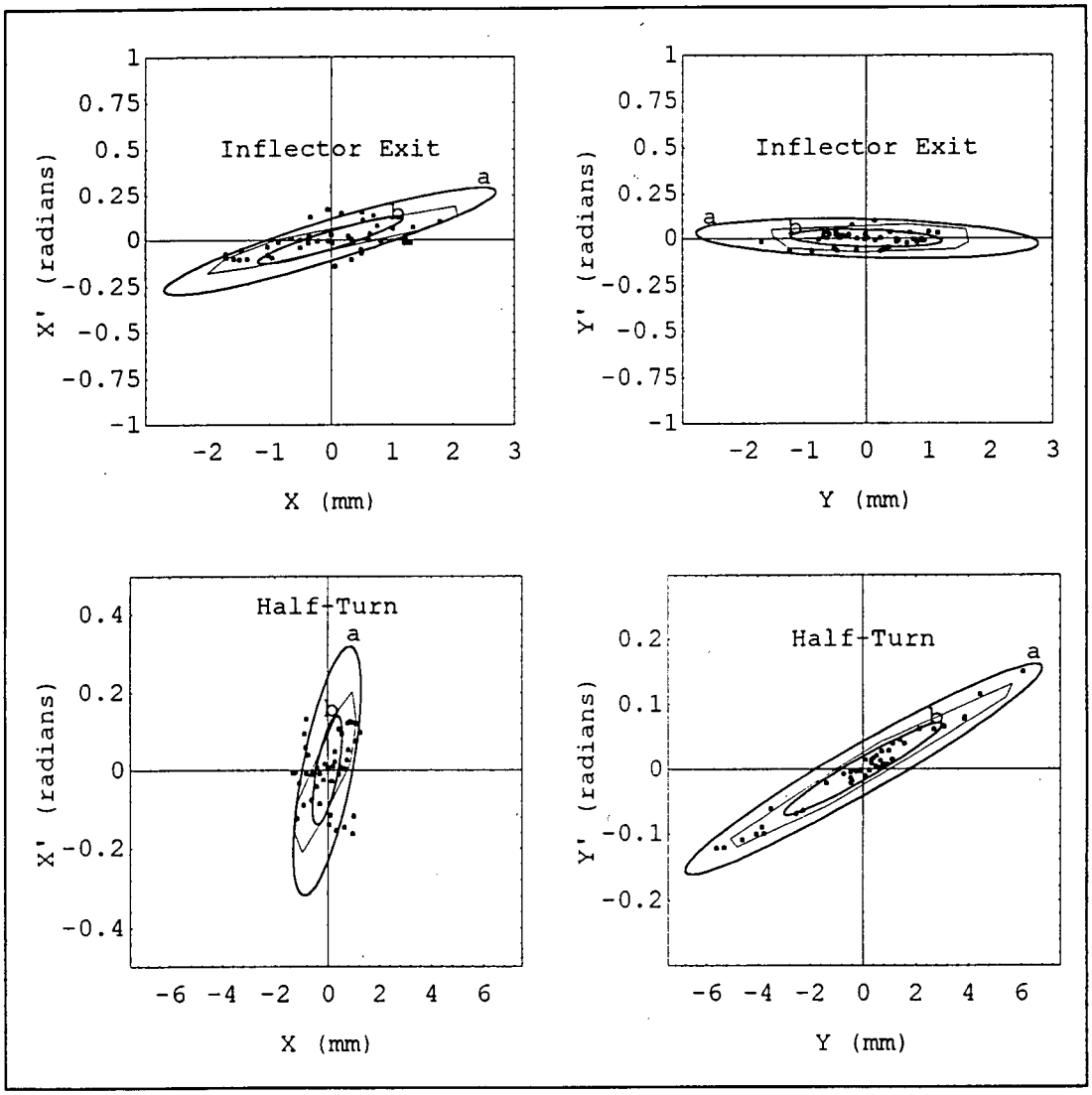

Figure 5.31: *The measurement based phase space coordinates of the beamlets at the inflector exit and half-turn scintillator positions overlaid with linearly simulated 4rms (curve b) and 99% (curve a) beam envelopes and a transported polygon which initially bounded the beamlets at the collimator.*

The best fit phase space ellipses in Figures 5.31 and 5.32 are quite important. This importance arises because phase space ellipses of this type are what are normally used by simulation software for accelerated beam studies, and because these ellipses are the first to have been checked against measured data from the immediate vicinity of a cyclotron inflector.

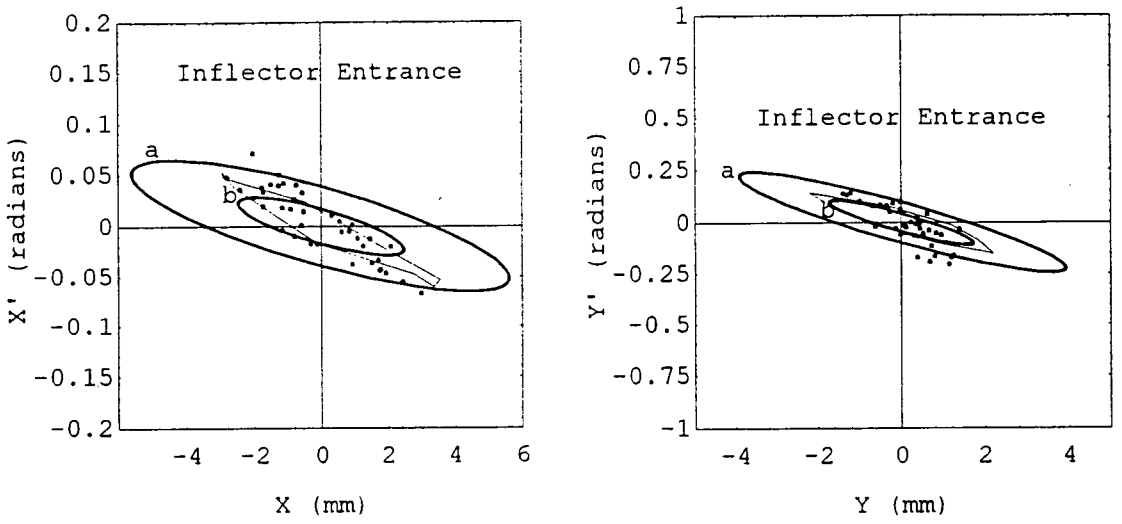

Figure 5.32: *The measurement based phase space coordinates of the beamlets at the inflector entrance scintillator position overlaid with linearly simulated 4rms (curve b) and 99% (curve a) beam envelopes and a transported polygon which initially bounded the beamlets at the collimator.*

5.5.2 EMITTANCE GROWTH DUE TO CROSS-PLANE COUPLING

In section 5.4 it was found that beam transport, at least for the 4rms beam, was linear to within experimental error. This indicates that emittance growth due to non-linear focusing by either the quadrupole magnets or the inflector, for the case of the 4rms beam, is quite small. The emittance growth due to cross-plane coupling is, however, very evident. The resultant (x, x') and (y, y') normalized emittances at each scintillator position and at the ion source waist are tabulated in Table 5.7, as well as the emittance growth factor.

Before analyzing Table 5.7 let's remind ourselves of what the data is representing. First of all, the emittances at each scintillator position are simply proportional to the area of the appropriate phase ellipses in Figures 5.31 and 5.32. These phase ellipses were obtained using the best fit linear system described in Table 5.4. The beam being characterized in Table 5.4 is the one which experimentally provided the best beam transmission to 1.125 MeV for an arc current of 6.4 amperes as described in Tables 4.17 and 5.1. Therefore, the emittance and emittance growth data in Table 5.7 are very important as they correspond to the actual optimal system tune.

It is also important to understand how the emittance data in Table 5.7 corresponds to the various coordinate systems used in this thesis. First of all, the emittances have been computed with respect to the coordinates (x, x') and (y, y'), where (x, y, z) form the curvilinear coordinate system illustrated in Figure 2.1. As a reminder of how the curvilinear coordinate system is aligned with the other coordinate systems used in this thesis consider the following:

- At the ion source waist and at the inflector entrance scintillator position, the (x, y) axes are aligned with and are in the direction of (the negative of the lab horizontal axis, the lab vertical axis), as described in Figure 2.17. The (z) axis points in the direction of the velocity vector of the beam's central ray.
- At the inflector exit scintillator position, the (x, y) axes are aligned with and are in the direction of (*h*, *-u*), as described in Figure 2.18. In addition, the (x) axis is in the median plane and points towards the center of curvature, and the (z) axis is in the median plane and points in the direction of the velocity vector of the beam's central ray.
- At the half-turn scintillator position, the (x) axis is in the median plane and points towards the center of curvature, the (z) axis is in the median plane and points in the direction of the velocity vector of the beam's central ray, and the (y) axis points in the direction necessary for (x, y, z) to form a right-handed coordinate system as illustrated in Figure 2.1.

At the ion source waist the beam emittances are uncoupled, and they were measured to be 0.24 mm-mrad in both the (x, x') and (y, y') phase planes, as reported in Tables 4.6 and 4.7. Due to the cross-plane coupling introduced by the rotated quadrupole magnets and the magnetic field of the cyclotron's axial bore, the emittances in the (x, x') and (y, y') phase planes at the inflector entrance scintillator position have grown. This is not an unexpected development when cross-plane coupling occurs, as is reported by Brown and Servranckx in [55] where the following statement is made:

> "If the initial emittances in the *x* and *y* planes at the beginning of a system are uncoupled and are equal to each other, then at any point downstream the projected *x* and *y* emittances will always be equal to each other, independent of the magnitude of the *x-y* coupling at that point. Their magnitudes may, however, be equal to or greater than the values of the initial, uncoupled emittances"

Contrary to this statement, it is clear from Table 5.7 that the emittance growth is not equal in each phase plane at the inflector entrance scintillator position. This anomaly is addressed by Baartman and Kleeven in [45]. The work of [55] assumes that (x, x') and (y, y') are sets of canonically conjugate variables. However, in [45] it is noted that at a position such as where the inflector entrance scintillator is located, midway through a solenoidal magnetic field, (x, x') and (y, y') are **not** sets of canonically conjugate variables. Consequently, emittance growth can be unequal in each phase plane, as shown in Table 5.7.

Baartman and Kleeven [45] also point out that once transport through to the inflector exit has been reached, then (x, x') and (y, y') are again sets of canonically conjugate variables. This is because transport through the axial bore and inflector fields has been completed and the dipole field of the cyclotron has been entered. Consequently, the emittances at the inflector exit scintillator position should exhibit balanced emittance growth as described in [55]. This is essentially true in Table 5.7, where the differences between the (x, x') and (y, y') emittances give an indication of the error associated with their computation.

Table 5.7: *The measured ion source waist 4rms emittance as per Table 4.7 and Table 4.8, and the 4rms emittances at each scintillator position as per Figures 5.31 and 5.32. The resultant emittance growth factor with respect to the ion source emittance at each scintillator position is listed for comparison.*

BEAM POSITION	Normalized 4rms Emittance (mm-mrad)	Emittance Growth Factor
Ion Source Waist (x, x')	0.24	–
Ion Source Waist (y, y')	0.24	–
Inflector Entrance (x, x')	0.31	1.3
Inflector Entrance (y, y')	0.55	2.3
Inflector Exit (x, x')	0.44	1.8
Inflector Exit (y, y')	0.41	1.7
Half-Turn (x, x')	0.44	1.8
Half-Turn (y, y')	0.41	1.7

No emittance growth is exhibited between the inflector exit scintillator position and the half-turn scintillator position, as no cross-plane coupling exists for the cyclotron's dipole magnetic field (with flutter) between these positions.

Refer to Appendix IV for a further discussion of canonical transport variables.

5.5.3 THE CIRCULATING EMITTANCE

So far we have established that emittance growth due to machine imposed non-linearity's is effectively zero for the 4rms beam. We have not specifically investigated the effects of space charge. However, given that a linear simulation matches the full beam images, the space charge effects cannot be large. In fact, it is already known that space charge is not an important factor for the TR30 where the

injected beam current is 2.5 times as large as in these experiments. The major contributing factors to emittance growth then are the cross-plane coupling effect introduced in the previous section and the, yet to be discussed, mixing of RF phases which yields the final circulating emittances. Additional emittance growth due to miscentered beam or to resonances during acceleration are dealt with in [111].

The circulating emittance in both the axial and radial phase planes can be computed using equation 3.1, as was done in sections 4.7.2 and 4.7.3. Equation 3.1 assumes that the cyclotron can be approximated as a weak focusing dipole with appropriate average radial and axial tunes. Table 5.8 gives the circulating emittance for a nominal TR type cyclotron using this approximation, as well as several measured emittances from TR type cyclotrons. One can see from Table 5.8 that there is rough agreement on the emittance values. Close agreement is not expected as the ion sources and injection systems were not identical for each machine.

Table 5.8: *The calculated or measured emittances at the inflector exit or circulating within several of the TR type cyclotrons.*

PARAMETER *	**Circulating (x, x') Plane**	**Circulating (y, y') Plane**
Normalized 4rms Emittance (mm-mrad)	3**	1**
Normalized C.R.M. 2σ Emittance @ 1 MeV (mm-mrad)***	3.0 ± 0.5	3 ± 2
Normalized TR13 Emittance @ 13 MeV (mm-mrad) [25]	1.5 ± 1	4 ± 1
Normalized TR30 Emittance @ 30 MeV (mm-mrad) [112]	2 ± 1	2 ± 1

* Strictly speaking, the emittance is the determinant of the beam sigma matrix (equation 2.19), where an emittance is read as "ε" mm-mrad. However, many authors include a π such that the very same quantity is read as "ε" π-mm-mrad. The addition of the π is meant to "clearly" indicate that the digits correspond to an emittance and not to an area. Unfortunately, the whole expression corresponds to an area with the insertion of π, so confusion is not wholly avoided.

** These circulating emittances are based on a nominal cyclotron with R_{cyc} = 19.6 mm, ν_x = 1.03, ν_y = 0.333 and $\beta\gamma$ = 0.0073. These values are appropriate for the C.R.M., the TR13 and the TR30.

*** Based on L155/PL10.8/EL10/NL ion source configuration. Data is from Chapter 4.

5.6 CENTER REGION BEAM DISPLACEMENT AS A FUNCTION OF THE MAGNETIC FIELD

The TR13's central magnetic field was originally predicted to be up to 10% lower than in the TR30 or the C.R.M., yet the very same inflector and central region electric focusing structure was to be

used for it. Under these circumstances it was very important that the beam centering not be greatly affected by the magnetic field so that the beam passes through the various center region apertures unimpeded. Also, during the commissioning of cyclotrons it is sometimes found that the commissioned RF frequency can be off by a fraction of a percent. This requires the cyclotron magnetic field to be adjusted to maintain isochronism. Another important issue that is pertinent to all of the TR type cyclotrons is the degree of radial re-centering that can be accomplished through magnetic field changes. This is important for obtaining balanced dual beam extraction at the outer radius of a particular machine. Further complicating the radial centering issue is the coupling of radial phenomena into the axial phase plane by the inflector. This causes small but measurable axial centering changes to be induced by magnetic field changes. This can result in axial emittance growth and beam loss in the axial plane.

Having established that it is important to know how the beam is displaced as a result of magnetic field perturbations, one should also note that it is important to verify CASINO's ability to simulate these effects. Figure 5.33 shows the measured results. The beam displacements for this plot were repeated eight times. Six different beamlets and two low current full beams were used. The error bars represent the standard error for these eight measurements. The (x', y') displacements were obtained using the technique of section 5.5.1. Also remember that the radius of curvature vector points in the opposite direction of the (x) coordinate.

The strong radial dependence of the beam with magnetic field is expected, however, the fairly strong axial dependence is somewhat surprising. Figure 5.34 compares the measured displacements to two CASINO simulations. CASINO simulation B shows agreement in the radial displacement. Both simulation B and C do not show agreement with the measured axial displacement. This could be attributed to the beam being off-centered at the inflector entrance as shown in Figure 5.13. Normally the full beam centroid at the entrance will not move off axis if the axial bore magnetic field changes, however, with the beam off axis to start with, a change in the magnetic field causes the full beam centroid to rotate about the cyclotrons axial bore axis. Such a rotation could place the full beam centroid along a trajectory which is axially off-nominal at the inflector exit.

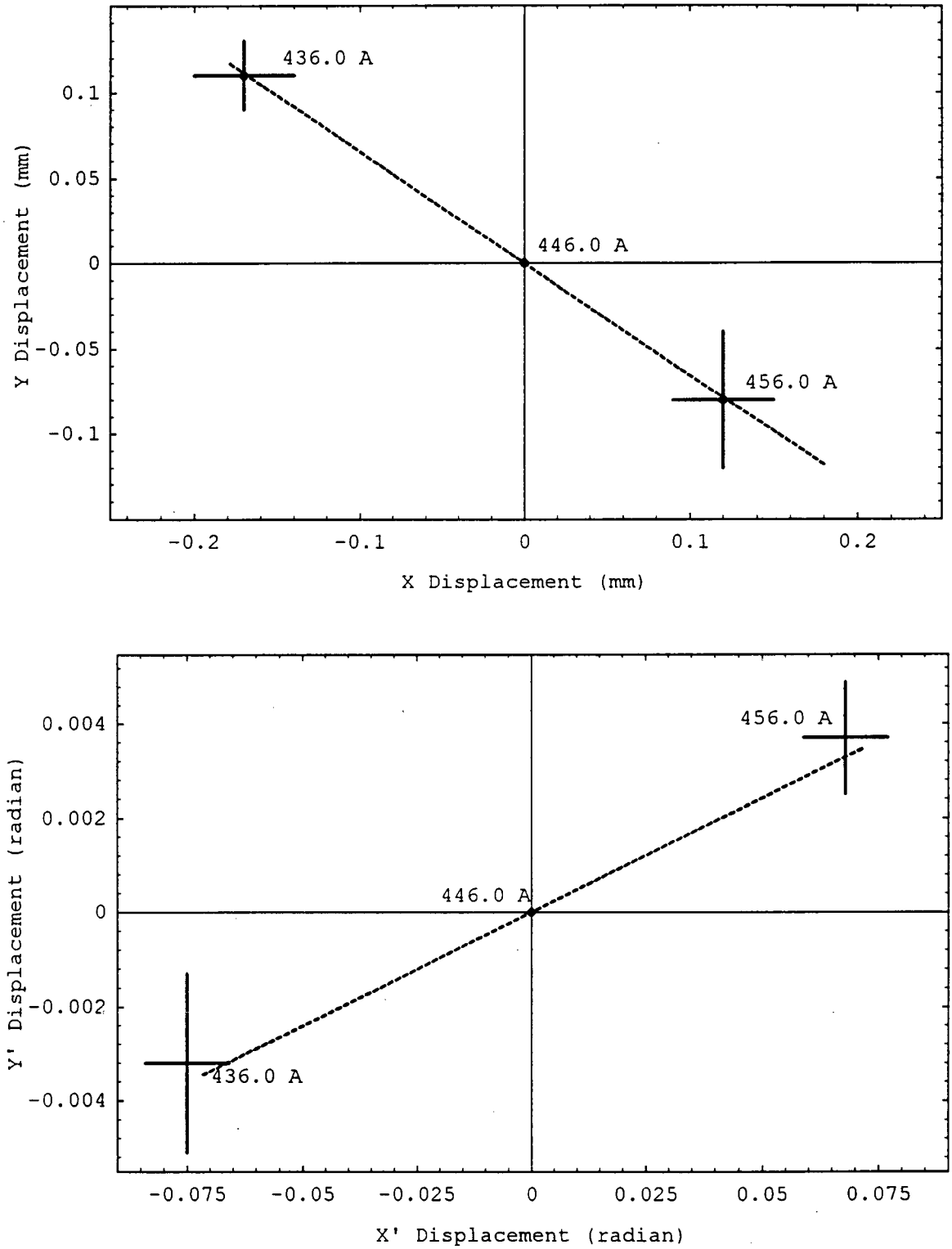

Figure 5.33: *The average central ray (x, y) and (x', y') displacements at the inflector exit scintillator position as a function of the C.R.M. main magnet excitation current.*

Using the measured data, one can see that for a 10% change in the excitation current a radial change of -0.7 ± 0.1 mm is induced accompanied by an axial change of 0.4 ± 0.1 mm. These effects are indeed rather small when compared to the aperture sizes of 10 mm and full beam sizes of about 4 mm. This indicates that it should be safe to use the C.R.M. type center region with the reduced central magnetic field of the TR13.

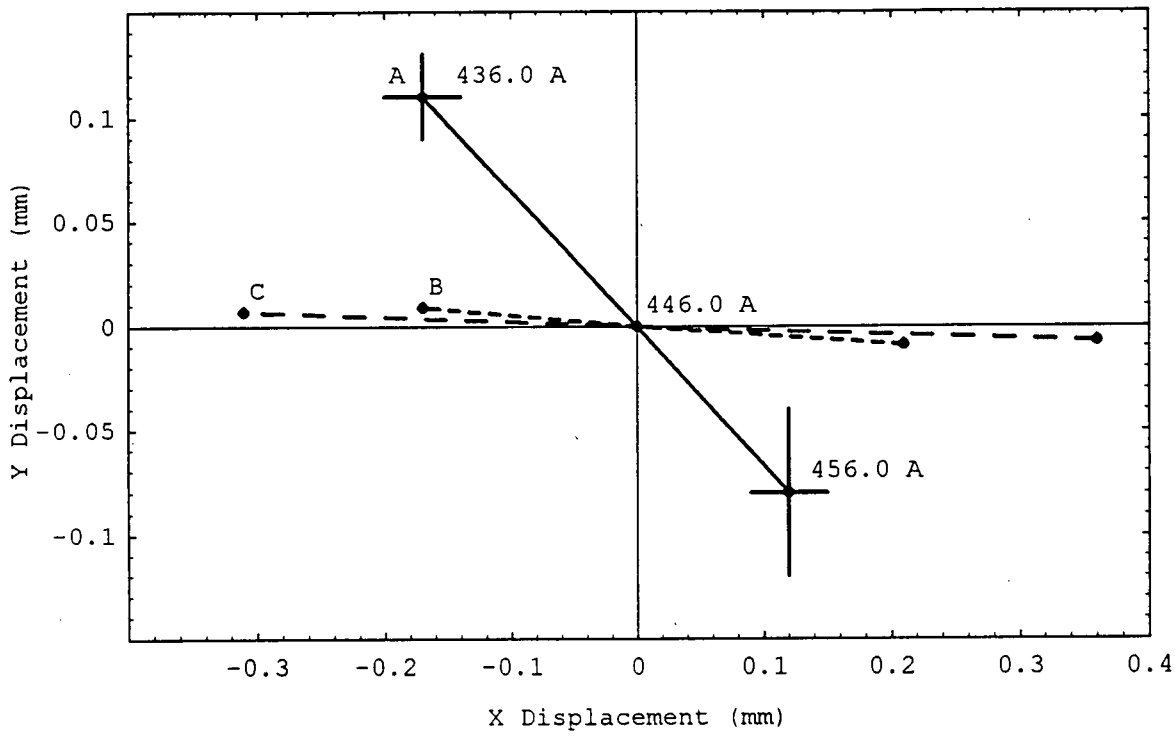

Figure 5.34: *The average central ray (x, y) displacements at the inflector exit scintillator as a function of the C.R.M. main magnet excitation current for three cases. Curve A illustrates the measured data, curve B illustrates the results of a CASINO simulation using the electric field file INF_RELAX_014.DAT, and the magnetic field file MAP29_DIGI.ZFLD, and curve C illustrates the results of a CASINO simulation using an ANALYTIC electric field and the MAP29_DIGI.ZFLD magnetic field map.*

5.7 CENTER REGION BEAM DISPLACEMENT AS A FUNCTION OF INFLECTOR POTENTIAL

In the previous section emphasis was placed on the importance of being able to re-center the beam at the inflector exit. Re-centering the beam with the magnetic field is limited to positions along a skewed line in phase space. This is typically not sufficient for most applications, as one may want to

center the beam at some position that is perpendicular to this line. As well, magnetic field changes must be fairly small so that isochronism is not destroyed. Consequently, it is of importance that other means are available for re-centering the beam, and one method for doing so is by adjusting the inflector electrode potentials. It is important to measure the displacement changes induced by inflector potential changes so that the full range of ways the beam may be adjusted can be determined. As well, it is of interest to assess the ability of CASINO to simulate symmetrical potential changes, and of even more interest to measure asymmetrical potential changes which CASINO cannot simulate.

The displacement changes obtained were relatively large. This provides an opportunity to overlay images of displaced beamlets without mutual interference, so that one can obtain a qualitative feel for the raw data. Figure 5.35 shows such an image. The radial displacement of each beamlet is about 0.3 mm and the axial displacement is about 0.9 mm. The beamlets are approximately 1.0 mm in diameter.

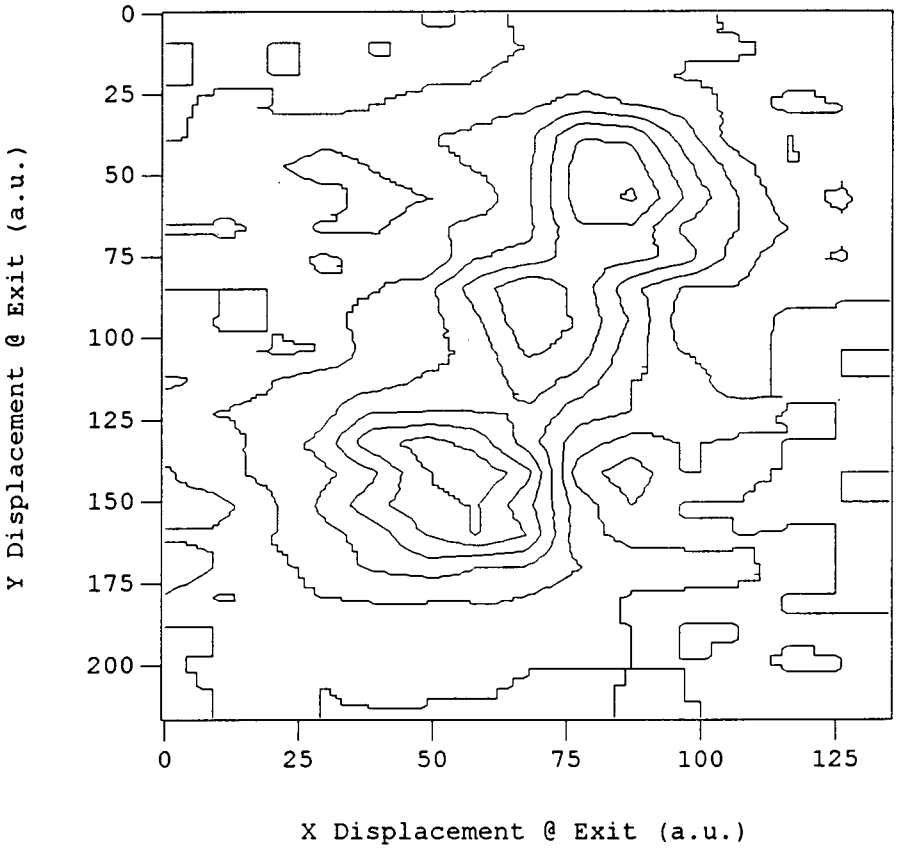

Figure 5.35: *Beamlets measured at the inflector exit. The beamlets came from the Y = –2 mm and X = 10 mm beamlet collimator position. Proceeding from bottom left to upper right the beamlets experienced inflector electrode potentials of ±7.9 kV, ±7.7 kV and ±7.5 kV, respectively. Note that the background is noisier than for a single beamlet image because three images were added together for this figure.*

The beam centering changes that were induced by each set of inflector electrode potentials were repeated eight times. Six separate beamlets and two different low current full beams were used. The induced changes were replicated quite closely by each of the eight test beams, and the resultant error used for each measurement was the statistical standard error. Figure 5.36 shows the (x, y) and (x', y') displacement of the injected beam at the inflector exit scintillator position. The (x', y') displacement was obtained by measuring the (x, y) displacement at the half-turn scintillator position and then using the technique of section 5.5.1 to solve for the divergence components.

The (x, y) plot in Figure 5.36 shows that the inflector potential changes couple rather strongly to the axial displacements relative to the perturbed magnetic field induced axial displacements of Figure 5.33. This is reasonable to expect as changing the potential difference changes the electric radius of curvature, which would result strictly in axial displacements if the magnetic field were not present.

It is interesting to note that the (x, y) displacements in Figure 5.36 form an angle of $\approx 70°$ with respect to the (x) axis whereas the displacements of Figure 5.33 form an angle of $\approx -33°$ with respect to the (x) axis. Since the two methods yield approximately orthogonal results, they can be very effectively used in tandem to produce (x, y) displacements spanning a plane normal to the nominal central ray position. Of course, if one uses the two parameters for the specific purpose of obtaining a particular (x, y) central ray position one must hope that the associated (x', y') coordinates are also acceptable.

CASINO simulations of symmetric potential changes on the inflector electrodes showed excellent agreement with the measured displacement data, as can be seen in Figure 5.37. As was the case for the magnetic field changes, the simulation using a RELAX3D electric field as opposed to an analytic electric field gave the best results.

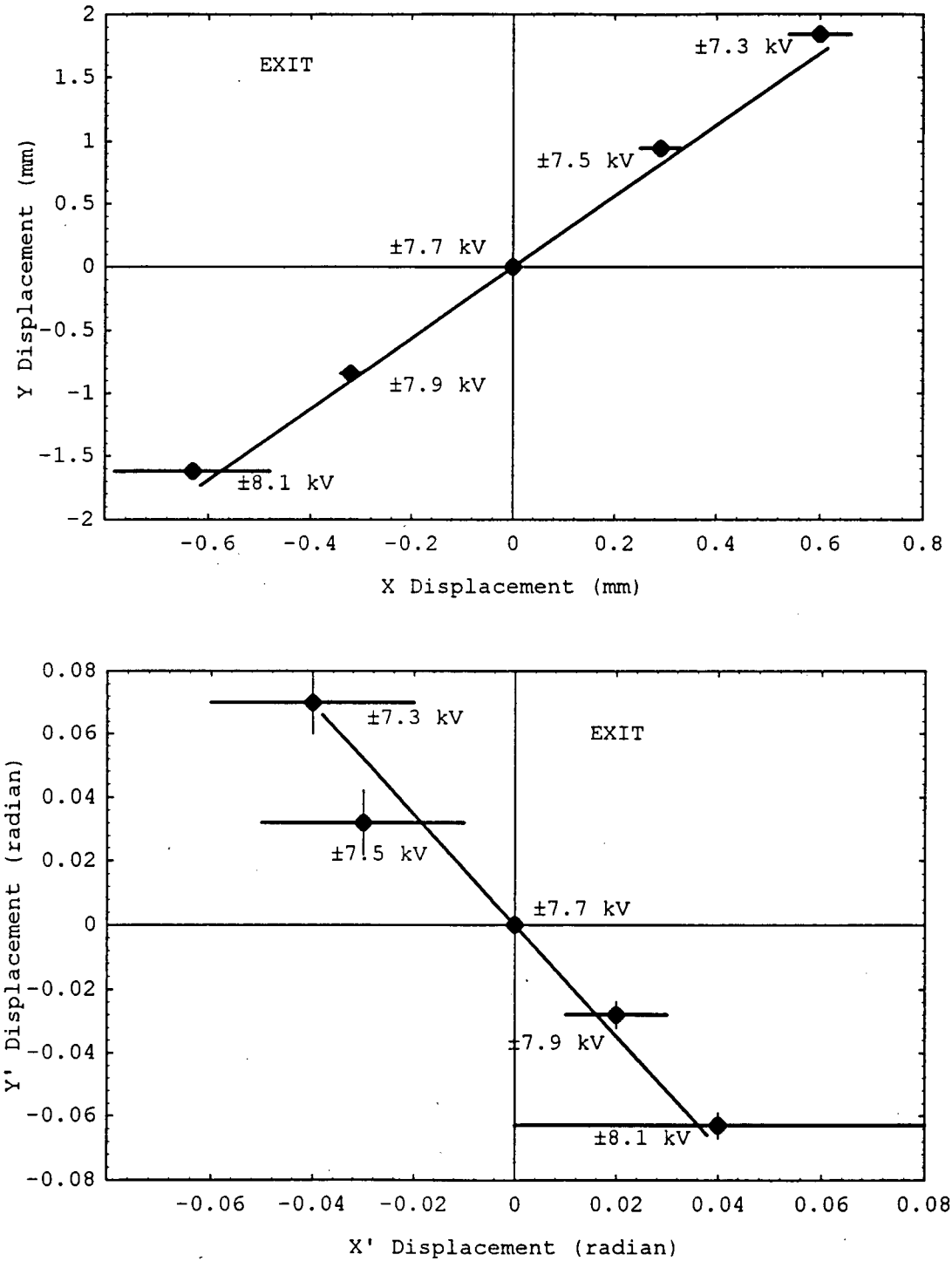

Figure 5.36: *The average central ray (x, y) and (x', y') displacements at the inflector exit scintillator position as a function of symmetrical inflector electrode potential changes.*

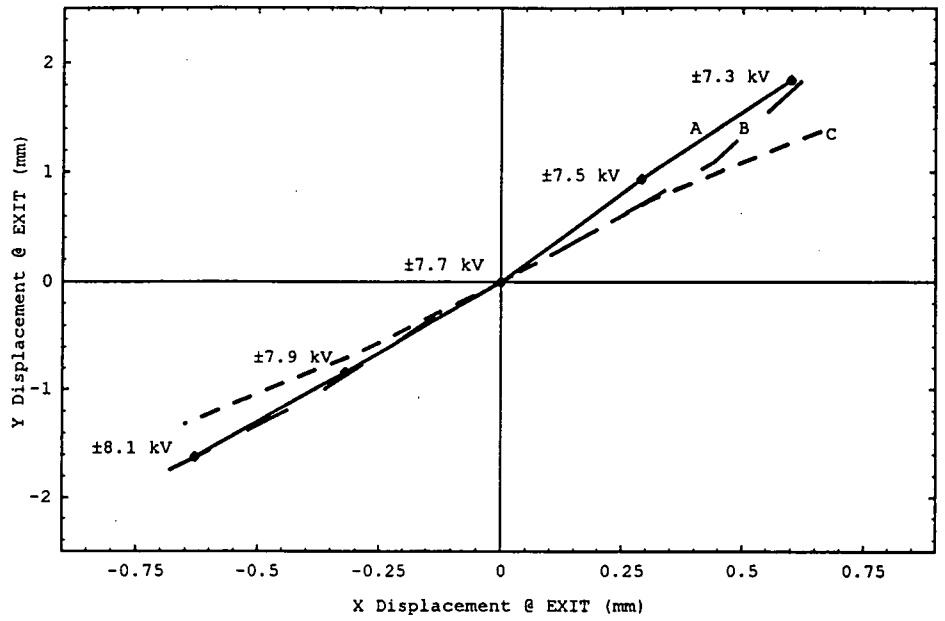

Figure 5.37: *The average central ray (x, y) displacements at the inflector exit scintillator as a function of symmetrical inflector electrode potential changes for three cases. Curve A illustrates the measured data, curve B illustrates the results of a CASINO simulation using the electric field file INF_RELAX_014.DAT, and the magnetic field file MAP29_DIGI.ZFLD, and curve C illustrates the results of a CASINO simulation using an ANALYTIC electric field and the MAP29_DIGI.ZFLD magnetic field map.*

Asymmetrical inflector electrode potential changes cannot be modeled by CASINO. However, asymmetric inflector electrode potential variations are used extensively during beam tuning. For example, Figure 4.37 shows that asymmetric potential settings peaked the beam current to 1.125 MeV, and, in addition, the nominal setting of Table 5.1 is –7.65/7.6 kV. Such variations can provide a useful means for achieving a particular (x, y) central ray position in conjunction with a magnetic field adjustment while yielding a different (x', y') central ray position than could be obtained using symmetric inflector potential changes. The number of asymmetric potential displacement data points obtained was not exhaustive, yet a sufficient number were taken to get a flavour for the types of adjustments possible. Figures 5.38 and 5.39 show the (x, y) and (x', y') displacements as a function of the asymmetric potentials, respectively.

Asymmetric inflector electrode potentials cause the central ray of the beam to travel at a non-zero electric potential through the inflector. This means that the central ray may be slightly accelerated or decelerated. In Figure 5.38 the general trend is for a decelerated central ray to be below the symmetrical displacement line, and for the accelerated central rays to be above this line.

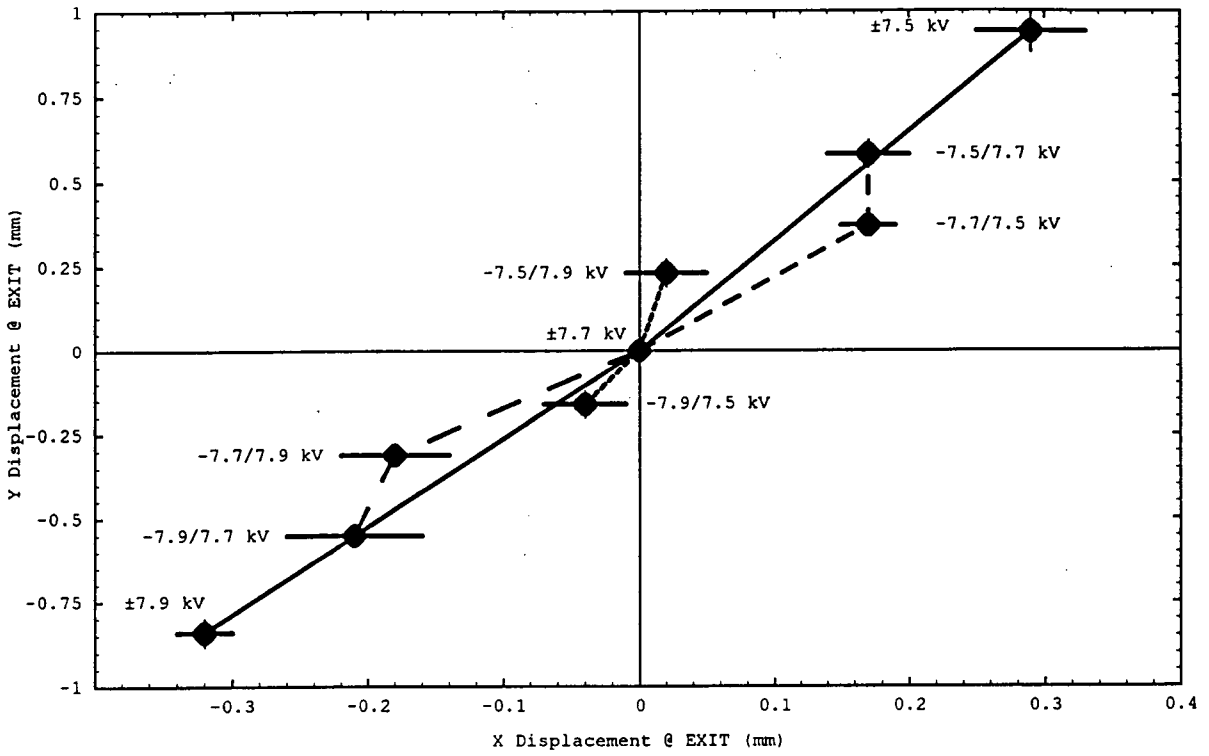

Figure 5.38: *The average central ray (x, y) displacements at the inflector exit scintillator position as a function of asymmetrical inflector electrode potential changes.*

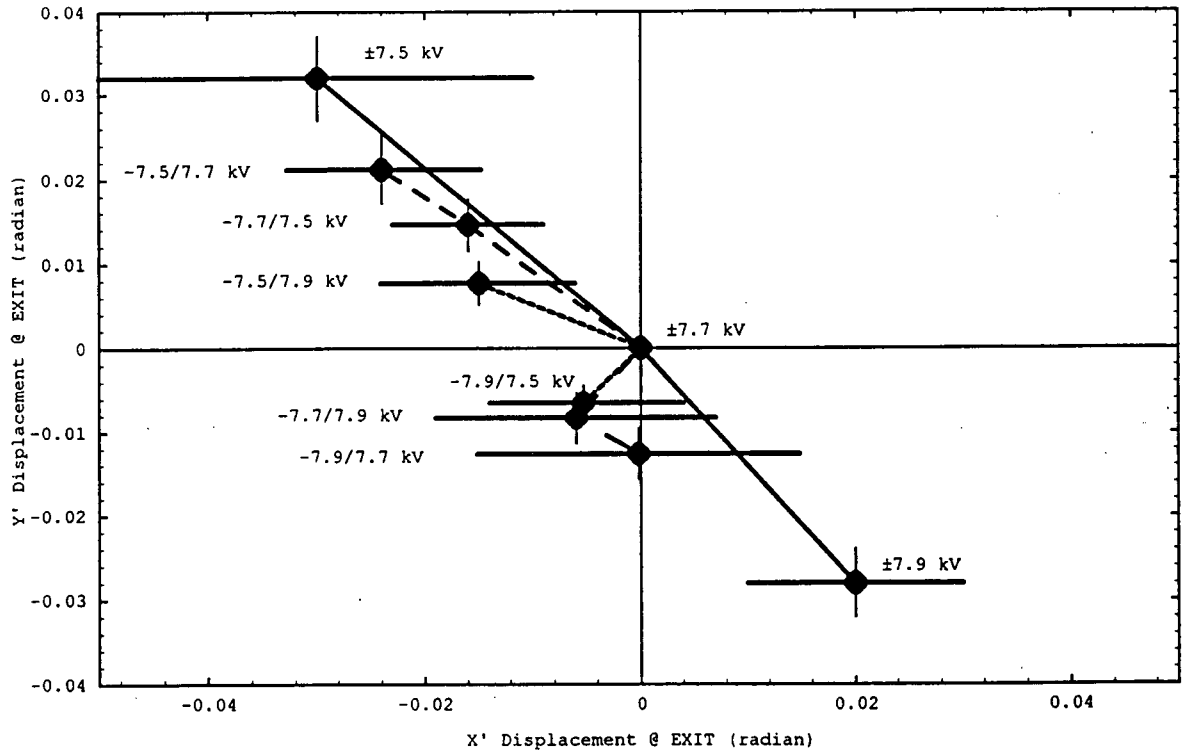

Figure 5.39: *The average central ray (x', y') displacements at the inflector exit scintillator position as a function of asymmetrical inflector electrode potential changes.*

5.8 CENTER REGION BEAM DISPLACEMENT AS A FUNCTION OF BEAM ENERGY

Adjusting the beam's injected kinetic energy is yet another on-line method for displacing the beam centroid at the inflector exit. This is easily accomplished by varying the ion source bias supply voltage. This form of beam adjustment has some interesting side effects, however. In particular, the beam focus through the quadrupole magnets will change as the beam energy is varied. Normally, this will not displace the full beam centroid upstream of the inflector as the beam has not passed through any dispersive elements in this portion of the system. In these experiments, though, the beam was found to be off-center at the inflector entrance for maximum beam transmission, and this meant that the full beam centroid must have been steered slightly by the quadrupole magnets and the C.R.M. axial bore field prior to the inflector entrance. Since, the beam's central ray was already off-center for a nominal 25 keV injection energy, it will be expected to be unpredictably shifted by injection energy changes. As in the case of the main magnetic field perturbations, the inflector exit displacements for beams of off-nominal injection energies will also be unpredictable. This of course will be confirmed when comparisons to CASINO simulations are made.

Figure 5.40 shows the displacements at the inflector exit as a function of the beam energy. The displacements are, in fact, unusual. The higher energy beam must have a larger cyclotron radius than the lower energy beams, yet the higher energy beam is displaced in the optical positive (x) direction which is toward the center of the orbit not away from it. The explanation is that even though the higher energy beam does indeed have a larger cyclotron radius, its center of curvature has been displaced in such a manner as to give a net displacement at the inflector exit which is closer to the machine center. Regardless of the reasons for the unusual displacements, they exist and must be taken into account during system tuning.

Figure 5.41 shows a CASINO simulation in which the beam centroid was centered at the inflector entrance, and the displacement for the higher energy beam is in the optical negative (x) direction which is radially farther away from the center of curvature as would normally be expected. The axial

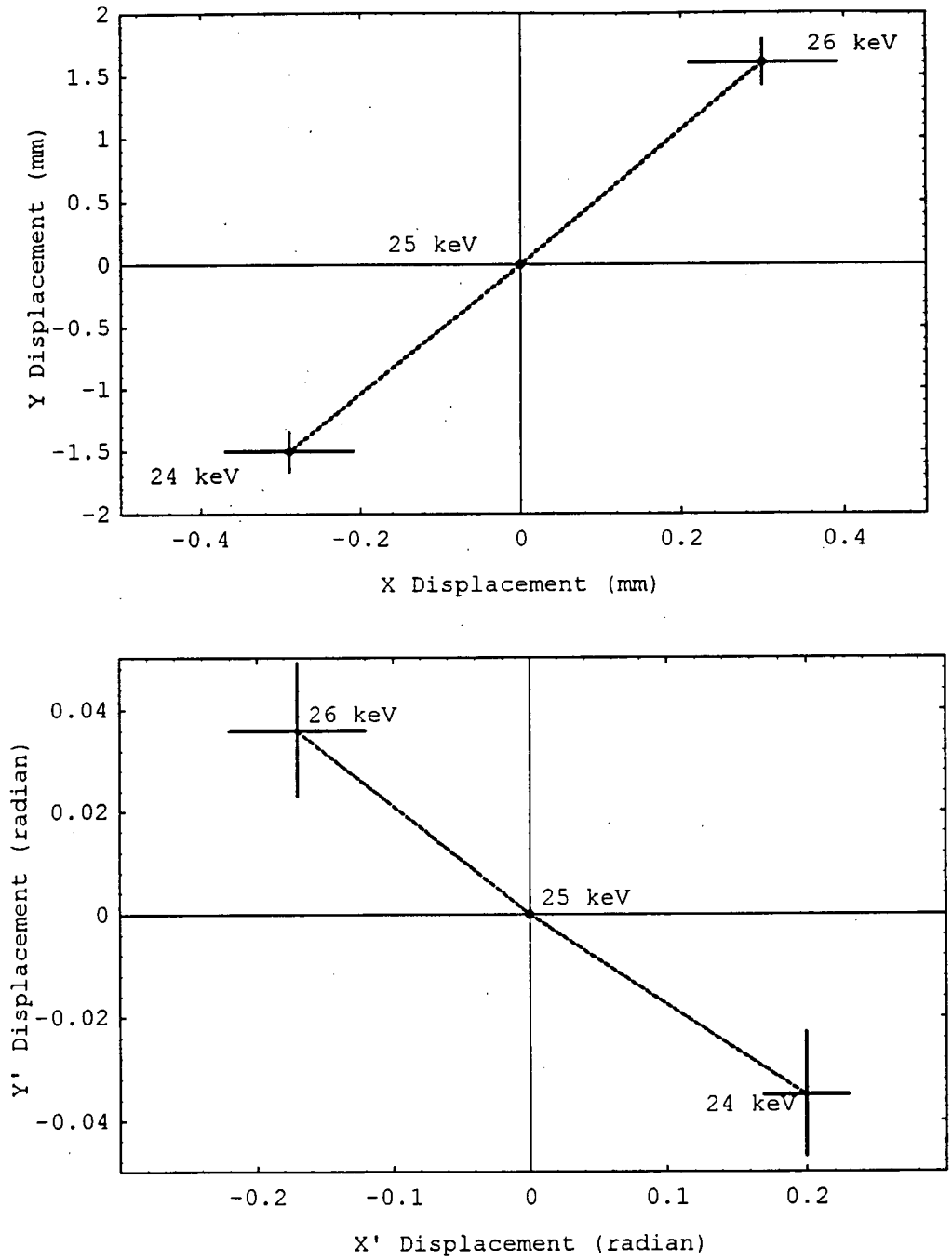

Figure 5.40: *The average central ray (x, y) and (x', y') displacements at the inflector exit scintillator position as a function of beam kinetic energy changes.*

displacement by both CASINO simulations is very small which is unusual as the electric radius of curvature, which couples strongly to the axial axis, varies substantially with the energy changes of these experiments. A back of the envelope calculation shows that the electric bending radius, given by

$$R_{electric} = \frac{2T}{qE}, \tag{5.16}$$

where T is the beam kinetic energy, q is the charge, and E is the electric field between the inflector electrode plates, which is nominally 25 mm, should increase by 1 mm when the beam energy goes from 25 keV to 26 keV.

Figure 5.42 illustrates measured and calculated changes in the beam radius of curvature and the axial displacement of the beam as a function of the beam energy. The change in radius of the beam was measured by using both half-turn and exit scintillator data, and, thus, the radial centering issue which affected Figures 5.40 and 5.41 was circumvented. The calculated displacements were done in a rough manner using equation 5.16 for the electric effects, which were assumed to couple to the axial phase space, and equations 2.29 and 2.30 for the magnetic effects, which were assumed to couple to the radial phase space. One can see that there is reasonable agreement between the measured and calculated results in Figure 5.42.

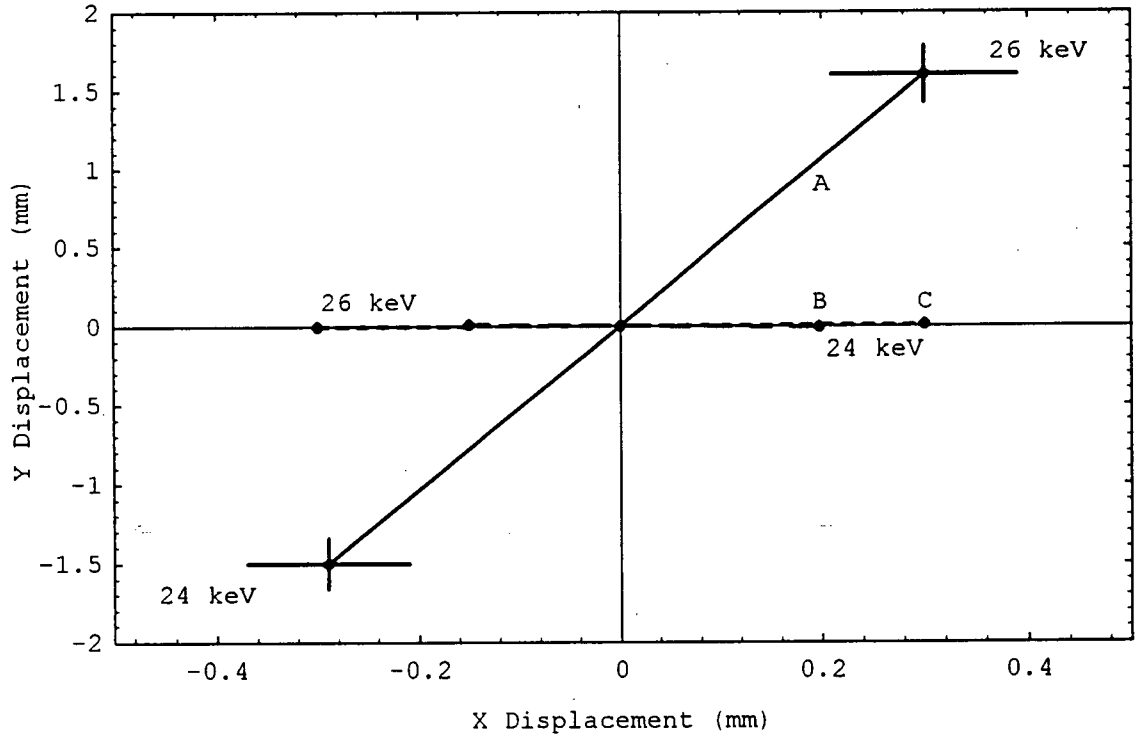

Figure 5.41: *The average central ray (x, y) displacements at the inflector exit scintillator as a function of beam kinetic energy changes for three cases. Curve A illustrates the measured data, curve B illustrates the results of a CASINO simulation using the electric field file INF_RELAX_014.DAT, and the magnetic field file MAP29_DIGI.ZFLD, and curve C illustrates the results of a CASINO simulation using an ANALYTIC electric field and the MAP29_DIGI.ZFLD magnetic field map.*

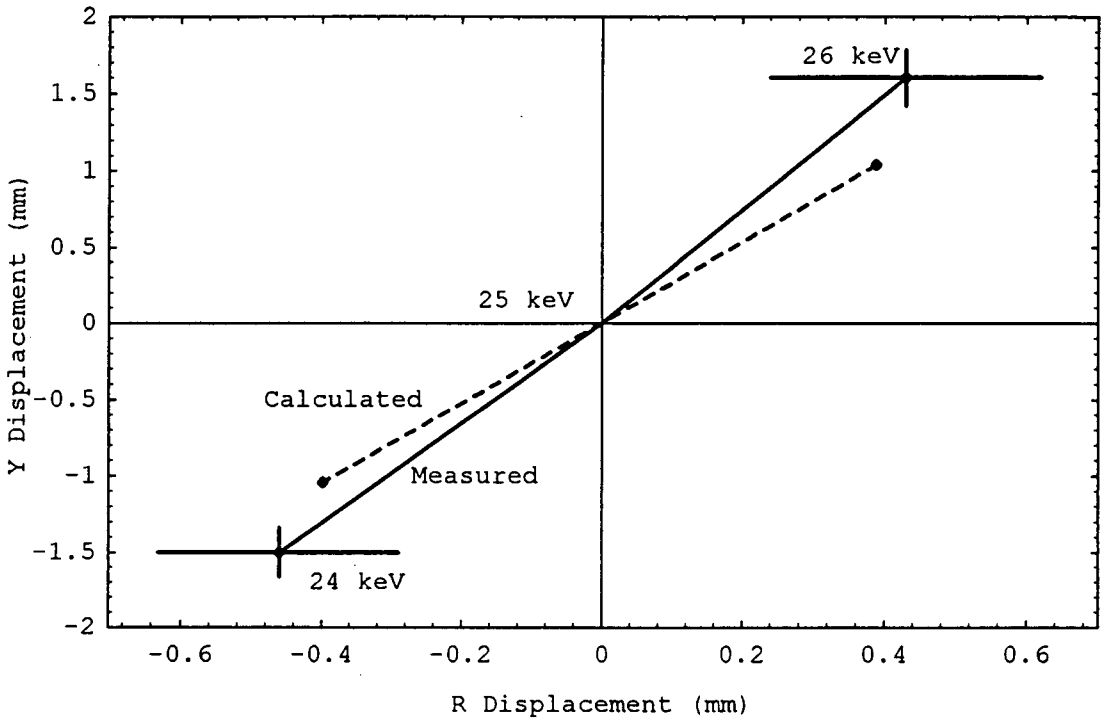

Figure 5.42: *The average change in the central ray radius of curvature and axial position as a function of beam kinetic energy changes for two cases. The solid line shows the measured results and the broken line shows calculated results.*

5.9 SUMMARY

This chapter introduced an experimental technique which allowed the first measurements of beam properties at the entrance and exit of a cyclotron's inflector to be made. The main thrust of these measurements was to produce results which permitted the first ever measured constraints to be placed on the elements of the linear transport matrix representing a cyclotron inflector in its actual operating environment. Other ancillary beam properties which were experimentally measured for the first time included the full beam size, shape, orientation and centering in the (x, y), (x, x') and (y, y') sub-spaces, and beam centroid displacements in phase space as a function of deviations in the cyclotron magnet's excitation current, the inflector electrode potentials and the injected beam energy.

This measurement technique can be divided into two main areas: hardware related and software related. The hardware consisted of specialized collimation equipment, equipment to expose the inflector to

view, scintillator supports and probes, vacuum ports and windows, a TV camera, a digital frame grabber and a personal computer. The software, which greatly facilitated image analysis, consisted of Super Video Windows Veditor for viewing the scintillating beamspot images in real time and for saving the images to disk, Optimetric for performing most of the image analysis tasks including background subtraction, thresholding and data extraction, Transform for graphically representing image data, and *Mathematica* for post-processing the image data, performing computations and illustrating the data.

In order to obtain the measured constraints on the first order transport matrix, beamlet ray tracing was undertaken through the system. The (x, x', y, y') coordinates of each beamlet were known at the collimator position. The (x, y) central ray coordinates of each beamlet were directly measured at each scintillator position, and the (x', y') central ray coordinates were determined using the measured data and the technique described in sections 5.4.2.2 and 5.5.1.

The measured constraints and the best fit linear system's representation of these constraints are listed in Tables 5.3 and 5.5. The measured and computed constraints compare quite favourably to each other. As a result, the best fit linear system parameters in Table 5.4 describe the definitive representation of the injection system, and equations 5.7 and 5.8 give the definitive optical representation of the axial bore and spiral inflector used in the TR type cyclotron. Since this is the first time that measured data has ever been used to constrain the optical representation of a cyclotron inflector, the level of confidence associated with this representation is much higher than has been achieved before. The computer code CASINO used to generate the matrices in equations 5.7 and 5.8 is the first inflector modeling code to be tested against detailed measured data. This code was shown to be capable of accurate modeling of the optical characteristics of the axial bore and the spiral inflector. However, one cannot expect the program to produce optimal simulations if the user does not have a good understanding of the system under investigation and of the many adjustable parameters within the program itself. The best fit linear transport matrices were obtained using the analytical electric field representations within CASINO, as opposed to the more elaborate numerically computed three-dimensional field map representations. This occurred because full three-dimensional electric/magnetic field map scenarios were not investigated exhaustively

whereas the easily manipulated analytical representations were studied more extensively. This resulted in the analytical representations more closely representing the measured data.

The best fit linear system was then used to generate simulated full-beam phase space ellipses in the (x, y), (x, x') and (y, y') sub-spaces, and these were compared to the measured full-beam results. Good agreement was found between the measured and simulated full-beam data, which further established the validity of the best fit linear system. The best fit simulated full-beam phase ellipses at the inflector exit are of great interest to TRIUMF accelerator physicists, for they can be used as input data for accelerated beam studies on the TR type cyclotrons, and they represent a significant level of improvement over the old input phase ellipses. In addition, the full-beam simulations were used to provide updated estimations of the emittance growth in the system. The emittance growth factors are given in Tables 5.7 and 5.8.

During the commissioning of a TR type cyclotron the axial and/or radial centering of the beam is usually adjusted for maximum beam transmission. Typically the cyclotron operator does this by searching through the parameter space spanned by the tunable variables such as the cyclotron magnet excitation current, the inflector electrode voltages and the injected beam energy. This search is typically done in a fairly arbitrary manner, and even when an optimal system tune is achieved the operator usually does not know what sort of re-centering has been achieved. Simulations have often been conducted in the past to determine what is occurring. However, this tactic is of limited utility because the actual system may be perturbed in a large number of possible ways relative to the ideally modeled system. The only measured parameter is typically the beam transmission rate, so the problem is relatively unconstrained. Therefore, the phase space re-centerings measured as a function of the cyclotron magnet excitation current, the inflector electrode voltages and the injected beam energy illustrated in sections 5.6, 5.7 and 5.8 provide a higher level of insight and constraint. This technique of measuring the behaviour of the beam in the immediate vicinity of the inflector will be of considerable interest to other researchers in the field. The figures shown in these sections will be very useful to TR type cyclotron operators, in particular, as they provide information specifically relevant to the TR type inflector and center region.

6.0 CONCLUSIONS AND FURTHER WORK

Detailed summaries of the work presented in this thesis are given in sections 3.4, 4.8, 5.4.2.4 and 5.9. This chapter discusses the major highlights of this thesis and suggests further work which could be fruitfully pursued as a direct consequence.

6.1 CONCLUSIONS

In this thesis useful design techniques were utilized to produce robust prototype injection systems which met the TR13 cyclotron's design specifications. In particular, these systems were compact, modular, and capable of transmitting at least 110 μA of beam current to 1 MeV with a reasonable level of emittance growth [47].

These prototype injection systems were tested using the C.R.M. 1 MeV test cyclotron facility. An axially rotated 4Q system was found to yield the best beam transmission to 1 MeV (275 μA), however, the axially rotated 2Q system was the most cost-effective system which met all of the TR13 specifications. The 2Q system was consequently chosen for use in the TR13 cyclotron system. In order for these injection systems to meet the beam transmission requirements, the ion source was physically re-optimized for the previously sparsely investigated low amperage arc current regime specified for the TR13 system [50]. The techniques used and the results obtained in these experiments were discussed in detail.

The 100 μA of 13 MeV protons specified for the TR13 cyclotron system was dually extracted onto external targets for the first time on May 26, 1994. This confirmed that the 2Q based I.S.I.S. selected in this thesis could be successfully implemented in the commercial version of the cyclotron.

Radial and axial differential probe scans were illustrated for the first five turns in the C.R.M.. These measurements verified that the injected beam was indeed of an acceptable quality, and also permitted the accelerated beam centering, RF phase band, and emittance to be established. Transmission studies as a function of main magnet excitation current, inflector electrode voltages, and injection line quadrupole magnet current settings established the sensitivity of the beam transmission to system perturbations. The work reported in chapter 4 concerning ion source optimization, injection line axial

rotation, and center region sensitivity testing has been very useful to the TRIUMF staff who are currently working towards doubling the output current of the TR30 cyclotron. The technique of axially rotating the injection line, in particular, has resulted in significant gains in total transmitted current.

The detailed beamlet based measurements at the entrance and exit of the TR type inflector were the first measurements of this type to be made at these locations in a cyclotron. The experiment based approach to optically characterizing the inflector and to determining the beam's properties in the vicinity of the inflector constitutes a change in approach to the inflector "problem". Until now the approach has been almost entirely simulation based. The traditional approach has certainly shed light on the various inflector/beam related ion optical issues, but it could never truly resolve an issue in the way that measured data can. The absence of measured data in this particular area of accelerator physics is related to the perceived difficulty in making measurements. Thus, one of the contributions of this thesis was the specification of an experimental technique which permits one to obtain detailed inflector/beam measurements. The results of these measurements fell into three main categories. The first was the full-beam size, shape, orientation and centering data obtained in the (x, y), (x, x') and (y, y') phase spaces. The second was the creation of an injection system linear transport matrix which best fit the measured transport matrix constraints obtained through beamlet ray-tracing. This work established the definitive representation of the 4Q injection system and the definitive TR type cyclotron's axial bore and spiral inflector optical transport matrices. The third type of information obtained was in the form of plots of (Δx, Δy) and ($\Delta x'$, $\Delta y'$) beam central ray variations at the inflector exit as a function of variations in the cyclotron's magnetic field, the inflector electrode potentials and the injected beam energy. This information is of substantial practical utility for determining the central region axial and radial displacements that are invoked as a function of system tuning during cyclotron commissioning or during specific center region experiments.

A consequence of the measurements is that CASINO is the first cyclotron inflector modeling code which has been tested against detailed measured data. CASINO was shown to be capable of providing best fit linear transport matrices for the axial bore of the cyclotron and the inflector that were

well matched to the data. Working with CASINO also highlighted the fact that if one does not have measured constraints to direct the process of parameter adjustment within an inflector and injection system simulation code, it is difficult to obtain a system representation of high accuracy.

The personal computer based software packages Optimetric, Transform and *Mathematica* have been shown to be useful for analysis in the field of accelerator physics. In addition, the programs TRANSOPTR, CASINO, CYCLONE and ZGOUBI have each been shown to be capable of addressing particular ion-optical simulations.

Lastly, I deemed the length of this thesis and the technical detail included in this thesis necessary for documenting the capabilities of the C.R.M. cyclotron and the TR type injection systems for future reference by TRIUMF and Ebco Technologies personnel.

6.2 FURTHER WORK

A two collimator beamlet selection system could be used in conjunction with the techniques of chapter 5 to place measured constraints on each element of the first order transport matrix for the injection system. This would represent an improvement over the constraints described in equations 5.3 through 5.6 and equations 5.11 through 5.14.

If further effort was expended to find an experimental set-up which could handle injected beam currents of 5 mA or higher, perhaps with the use of a beam pulser, the techniques of chapter five could be used to study space charge effects in the vicinity of the inflector exit. In addition, scintillator based full-beam studies of the effects of injection system axial rotations and quadrupole magnet current setting variations could also be undertaken.

An experiment which tests beam transmission to 30 MeV in the TR30 cyclotron, and to 13 MeV in the TR13 cyclotron as a function of injection system axial rotation angle would be of scientific interest.

It would also be of interest to use the full-beam phase space specifications established in chapter 5, as input data for accelerated beam transport simulations in the TR type cyclotrons. These simulations should yield a good match to the measured data described in [25], for example.

A more exhaustive study of CASINO's ability to simulate the results of chapter 5 could be undertaken. In particular, one would expect that three-dimensional field map simulations could be found which provide a best fit linear system which is at least as good as the system described in this thesis. If this was found not to be the case, CASINO should be upgraded.

The results of the work described in chapters 3 and 4 indicate that an even more compact TR13 type injection line could be designed. This would be desirable, as the present TR13 design calls for a substantial amount of costly radiation shielding material to surround the portion of the ion source and injection system which protrudes from the TR13 cyclotron's axial bore. If the two injection line quadrupole magnets were buried within the axial bore to within about 14 cm of the median plane, and if the injection line cryo-pump was removed from the system (vacuum pumping would come from the cyclotron's main tank), almost all of the injection line would be hidden within the bore hole in the cyclotron. This would mean that both the injection line and shielding costs would be greatly reduced. Of course, substantial prototype testing would have to be undertaken to verify whether such a system was actually practical.

REFERENCES

[1] T.J. Ruth, B.D. Pate, R. Robertson and J.K. Porter, "Radionuclide Production for the Biosciences", *Nucl. Med. Biol.*, Vol. 16, No. 4, pp. 323–336, 1989.

[2] J.J. Burgerjon, "H^- Cyclotrons for Radioisotope Production", *Nucl. Instr. and Meth.*, Vol. B10/11, pp. 951–956, 1985.

[3] C. Birattari, M. Bonardi, F. Resmini and A. Salomone, "Status Report on Radioisotope Production for Biomedical Purposes at Milan AVF Cyclotron", *Proc. 9th Int'l Conf. on Cyclotrons and their Applications,* pp. 693–695, Caen, 1981.

[4] T.J. Ruth,"The Production of Radionuclides for the Biosciences", *Proc. 13th Int'l Conf. on Cyclotrons and their Applications*, pp. 206–208, Vancouver, 1992.

[5] D.K. Bewley, "Medical Uses of Cyclotrons: Treatment and Diagnosis", *Proc. 9th Int'l Conf. on Cyclotrons and their Applications*, pp. 653–660, Caen, 1981.

[6] D. Comar, "Production of Cyclotron Radioisotopes and Radiopharmaceuticals for Medical Use", *Proc. 9th Int'l Conf. on Cyclotrons and their Applications*, pp. 645–652, Caen, 1981.

[7] M.A. Chaudhri, "The Yields of Cyclotron Produced Medical Isotopes", *Proc. 9th Int'l Conf. on Cyclotrons and their Applications*, pp. 683–692, Caen, 1981.

[8] H. Ayvazian, "A New Design for an EMIS-Cyclotron System, for Direct Production of Gaseous PET Radioisotopes", *Proc. I.E.E.E. Part. Acc. Conf.*, Vol. 3, pp. 1750–1752, Washington, 1993.

[9] V. Bechtold, "Commercially Available Compact Cyclotrons for Isotope Production", *Proc. 13th Int'l Conf. on Cyclotrons and their Applications*, pp. 110–114, Vancouver, 1992.

[10] T. Grey-Morgan and R.E. Hubbard, "The Operation of Cyclotrons Used for Radiopharmaceutical Production", *Proc. 13th Int'l Conf. on Cyclotrons and their Applications*, pp. 115–118, Vancouver, 1992.

[11] H.R. Schneider, R. Baartman, R.E. Laxdal, B.F. Milton, A.J. Otter, J.B. Pearson, R.L. Poirier and P.W. Schmor, "A Compact H^- Cyclotron for Isotope Production", *Proc. 1st European Part. Acc. Conf.*, pp.1502–1504 , Rome, 1988.

[12] R. Baartman, K.L. Erdman, W.J. Kleeven, R.E. Laxdal, B.F. Milton, A.J. Otter, J.B. Pearson, R.L. Poirier, P.W. Schmor, H.R. Schneider and Q. Walker, " A 30 MeV H^- Cyclotron for Isotope Production", *Proc. I.E.E.E. Part. Acc. Conf.*, pp. 1623–1625 , Chicago, 1989.

[13] B.F. Milton, R. Dawson, K.L. Erdman, W. Gyles, W.J. Kleeven, R.E. Laxdal, L. Milinkovic, J.B. Pearson, R.L. Poirier, P.W. Schmor, H.R. Schneider, Q. Walker and G. Dutto, "A 30 MeV H^- Cyclotron for Isotope Production", *Proc. 12 th Int'l Conf. on Cyclotrons and their Applications*, pp. 145–148 , Berlin, 1989.

[14] B.F. Milton, G. Dutto, R. Helmer, R. Keitel, W.J. Kleeven, P. Lanz, R.L. Poirier, K. Reiniger, T. Ries, P.W. Schmor, H.R. Schneider, A. Sliwinski, J. Sura, W. Uzat, J. Yandon, R. Dawson, M. Dehnel, K.L. Erdman, W. Gyles, J. Sample, Q. Walker and R. Watt, "First Beam in a New Compact Intense 30 MeV H^- Cyclotron for Isotope Production", *Proc. 2nd European Part. Acc. Conf.*, Vol. 2, pp.1812–1814 , Nice, 1990.

[15] K. Erdman, R. Dawson, B. Milton and N. Stevenson, "Operation of the TR30 Industrial Cyclotron", *Proc. I.E.E.E. Part. Acc. Conf.*, Vol. 3, pp. 1733–1734, Washington, 1993.

[16] Y. Jongen, "Conceptual Design for a High Intensity (5 mA) Industrial Cyclotron", *Proc. 10th Int'l Conf. on Cyclotrons and their Applications*, pp. 465–468, East Lansing, 1984.

[17] Y. Jongen, M. Lacroix, G. Ryckewaert and S. Zaremba, "Beam Dynamics Aspects of a High Intensity Isotope Production Cyclotron", *Proc. 11th Int'l Conf. on Cyclotrons and their Applications*, pp. 260–262, Tokyo, 1987.

[18] T. Vanderlinden, E. Conard, Y. Jongen, "Three Years of Operation of Cyclone 30 in Louvain-La-Neuve", *Proc. 2nd European Part. Acc. Conf.*, Vol. 1, pp. 437–439, Nice, 1990.

[19] J.L. Bol, A. Chevalier, E. Conard, Y. Jongen, M. Ladeuze, G. Lannoye, T. Ledocte, M. Lacroix, A. Ninane, G. Ryckewaert and S. Zaremba, "High Intensity H^- Cyclotrons for Radioisotope Production", *Proc. 12th Int'l Conf. on Cyclotrons and their Applications*, pp. 149–151, Berlin, 1989.

[20] E. Conard, J.L. Morelle, J.C. Clark and D.B. MacKay, "Experiences with the Cyclone 3 Oxygen 15 Generator", *Proc. 13th Int'l Conf. on Cyclotrons and their Applications*, pp. 218–221, Vancouver, 1992.

[21] K. Ito, S. Sakuma, T. Kato, M. Tadokoro, T. Ota, M. Nishino, T. Ishigaki, Y. Kasugai, H.Yamamoto, M. Osakabe, T. Misawa, S. Itoh, Y. Toda and Y. Yamashita, "A Newly Developed Compact Cyclotron for Neutron Therapy and Positron Nuclear Medicine", *Proc. 13th Int'l Conf. on Cyclotrons and their Applications*, pp. 129–132, Vancouver, 1992.

[22] M.F. Finlan, M. Kruip and M.N. Wilson, "A Light, Superconducting H^- Cyclotron for Medical Diagnostics and Neutron Radiography", *Proc. 11th Int'l Conf. on Cyclotrons and their Applications*, pp. 689–692, Tokyo, 1987.

[23] Y. Adachi, K. Fujii, M. Maruyama, Y. Nishihara, A. Tanaka, T. Hiroishi, H. Suzuki and G. Meyrand, "In-House Cyclotron and Radioisotopes Production System", *Proc. 11th Int'l Conf. on Cyclotrons and their Applications*, pp. 622–625, Tokyo, 1987.

[24] M. Dehnel, G. Dutto, K. Erdman, B. Gyles, B. Milton, P.W. Schmor, and Q. Walker, "The TR16/8, A Dual Particle Cyclotron for Clinical Isotope Production", *Proc. 3rd European Part. Acc. Conf.*, Vol. 2, pp. 1682–1684, Berlin, 1992.

[25] R.E. Laxdal, A. Altman, T. Kuo and T. Kadantsev, "Beam Measurements on a Small Commercial Cyclotron", *Proc. 4th European Part. Acc. Conf.*, London, 1994, in press.

[26] R. Baartman, "Matching of Ion Sources to Cyclotron Inflectors", *Proc. 1st European Part. Acc. Conf.*, Vol. 2, pp. 947–948, Rome, 1988.

[27] W. Kleeven and R. Baartman, "Beam Matching and Emittance Growth Resulting from Spiral Inflectors for Cyclotrons", *Particle Accelerators*, Vol. 41, pp. 55–70, 1993.

[28] R.J. Balden, W. Kleeven, L.S. Milinkovic, B.F. Milton and J.B. Pearson, "Aspects of Phase Space Dynamics in Spiral Inflectors", *Proc. 12th Int'l Conf. on Cyclotrons and their Applications*, pp. 435–438, Berlin, 1989.

[29] J.I.M. Botman, J. Reich, P. Wucherer and H.L. Hagedoorn, "Analytical Treatment of Ion Inflectors", *Proc. 11th Int'l Conf. on Cyclotrons and their Applications*, pp. 263–265, Tokyo, 1987.

[30] J.I.M. Botman, J. Reich, P. Wucherer and H.L. Hagedoorn, "Examples of Ray Tracing in Ion Inflectors", *Proc. 11th Int'l Conf. on Cyclotrons and their Applications*, pp. 267–270, Tokyo, 1987.

[31] M. Rinta-Nikkola, "Ion_Tracker, A Trace Tracking Program for Cyclotron Design", *Proc. 13th Int'l Conf. on Cyclotrons and their Applications*, pp. 388–391, Vancouver, 1992.

[32] P. Heikkinen and M. Rinta-Nikkola, "Ion Optics in the Jyväskylä K130 Cyclotron", *Proc. 13th Int'l Conf. on Cyclotrons and their Applications*, pp. 392–395, Vancouver, 1992.

[33] B.F. Milton and J.B. Pearson, "CASINO: **C**alculation of Spiral **I**nflector **O**rbits - User's Guide and Reference Manual", TRIUMF design note TRI–DN–19, 1989.

[34] J.L. Belmont, "Axial Injection and Central Region of the AVF Cyclotron", Lecture notes of RCNP Kikuchi Summer School on Accelerator Technology, Osaka, Japan, 1986.

[35] G.H. Ryckewaert, "Axial Injection Systems for Cyclotrons", *Proc. 9th Int'l Conf. on Cyclotrons and their Applications*, pp. 241–248, Caen, 1981.

[36] W.B. Powell and B.L. Reece, "Injection of Ions into a Cyclotron from an External Source", *Nucl. Instr. and Meth.*, Vol. 32, pp. 325–332, 1965.

[37] J.L. Belmont and J.L. Pabot, "Study of Axial Injection for the Grenoble Cyclotron", *IEEE Trans. Nucl. Sci.*, Vol. 13, pp. 191–193, 1966.

[38] R.W. Müller, "Novel Inflectors for Cyclic Accelerators", *Nucl. Instr. and Meth.*, Vol. 54, pp. 29–41, 1967.

[39] L.W. Root, "Design of an Inflector for the TRIUMF Cyclotron", M.Sc. Thesis, Univ. of British Columbia, Vancouver, 1972.

[40] L.W. Root, "Experimental and Theoretical Studies of the Behaviour of an H^- Ion Beam during Injection and Acceleration in the TRIUMF Central Region Model Cyclotron", Ph.D. Thesis, Univ. of British Columbia, Vancouver, 1974.

[41] F. Marti, J. Griffin and V. Taivassalo, "Design of the Axial Injection System for the NSCL Cyclotrons", *IEEE Trans. Nucl. Sci.*, Vol. 32, pp. 2450–2452, 1985.

[42] F. Marti and A. Gavalya, "Axial Injection in the K500 Superconducting Cyclotron", *Proc. 11th Int'l Conf. on Cyclotrons and their Applications*, pp. 484–487, Tokyo, 1987.

[43] N. Hazewindus, "The Axial Injection System of the SIN Injector Cyclotron", *Nucl. Instr. and Meth.*, Vol. 129, pp. 325–340, 1975.

[44] G. Bellomo, "The Central Region for Compact Cyclotrons", *Proc. 12th Int'l Conf. on Cyclotrons and their Applications*, pp. 325–334, Berlin, 1989.

[45] R. Baartman and W. Kleeven, "A Canonical Treatment of the Spiral Inflector for Cyclotrons", *Particle Accelerators*, Vol. 41, pp. 41–53, 1993.

[46] M. Berglund, K. Hedblom, G. Norman, O. Jonsson, D. Reistad and D. Wessman, "Beam Dynamics Studies at the Gustaf Werner Cyclotron", *Proc. 4th European Part. Acc. Conf.*, London, 1994, in press.

[47] M. Dehnel, K. Erdman, T. Kuo, L. Root, "Injection System Design and Tests for the TR13 Cyclotron", *Proc. 4th European Part. Acc. Conf.*, London, 1994, in press.

[48] W. Kleeven, P. Lanz, M. McDonald, B.F. Milton, P.W. Schmor, H.R. Schneider, K. Jayamanna, J. Sura,W. Uzat and B. Gyles, "Status and Results from the TR30 Cyclotron Centre Region Model", *Proc. 2nd European Part. Acc. Conf.*, Vol. 1, pp. 434–436, Nice, 1990.

[49] R. Baartman, "Injection Line Optics", TRIUMF design note TRI–DN–25, 1989.

[50] T. Kuo, L. Root, R. Laxdal, A. Altman, K. Jayamanna, D. Yuan, M. McDonald, W. Uzat, P. Schmor, G. Dutto, M. Dehnel and K. Erdman, "Performance of an ISIS system Using Compact Magnetic Quadrupoles", *Proc. 4th European Part. Acc. Conf.*, London, 1994, in press.

[51] J.I.M. Botman, H.L. Hagedoorn and J. Reich, "Axial Inflectors and the Correlation Between Phase Spaces", *Proc. 12 th Int'l Conf. on Cyclotrons and their Applications*, pp. 443–446 , Berlin, 1989.

[52] J. Reich, H. Beuscher, R.K. Bhandari, J.I.M. Botman and H.L. Hagedoorn, "Partial Beam Decorrelation of Sources Providing Ions out of Axial Magnetic Fields", *Proc. 1st European Part. Acc. Conf.*, Vol. 2, pp. 833–835, Rome, 1988.

[53] J.I.M. Botman, H.L. Hagedoorn and J. Reich, "The Beam Emittance of Cyclotrons with an Axial Injection System", *Proc. 1st European Part. Acc. Conf.*, Vol. 1, pp. 651–653, Rome, 1988.

[54] A.R. Beck, S. Chel, B. Bru and C. Ricaud, "Six-Dimensional Beam Matching for Axial Injection into a Cyclotron", *Proc. 12 th Int'l Conf. on Cyclotrons and their Applications*, pp. 432–434 , Berlin, 1989.

[55] K.L. Brown and R.V. Servranckx, "Cross–Plane Coupling and Its Effect on Projected Emittance", *Particle Accelerators*, Vol. 36, pp. 121–139, 1991.

[56] J.J. Livingood, PRINCIPLES OF CYCLIC PARTICLE ACCELERATORS, New Jersey: D. van Nostrand Company, Inc., 1961

[57] A.P. Banford, TRANSPORT OF CHARGED PARTICLE BEAMS, London: E. & F. N. Spon Ltd., 1966.

[58] M. Month (Ed.), PHYSICS OF HIGH ENERGY PARTICLE ACCELERATORS, *AIP Conf. Proc.*, No. 105, 1983.

[59] M. Month and M. Dienes (Eds.), PHYSICS OF PARTICLE ACCELERATORS, *AIP Conf. Proc.*, No. 184, Vol. 1 & 2, 1989.

[60] M. Month and M. Dienes (Eds.), THE PHYSICS OF PARTICLE ACCELERATORS, *AIP Conf. Proc.*, No. 249, Vol. 1 & 2, 1992.

[61] H. Wiedemann, PARTICLE ACCELERATOR PHYSICS, Berlin: Springer-Verlag, 1993.

[62] D.A. Edwards and M.J. Syphers, AN INTRODUCTION TO THE PHYSICS OF HIGH ENERGY ACCELERATORS, New York: John Wiley & Sons, 1993.

[63] K.L. Brown, D.C. Carey, Ch. Iselin and F. Rothacker, "TRANSPORT, A Computer Program for Designing Charged Particle Beam Transport Systems", SLAC 91 (1973), NAL 91 and CERN 80 –04.

[64] E.D. Courant and H.S. Snyder, "Theory of the Alternating Gradient Synchrotron", *Ann. Phys.*, No. 3, pp. 1–48, 1958.

[65] K.L. Brown, "A First- and Second-Order Matrix Theory for the Design of Beam Transport Systems and Charged Particle Spectrometers", *Adv. Particle Phys.*, No. 1, pp. 71–134, 1968.

[66] K.L. Brown, "Beam Envelope Matching for Beam Guidance Systems", *Nucl. Instr. and Meth.*, Vol. 187, pp. 51–65, 1981.

[67] K.L. Brown and R.V. Servranckx, "First- and Second-Order Charged Particle Optics", SLAC–PUB–3381, 1984.

[68] K.L. Brown and R.V. Servranckx, "Optics Modules for Circular Accelerator Design", SLAC–PUB–3957, 1986.

[69] G.M. Stinson, "A Brief Course in Beam Optics", Physics 675 Course Notes, University of Alberta, 1990.

[70] B.F. Milton, "CYCLONE Version 6.4", TRIUMF internal report, 1991.

[71] I.M. Kapchinsky and V.V. Vladimirsky, *Proc. Int. Conf. on High-Energy Accelerators and Instrumentation*, CERN, pp. 274–288, 1959.

[72] E.A. Heighway and R.M. Hutcheon, "TRANSOPTR – A Second Order Transport Design Code with Optimization and Constraints", *Nucl. Instr. and Meth.*, Vol. 187, pp. 89–95, 1981.

[73] M.S. de Jong and E.A. Heighway, "A First Order Space Charge Option for TRANSOPTR", *IEEE Trans. Nucl. Sci.*, Vol. 30, pp. 2666–2668, 1983.

[74] Y.T. Yan, "Application of Differential Algebra to Single-Particle Dynamics in Storage Rings", *AIP Conf. Proc.*, No. 249, pp. 380–455, 1992.

[75] M. Berz, "High-Order Computation and Normal Form Analysis of Repetitive Systems", *AIP Conf. Proc.*, No. 249, pp. 456–489, 1992.

[76] F. Méot and S. Valéro, "ZGOUBI USERS' GUIDE", SATURNE Note LNS/GT/93–12, 1993.

[77] W.T. Weng and S.R. Mane, "Fundamentals of Particle Beam Dynamics and Phase Space", *AIP Conf. Proc.*, No. 249, pp. 3–45, 1992.

[78] Lejeune and J. Aubert, "Emittance and Brightness: Definitions and Measurements", *Adv. Electronics and Electron Phys.*, Supplement 13A, pp. 159–259, 1978.

[79] K.N. Leung, W.F. DiVergilio, C.A. Hauck, W.B. Kunkel and D.S. McDonald, "Optimization of an RF Driven H^- Ion Source", *IEEE Part. Acc. Conf.*, Vol. 3, San Francisco, pp. 1919–1921, 1991.

[80] R.L. York and R.R. Stevens, "A Cusped Field H^- Ion Source for LAMPF", *IEEE Trans. Nucl. Sci.*, Vol. 30, pp. 2705–2707, 1983.

[81] K.R. Kendall, M. McDonald, D.R. Mosscrop, P.W. Schmor, D. Yuan, G. Dammertz, B. Piosczyk and M. Olivo, "Measurements on a DC Volume H^- Multi-Cusp Ion Source for TRIUMF", *Rev. Sci. Instr.*, Vol. 57, No. 7, pp. 1277–1281, 1986.

[82] R. Baartman, K.R. Kendall, M. McDonald, D.R. Mosscrop, P.W. Schmor, D. Yuan and M. Olivo, "An Intense Ion Source for H^- Cyclotrons", *Proc. 11th Int'l Conf. on Cyclotrons and their Applications*, pp. 717–487, Tokyo, 1987.

[83] I.G. Brown, THE PHYSICS AND TECHNOLOGY OF ION SOURCES, New York: John Wiley & Sons, Inc., 1989.

[84] K.S. Golovanivsky, K. Jayamanna and P.W. Schmor, "Physical Fundamentals of H^- Ion Sources", TRIUMF design note TRI–DN–25, 1993.

[85] A.T. Young, P. Chen, W.B. Kunkel, K.N. Leung, C.Y. Li and G.C. Stutzin, "Laser Diagnostics of H^- Formation in a Magnetic Multi–Cusp Ion Source", *IEEE Part. Acc. Conf.*, Vol. 3, 1916–1918, 1991.

[86] B.F. Milton, "Central Region Specification", TRIUMF design note, TRI–DN–19, 1989.

[87] B.F. Milton, "Central Region Specification - Revision 1", TRIUMF design note, TRI–DN–19, rev. 1, 1989.

[88] W.J. Kleeven and J.B. Pearson, "Acceptance Calculations for Spiral Inflectors", TRIUMF design note, TRI–DN–30, 1989.

[89] R. Baartman, "Space Charge Contribution to ν_z", TRIUMF design note, TRI–DN–17, 1988.

[90] R. Louis, "The Properties of Ion Orbits in the Central Region of a Cyclotron", Ph.D. Thesis, Univ. of British Columbia, Vancouver, 1971.

[91] G.H. MacKenzie, P.W. Schmor and H.R. Schneider, "Cyclotrons", Encyclopedia of Applied Physics, Vol. 4, New York: VCH Publishers Inc., pp. 427–462, 1992.

[92] W.J. Kleeven, "The Influence of Magnetic Field Imperfections on the Transverse Orbit Behaviour in the TR30 H^- Cyclotron", TRIUMF design note, TRI–DN–15, 1988.

[93] W.K. Dehnel, "Design for TR13 Injection Line Quadrupole Magnets", Ebco Technologies design note, EBDN–45–92, 1992.

[94] M. Dehnel, "CRM/TR13 Injection Line", Ebco Technologies design note, EBDN–54–93, 1993.

[95] M. Dehnel, "Injection Beam Matching Techniques", Ebco Technologies design note, EBDN–95–94, 1994.

[96] R. Baartman and D. Yuan, "Space Charge Neutralization Studies of an H^- Beam", *Proc. 1st European Part. Acc. Conf.*, Vol. 2, pp. 949–950, Rome, 1988.

[97] C. Bovet, R. Gouiran, I. Gumowski and K.H. Reich, "A Selection of Formulae and Data Useful for the Design of A.G. Synchrotrons", CERN/MPS-SI/Int. DL/70/4, 1970.

[98] A.J. Otter, "An Injection Quadrupole for the 30 MeV Cyclotron", TRIUMF design note, TRI–DN–11, 1988.

[99] L. Root, R. Laxdal and A. Papash, "TR13 Magnet Design", TRIUMF design note, TRI–DN–14, 1993.

[100] P.W. Allison, J.D. Sherman and D.B. Holtkamp, "An Emittance Scanner for Intense Low-Energy Ion Beams", *IEEE Trans. Nucl. Sci.*, Vol. 30, pp. 2204–2206, 1983.

[101] *Mathematica*® Version 2.2, Wolfram Research, Inc., 100 Trade Center Drive, Champaign, IL 61821–9910.

[102] J.B. Pearson, "The Injected Beam Envelope for a Beam at $\phi^0 = 0°$.", TRIUMF VAX Cluster, SCR0:[PEARSON.RELAX.NEW]RELAX3D_078.OUT;6, 1988.

[103] M. Dehnel, R.J. Dawson, G.M. Stinson, R. Helmer, R. Keitel, D.J. Dale, E.W. Pattyn and A. Wilson, "The Design and Operation of an Industrial Beam Transport System for 15–30 MeV Protons", *IEEE Trans. Ind. App's.*, Vol. 28, No. 6, 1992.

[104] R.E. Laxdal, A. Altman, T. Kadantsev and T. Kuo, "Beam Quality Tests on the TR13 Cyclotron", TRIUMF design note, to be circulated, 1994.

[105] SPYGLASS® TRANSFORM Version 3.0, Spyglass, Inc., 1800 Woodfield Drive, Savoy, IL 61874.

[106] F. Marti and S. Snyder, "Internal Beam Dynamics Studies with a TV Probe", *Proc. 13th Int'l Conf. on Cyclotrons and their Applications*, pp. 435–438, Vancouver, 1992.

[107] L.R. Evans and D.J. Warner, "A Critical Study of Emittance Measurements of Intense Low-Energy Proton Beams", *Nucl. Instr. and Meth.*, Vol. 104, pp. 61–70, 1972.

[108] Veditor™ Version 3.1, New Media Graphics Corporation, 780 Boston Road, Billerica, MA 01821–5925.

[109] OPTIMETRIC™, BioScan® Incorporated, 170 West Dayton, Suite 204, Edmonds, WA 98020.

[110] Harvey Schneider's private center region model (C.R.M.) magnet survey notes, May 1989.

[111] A. Papash, "Radial and Vertical Orbit Behaviour in the TR13 H^- Cyclotron due to Magnetic Field Imperfections", TRIUMF design note, TRI–DN–6, 1993.

[112] B.F. Milton, "A Revised Extraction Calculation for the TR30", TRIUMF design note, TRI–DN–35, 1990.

[113] E.H. Isaaks and R.M. Sribaslava, APPLIED GEOSTATISTICS, London: Oxford University Press, 1989.

APPENDIX I: TRANSOPTR COMMAND FILES

COMMAND FILE: OPTR.LNK

```
$FOR 4q_b9200g_ana
$LINK OPTR,4q_b9200g_ana,scinf,IMSL/LIB
$DELETE/NOCONFIRM 4q_b9200g_ana.OBJ;*
$assign 4qsk.dat sys$input
$assign out.dat sys$output
$run optr
$deassign sys$input
$deassign sys$output
```

DATA FILE: 4QSK.DAT

```
.025 0 0 939.3 1 0.E-12
1 3 0.5 .5E-5
0 -20.
1.4 12.5 2.4 12.5 1. 0.
0
18
2.5  1. 41. 0
-00. -100. 100. 0
48.0 0. 100. 0
50.0 -0. 300. 0
0.02                    0.0 1.0 0
0.0188 -.06 .06 1
10. 5. 15. 0
-0.0561 -.09 .06 1
10. 5. 15. 0
.0600 -.06 .09 1
-.02486 -.06 .06 1
16.4 -0. 50. 0
143.323  -180. 180. 1
 -1.29418 -180. 180. 0
.09 0. 1. 0
1.0                     0.0 1.0 0
2.0                     0.0 3.0 0
0.0                     0.0 1.0 0
3.E-4 400 1.
0
```

SYSTEM SUB-ROUTINE FILE: 4Q_B9200G_ANA.FOR

```
      SUBROUTINE SYSTEM
      COMMON /MOM/P,BRHO
      COMMON /PRINT/IPRINT
      COMMON /SIGS/SX(6,6)
      COMMON /BLOC1/X,XP,EX,D0,WW,Q0,
     *D1,Q1,D2,Q2,Q3,D3,TWIST,THETA,EN,W,EXP,PR
      REAL A(6,6)
      REAL B(6,6)
      REAL C(6,6)
      REAL D(6,6)
      REAL E(6,6)
      REAL F(6,6)
      REAL G(6,6)
Remember: each row is a column and units are cm, ,cm, ,cm, .
    RR(120,0) BEAMLINE COORDINATES PRIOR TO INFLECTOR
      DATA A/  .99968, -.00061, -.01981, -.01921, 0.0, 0.0,
     ,      3.9883, .9973, -.0870, -.1005, 0.0, 0.0,
     ,      .01981, .01921, .99968, -.00061, 0.0, 0.0,
     ,       .0870, .1005, 3.9883, .9973,0 .0, 0.0,
     ,        0.0   , 0.0    , 0.0    , 0.0    , 1.0    , 0.0,
     ,       .0, 0.0, 0.0, 0.0, 3.9896, 1.0/
    R(240,120) BEAMLINE COORDINATES PRIOR TO INFLECTOR
      DATA B/  .97980, -.01620, -.12258, -.05071, -.00006, -.00003,
     ,      3.87732,  .89169, -.80044, -.48004,  .00004,  .00002,
     ,       .12258,  .05071,  .97980, -.01621, -.00006, -.00003,
     ,       .80044,  .48004, 3.87733,  .89169,  .00004,  .00002,
     ,      0.0, 0.0, 0.0, 0.0, 1.0, 0.0,
     ,      0.0, 0.0, 0.0, 0.0, 3.9896, 1.0/
    R(317,240) BEAMLINE COORDINATES PRIOR TO INFLECTOR
      DATA C/  .99464, -.00527, -.03767, -.03663, -.00004, -.00004,
     ,        2.48381,  .88653, -.57255, -.49363, -.00009, -.00007,
     ,         .03767,  .03778,  .99464, -.00778, -.00001, -.00002,
     ,         .57255,  .49627, 2.48381,  .88214, -.00004, -.00004,
     ,      0.0, 0.0, 0.0, 0.0, 1.0, 0.0,
     ,      0.0, 0.0186, 0.0, 0.0, 2.5603, 1.0/
    R(367,317) ROTATED COORDINATES INSIDE INFLECTOR
      DATA D/  .48785, -.09839,  .81684, -.04813,  .46980,  .18367,
     ,      1.06671,  .66020, 1.18593,  .51449,  .61278,  .40591,
     ,      -.78341,  .17840,  .55290,  .03593, -.40700, -.29975,
     ,     -1.13683, -.35373, 1.14434,  .85791, -.44368, -.43606,
     ,      0.0, 0.0, 0.0, 0.0, 1.0, 0.0,
     ,      -.27504, -.58808, -.10836, -.10577, 1.59310, .89445/
    R(417,367) ROTATED COORDINATES INSIDE INFLECTOR
      DATA E/  .35780,  .19501, 1.01296,  .05910,  .24849, -.22188,
     ,       .65650,  .38352, 1.36948,  .76821,  .66010,  .30175,
     ,      -.60120,  .55794,  .37860, -.05525, -1.01069, -.27637,
     ,     -1.13748, -.13996,  .89798,  .58182, -1.00042, -.52463,
     ,      0.0, 0.0, 0.0, 0.0, 1.0, 0.0,
     ,      -.97305, -1.24214, -.49622, -.27514, 1.12565, .56254/
    R(467,417) ROTATED COORDINATES INSIDE INFLECTOR
      DATA F/  .79541,  .00088,  .65029,  .23778, .76297, -.27744,
     ,      1.12273,  .31503,  .72254,  .59637, 1.12773, .25955,
     ,       .01259,  .52772,  .80023, -.15505, -.74283, -.00084,
     ,      -.24805,  .23627, 1.48904,  .79736, -.69545, -.05357,
     ,      0.0, 0.0, 0.0, 0.0, 1.0, 0.0,
     ,     -1.39563, -1.45636,  .02781,  .03622, .76589, .65967/
    R(485,467) BACK TO UNROTATED COORDINATES AT INFLECTOR EXIT
      DATA G/  .75207,  .03218, -.62258,  .02513,  .08429, -.21210,
```

```
     ,      .51329,  .78309, -.39455, -.61477,  .05614, -.02897,
     ,      .62874,  .03025,  .74495, -.08479, -.18379,  .01585,
     ,      .43931,  .66237,  .44206,  .74806, -.05408, -.02812,
     ,     0.0, 0.0, 0.0, 0.0, 1.0, 0.0,
     ,     -.06153, -.05689,  .12996,  .28808,  .59040, 1.00755/
      Y=X
      YP=XP
      IPR=0
      IF(PR.NE.0.)IPR=1
      NEX=JNINT(EXP)
      W1=SQRT(1.-EN)
      W2=SQRT(EN)
      TH1=90./W1
      TH2=90./W2-TH1
      SX(1,1)=X**2/100.
      SX(1,2)=X*XP/1.E4
      SX(2,1)=SX(1,2)
      SX(2,2)=((EX/1.E4)**2+SX(1,2)**2)/SX(1,1)
      SX(3,3)=Y**2/100.
      SX(3,4)=Y*YP/1.E4
      SX(4,3)=SX(3,4)
      SX(4,4)=((EX/1.E4)**2+SX(3,4)**2)/SX(3,3)
      CALL DR(0.,IPR,IPR)
      D11=D1/2
      CALL DR(D0,IPR,IPR)
      CALL RT(THETA,IPR,IPR)
      DO  12 I=1,2
   12 CALL Q(Q0,2.5,D11,IPR,IPR)
      CALL RT(-THETA,IPR,IPR)
      CALL DR(2.3,IPR,IPR)
      DO  13 I=1,2
   13 CALL Q(Q1,2.5,D11,IPR,IPR)
      CALL DR(2.3,IPR,IPR)
      CALL FIT(1,3,3,0.,WW,NEX)
      CALL FIT(1,1,1,0.,WW,NEX)
      DO  14 I=1,2
   14 CALL Q(Q2,2.5,D11,IPR,IPR)
      CALL DR(2.3,IPR,IPR)
      DO  15 I=1,2
   15 CALL Q(Q3,2.5,D11,IPR,IPR)
      CALL RT(TWIST,IPR,IPR)
      CALL TMAT(A,IPR,IPR)
      CALL TMAT(B,IPR,IPR)
      CALL TMAT(C,IPR,IPR)
      CALL TMAT(D,IPR,IPR)
      CALL TMAT(E,IPR,IPR)
      CALL TMAT(F,IPR,IPR)
      CALL TMAT(G,IPR,IPR)
      WX=W*SQRT(W1)
      WY=SQRT(W2)
      CALL FIT(1,1,1,0.,1.05*WX,NEX)
      CALL FIT(1,3,3,0.,WY,NEX)
      CALL BE(1.9,TH1,EN,IPR,IPR)
      CALL FIT(1,1,1,0.,1.05*WX,NEX)
      CALL BE(1.9,TH2,EN,IPR,IPR)
      CALL FIT(1,3,3,0.,WY,NEX)
      ANG=9./W2
      DO 22 I=1,20
   22 CALL BE(1.9,ANG,EN,IPR,IPR)
      RETURN
      END
```

APPENDIX II: THE C.R.M. AND ITS CALIBRATIONS

II.1 THE C.R.M. CYCLOTRON SYSTEM

The major sub-systems of the C.R.M. cyclotron system include the ion source, the injection line, the vacuum devices, the diagnostic equipment and the cyclotron itself. The following paragraphs describe these sub-systems.

The H^- type of ion source described in section 2.2.1 is the type used in the C.R.M. facility. The ion source sub-system comes complete with a high voltage cage in which power supplies and the ion source operate at a biased potential of –25 kV with respect to ground. A fiber-optic light link permits the system operator to adjust the various ion source power supplies from a control panel at ground potential. The control panel has hard wired feedback control circuitry to maintain the arc current at any desired setting. The ion source is provided with a number of insulated water cooling lines, and a hydrogen feed line. It is mounted to a diagnostic box to which the source lenses are attached. The diagnostic box is designed to maintain differential pumping between the relatively low vacuum environment of the ion source extraction region (10^{-4} Torr) and the relatively high vacuum environment of the injection line (10^{-6} Torr). A compact industrial programmable logic computer (PLC) monitors the water flow rates, the integrity of the high voltage cage, and the vacuum gauge readings. It is programmed to appropriately interlock the system devices if a fault should occur.

The ion source diagnostic box is mounted on rails so that its position can be varied according to the needs of the particular injection line being tested. As its name indicates, the diagnostic box can be fitted with various beam diagnostic devices. The standard diagnostic devices are a beamstop with collimator and secondary electron screen, and an emittance scanner of type [100]. Other devices which have been mounted for special experiments are a four-jawed collimator for beam centering, a Faraday cup for calibrating the beamstop, a scintillator for measuring the size of the beam in two dimensions, and a water-cooled pinhole collimator mounted on a vacuum feedthru micrometer for the production of beamlets used in center region scintillator experiments. The diagnostic box also contains the extraction lenses for the ion source, one xy beam steering magnet and can be outfitted with permanent magnet solenoids for extra beam focusing.

The overall C.R.M. vacuum system is divided into two parts. The ion source and diagnostic box have a roughing pump, a turbo pump, and a cryo-pump for their vacuum needs. The ion source and diagnostic box vacuum environment can be isolated from the rest of the injection line and the C.R.M. main tank vacuum by a gate valve. As well, the cryo-pump is separated from the diagnostic box by a large gate valve, so that it is only used when the box has already been brought to a rough vacuum of about 20 mTorr or better.

The main C.R.M. vacuum tank is serviced by two large 8" diameter cryo-pumps and a roughing pump. The main tank vacuum environment is connected to the injection line vacuum environment through the inner ends of the valleys and the inflector aperture. The inflector aperture is small and the valley ends are at right angles to the injection line beampipe, so the two vacuum regions are somewhat de-coupled from each other. Each of the cryo-pumps can be isolated from the main tank by their respective gate valves.

Both the diagnostic box and the main tank vacuum regions are monitored by Convectron gauges for high pressure readings and by ion gauges for low pressure readings. The PLC uses the gauge readings to properly interlock the various components of the vacuum system. For example, the gate valve between the diagnostic box and the injection line cannot be opened unless the vacuum readings on either side of the gate valve are of the same order of magnitude.

The injection line portion of the C.R.M. is made up of a beam pipe from the downstream side of the injection system gate valve to the inflector entrance, and an array of focusing and/or steering magnets for transporting the beam to the inflector. In the SQQ configuration there is one xy beam steering magnet, one solenoid magnet, one long quadrupole magnet and one short quadrupole magnet. In the 4Q, 3Q and 2Q configurations the quadrupoles are identical, and no steering magnets are used.

The C.R.M. inflector is as described in section 2.2.3. The rectangular entrance of the inflector is oriented with the 17 mm long electrode edges at 14° to the vertical. The entrance gap is 8 mm and the electrodes are held at approximately +7.5 kV and −7.5 kV, respectively. The entrance of the inflector is protected by a water-cooled collimator whose rectangular aperture dimensions are 14 mm by 6 mm.

The C.R.M. cyclotron accelerates the H^- beam through 5.5 turns to an energy of 1.125 MeV. This corresponds to a radius of approximately 13 cm for the nominal magnetic field strength of 12 kG. The magnet has a four sector geometry with poles of radius 16 cm. Acceleration is provided by two 45° dees located in opposite valleys within the magnet. The peak voltage attained by the RF is about 50 kV for an energy gain per turn of 200 kV. The RF operates at about 73 MHz and the RF power is transmitted to the dees via a capacitive coupling to a 50 ohm transmission line that passes through the vacuum wall. The RF amplifier operates in a self-excited mode, as opposed to a driven mode as is done in the TR30 or TR13.

The C.R.M. cyclotron comes equipped with a number of diagnostic devices. For dc beam current measurements at the inflector exit, a beamstop with current readout and secondary electron traps can be installed. As well, a similar beamstop is located at turn 5.5 to stop the beam at 1.125 MeV and to provide a current readout. Computer controlled diagnostic probes are located in each of the unoccupied valleys. These probes can be translated radially and each has fixtures which provide integral and differential beam current readings. In fact, one such probe is outfitted with a differential three-finger scanning head whose current readbacks provide beam information in the vertical (axial) plane, as well as the radial.

II.2 C.R.M. SYSTEM CALIBRATIONS

System calibrations were undertaken prior to conducting experiments. The nameplate accuracy of the readback information from most devices was sufficiently high to make detailed calibration measurements unnecessary. However, the custom designed readback meters for the power supplies in the high voltage cage, the hydrogen flow rate meter, and the beam current diagnostic devices required careful calibration. All measured values are presented in their corrected form within this thesis.

II.2.1 HIGH VOLTAGE CAGE POWER SUPPLIES

The arc, filament, plasma and extractor power supplies all reside in the high voltage cage. The readback and setpoint control signals for these supplies are brought out to the main control rack via a fiber optic link. A custom made electronic conversion unit translates the optical signals into impulses which can be displayed on digital meters. Unfortunately, the control rack meter readings could not be readily made to match the readings on the power supply displays. Consequently, the power supply display readings as a function of control panel meter readings were tabulated, and graphed. Figures II.1 through to II.6 illustrate the calibration curves for the arc current, the arc voltage, the plasma current, the plasma voltage, the filament current and the extractor voltage, respectively. All the calibration curves are shown to be very linear.

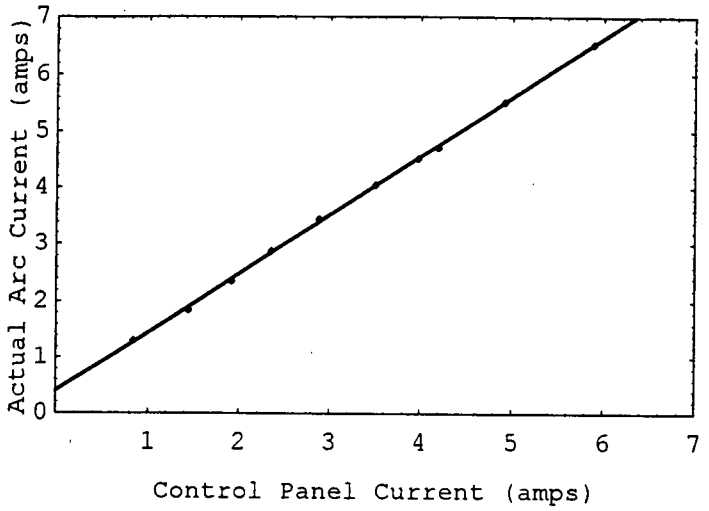

Figure II.1: *Arc current calibration curve.*

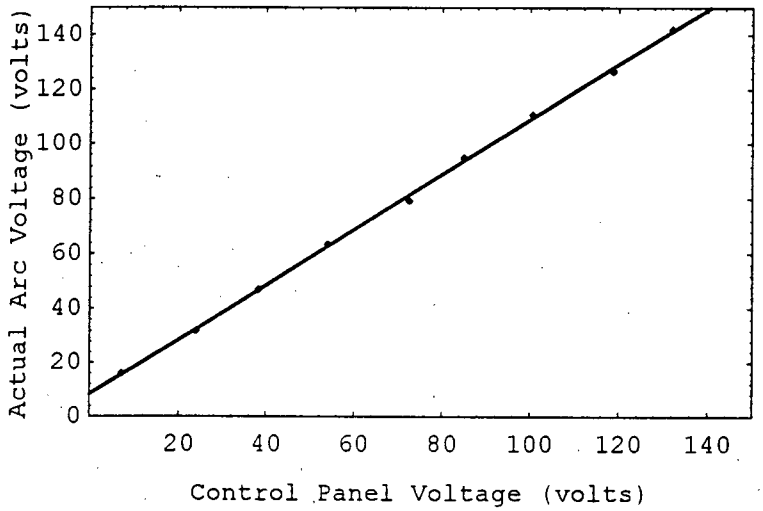

Figure II.2: *Arc voltage calibration curve.*

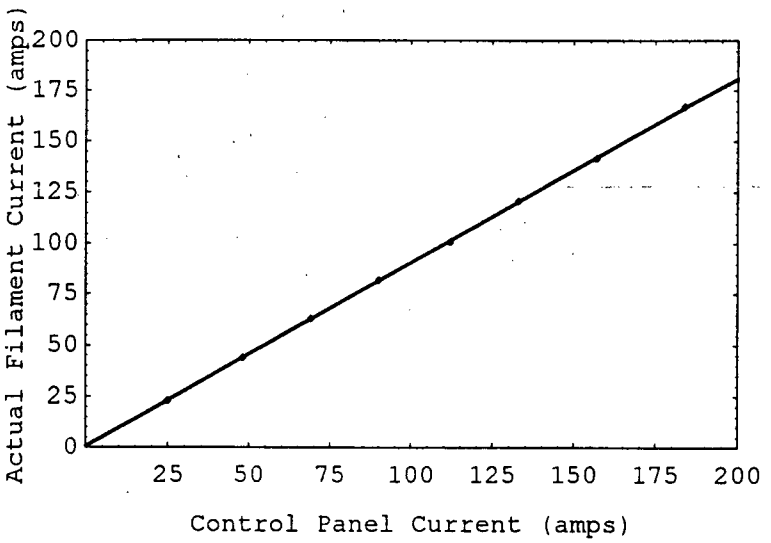

Figure II.3: *Filament current calibration curve.*

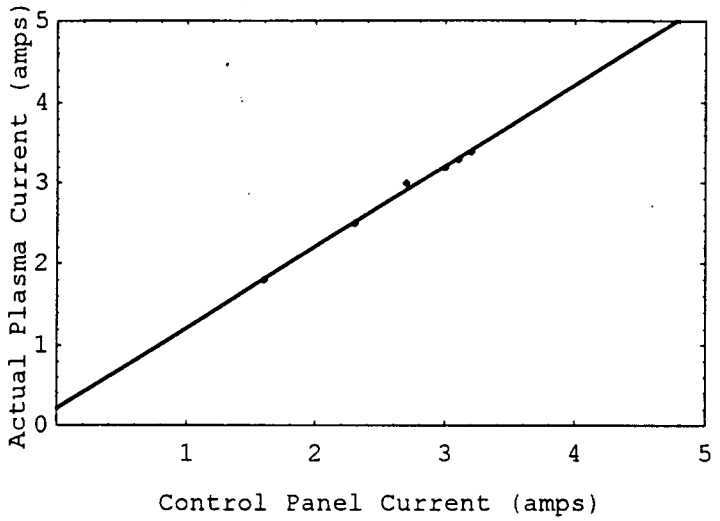

Figure II.4: *Plasma current calibration curve.*

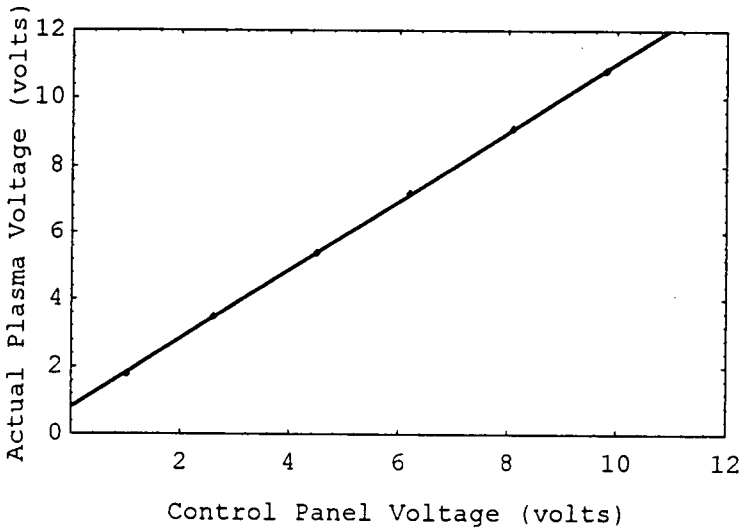

Figure II.5: *Plasma voltage calibration curve.*

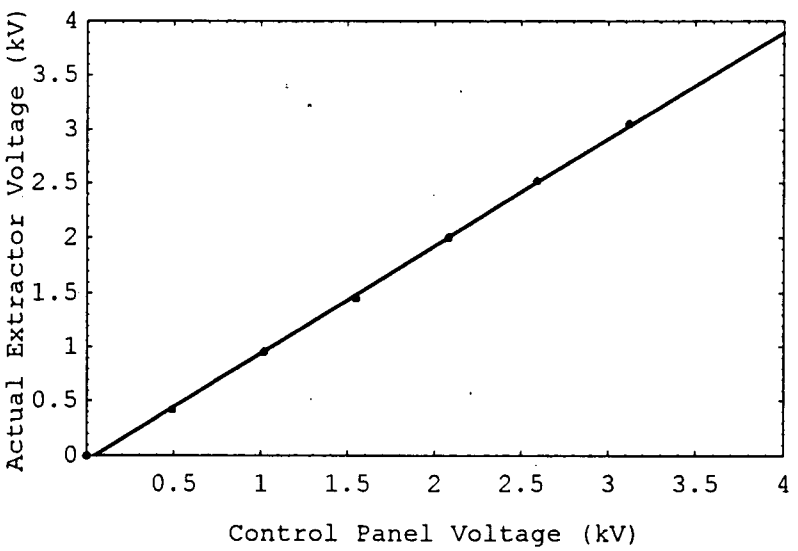

Figure II.6: *Extractor voltage calibration curve.*

II.2.2 HYDROGEN FLOW RATE METER

The hydrogen gas flow rate into the ion source was regulated by a mass flow controller and the flow rate was displayed on a custom designed digital output meter. The meter readings are compared to the actual flow rate measurements in Figure II.7. The actual flow rate was determined by measuring the amount of water displaced from a calibrated beaker by the hydrogen gas over a period of time at standard temperature and pressure.

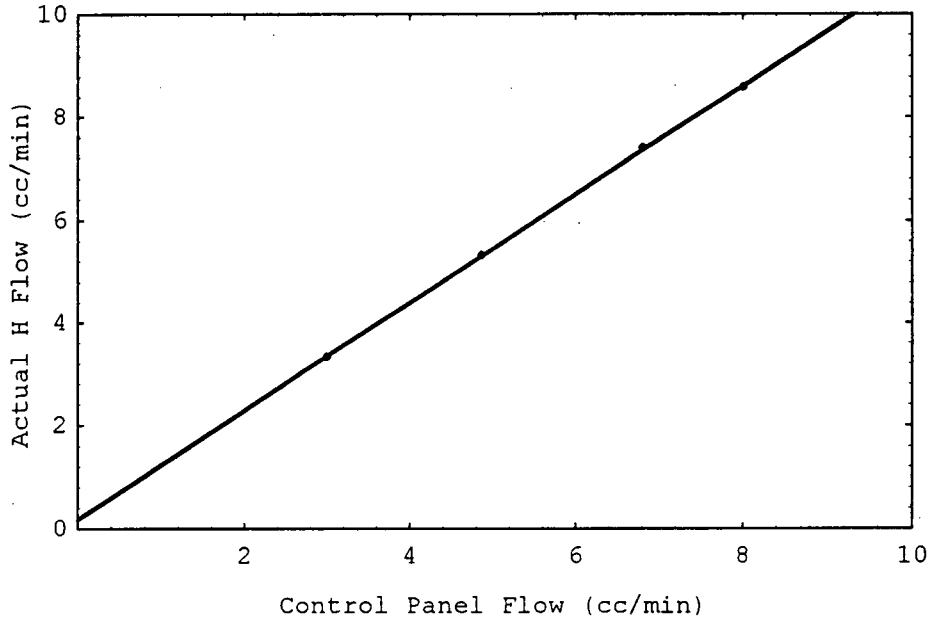

Figure II.7: *Hydrogen flow meter calibration curve.*

The turbo-pump backing pressure reading (convectron gauge) and the upstream diagnostic box pressure reading (ion gauge) were found to be linearly related to the hydrogen flow rate, and, therefore, these readbacks provided useful diagnostic information above and beyond that required for the vacuum system. The calibration curves for these two readbacks are shown in Figures II.8 and II.9.

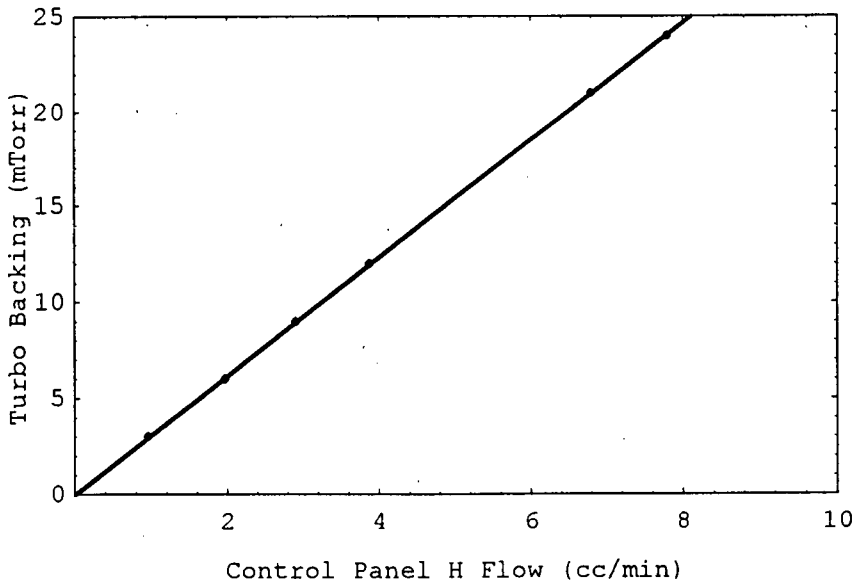

Figure II.8: *Turbo-pump backing pressure as a function of hydrogen flow rate.*

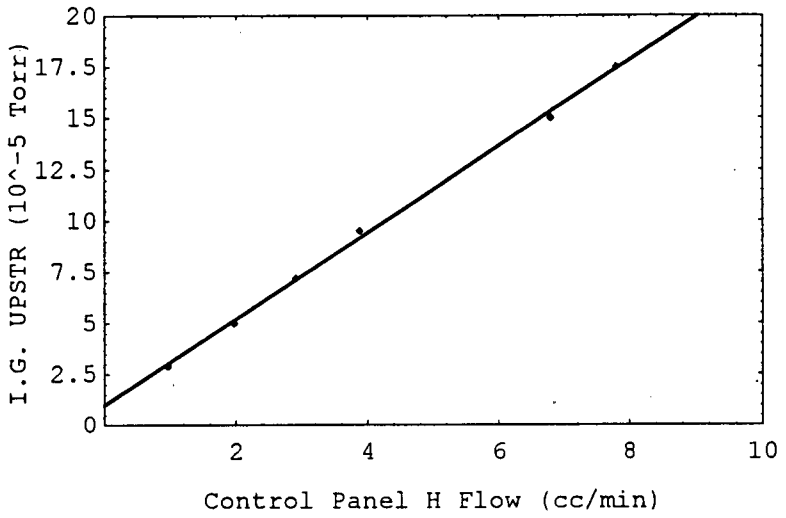

Figure II.9: *Upstream diagnostic box ion gauge (I. G.) pressure as a function of hydrogen flow rate.*

II.2.3 BEAM DIAGNOSTIC DEVICES AND METERS

Errors in H^- beam current readings can be introduced from a number of sources. One obvious potential source of error is the calibration of the current meters. On a more subtle level, the beam current reading devices must be properly biased to read the correct amount of H^- current. A bias voltage is often needed to ensure that secondary electrons emitted as a result of the collisions of the beam ions with the diagnostic device are captured.

II.2.3.1 Beam Current Meters

The five digital beam current meters in the control rack were each checked with respect to a high precision Keithley meter. Table II.1 lists the results of the comparison. The scale factor is the number which each meter's reading must be multiplied by in order to obtain the same reading as the Keithley meter.

Table II.1: *Beam current meter calibration factors.*

BEAM CURRENT METER	SCALE FACTOR
Channel 1	1.40
Channel 2	1.08
Channel 3	Not Used
Channel 4	1.04
Channel 5	1.85

The current meters had zero offset correction and the scale factors were accurate to $\pm$ 0.5%.

II.2.3.2 Faraday Cup

The Faraday cup used in these experiments is a device that can measure the absolute magnitude of the H^- beam current to within a few percent. Its primary use was to corroborate the beam current measurements of the combined function diagnostic box beamstop and collimator probe which was the diagnostic tool most used on a day to day basis. A schematic of the Faraday cup is illustrated in Figure II.10.

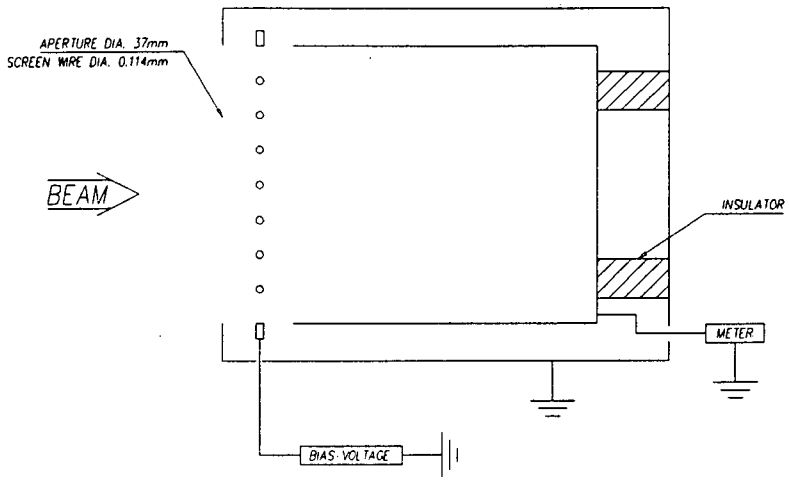

Figure II.10: *Faraday cup assembly.*

The Faraday cup entrance screen was negatively biased so that free electrons outside the cup were repelled from the cup, and free positive ions were removed from the environment by the screen. The beam had sufficient energy to pass through the potential barrier provided by the screen, but the screen had a sufficient negative voltage bias to force any secondary electrons liberated by the incident beam to return to the cup from whence they came. The Faraday cup gave beam current readings which were accurate to within ± 2% of the absolute current.

The Faraday cup was positioned so that its aperture was centered on the beam axis and mounted at the downstream end of the diagnostic box during normal operation. Figure II.11 shows the measured beam current from the cup as a function of the bias voltage applied to the screen. A screen bias of between −50 and −300 volts was sufficient to yield consistent results. Readily accessible 300 volt batteries were eventually chosen as the standard for providing the Faraday cup bias.

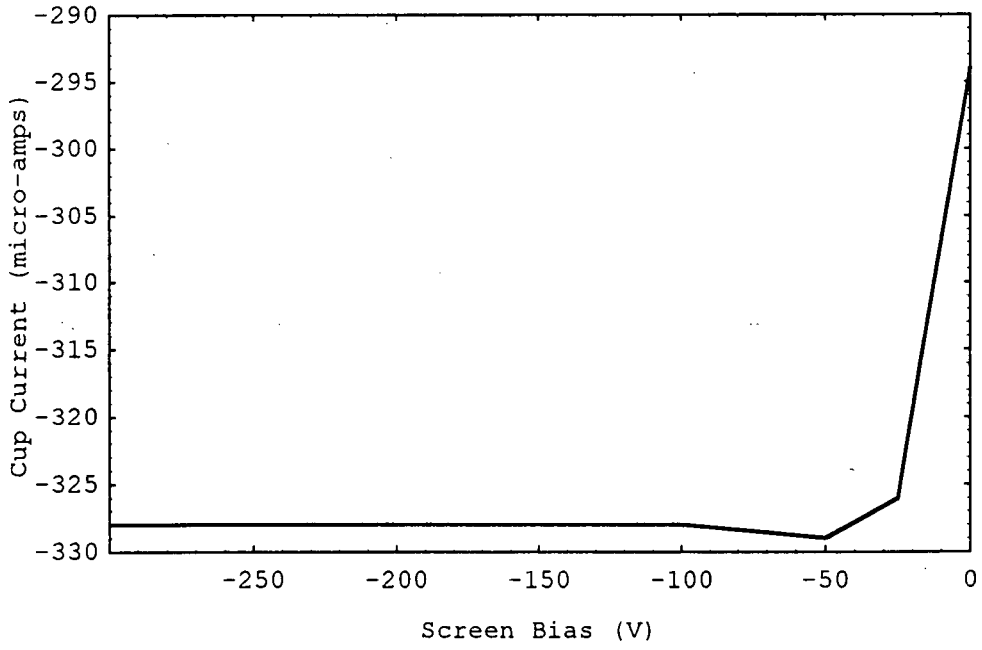

Figure II.11: *The Faraday cup beam current readback as a function of screen bias.*

II.2.3.3 Ion Source Beamstop

The ion source beamstop (IBS) is an air-actuated water-cooled beamstop complete with a collimator and a secondary electron screen. A schematic of the device is shown in Figure II.12. The IBS was useful as it facilitated local optimization of the ion source beam. Once the ion source settings were adjusted so that the beam current was maximized and the beam position was centered with respect to the collimator aperture, the IBS was pneumatically removed from the beam path.

A number of possible voltage bias schemes could have been used on the IBS elements. For example, positive or negative biases could have been used, elements could have been shorted together or left floating, and of course the ratio and magnitude of the bias voltages could have been varied. It turned out that the summed beam current readback from the collimator and the beamstop varied by up to a factor of three from the Faraday cup readback depending on the biasing scheme. Figure II.12 illustrates the voltage bias scheme that produced beam current readback results in good agreement with the Faraday cup readings. Figure II.13 shows the beam current readback results for the collimator, the beam stop and the sum of the collimator and beamstop as a function of the bias voltage on the collimator. Of significant importance is that the summed current varied by only ± 0.6% over the full range of the collimator bias voltage changes, and the average value of the summed current was within 1.0 % of the Faraday cup measurement of the full beam current.

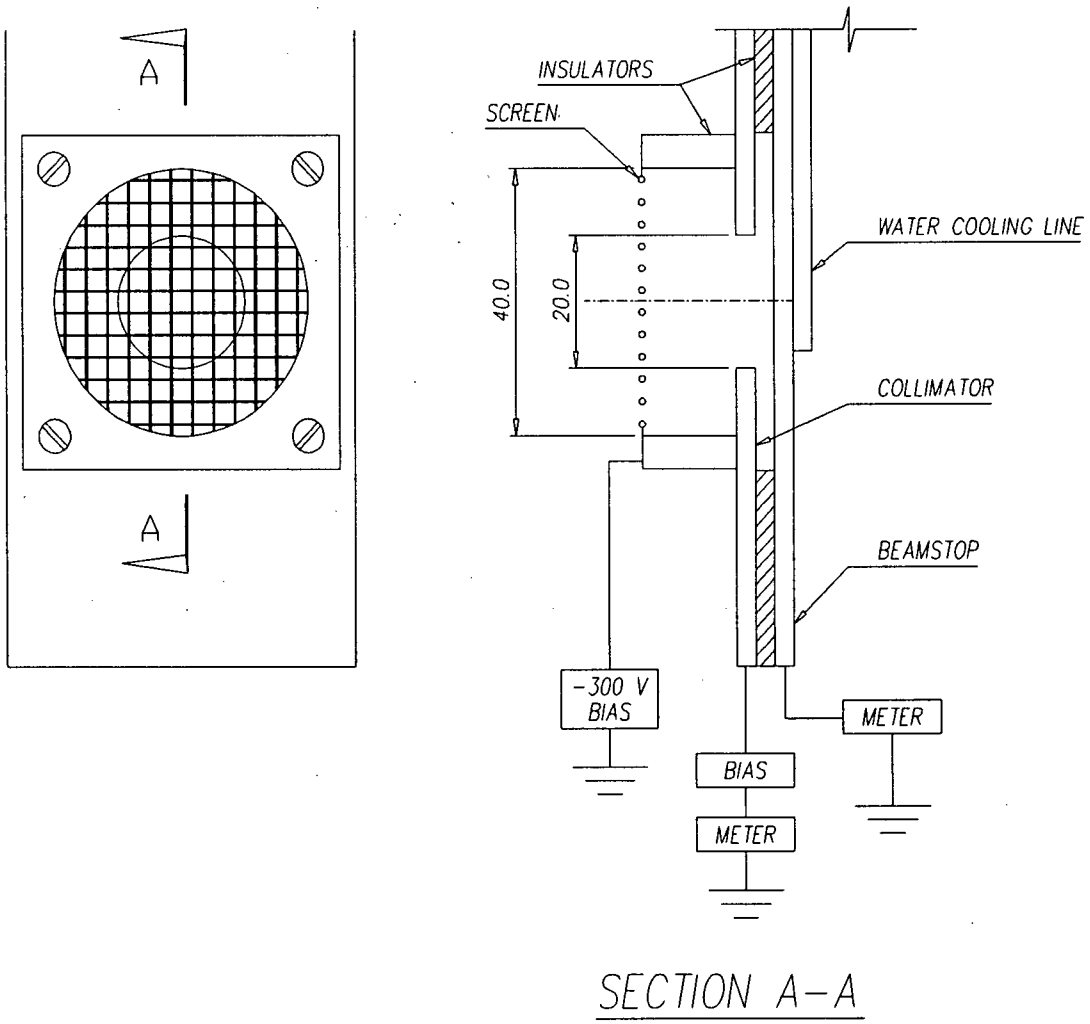

Figure II.12: *Ion source beamstop assembly. Dimensions in millimetres.*

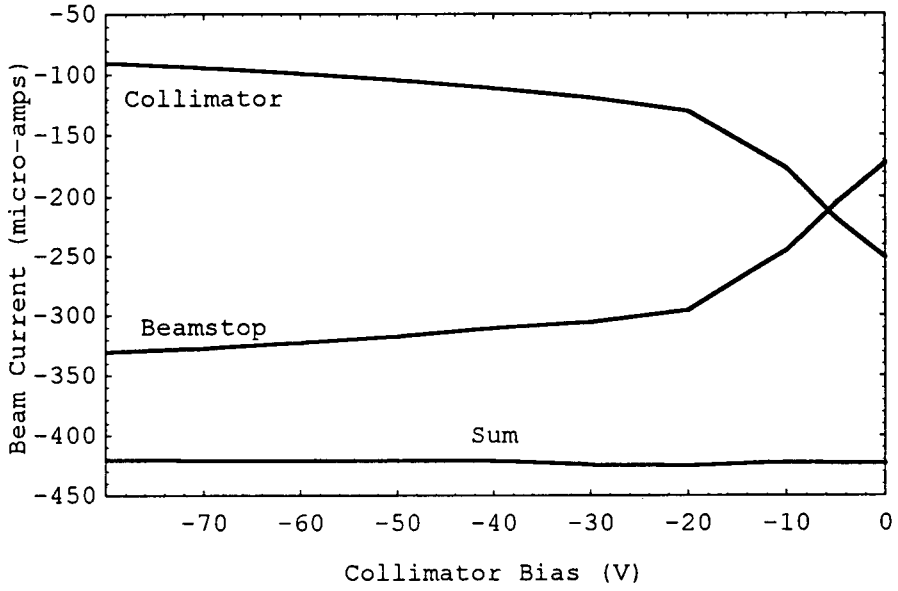

Figure II.13: *Ion source beamstop current readbacks as a function of collimator bias voltage.*

In summary, a collimator bias voltage of about −30 volts gave a reasonable collimator to beamstop current ratio, and the sum current very closely approximated the Faraday cup total current reading. In terms of beam transmission experiments, an accurate sum current was very important. However, the separate collimator and beamstop current readback results were useful during beam centering and beam focusing adjustments.

II.2.3.4 Injection Line Collimators

Two types of injection line collimators were used. One of these collimators was the inflector entrance collimator, and the other was a four-jawed collimator which was mounted at a number of places within the injection line at different times.

The inflector entrance collimator was water-cooled and had a rectangular aperture measuring 14 mm by 6 mm. The collimator was biased by a positive voltage of between 45 and 300 volts depending on the types of batteries available. The collimator current readback registered zero when the beam current was off indicating that free electrons were absent in this region of the injection line. With the collimator biased the beam could be very accurately centered within the aperture by minimizing the beam spilled onto the collimator. Very slight changes in the focus of the beam were ascertained by monitoring the beam spill as a function of perturbations in the injection line magnet settings. This level of information was sufficient for the injection line experiments.

The four-jawed collimator was not water-cooled and had a 7 mm diameter aperture. This collimator was used to center the beam within the injection line. This was accomplished by centering the collimator within the injection line and then tuning the beam so that it was centered within the collimator. This was deduced by balancing the left/right/top/bottom current readbacks. This process was then repeated at another point within the injection line. In this manner injection line magnet and ion source settings were found which gave a centered beam. This collimator could have each jaw individually biased with equal

bias voltages ranging in value between 45 and 300 volts, or the jaws could be shorted together and biased by a single voltage. The effectiveness of this collimator and this centering technique was confirmed by removing the collimator and then using the new found ion source and injection line magnet settings to transport the beam through the inflector without significant re-adjustment of the magnet settings.

II.2.3.5 C.R.M. Cyclotron Internal Fixed Beamstops

Two fixed beamstops were used within the C.R.M. cyclotron. One such beamstop is the inflector exit beamstop, and the other is the 1.125 MeV beamstop.

The inflector exit beamstop was mounted approximately one sixth of a turn (20 mm) downstream of the inflector exit. The device was not water-cooled, so high current beams could only be stopped for short periods of time. The beamstop was 17 mm wide, 20 mm high and used overhanging electron catchers as shown in Figure II.14. The maximum energy of the secondary electrons was on the order of tens of electron volts and the radius of curvature of such electrons in a 12 kiloGauss magnetic field is a few hundredths of a millimeter. Thus, any secondary electrons emitted from the beamstop spiral along the magnetic field lines with a very tight radius of curvature eventually striking the catchers. All of the secondary electrons were captured in this manner and, thus, the absolute accuracy of the current measurement was very good. This was verified by applying a positive bias voltage to the beamstop and noting that the beam current readback remained the same to within ± 1%.

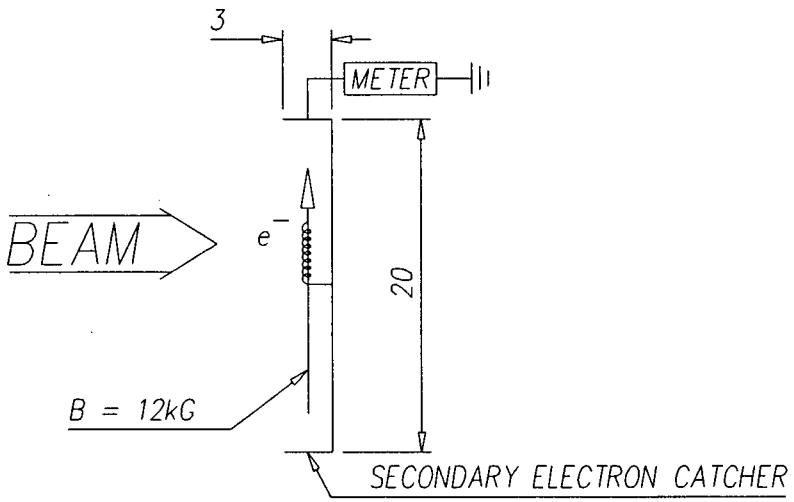

Figure II.14: *Inflector exit beamstop.*

The 1.125 MeV beamstop was a cylindrical water-cooled probe of diameter 15 mm. Unfortunately, this probe did not come complete with overhanging secondary electron catchers. However, when the beam current readback from this beamstop biased at 300 volts was compared to the case where temporary overhanging secondary electron catchers were used, agreement to within ± 1% was found. All experiments were conducted with the original probe biased at 300 volts.

II.2.3.6 Emittance Scanner

This scanner could calculate the two dimensional beam emittance in either the (x, x') or (y, y') planes. As well, it could measure the phase-space density contours in these planes, and the beam intensity profile as a function of either (x) or (y).

In terms of measuring the (x, x') phase space density contours, for example, the scanner presented a narrow vertical slit to the beam which was tall enough to allow the full vertical height of the beam to pass

through. At each point (x) along the beam, the collimated narrow vertical strip of beam was deflected by electric deflection plates and the portion of the strip of beam which managed to pass through a second narrow vertical slit was measured in a beamstop. The voltage of the electric deflection plates was related to the divergence of the beam, and, thus, at each (x) determined by the slit position in the horizontal direction and at each (x') determined by the deflection voltage, a beam intensity measurement was made that was proportional to $d^2i/dxdx'$. A phase space density contour map was made by accumulating the intensity information over the complete (x, x') extent of the beam.

The translational accuracy of the scanner was to within ± 0.05 mm and the angular accuracy was to within ± 0.5 mrad. The total integrated current measured by the device agreed with the Faraday cup readings when divided by 1.07. In terms of the reliability of phase space contour measurements, the experiments of [100] showed that excellent agreement between measured phase space contours and those of physically prepared beams was obtained.

II.2.4 ION SOURCE LENS SPACING

In Figure 4.4 a nominal lens distance "d" is given. This distance is the sum of the plasma lens width "w" and the plasma lens to extraction lens spacing "s". These lengths varied as a function of the particular ion source configuration under investigation. Table II.2 lists "w" and "s" as a function of each ion source configuration.

Table II.2: *"w" and "s" dimensions as a function of ion source configuration.*

ION SOURCE CONFIGURATION	w (mm)	s (mm)
L155/PL10.8/EL10/NL	3.0	3.5
L155/PL10/EL10/NL	2.8	2.5
L155/PL9/EL10/NL	3.1	2.5
L155/PL8/EL10/NL	3.1	2.5
L155/PL10/EL10/WL	2.8	2.5
L155/PL9/EL10/WL	3.1	2.5
L155/PL8/EL10/WL	3.1	2.5
L155/PL8/EL8/NL	3.1	2.5
L155/PL6/EL8/NL	3.0	2.5
L155/PL8/EL8/WL	3.1	2.5
L155/PL6/EL8/WL	3.0	2.5
L105/PL8/EL8/WL	3.1	2.5

The plasma electrode aperture was counterbored at an angle of 30°. The distance between the second electrode and the extraction electrode was 18 mm.

II.2.5 KRIGING

The commercial software package Transform [105] does not describe kriging in detail. Refer to [113] for a detailed description of this technique used in sections 4.7.3 and 4.7.4.

APPENDIX III: CASINO COMMAND FILES

1. B Field Data File: MAP29_DIGI.ZFLD, E Field Data File: ANALYTIC

```
12., -1., .025, 939.277, 1.0,                !B0, q, Energy, E0, convert
14.0, 2.5, 2.5, 0.15, 0.973,                 !zint, zinf, max_radius, fringe_constant, exit_fudge
-1, 4, 40,                                   !nstep, nprint, nafter
2.5, 0.0, 1.0, 0.4,                          !A, einf, emult, spacing
0.83, 2.5, 2.5,                              !tilt, tilt_numerator, tilt_denominator
T, T, T, F, F,                               !kick, ltaper, linear, lcompare, lfringe
6, 8, 9, 11,                                 !print_options
map29_digi.zfld
ANALYTIC
0.01, -0.00, 0.000, -0.000, 0.000,           !u, -h, pu, -ph, pv
0.00, -0.01, 0.000, -0.000, 0.000,           !u, -h, pu, -ph, pv
0.00, -0.00, 0.001, -0.000, 0.000,           !u, -h, pu, -ph, pv
0.00, -0.00, 0.000, -0.001, 0.000,           !u, -h, pu, -ph, pv
0.00, -0.00, 0.000, -0.000, 0.001,           !u, -h, pu, -ph, pv
```

2. B Field Data File: T32_I_SMALL.ZFLD, E Field Data File: ANALYTIC

```
12., -1., .025, 939.277, 1.0,                !B0, q, Energy, E0, convert
3.5, 2.5, 2.5, 0.15, 1.0,                    !zint, zinf, max_radius, fringe_constant, exit_fudge
-4, 4, 140,                                  !nstep, nprint, nafter
2.64, 0.0, 1.0, 0.4,                         !A, einf, emult, spacing
0.83, 2.5, 2.5,                              !tilt, tilt_numerator, tilt_denominator
T, T, T, F, T,                               !kick, ltaper, linear, lcompare, lfringe
6, 8, 9, 11,                                 !print_options
T32_I_SMALL.ZFLD
ANALYTIC
0.01, -0.00, 0.000, -0.000, 0.000,           !u, -h, pu, -ph, pv
0.00, -0.01, 0.000, -0.000, 0.000,           !u, -h, pu, -ph, pv
0.00, -0.00, 0.001, -0.000, 0.000,           !u, -h, pu, -ph, pv
0.00, -0.00, 0.000, -0.001, 0.000,           !u, -h, pu, -ph, pv
0.00, -0.00, 0.000, -0.000, 0.001,           !u, -h, pu, -ph, pv
```

3. B Field Data File: T32_I_SMALL.ZFLD, E Field Data File: INF_RELAX_014

```
12., -1., .025, 939.277, 1.0,                !B0, q, Energy, E0, convert
3.5, 2.5, 2.5, 0.15, 1.0,                    !zint, zinf, max_radius, fringe_constant, exit_fudge
-4, 4, 10,                                   !nstep, nprint, nafter
2.64, 0.0, 0.986, 0.4,                       !A, einf, emult, spacing
-0.84, 2.5, 2.5,                             !tilt, tilt_numerator, tilt_denominator
T, T, T, F, T,                               !kick, ltaper, linear, lcompare, lfringe
6, 8, 9, 11,                                 !print_options
T32_I_SMALL.ZFLD
prv24:[milton.inf_relax]inf_relax_014
0.01, -0.00, 0.000, -0.000, 0.000,           !u, -h, pu, -ph, pv
0.00, -0.01, 0.000, -0.000, 0.000,           !u, -h, pu, -ph, pv
0.00, -0.00, 0.001, -0.000, 0.000,           !u, -h, pu, -ph, pv
0.00, -0.00, 0.000, -0.001, 0.000,           !u, -h, pu, -ph, pv
0.00, -0.00, 0.000, -0.000, 0.001,           !u, -h, pu, -ph, pv
```

APPENDIX IV: SYMPLECTIC CONDITIONS

In Chapter 2 (equation 2.18) it was shown that the determinant of a linear transport matrix must equal one if the transport system is described by a Hamiltonian. This condition ensures that Liouville's theorem is upheld. Additional conditions, called symplectic conditions, are also satisfied by a linear transport matrix if it properly describes ion-optical motion in terms of canonical variables.

The symplectic conditions are the following (refer to [55] for a derivation of these conditions):

$$S1 = R_{11}R_{22} - R_{21}R_{12} + R_{31}R_{42} - R_{41}R_{32} = 1 \quad \text{(IV.1)}$$
$$S2 = R_{13}R_{24} - R_{23}R_{14} + R_{33}R_{44} - R_{43}R_{34} = 1 \quad \text{(IV.2)}$$
$$S3 = R_{11}R_{23} - R_{21}R_{13} + R_{31}R_{43} - R_{41}R_{33} = 0 \quad \text{(IV.3)}$$
$$S4 = R_{11}R_{24} - R_{21}R_{14} + R_{31}R_{44} - R_{41}R_{34} = 0 \quad \text{(IV.4)}$$
$$S5 = R_{12}R_{24} - R_{22}R_{14} + R_{32}R_{44} - R_{42}R_{34} = 0 \quad \text{(IV.5)}$$
$$S6 = R_{12}R_{23} - R_{22}R_{13} + R_{32}R_{43} - R_{42}R_{33} = 0 \quad \text{(IV.6)}$$

When matrices such as $\mathbf{R}_{BORE}$ (equation 5.7) and $\mathbf{R}_{INF}$ (equation 5.8) are computed using particle tracking codes such as CASINO, it is good practice to verify whether they satisfy the applicable conditions. This check is a good method for determining whether a computed transport matrix represents a physically realizable system or not.

The determinants of $\mathbf{R}_{BORE}$ and $\mathbf{R}_{INF}$ are 1.00013 and 0.997276, respectively. These values are sufficiently close to one to be considered acceptable. As pointed out in [45], $\mathbf{R}_{BORE}$ and $\mathbf{R}_{INF}$ are not expected to satisfy the symplectic conditions because they describe linear transport, in terms of (x, x') and (y, y'), to and from a point, the inflector entrance scintillator position, where (x, x') and (y, y') are not the proper set of canonical variables. However, the product $\mathbf{R}_{INF}\cdot\mathbf{R}_{BORE}$ describes transport from the entrance of the cyclotron's axial bore to the inflector exit, and (x, x') and (y, y') are the proper sets of canonical variables at both of these points. Therefore, $\mathbf{R}_{INF}\cdot\mathbf{R}_{BORE}$ which is given by

$$R_{INF}\cdot R_{BORE} = \begin{pmatrix} 0.28324 & 11.618 & -0.0226205 & 7.27393 \\ 0.03192 & 3.9107 & -0.0231161 & -4.11741 \\ 0.54286 & 45.459 & 0.655099 & 85.8719 \\ 0.037044 & 3.5835 & 0.055529 & 8.4051 \end{pmatrix}, \quad \text{(IV.7)}$$

should satisfy the determinant condition and the symplectic conditions.

The determinant of $\mathbf{R}_{INF}\cdot\mathbf{R}_{BORE}$ is 0.997405, which is acceptable. The symplectic equations resulted in the following values: S1 = 0.998174, S2 = 0.999074, S3 = 0.000052, S4 = -0.016649, S5 = -1.916820 and S6 = -0.003355. These values are all acceptable except for S5. After some experimentation, it was found that S5 is very sensitive to slight changes in the $\mathbf{R}_{INF}\cdot\mathbf{R}_{BORE}$ matrix elements. A slight adjustment of the elements of $\mathbf{R}_{INF}\cdot\mathbf{R}_{BORE}$ to the values shown in

$$R_{ADJUSTED} = \begin{pmatrix} 0.28324 & 11.618 & -0.02262 & 7.274 \\ 0.03192 & 3.9107 & -0.023116 & -4.1174 \\ 0.54286 & 45.459 & 0.6551 & 85.337 \\ 0.037044 & 3.5835 & 0.055529 & 8.4051 \end{pmatrix} \quad \text{(IV.8)}$$

resulted in an acceptable determinant of 1.0269 and symplectic equations with the reasonable values of: S1 = 0.998176, S2 = 1.028780, S3 = 0.000052, S4 = 0.003170, S5 = -0.000084 and S6 = -0.003360. The differences between the elements in equations IV.7 and IV.8 are small, and are less than the uncertainty in each of the elements. Therefore, $\mathbf{R}_{INF} \bullet \mathbf{R}_{BORE}$ is deemed to satisfy the determinant condition and the symplectic conditions (at least to within the bounds of computational errors), which indicates that this matrix represents a physically realizable transport process.